University of Nottingham
UK | CHINA | MALAYSIA

Towards optimised portable quantum technologies via additive manufacturing

Author:
Somya H. Madkhaly

Main supervisor:
Lucia Hackermüller

A thesis submitted to the University of Nottingham for the degree of Doctor of Philosophy.

Cold Atom Research Group
School of Physics and Astronomy

October 20, 2022

To my family.

Abstract

Cold atom experiments open wide prospects for applications in metrology, quantum computing, quantum information processing, and many other fields. They also present a promising avenue for experiments in fundamental physics, such as testing new states of matter like Bose-Einstein condensates, the precision probing of gravity and general relativity, and simulations of condensed matter. The first step of most cold atom-based experiments and applications is to form magneto-optical traps (MOT). Typically, these experiments are bulky, complicated, high-cost, and usually occupy room-size benches of optical elements. Nevertheless, because these experiments serve as the foundation for future generations of quantum technologies, there is growing interest in utilising them in real life applications.

We exploit the method of additive manufacturing to build a portable and compact cold atom system that outperforms conventional apparatus in terms of size, weight, power, and cost (SWAP-C), all of which are critical criteria for portable quantum technologies. By demonstrating the successful operation of the first AM UHV chamber, and AM optical frameworks for frequency stabilising and MOT beams' power distribution, we prove how the AM approach, when combined with optimisation algorithms, enables radical mass reduction and offers superior stability and performance.

Our compact device described herein has a volume of less than 5% of the total volume of conventional cold atom systems. The device is $55\times60\times45\,\mathrm{cm}^3$ in size, and weighs $\sim3.2\,\mathrm{kg}$ (excluding commercial components). Using the permanent magnetic field generated purely from an array of neodymium magnets, the apparatus is capable of creating magneto-optical traps of $>2\times10^8$ ^{85}Rb atoms in the AM UHV chamber. By characterising the response of the system to changes in environmental temperature between 10 and 30 °C and exposure to vibrations between DC to a few tens of kilohertz, the reliability of our system to operate in outdoor applications is proven.

To sum up, the miniaturisation of cold atom setups is critical for various experiments and applications, as existing conventional arrangements are large, complicated, and extremely sensitive to even minor environmental fluctuations. By leveraging the advantages of the AM approach, our system addresses these issues and complies with SWAP-C requirements. The results presented in this thesis will be of great interest to the community of quantum technology, UHV, and a broader range of atomic and optical physics researchers.

Acknowledgements

I would like to express my sincere appreciation and gratitude to everyone helped in this thesis throughout the five years of my PhD study. Thank you very much to:

- My supervisor, Dr. Lucia Hackermüller, who has been a tremendous source of help, support, and encouragement. Thank you so much, Lucia, for giving me the opportunity to work in the exciting, stimulating, and promising fields of cold atom and portable quantum technologies. I will remain grateful to you, for your effective supervision and understanding.
- My examiners, Dr. Michael Holynski and Dr. Kasper Jensen, for the instructive viva voce and invaluable feedback that greatly aided me to improve and submit a polished version of my thesis.
- Dr. Nathan Cooper, the main postdoctoral researcher on this project, for consistently providing insightful ideas and unconventional solutions to the lab issues.
- Elisa Da Ros, for proof-reading my thesis. Thank you, Eli, for being a wonderful friend, an honest mentor, and an excellent cake maker.
- Vineetha Naniyil, for her assistance and patience in teaching and sharing her knowledge with me in my first year in the lab.
- Craig Colquhoun, my only Scottish friend, for his enormous help in the lab, despite his brief time as a researcher in the group, and above all, for his kindness and generosity.
- All members of the cold atom group: Bethany, Hayat, Bradley, Sindhu, Danielle, Guy, Lucas, David, Matt, Jamie, Tadas, Vilius, Clément, Pierre, and for the friends in the other groups in the department: Manon, Nouf, Maryam, Manal, Amra, Maha, Kholoud... and everyone else whose name I may have forgotten because of my bad memory. Thank you, everyone, for the enjoyable time, chatting, laughing, and venting about our labs and experiments during lunch, coffee, cake, and break times, inside and outside the school.
- The technicians and administrators in the School of Physics, who made much of the work of this thesis easier and doable.
- Dr. Mohamed Qasem, for his enthusiasm and support for science and technology, and for using his social media publicity to help me introducing the field of cold atoms to the Arab scientific community.
- My lifetime friends, in the UK, Saudi Arabia, the US, and anywhere else, who believed in me and have been a great source of support and a shoulder to cry on.

- The Saudi Arabian Ministry of Education for the fully funded, ten-year scholarship to pursue my graduate studies.

A very special thank you to the supportive and precious person who asked not to be named but knows well that their imprint is engraved in my heart and soul.

Warmest, most profound, and heartfelt thanks to my siblings, with whom I shared the journey of studying in Nottingham, my life and study buddies: Asma, Ali, Abdullah, and Sara. Thank you for everything you've done to make my life in the UK easier and more bearable. And to the rest of my family in Saudi Arabia: my mom Fatima, my dad Hadi, my sisters Nusaiba and Hafsa, and my brother Abdulmajeed. Thank you all for always being the sturdy back I lean on when I'm weak and for the steadfast spiritual and moral support during the whole decade I was away: *I dedicate this thesis to you.*

Contents

List of Tables

List of Figures

Chapter 1

Introduction

It is extremely difficult to observe tiny objects moving randomly at high speeds with precision and subtlety. At room temperature, these particles, referred to as atoms, move at hundreds of metres per second. The most effective way to study the behaviour of atoms is to keep them still, hence the need for what are known as 'atomic traps'. The magneto-optical trap (MOT) has played a significant role in achieving this goal, and it has proven to be an essential and useful tool in the field of atomic physics.

The magneto-optical trap has progressed from being a research tool within the laboratory to being a critical element in experiments and applications that extend beyond the confines of laboratories. However, this transfer process is fraught with challenges that need to be resolved, which are still being addressed to this day. The purpose of this thesis is to demonstrate that optimised 3D-printed components can be used to fabricate MOT systems that satisfy the size, weight, power, and cost (SWAP-C) requirements for portable cold atom-based devices, thereby paving the way for the expansion of these experiments into practical technologies, including applications beyond the planet Earth.

1.1 Ultracold Atom Overview

Although the field of cold atoms is still a relatively young branch of research [1–5], it has already rapidly grown to be a multidisciplinary field with multiple

subfields and aims. It may be difficult to discuss each subfield in detail, but describing the commonalities will give a general idea of the domain of cold atoms in a nutshell: the manipulation of atoms using an external electromagnetic field.

Atoms are a useful tool for physicists, since they exhibit repeatable behaviour and interact consistently with light, making them an ideal option for applications such as sensing and metrology. Additionally, the precise control of atoms and the measurement of their interactions via magnetic or electrical manipulation have proven to be promising tools for quantum mechanics applications such as quantum computation and simulation.

Recently, there has been a drive to begin developing experimental atomic systems for use as tools outside of lab environments, and thus the distinction between these subfields has become increasingly complex. There are often obvious elements in common between these systems, and these common elements are often identified, arranged, simplified, and miniaturised individually to pave the way towards a truly portable atomic and quantum device.

The work here presented is a part of this new direction of research, which covers the gap between pure fundamental physics and applied systems engineering. Specifically, it investigates the pursuit of an integrated cold atom source through additive manufacturing (AM) processes which include all parts of cold atom devices: lasers, optical and magnetic components, and stabilisation electronics, as well as introduces the first successful ultra-high vacuum (UHV) chamber.

1.1.1 Atomic Traps

Atomic traps have been used for almost three decades. These traps come in various types, each with distinctive properties. Existing traps that confine atoms using lasers, optical or magnetic fields, or a combination of the two, have become standard instruments for the construction of all cold atom experiments.

Among the many types of atomic traps available, the magneto-optical

trap, which uses a combination of lasers and magnetic fields, has become the essential tool for cooling and trapping neutral atoms. The MOT has grown in popularity as the starting point for many cold atom experiments. For example, formation of Bose-Einstein condensate (BEC) begins with a MOT cloud, which is then transferred to a magnetic trap and then further cooled by evaporation. Moreover, slow light experiments can be performed on BEC clouds [6] as well as to investigate other nonlinear light-matter interactions, such as electromagnetically induced transparency (EIT) [7]. Atomic traps are also used in experiments of atomic interferometry [8–10], quantum computing [11–13], fundamental physics research, such as the study of quantum gases in microgravity [14], and many more.

Magneto-optical traps come in a variety of shapes, designs, and geometries. They can be 2D MOTs, in which the atoms are confined in two dimensions through orthogonal beams, or 3D MOTs, composed of three pairs of beams [15]. Figure 1.1 shows examples of some MOT geometries: (a) conical MOT [16], (b) near the surface (chip) MOT [17], (c) ball-lens MOT [18], (d) grating MOT [19], and (e) pyramidal MOT [20, 21]. Although MOTs have become widely common and have evolved in design and construction, they are still complex and not very straightforward to build. Furthermore, despite the vast customisation options available when planning a MOT setup, they are not yet commonly accessible for 'off-the-shelf' purchasing.

1.2 Overview of portable quantum devices

Using exotic quantum phenomena in real-life applications has been a dream since the discovery of quantum mechanics a century ago. In the past few decades, serious work has been done to transfer quantum applications outside of the walls of laboratories. This work is still ongoing today, despite the challenges associated with the complex nature of such experiments.

Cold atom-based experiments play a critical role in the realm of quantum technology and its numerous applications. These experiments, however,

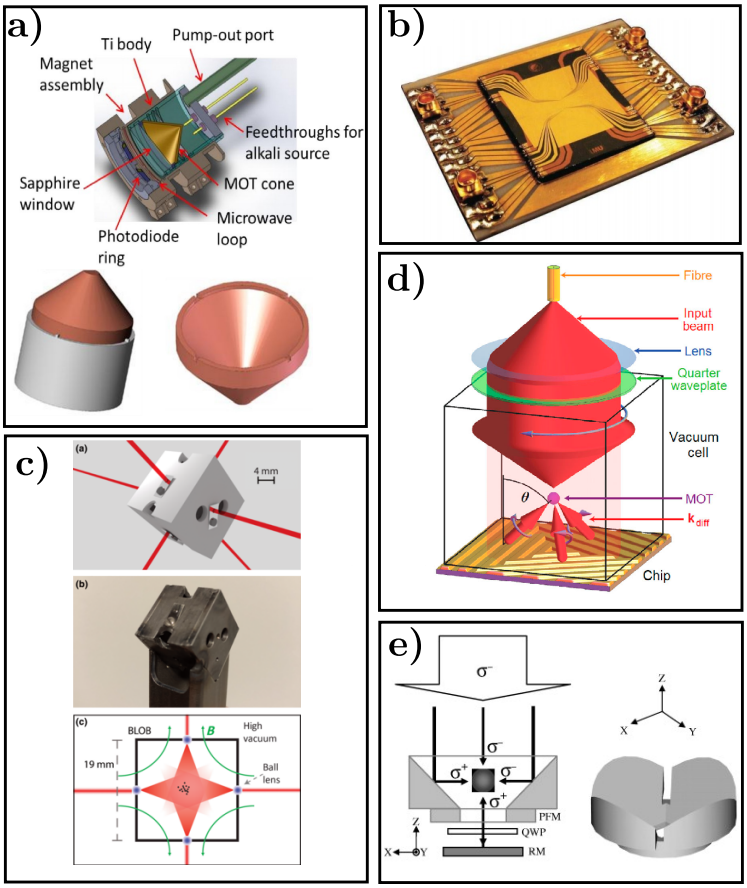

Figure 1.1: *Different configurations of magneto-optical traps: cone MOT [16] (a), chip MOT [17] (b), ball-lens MOT [18] (c), grating MOT [19] (d), and pyramidal MOT [21] (e).*

are extremely difficult and complicated to carry out outside of the laboratory, due to the complexity of their design and the sensitive components they involve. Optimising and reducing the size of integrated cold atom sources has been contemplated by developing each part separately. Nevertheless, experimental advances in this field have reached a point of maturity where their implementation in practical applications is imminent [22–24].

Numerous configurations of portable and compact quantum devices, which typically occupy much less than one cubic metre of space, have been developed in recent years for use in applications ranging from fundamental physics research [25–27] to commercial quantum technologies [28]. Space-borne atom interferometers [29] and the first successful demonstration of BEC in a drop tower and onboard a sounding rocket have also been achieved by the Quantengase Unter Schwerelosigkeit (QUANTUS) and the Materiewelleninterfer-

ometrie Unter Schwerelosigkeit (MAIUS) projects [30–33]. The Cold Atom Space Payload (CASPA) project, funded by Innovate UK and Engineering and Physical Sciences Research Council (EPSRC), has been operated onboard a 6U CubeSat to be used as a gravity sensor for future Earth observation missions [34]. The Cold Atom Laboratory (CAL) onboard the International Space Station (ISS) to produce BEC is another example of a robust portable cold atom system [14, 35]. Similarly, an in-orbit cold atom clock is currently operating onboard the Chinese Space Laboratory Tiangong-2 [36]. Gravitation and spacetime studies based on a correlated array of atom interferometers have been proposed by the European Laboratory for Gravitation and Atom-Interferometric Research (ELGAR) [37]. The atomic gravimeter for civil engineering [38] and the cold-atom device for an unmanned aerial vehicle [39] are both promising projects involving portable cold atom systems being developed at the University of Birmingham. In addition, the mass production of cold atom chips could be viable in the near future, as University of Strathclyde is developing a chip-scale laser cooling platform consisting of a diffraction grating MOT (gMOT) chip and MEMS components [40].

The aforementioned projects are just a few examples of the state-of-the-art portable cold atom systems from various research institutions around the world. This industry is growing rapidly, and as time goes on, new configurations with improved capabilities and fewer challenges are being introduced. However, a realistic handheld quantum product won't be feasible until an integration equivalent to that of chip-scale atomic clocks is accomplished [41, 42] with an enhanced technological readiness level (TRL) [24, 43].

1.2.1 Magnetic Field Generation

The generation of quadrupole magnetic field with a central field zero is a necessary component for MOT to aid the confinement of the atoms together with the laser beam. The work on shaping the magnetic field required to form atomic traps has developed in many ways since the invention of laser cooling

and trapping. Attempts have been made to generate magnetic potentials for MOT using near-surface free-standing wires, which is thought to be advantageous for applications in complex and miniaturised setups, due to its proximity to the atomic cloud [44–46]. As a result, atom chips, which employ thin layers of metallic conductors to produce traps that are just millimetres above the surface, have been developed [47–49].

Recent research has proposed the use of AM technology to miniaturise and optimise magnetic field sources for atomic traps, and the fabrication of 3D-printed current-carrying structures and magnetic shielding for MOTs has been accomplished [50–52]. In addition to the extreme SWAP reduction offered by these AM coils, they have demonstrated unprecedented efficiency in producing dense atomic clouds [50].

1.2.2 UHV chambers

An ultra-high vacuum (UHV) environment ranging between $\sim 10^{-7}$ to $\sim 10^{-11}$ mbar is a key element for the efficient cooling, trapping and manipulation of atoms. This condition is necessary to prevent atomic losses from the trap caused by atomic collisions and heating processes. However, in addition to being high-power consuming, conventional UHV chambers are typically made of stainless steel, making them bulky and very heavy. Therefore, when considering out-of-lab operation, the miniaturisation of UHV chambers is crucially important, yet a major challenge for several reasons, including design constraints and pumping limitations. Numerous techniques have been suggested for overcoming these constraints, with overall chamber size reduction being one of the simplest and most straightforward solutions [53, 54]. However, this approach may not be optimal, as chambers become more difficult to machine as they get smaller.

Other alternatives and options have also been considered, including using AM UHV-compatible parts [55], novel pumping methods based on passive adsorption elements [56, 57], smaller sizes of titanium or stainless steel vacuum chambers [53], or non-metallic UHV-based parts, such as glass [58, 59] and

quartz [60]. Additionally, the atom source, which is typically a hot dispenser, has been improved by reshaping the dispensers [61, 62], emitting the atoms into the chamber using ultra-violet light [63], or using a magnetic-less ion pump based on a nanostructured Si electron source and a Ti particle collector [64].

Furthermore, pumps and pressure gauges are essential UHV components used in cold atom experiments to monitor the pressure and maintain the UHV conditions. Nevertheless, these instruments are typically bulky and power-hungry, rendering them impractical for transportable applications. Therefore, to enhance the portability of cold atom setups, it is imperative to replace these key devices with alternatives that fulfill the requirements of SWAP reduction. It has long been understood that the pressure affects the lifetime of an atom in a cold atom trap, and this relationship can be utilised in reverse to reliably measure the pressure [65, 66].

The method of using atom loading dynamics to determine the pressure in the MOT location has been characterised in Ref.[67]. This approach can further be used in several applications, including the atom number estimation [68], the study of atomic collisions and resulting loss rates [66, 69, 70], characterisation of MOT trap depth [71, 72], and leaks and outgassing detection to test the vacuum quality [73]. This demonstrates the advantage of this approach for use in portable systems, as it enhances the compactness of cold atom setups by allowing for the elimination of heavy vacuum devices.

The characterisation of MOT loading curves has already been used in several cold atom systems that are meant to operate outside walls of the laboratory [74, 75], and other mobile setups, such as in space applications [76–78], quantum and gravity sensors [60], quantum communication technology [79], and others. For similar purpose, the method was used in our system [80] to evaluate the atom number and estimate the upper limit of the background vacuum pressure in the 3D-printed UHV chamber [81].

1.2.3 Optical Systems

In common cold-atom setups, an optical system of three pairs of laser beams and a number of optical guiding parts is required to create the MOT. These optical subsystems, in some laboratories, extend across a bench or several benches and can reach the size of an entire room. Therefore, shrinking the size of the optical system is crucially necessary to develop compact cold atom technologies.

Bespoke and commercially available optics and optomechanics and the use of microsystems technology [82–85] allow for higher packaging density by providing space-saving solutions. The use of fewer optical components to realise compact setups is also considered, similar to the use of 2D MOT realised three decades ago, in which four beams were used instead of six beams, as in the standard 3D MOT [86, 87].

In a configuration comparable to the standard 3D MOT, which uses six beams, mirror MOT (MMOT) employs only four incident beams to create an optical overlap volume, with the other two generated by the reflected orders [88–90]. Different types were developed for MMOT, such as hybrid-MOT and vortex-MOT [91], for applications with restricted optical access to the vacuum chamber.

The large and bulky refractive optics commonly used in cold atom experiments for beam alignment, shaping, and polarisation hinders their practical use in portable applications. The miniaturisation of these optics into diffractive optical elements (DOEs) and meta surface materials has facilitated the simplification of devices and mass production of lenses, gratings, and mirrors. The DOEs and meta surface materials have been demonstrated in compact atomic applications, including chip-scale alignment [92], atom-embedded optical elements [93], cold-atom waveguides [94], and to demonstrate the simplified and innovative geometries of MOT systems [95, 96].

The use of one beam to confine and cool the atoms instead of two or

three light sources plays an important role in downsizing the optical systems in particular and forms the basis of a large number of miniature quantum technologies. A variety of single-beam arrangements have been realised, such as some of the examples stated in Sec. 1.1.1 [20, 21, 97, 98], in which all required beams with correct optical polarisations can be generated from a single light source. In these structures, atoms are trapped using a single light source that is reflected in specific geometric patterns around the point where the atomic cloud is formed [19, 99, 100]. This has found application in interferometers [101] and gravimeters [102], among others.

The gMOT mentioned in Sec. 1.2 is a promising chip-scale technology that outperforms the tetrahedral and pyramidal systems in terms of attainable atom number [19]. The gMOT has demonstrated excellent results in cooling and trapping atoms, in addition to its adaptability to a variety of portable and lab-based configurations and setups [57, 103, 104].

Cold atom experiments utilise spectroscopic techniques for laser referencing to atomic wavelengths in atomic vapour, which typically occupy a significant portion of optical systems [105]. For this, on-chip integrated laser systems for portable quantum applications [106–108] have been successfully achieved. Microfabricated [109] and laser-written [110] vapor-cells are also examples of extremely compact precision spectroscopy of atomic vapours that can be integrated with chip-scale systems. In addition, the realisation of robust optical frequency references for laser stabilisation that has been achieved for applications in space [111–113], and as commercial laser frequency stabilisers [114].

1.3 Additive manufacturing

Additive manufacturing (AM) is defined as the process of joining materials through layer-by-layer shaping to make objects from 3D data models, as opposed to subtractive manufacturing, which involves cutting and subtracting parts from large blocks [115]. The concept of mass production has been around since the twentieth century, when Henry Ford introduced the idea of a moving

assembly line, which revolutionised manufacturing. The first 3D printer in its current form appeared in 1984, but due to its high cost in those days, it was not available on the public market until the beginning of the twenty-first century [116]. The term AM or 3D-printing nowadays covers a broad range of techniques, from the manufacture of nanoscale devices to the printing of entire components for aerospace or industrial applications.

Additive manufacturing is a promising technology that has several advantages over traditional manufacturing [117, 118], including design freedom, the scalable production of individually customised components, and easy SWAP-C reduction. Methods of AM have evolved to include fused deposition modeling (FDM), stereolithography (SLA), and selective laser melting (SLM), to name a few [119]. Although many types of materials have been employed in 3D printing, metal AM manufacturing had been thought impossible for a long time, for reasons related to the rough surfaces, pores, and limited hardness of the materials produced by AM processes. Until this day, metal-based AM is still limited to a few types of metallic alloys, which are Ti-6Al-4V, TiAl, stainless steel, Inconel 625/718, and Al-Si-10Mg [120, 121], from which the latter the UHV chamber in our system was fabricated [81].

1.3.1 AM in Portable QT

There are certain constraints and obstacles when considering 3D printing over traditional manufacturing, such as device dimension constraints and material selection. Ultracold atom experiments, in particular, require UHV-compatible structures that do not desorb particles into the vacuum, are dense enough to prevent particle passage, and can withstand temperatures of up to 200°C. In addition, portable quantum apparatuses demand robust and durable components for use in unstable and changeable environments outside of laboratories. For the requirements of UHV conditions to be met, selective laser melting (SLM) has been presented as the candidate technique. This is a method of 3D printing that utilises a high-power-density laser to melt and fuse metallic

powders, resulting in monolithic parts with 100–250 μm resolution [122].

The employment of 3D printing in the production of UHV components has recently been studied [123]. The testing of SLM-manufactured with a stainless-steel powder tubes has been done [124], yet the UHV compatibility of the AM tubes could not be confirmed, due to the poor quality of the flanges used in the experiment. On the other hand, 3D-printed silver and titanium samples placed in a UHV chamber exhibited UHV compatibility by withstanding a maximum pressure in the 10^{-10} Torr range [123, 125]. Moreover, 3D-printed magnetic shielding and vacuum flange demonstrator devices constituted the first successful demonstration of the suitability of the AM technique for use in quantum sensors [55], and the development of an UHV-compatible AM cold atom source with low power consumption [50].

In addition to the use of the AM technique in UHV applications, it has been considered for optimising the performance of portable quantum sensors. For example, designs for 3D-printed MOTs made of electrical current-carrying components have been realised [126]. The 3D printing approach has been also used to make optically active structures in diamond, which is a competitive candidate in the field of quantum technologies based on semiconductors [127]. Additionally, AM has been utilised to fabricate optical elements such as 3D-printed micro-optics for quantum technologies [128], and 3D-printed polymer photodetectors [129]. In addition to the above-mentioned efforts, this thesis highlights the use of AM techniques to optimise portable cold atom sensors.

1.4 Thesis Overview

This thesis aims to examine the feasibility of the technology of additive manufacturing to create complex and bespoke components for realising portable cold atom devices. Through the successful creation of a SWAP-C MOT and the findings reported in the thesis, the practicality of using AM technology to enable the production of optimised and high-performance components without the constraints associated with traditional manufacturing is demonstrated. It

is hoped this research will contribute to the study of AM adaptability in atomic sensors.

Some chapters of the thesis are based on published materials. All of the publications included herein investigated various AM-fabricated components and optical techniques in an effort to realise a performance-optimised cold atom source for portable quantum technologies. Chapters 4–6, in particular, shed light on the capability of 3D printing to supply robust and SWAP-C components for real-world quantum devices, while the preprint in Chapter 7 assesses an optical approach that can be implemented in miniature systems to aid both compactness and laser stabilisation.

The components of the experimental setup described in this thesis were designed collaboratively by the University of Nottingham and Added Scientific Limited. Lawrence Coles and Sarah Everton of Added Scientific Limited designed the apparatus, which was installed, operated, and tested, at the University of Nottingham under the direct supervision and assistance of Dr. Lucia Hackermüller and Dr. Nathan Cooper,except for the magnetic field source, which Dr. Christopher Morley designed under the supervision of Prof. Mark Fromhold.

The proof of principle of additive manufacturing was the primary outcome of 'The OPTAMOT Project', which stands for **OP**timised designs for **A**dditively manufactured **M**agneto **O**ptical **T**raps, a collaborative work with the industry partner Added Scientific. After the successful creation of a 3D-printed cylinder trap with the aid of the same manufacturer [50], the idea was conceived to use the same AM technology to create a UHV containing environment [81]. It was then followed by a series of meetings and discussions aimed at expanding 3D printing techniques to fabricate polymer-optimised frameworks for cold atom subsystems, which resulted in the successful production of published works [80, 81, 130].

Chapter 2: Theoretical Background – In this chapter, the theoretical background of the experiments covered in this thesis is reviewed. The chapter

begins with an introduction on atom-light interactions, the forces imposed by the electromagnetic fields on atoms, and on how to exploit these forces to confine and manipulate atoms spatially. Also, it provides a brief summary about atomic collisions, loading and loss dynamics in MOTs, and the relationship of this dynamic to determining background pressure.

Chapter 3: MOT characterisation and background pressure estimation – This chapter describes experiments with the AM-based device and other remaining measurements which are not addressed in the subsequent chapters based on published work. Additionally, it provides a general overview of the setup and discusses the methods followed in the system, such as laser frequency stabilisation techniques. The chapter also demonstrates the MOT characterisation and how to determine the background pressure using MOT loading curves.

Chapter 4: Additively manufactured ultra-high vacuum chamber for portable quantum technologies – This chapter is dedicated to the successful production of an UHV chamber made with AM technology. The chamber design and manufacturing techniques and processes are discussed in detail, and images of surface tests are reviewed, as well as the preliminary results of temperature and pressure tolerance tests. A cloud of ^{85}Rb atoms trapped into a MOT inside the UHV chamber is also shown as proof of its potential as an alternative candidate for bulky metal UHV chambers in portable quantum technology applications based on cold atom experiments.

Chapter 5: Performance-optimised components for quantum technologies via additive manufacturing – This chapter discusses our portable cold atom system, which is mainly composed of components made with AM technology. In addition to the UHV chamber characterised in the previous Chapter 4, this Chapter presents the improvement and development of 3D-printed parts, such as optical elements and lasers mounts. It is demonstrated that the size, weight, power and cost of traditional cold atom systems can be reduced by $\sim$80% via using the AM technique. This is achieved by

reviewing results such as the spectroscopic response to thermal changes, the $\vec{\mathbf{B}}$-field generated by neodymium permanent magnets, and dense atomic clouds of $\sim 2 \times 10^8$ ^{85}Rb atoms.

Chapter 6: High-performance, additively-manufactured atomic spectroscopy apparatus for portable quantum technologies – This chapter is an extension of the previous Chapter 5, as it is another further proof of the efficiency of 3D printing in quantum technologies. The chapter is devoted to characterising a triple-frequency optical atomic reference, also made with the AM technique. The AM framework has been subjected to rigorous tests, including exposure to various environmental (thermal) and mechanical changes. The results of these tests are reviewed, showing that the AM mount has superior stability comparable to the heavier, more expensive frequency references available.

Chapter 7: Dual-frequency Doppler-free spectroscopy for simultaneous laser stabilisation in compact atomic physics experiments – This chapter represents the dual-frequency spectroscopy method using two counter-propagating laser beams through a common atomic vapour cell tuned to two atomic transitions. The chapter reviews theoretically and experimentally the advantages of the dual spectroscopy technique over the standard spectroscopy method in enhancing the stabilisation of the laser frequency. The potential of using this approach in compact systems for further size, weight, power and cost reductions is also demonstrated in the chapter.

Chapter 8: Conclusion – This chapter provides a summary of all the chapters, and an overview of the necessary future steps for developing the apparatus.

Appendices – Supplementary materials and overviews of the side projects undertaken during my PhD study are appended to the end of the thesis. A summary of the ^{6}Li D_1 line sub-Doppler cooling project is provided in Appendix A. After that, Appendix B briefly discusses the experiment of winding the MOT coils intended for use with the AM chamber and the measurement

of the generated magnetic field. Next, Appendix C contains illustrations and CAD drawings of the AM parts and electronics. Finally, additional information regarding the stability tests of the AM spectroscopy apparatus covered in Chapter 6 are provided in Appendix D.

1.5 Publications

During my PhD, I co-authored the following papers:

- [81] N. Cooper, L. Coles, S. Everton, I. Maskery, R. Campion, S. Madkhaly, C. Morley, J. O'Shea, W. Evans, R. Saint, P. Krüger, F.Oručević, C. Tuck, R. Wildman, T. Fromhold, and L. Hackermüller, "Additively manufactured ultra-high vacuum chamber for portable quantum technologies." Additive Manufacturing, **40**, 101898, (2021).

- [80] S. H. Madkhaly, L. A. Coles, C. Morley, C. D. Colquhoun, T. M. Fromhold, N. Cooper, and L. Hackermüller. "Performance-optimized components for quantum technologies via additive manufacturing." PRX Quantum **2** (3) 030326, (2021).

- [130] S. H. Madkhaly, N. Cooper, L. Coles, and L. Hackermüller. "High-performance, additively-manufactured atomic spectroscopy apparatus for portable quantum technologies." Optics Express, **30**, 25753, (2022).

- [131] N. Cooper, S. Madkhaly, D. Johnson, D. Baldolini, and L. Hackermüller, "Dual-frequency doppler-free spectroscopy for compact atomic physics experiments," arXiv preprint, arXiv:2106.11014, (2021).

Statement of contribution

The research presented in this thesis reflects a significant portion of the author's experimental work during her PhD study. Except for the four publications listed above, which are co-authored and included in the thesis in separate chapters (4–7), the author's contribution has to be highlighted. The author

contributed to Chapter 4 by assisting with the assembly of the AM chamber into the UHV setup, baking out, taking pressure readings, forming atomic clouds, and reviewing the paper content. Installing the AM-based apparatus, including the optical system, and ensuring that its performance was comparable to conventional systems was the author's contribution to Chapter 5. In addition to the results and graphs in the section on magnetic field generation, the author co-wrote, reviewed, collected data, and created graphs for the majority of the paper and its supplementary materials/appendices. Except for Fig.5 and its explanatory paragraphs, the author's contribution to Chapter 6 consisted of writing, reviewing, collecting data, and creating graphs and CAD drawings for the majority of the paper. In Chapter 7, the author assisted in creating Fig.1 and reviewing the content of the manuscript.

Chapter 2

Theoretical Background

Cold atom experiments involve the trapping, cooling and probing of the atoms in the μK regime, close to absolute zero. These experiments demand a great capacity to control and manipulate atoms' positions and momenta, and require an understanding of theoretical concepts of atoms interactions with external fields. This section will discuss the theoretical foundations underlying the experiments discussed in this thesis.

2.1 Atom-light interaction

The fundamental process of atom-light interaction exerts external forces on the atom and changes the atom's internal states and external degrees of freedom. This process involves light absorption and emission: an atom is stimulated from its ground state to an excited state and spontaneously emits light before returning to its stable ground state. Atom-light interaction processes can be treated semi-classically by considering a 'quantum mechanically described' two-level atom interacting with an external 'classical' electric field.

For a two-level atom of ground state $|g\rangle$ and excited state $|e\rangle$ interacting with a near resonant classical electric field $\vec{\boldsymbol{E}} = \hat{\boldsymbol{\epsilon}} E_0 cos(kr - \omega t)$ where $\hat{\boldsymbol{\epsilon}}$ is the unit polarisation vector, k is the wavevector, and ω is the angular frequency,

the Hamiltonian describing the atom is given by [132]:

$$H = H_{atom} + H_{atom-field} = \hbar\omega_0|e\rangle\langle e| - \boldsymbol{d}\cdot\vec{\boldsymbol{E}}, \tag{2.1}$$

where H_{atom} represents the unperturbed Hamiltonian, $H_{atom-field}$ is the time-dependent Hamiltonian, which describes the interaction of the atom with the oscillating field, and $\boldsymbol{d} = -e\boldsymbol{r}$ is the electric dipole moment.

By simplifying the atom to a two-level system, it is assumed that the driving field frequency is close to the atomic transition frequency, allowing for the rotating-wave approximation to be made. In this approximation, the fast oscillating terms in the interaction Hamiltonian are excluded, which holds true as long as we are interested in the interaction of 'slow' signals with frequencies below optical frequencies. The Rabi frequency Ω, which represents atom-field coupling, can be defined by [133]:

$$\Omega = \frac{-\langle g|\hat{\boldsymbol{\epsilon}}\cdot\boldsymbol{d}|e\rangle E_0}{\hbar}. \tag{2.2}$$

In the rotating frame approximation, the Hamiltonian can be written as:

$$\tilde{H} = \hbar\Delta|e\rangle\langle e| + \frac{\hbar}{2}[\Omega^*\sigma + \Omega\sigma^\dagger], \tag{2.3}$$

where the lowering operator $\sigma = |g\rangle\langle e|$ and the raising operator $\sigma^\dagger = |e\rangle\langle g|$ are used. Solving the time-dependent Schrödinger equation allows for the calculation of the probability of finding the atom in each of $|g\rangle$ and $|e\rangle$ states. Rabi-oscillation occurs when atoms interact with monochromatic light, in which the population oscillates between the two levels. These damped oscillations eventually bring the atom to a steady state, where the decay rate equals the excitation rate. The wavefunction picture does not take into account the decay of the atomic excited state via spontaneous emission processes. Therefore, it is important to replace the wavefunction with the density matrix to obtain a statistical description of atom-light interactions. The density operator ρ is

defined as:

$$\rho = \begin{pmatrix} \rho_{gg} & \rho_{ge} \\ \rho_{eg} & \rho_{ee} \end{pmatrix}, \tag{2.4}$$

where the diagonal terms ρ_{gg} and ρ_{ee} are the probabilities of finding the atom in $|g\rangle$ or $|e\rangle$ states, and the off-diagonal elements represent the coherences. The time evolution of the density matrix is described through the optical Bloch equation, which is governed by Liouville's equation, expressed as [132],

$$\frac{d\rho}{dt} = \frac{i}{\hbar}[\hat{\rho}, \hat{H}]. \tag{2.5}$$

The time evolution can be expanded to include the effect of spontaneous emission:

$$\frac{d\rho}{dt} = \frac{i}{\hbar}[\hat{\rho}, \hat{H}] - \begin{pmatrix} -\Gamma\rho_{ee} & \frac{\Gamma}{2}\rho_{ge} \\ \frac{\Gamma}{2}\rho_{eg} & \Gamma\rho_{ee} \end{pmatrix}, \tag{2.6}$$

where Γ is the decay rate of the excited state and $\hat{H}$ is the time-dependent Hamiltonian, $\hat{H} = \frac{\hbar}{2}\begin{pmatrix} 0 & \Gamma \\ \Gamma & -2\Delta \end{pmatrix}$. The steady state solution of Eq. 2.5 takes the form:

$$\tilde{\rho_{ee}} = \frac{|\Omega|^2/\Gamma^2}{1 + (2\delta/\Gamma)^2 + 2|\Omega|^2/\Gamma^2} = \frac{1}{2}\frac{s}{1 + s + 4\Delta^2/\Gamma^2}, \tag{2.7}$$

where s is the on-resonant saturation parameter, which is defined in terms of saturation intensity I_s as $s = \frac{I}{I_s} = \frac{2\Omega^2}{\Gamma^2}$. The saturation intensity I_s represents the strength of the atomic transition and is defined as:

$$I_s = \frac{2\pi^2\hbar\Gamma c}{3\lambda^3}, \tag{2.8}$$

where the inverse of Γ is the lifetime of the atomic excited state, τ. The saturation intensity I_s for ^{85}Rb D_2 cooling transition is $1.7\,\mathrm{mW/cm^2}$ [134]. The saturation parameter s characterises the atoms occupation in ground or excited states, i.e. when ($s \ll 1$), the atom has a higher probability to be in ground state, while when ($s \gg 1$), the atom has a higher probability to be in

the excited state.

The dipole moment can be expressed as:

$$\boldsymbol{d} = \alpha \boldsymbol{E}, \tag{2.9}$$

where α is the atomic polarisability and it is a complex proportionality constant. For a two-level atom, the polarisability α takes the form:

$$\alpha = i\frac{c\epsilon_0\hbar\Gamma}{2I_{sat}}\frac{(1+i2\delta/\Gamma)}{1+(2\delta/\Gamma)^2+I/I_{sat}}. \tag{2.10}$$

The polarisability α is useful to summarise the atom-light interactions, where from which, the steady-state photon scattering rate R_{sc} can be obtained:

$$R_{sc} = \Gamma\tilde{\rho_{ee}} = \frac{\Gamma}{2}\frac{s}{1+s+4\Delta^2/\Gamma^2}. \tag{2.11}$$

In the case of $s \gg 1$, this can be written as $R_{sc} = \frac{\Gamma}{2}$, since the maximum population of the excited state is $\tilde{\rho}_{ee} = \frac{1}{2}$. The photon scattering R_{sc} has a Lorentzian profile, with width $\Gamma' = \sqrt{\Gamma^2(1+s)}$, where, at low intensities, the profile's width becomes the natural linewidth Γ, while the width becomes power-broadened at high intensities.

2.2 Laser Cooling and Doppler Limit

Laser cooling depend on the forces exerted from atom-light interaction. To understand that, we consider a two-level atom that undergoes an external electromagnetic field [132]. The atom interacts with the light in three ways: photon absorption, spontaneous emission, and stimulated emission. Laser cooling methods rely on photon absorption and the following spontaneous emission process.

When an atom is subjected to a laser field, the process starts with the absorption of a photon of a momentum $\hbar\boldsymbol{k}$, i.e. the photon momentum transfers to the atom. The atom is excited to a higher state and then withdraws

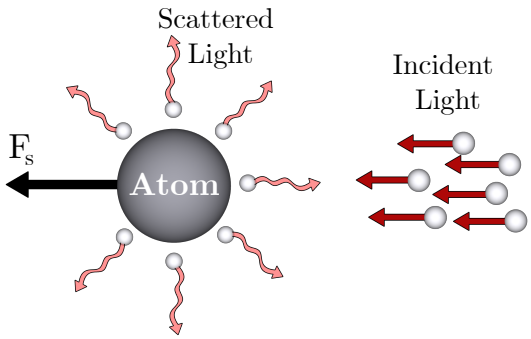

Figure 2.1: *Sketch of the photon momentum transfer that takes place when an atom absorbs photons, yielding a net scattering force in the direction of light propagation.*

back to the ground state and re-emits a photon of a momentum equal to the absorbed one in a random direction – see Fig.2.1. The recoil direction of the atom is considered to be isotropic over many cycles of absorption and emission and it averages to zero, so it can be neglected. The scattering or 'kick' force $\boldsymbol{F}_s$ acts on the atom on the opposite direction of the laser beam is given in terms of the scattering rate and the photon momentum as,

$$F_s = \hbar \boldsymbol{k} \Gamma \tilde{\rho}_{ee}, \tag{2.12}$$

where: $\hbar k$ is the photon momentum, Γ is the natural linewidth, and $\tilde{\rho}_{ee}$ is the probability of the atom to be in the excited state and has been previously defined in Eq. 2.7. In both Doppler cooling and magneto-optical trapping, this force is the most essential element.

To explain the laser cooling mechanism, consider atoms that undergo counter-propagating laser beams with a frequency slightly tuned below the atomic resonance frequency. Each atom in this scenario experiences forces in opposite directions and sees Doppler shifts in the frequencies. An atom moving with velocity $\boldsymbol{v}$ towards light of frequency ω and wavevector $\boldsymbol{k}$ sees the laser frequency as $\omega' = \omega - \boldsymbol{k} \cdot \boldsymbol{v}$, while an atom moving away from light of frequency ω and wavevector $\boldsymbol{k}$ sees the laser frequency as $\omega' = \omega + \boldsymbol{k} \cdot \boldsymbol{v}$. This Doppler effect results in an imbalance in the forces experienced by the atom, thereby dampening its motion. When an atom of velocity $\boldsymbol{v}$ absorbs a photon

of wavevector $\boldsymbol{k}$, a change in the atom momentum by $\hbar\boldsymbol{k}$ occurs. This cooling mechanism is called Doppler cooling because it exploits the Doppler effect, and it is the main working principle applied in cooling and trapping gaseous atoms. However, there is a limit to the temperature that can be achieved using Doppler cooling alone, thus some experiments require the use of sub-Doppler techniques to cool the atoms even further, – see Appendix A.

Due to the recoil heating effect resulting from the random directionality of spontaneous emission processes, the motion of the atom cannot be completely stopped by laser cooling. The temperature at which atoms have an average momentum of one photon recoil $\hbar k$, is called recoil temperature, and given by $T_r = (\hbar k)^2/mk_B$, where k_B is the Boltzmann constant. For ^{85}Rb atoms, the value of this temperature is $T_r = 370.47\,\text{nK}$ [134]. This recoil heating effect is comparable to the rate of cooling at lower temperatures, and eventually, these two competing heating and cooling rates reach and equilibrium resulting in a lower temperature limit for Doppler cooling. The value of Doppler temperature, which is defined as $T_D = \hbar\Gamma/2k_B$, for ^{85}Rb atoms is $145.75\,\mu\text{K}$ [134].

2.3 Rubidium-85

For decades, alkali atoms have been considered the ideal candidate for experiments in atomic and molecular physics and quantum optics. Although they are multi-level atoms, alkali atoms have simple and accessible electronic transitions, due to their property of having only one valence electron in the outer shell [132]. The hyperfine structure, which results from the coupling between the total electron angular momentum $\mathbf{J}$ of the outer electron and the total nuclear angular momentum $\mathbf{I}$, is the most relevant atomic level structure for alkali atoms. The Hamiltonian that describes this interaction is given in terms of the magnetic dipole moment A_{HFS} as:

$$\hat{H}_{HFS} = A_{HFS}\boldsymbol{I}\cdot\boldsymbol{J}. \tag{2.13}$$

The atomic eigenvalues associated with this Hamiltonian can be written in the form:

$$|nIJFm_F\rangle, \tag{2.14}$$

where n is the principal quantum number, and m_F is the projection on the magnetic quantisation axis of the total angular momentum **F**, which is given by:

$$\boldsymbol{F} = \boldsymbol{J} + \boldsymbol{I}, \tag{2.15}$$

where **I** is the nuclear angular momentum, and **J** is the total electron angular momentum, which can be given by:

$$\boldsymbol{J} = \boldsymbol{L} + \boldsymbol{S}, \tag{2.16}$$

where **L** is the orbital angular momentum and **S** is the spin angular momentum. Therefore, the total angular momentum can be represented as $\boldsymbol{F} = \boldsymbol{L} + \boldsymbol{S} + \boldsymbol{I}$. The magnitude of the quantum number **F** ranges through all integer values between $|J - I| \leq F \leq (J + I)$. The energy eigenvalues in m_F are degenerate in the absence of an external magnetic field $\vec{\mathbf{B}}$. In the case of ^{85}Rb ground state, $J = 1/2$ and $I = 5/2$, thus $F = 2$ or 3. While in the excited state of D_2 line ($5^2P_{3/2}$), F takes values of 1, 2, 3, and 4.

In the existence of an external magnetic field, Eq. 2.13 becomes

$$\hat{H}_{HFS} = A_{HFS}\boldsymbol{I} \cdot \boldsymbol{J} - (\boldsymbol{\mu}_I + \boldsymbol{\mu}_J).\vec{\mathbf{B}}, \tag{2.17}$$

where $\boldsymbol{\mu}_I$ is the nuclear magnetic dipole moment and $\boldsymbol{\mu}_J$ is the total magnetic moment. The Hamiltonian of the interaction of atoms with a magnetic field $\vec{\mathbf{B}}$ with quantisation axis taken for example along the z direction, $\hat{H}_{int}$, can be described as:

$$H_{int} = g_F \mu_B F_z \vec{\mathbf{B}}_z, \tag{2.18}$$

where g_F is Landé factor, and $\mu_B = e\hbar/2m_e c$ is the Bohr magneton. In the case of weak magnetic fields, the interaction Hamiltonian H_{int} can be treated as a perturbation of the hyperfine structure Hamiltonian H_{HFS}, and the Zeeman splittings in the energy levels can be approximated to the first order as:

$$\Delta E_{Zeeman} = g_F \mu_B m_F \vec{\mathbf{B}}_z. \tag{2.19}$$

Due to its laser-cooling-friendly atomic level structure, rubidium is the most widely used element in atomic physics experiments [135]. It is found naturally in two isotopes: ^{85}Rb and ^{87}Rb. Although both isotopes are available in the chamber in our lab, ^{85}Rb atoms are trapped in the MOT in our experiment.

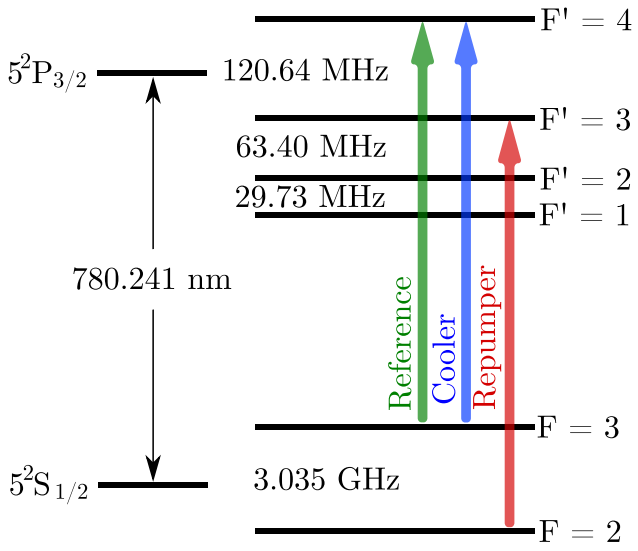

Figure 2.2: *^{85}Rb energy levels of D_2 line transitions. Atomic transitions used for MOT are $F = 3 \rightarrow F' = 4$ as the cooler, and $F = 2 \rightarrow F' = 3$ as the repumper and the reference adapted from Ref. [134].*

The diagram of hyperfine structure energy levels of ^{85}Rb D_2 line: $5S_{1/2}$ ground state to $5P_{3/2}$ excited state based on Ref. [134] is shown in Fig. 2.2, and the calculated Zeeman splittings of ^{85}Rb D_2 manifolds in the existence of an external magnetic field are depicted in Fig. 2.3. The cooling and trapping transition is $F = 3 \rightarrow F' = 4$, and spontaneous emission from the $F' = 4$ state to any ground state, other than $F = 3$, is dipole forbidden. It is a so-called closed transition, which enables the atom to scatter light over many events

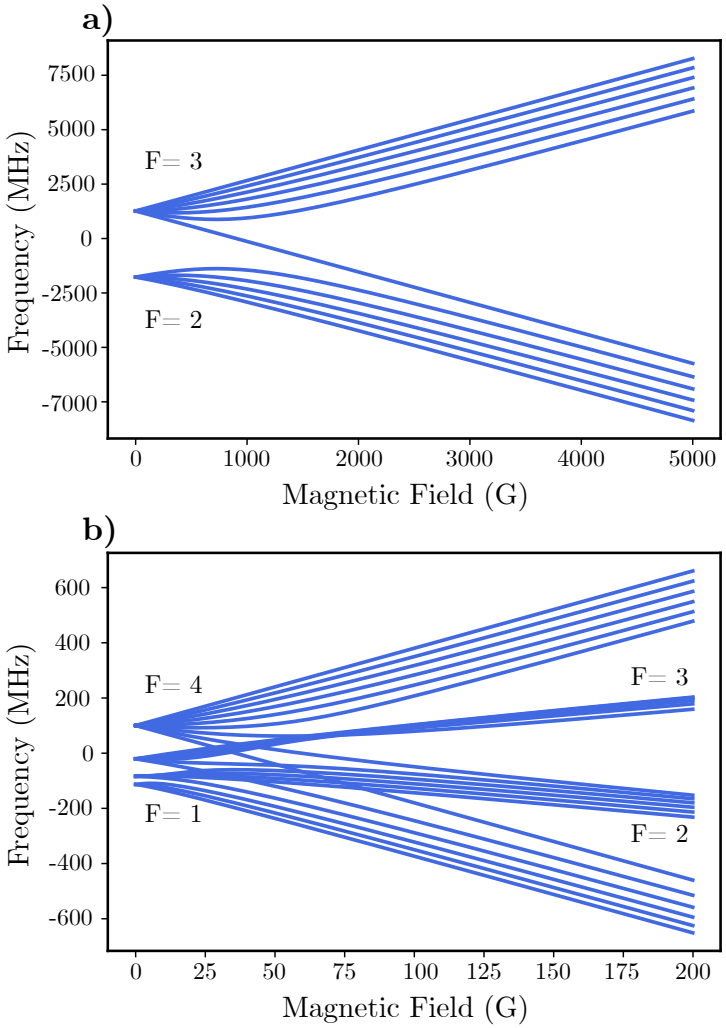

Figure 2.3: *Breit-Rabi diagram for D_2 ^{85}Rb $5^2S_{1/2}$ ground state (a) and excited state $5^2P_{3/2}$ (b) in an external magnetic field adapted from Ref. [134]. It can be seen that at high-field regime the splittings get more distinct.*

of absorption and spontaneous emission cycles. However, due to the optical pumping, there is a small probability of a magnetic quadrupole transition to the $F = 2$ state, which causes the atom to be lost from the cooling cycle. To overcome this and prevent atoms from decaying to 'wrong' ground manifolds which are not accessible by the frequency of the cooling laser, a 'repumper' beam resonant with the $F = 2 \rightarrow F' = 3$ transition is needed to bring the atoms back into the cycle. Further details about the physical and optical properties of ^{85}Rb and its interactions with static external fields are found in [134].

2.4 Magneto-optical traps

It was shown in Sec. 2.2 that counter-propagating laser beams exert a net forces on the atom in nearly all directions due to the Doppler shift, which depletes the atomic motion after several absorption/emission cycles [132, 136]. However, using only lasers to trap atoms is insufficient, as when atoms are slow enough and the Doppler effect is small, atoms are equally likely to absorb photons from all directions, and hence escape from the trap.

As previously mentioned, magneto-optical traps (MOT) are considered the ideal pre-cooling technique and have been widely used since a few decades [137]. The confinement in the MOT works by using atom-light interaction processes together with a quadrupole magnetic field. In this arrangement, atoms are decelerated by the dissipative force resulting from photon scattering, while the magnetic field tailors this force to allow for the spatial confinement. The most common MOT approach involves using three orthogonal pairs of counter-propagating circularly polarised light beams, as illustrated in Fig. 2.4. The MOT beams intersect in the centre of the quadrupole field, which can be produced by a pair of coils in an anti-Helmholtz configuration. The use of red-detuned light increases the probability of light scattering in the opposite direction of the atom's velocity, due to the Doppler effect.

A hypothetical two-level atom with transition $J = 0 \rightarrow J' = 1$ is shown in Fig. 2.5 to illustrate the concept of MOT in 1D. In this scheme, the magnetic fields produced by the coils cancel out at the point in the middle, resulting in $\vec{\mathbf{B}} = 0$, while the magnetic field close to the zero point causes a spatially-varying energy shift in the sub-levels, and this energy perturbation gradually increases away from the centre. As seen from the diagram, the $J = 1$ state is divided into magnetic substates of m_J= 0, and $\pm$1, and the Zeeman-shifted sub-state m_J= 1 (m_J= -1) is always above (below) the excited state. The polarisation of the lasers is set to be circular and the frequency of the lasers is slightly below the resonance frequency as shown in the figure.

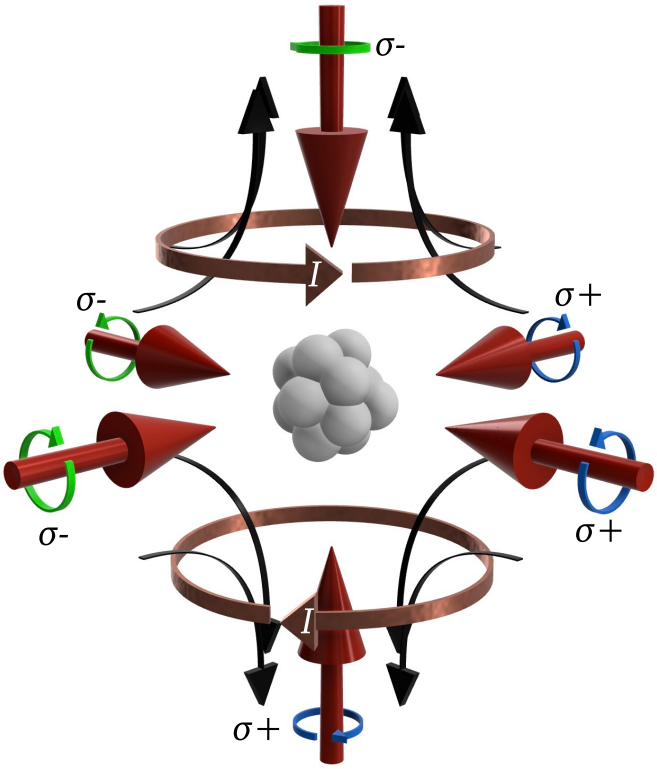

Figure 2.4: *Sketch of a magneto-optical trap created using three orthogonal circularly-polarised pairs of laser beams (thick red arrows) intersecting at the centre of the magnetic field generated from a pair of anti-Helmholtz coils, in order to cool and trap gaseous atoms*

To understand the MOT basic principle, consider an atom that moves away from the trap centre along the z-axis with $z > 0$, so that the $m_J = -1$ transition is near resonant with the laser frequency, ω. Following the selection rules, photons from the laser that excites a σ^- transition are absorbed, resulting in a scattering force that pushes the atom back to the $z = 0$ position. A similar process occurs at the opposite side, where the selection rules preferentially lead to the absorption of photons from the laser that excites a σ^+ transition, which causes the atoms to be pushed back to the trap centre.

The magneto-optical trap can be described mathematically beginning with the optical molasses equation [138]:

$$\begin{aligned} F_{molasses} &= F_{scatt}(\omega - \omega_0 - kv) - F_{scatt}(\omega - \omega_0 + kv) \\ &\simeq -2kv\frac{\partial F_{scatt}}{\partial \omega} = -\alpha v, \end{aligned} \tag{2.20}$$

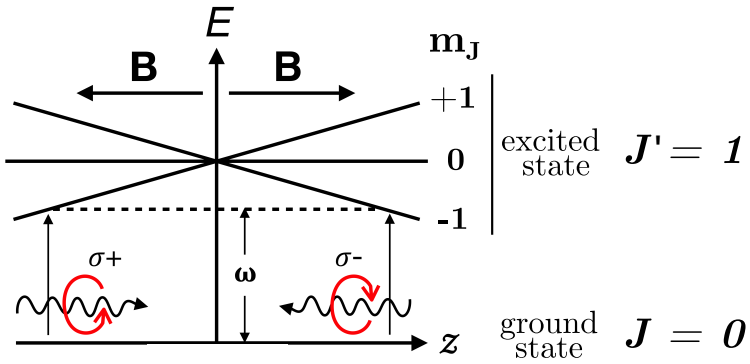

Figure 2.5: *A one-dimensional arrangement for a MOT. At the centre of the trap, the atoms experience no magnetic field and they absorb equal number of photons from each beam. As they drift from the centre, the energy levels are Zeeman shifted by Eq. 2.19.*

where low velocities $kv \ll \Gamma$ are assumed to be the case. Equation 2.20 describes the frictional force acting upon an atom by light, given α as the damping coefficient:

$$\alpha = 2k\frac{\partial F_{scatt}}{\partial \omega} = 4\hbar k^2 \frac{I}{I_{sat}} \frac{-2\delta/\Gamma}{[1+(2\delta/\Gamma)^2]^2}. \tag{2.21}$$

Resonant absorption frequencies for the transitions $m_J = +1$ and $m_J = -1$ at position z are $\omega_0 + \beta z$ and $\omega_0 - \beta z$, respectively. Incorporating these Zeeman frequency shifts caused by the Zeeman effect with Eq. 2.20, we get the MOT equation:

$$F_{MOT} \simeq -2\frac{\partial F_{scatt}}{\partial \omega} kv + 2\frac{\partial F_{scatt}}{\partial \omega}\beta z, \tag{2.22}$$

where βz is the Zeeman shift at displacement z (see Sec. 2.3) and is given by:

$$\beta z = \frac{g\mu_B}{\hbar}\frac{dB}{dz} z. \tag{2.23}$$

Because the damping force depends on the frequency detuning $\delta = \omega - \omega_0$, $\frac{\partial F}{\partial \omega_0} = \frac{\partial F}{\partial \omega}$ is assumed. The MOT radiation force (Eq. 2.22) can be re-written as:

$$F_{MOT} = -2\frac{\partial F_{scatt}}{\partial \omega}(kv + \beta z) = -\alpha v - \frac{\alpha\beta}{k} z. \tag{2.24}$$

2.5 MOT loading and loss

2.5.1 Atomic Collisions

In cold atomic and molecular gases, elastic and inelastic (or reactive) collisions are critical. Elastic collisions exchange momentum and do not destroy the trapped states and thereby are useful to control cold gases, whereas inelastic collisions remove atoms from the traps and hence limit the lifetime of the trap. Rethermalisation of the atoms is aided by the elastic collisions, a phenomenon that already occurs in the MOT, but is crucial for other cooling techniques, such as evaporative cooling. In this project, though, evaporative cooling is not used, and thus only a brief explanation of losses due to inelastic collisions will be given.

2.5.1.1 Inelastic collisions

There are three major processes linked to atomic collisions that contribute to atom losses and reduce an atom's lifetime within a trap [66]:

1- **Background 'one-body' collisions:** Collisions between cold trapped atoms and hot atoms in the background gases result in a loss rate that is only dependent on the background vapour pressure, and hence, can be reduced by improving the vacuum quality. One-body losses induce an exponential decay of the atom number: $dN/dt = -N/\tau$, and are independent of the atomic cloud density.

2- **Two-body collisions:** These are collisions between two cold, trapped atoms within the trap region. These collisions are caused by both direct magnetic dipole-dipole interactions and second-order spin-orbit interactions between two confined atoms. The atoms in this collision exchange angular momenta between their orbital motions and their intrinsic spins, resulting in a change in their internal states. Two-body losses can take three forms: hyperfine-changing collisions, radiative escape, and fine-structure-changing collisions. These three types of collisions are the primary exoergic collisional

processes in a MOT. They are the primary loss mechanisms that typically constrain the maximum density and atom number achievable in MOTs [66].

3- **Three-body collisions:** When three trapped atoms collide, two of them combine to create a molecule, while the third atom carries away the released energy and momentum. If the molecule's binding energy is greater than the trap depth, both the molecule and the atom escape the trap. This process contributes only in a minor way to the losses in uncondensed alkali clouds trapped in MOT; however, it results in substantial losses at significantly higher densities, such as the ones achievable in Bose-Einstein condensates (i.e. densities $\gtrsim 10^{11}$ cm^{-3}) [139, 140].

These aforementioned collisions are the dominant loss mechanisms that usually limit the attainable maximum density and number of atoms in the magneto-optical trap.

2.5.2 MOT loading and loss dynamics

The atom number in a MOT as a function of time can be described in terms of atoms loading and loss using the rate equation [72]:

$$\frac{dN}{dt} = R - \Gamma N - \beta \int \bar{n}^2 d^3r, \tag{2.25}$$

where R is the rate at which atoms are loaded via laser cooling. The loss rate coefficient due to collisions with non-rubidium background species is expressed by Γ. It is the inverse of the trap lifetime τ and has the unit of s^{-1}. The term β is the loss rate coefficient due to collisions with thermal Rb atoms. The trap mean density is $\bar{n}$, where $\bar{n} = \frac{1}{N}\int n^2 dr$ for low density MOT.

To solve Eq. 2.25, the variation of $\bar{n}$ in terms of N must be known. This can be done by distinguishing between two classes in terms of multiple scattering forces within the MOT: fixed-volume and fixed-density regimes [141]. At small atom numbers ($N < 10^5$), the scattering forces are weak and the density is given by $\bar{n} \approx N(t)/V$, with constant-volume V. At larger values of N, the

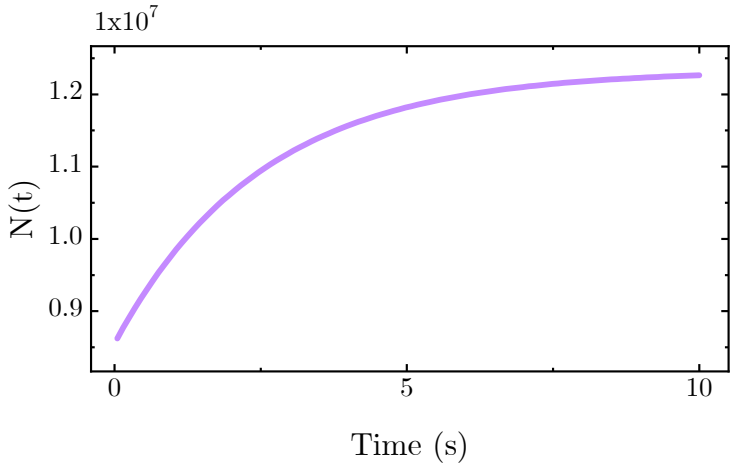

Figure 2.6: *An example of exponential MOT loading curve of atom number, N(t), as a function of time, t.*

scattering forces within the MOT become significant, the cloud grows with N, and the density $\bar{n}$ becomes constant. For the latter regime, which is mostly the case in our system, Eq. 2.25 can be rewritten as:

$$\frac{dN}{dt} = R - \gamma N - \beta \bar{n} N = R - (\gamma + \beta \bar{n}) N. \tag{2.26}$$

The solution of Eq. 2.26 has the form of an exponential equation [67]:

$$N(t) = \frac{R}{\Gamma}(1 - e^{-\Gamma t}), \tag{2.27}$$

with

$$\Gamma = \beta \bar{n} + \gamma. \tag{2.28}$$

Figure 2.6 shows an example of an exponential MOT loading curve. In the regime where ($N > 10^5$), the atom loading dynamics can be used to reliably determine the pressure at the MOT location (see Sec. 3.4).

The lifetime of an atom in a cold atom trap is directly related to the pressure, and this relationship can be used to measure the vacuum pressure. The rate equation of MOT dynamics can be approximated to include the

pressure term by [73]:

$$\frac{dN}{dt} = \alpha P_{Rb} - (\beta P_{Rb} + \gamma)N(t), \tag{2.29}$$

where the first term on the right hand side represents the atoms loaded in the trap, while the second term represents the losses from the trap. The constant α is the MOT trapping cross section constant, and P_{Rb} is the rubidium pressure. The losses in the trap due to collisions with thermal Rb atoms in the background are given by the term $\beta P_{Rb} N$, and the losses due to collisions with other non-rubidium species are described by γN. This equation is used to estimate the background pressure experimentally in Chapter 3.

Chapter 3

MOT characterisation and background pressure estimation

3.1 Experimental apparatus

Our setup, like many cold atom systems, consists of a number of complex components that employ a range of techniques based on several physical principles and concepts. There are various key components that must be present in any cold atom system, including an UHV environment, an optical system that includes lasers and optical elements, and a controlled magnetic field. The UHV environment is the necessary medium in which atoms are confined in isolation from heat and background particles in order to minimise atomic losses, while the optical system and magnetic field are the primary means by which atoms are cooled and manipulated. This chapter describes the system in general, highlighting the techniques employed and the experiments conducted with it. All experiments presented in this chapter were carried out using the AM-based setup characterised in detail in chapters 4, 5, and 6.

A rendered representation of the system used with its main parts is shown in Fig. 3.1, and further drawings of the parts are given in Appendix C. The UHV system consists of a 3D-printed chamber with an outer diameter of 80 mm and a weight of ∼250 g; see Chapter 4 for more details about the AM UHV

chamber. The chamber is mounted using stainless steel brackets and pillars, and lifted ∼20 cm above the surface of the optics table to allow the installation of optical components needed to pass and reflect the MOT beams through its windows. An ion pump attached to the chamber is always in operating mode, whereby the quality of the UHV is maintained. The pressure in the chamber is usually below 10^{-10} mbar, and the pressure value rose up to the range of 10^{-9} mbar during the few times the ion pump was turned off (see Chapter 4). The atomic source is a set of rubidium dispensers that provide the rubidium gas in the chamber, where the Rb vapour density varies according to the value of the electric current supplied to the dispenser. The atoms emitted by the

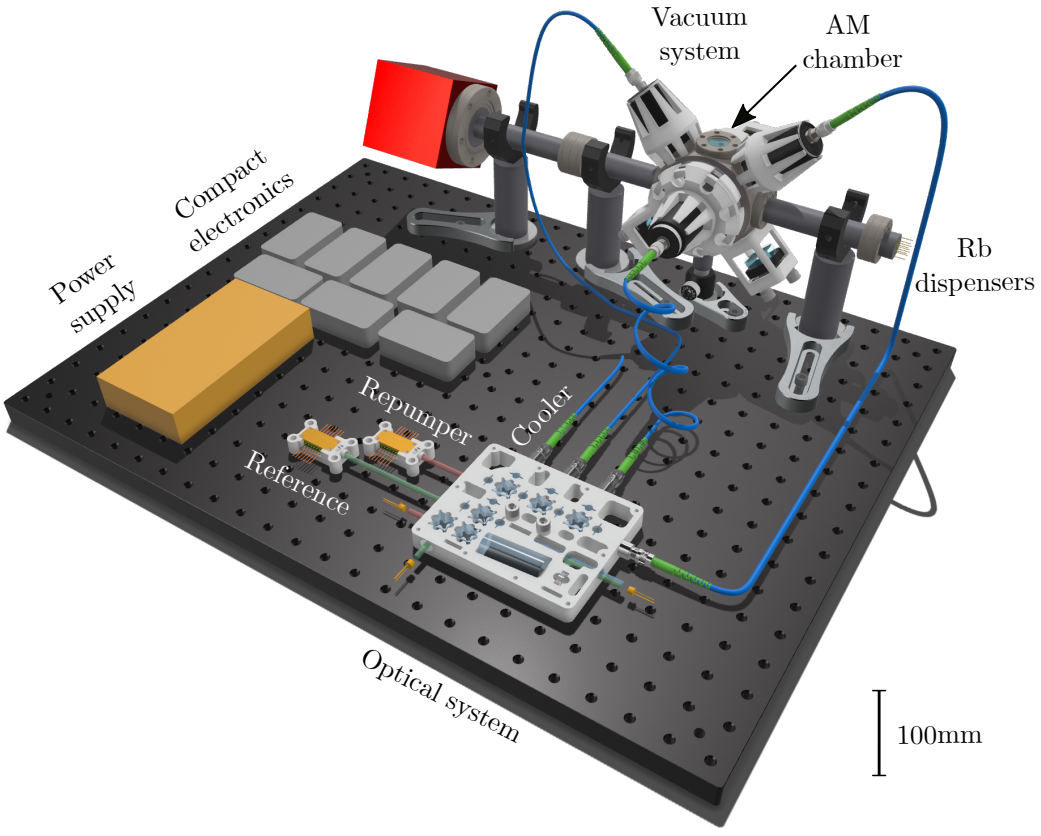

Figure 3.1: *3D render of the setup used for measurements in this chapter.*

Rb source are loaded into a magneto-optical trap (MOT) formed by three retro-reflected beams: one beam is mounted horizontally, and the other two beams are installed at 45° relative to the vertical direction. A CCD camera is mounted in the chamber's lower window to monitor the atomic cloud, while a

photodiode is mounted on the top window to collect the MOT beam for trap characterisation. The magnetic gradient source is a set of neodymium magnets attached and arranged around a pair of AM rings and glued to the chamber's outer CF40 flanges. The magnetic source was designed and developed by Christopher Morley [142].

The optical system involves lasers, optical fibres, optical elements, and 3D-printed and conventional mounts. The lasers employed in the system are two distributed feedback (DFB) lasers (EYP-DFB-0780-00080-1500-BFW01-0005) used as reference and repumper lasers, and a fibre-coupled laser from an external Toptica TA laser mounted on a preset setup on the same optical bench is used as a cooling beam. The DFB lasers are in butterfly configuration and fixed on 3D printed mounts with built-in miniature optical isolator (I-780-LM-1.4-4). Each DFB laser has an optical output power of ∼42 mW after the optical isolator, while the cooling laser optical power is ∼100 mW. The lasers are positioned around the AM compact spectroscopy and power distribution (CSPD) mount inputs, as shown in Fig. 3.1. The push-fitted optical components and the rotating $\lambda/2$-waveplates distribute the beams for saturated absorption spectroscopy, offset lock, and towards the UHV chamber (MOT beams). The MOT beams emerging from the CSPD framework are optical fibre-coupled and sent to the UHV system to be magnified and aligned using lens tubes attached to the edges of the chamber windows via 3D-printed mounts. For more details about the setup, see Chapter 5.

3.2 Experimental methods

This section covers the techniques employed in the system in detail.

3.2.1 Laser frequency stabilisation techniques

To access the cooling and repumping transitions for the MOT, the lasers need to be stabilised. In the following section, the spectroscopic techniques are discussed that are used in order to achieve a compact stabilisation setup, as

displayed in Fig. 3.6.

3.2.1.1 Saturated absorption spectroscopy

A common issue in conventional laser spectroscopy is the difficulty of resolving the fine or hyperfine structure of the atomic sample, due to Doppler broadening [143]. Detecting the absorption spectrum of room temperature alkali atoms in vapour cells makes it possible to measure and monitor the frequencies of the lasers and reveal the atomic transitions. This can be achieved using two counter-propagating beams, one is strong named 'pump' and a weaker one called 'probe', both travel across a vapour cell with frequencies near an atomic resonance. This procedure is referred as Doppler-free saturated absorption spectroscopy, – see Fig. 3.3. The pump beam is exploited to deplete the atoms via continuous cycles of absorption and emission interactions, so that the atoms become transparent to the probe beam and hence can be used to reveal the hyperfine spectrum on a photodetector [138]. Figure 3.2 illustrates the photodiode signals for the saturated absorption spectroscopy of the ^{85}Rb D^2 line.

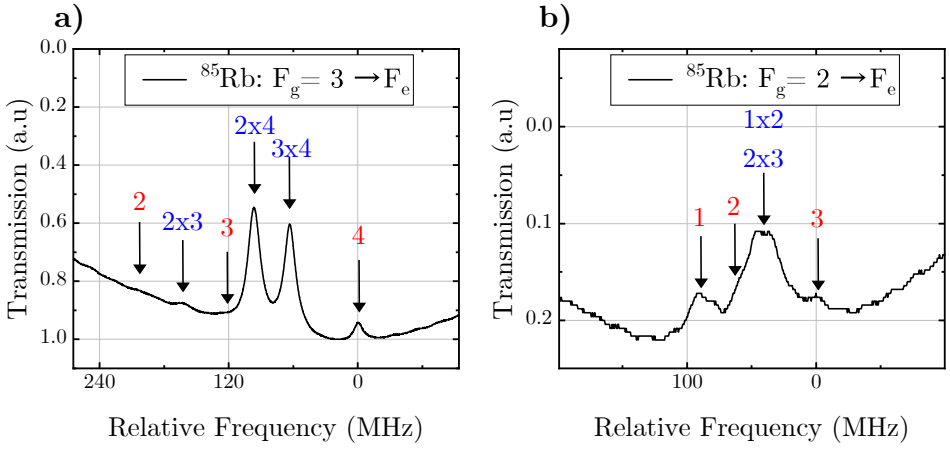

Figure 3.2: *Saturated absorption spectra of ^{85}Rb atoms at room temperature for cooler (a) and repumper (b) lasers. The cooling laser spectrum illustrates the transitions from the $F_g = 3$ to allowed excited states indicated, as well as the crossover points between these transitions. The repumper laser spectrum illustrates all transitions possible from the $F_g = 2$ to allowed excited transitions.*

In saturated absorption spectroscopy, the light frequency is classified into

three regimes: on resonance, in the centre between two transitions, and off resonance. In the case of a beam resonant with a hyperfine transition, the light is absorbed by atoms with zero longitudinal velocity, $v = 0$, along the beam axis. Due to the pump beam being near the saturation intensity of the transition, most of $v = 0$-atoms in its path are pumped into the excited state. The probe beam that travels in the opposite direction is also resonant with the $v = 0$ atoms, which are now transparent to the probe beam, so this beam is barely absorbed by these atoms. The transitions of this case are displayed in red colour in Fig. 3.2.

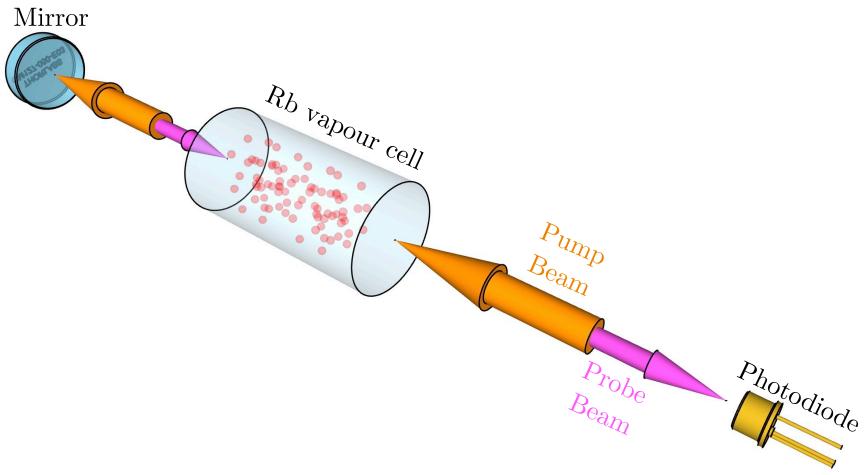

Figure 3.3: *In saturated absorption spectroscopy, a laser beam is passed through an atomic vapour before being retro-reflected back through the vapour (though much weaker because of absorption) and onto a photodiode, where the intensity is measured.*

In the second regime, when the laser is between resonances, the pump beam and probe beam are both resonant with different parts of the thermal distribution of the velocities of the atoms, resulting in the probe beam being absorbed in an equivalent amount to when there is no pump beam present. In this case, 'crossover' peaks appear, where the lasers interact with atoms of two different groups of velocity. The pump beam is absorbed by the atoms of velocity $-v$ and hence the laser frequency is blue-shifted into upper transitions, and absorbed by atoms of velocity v and the laser frequency is red-shifted to lower transitions. This results in 'crossover' peaks which are typically stronger than resonance peaks because they derive from two different velocity classes in-

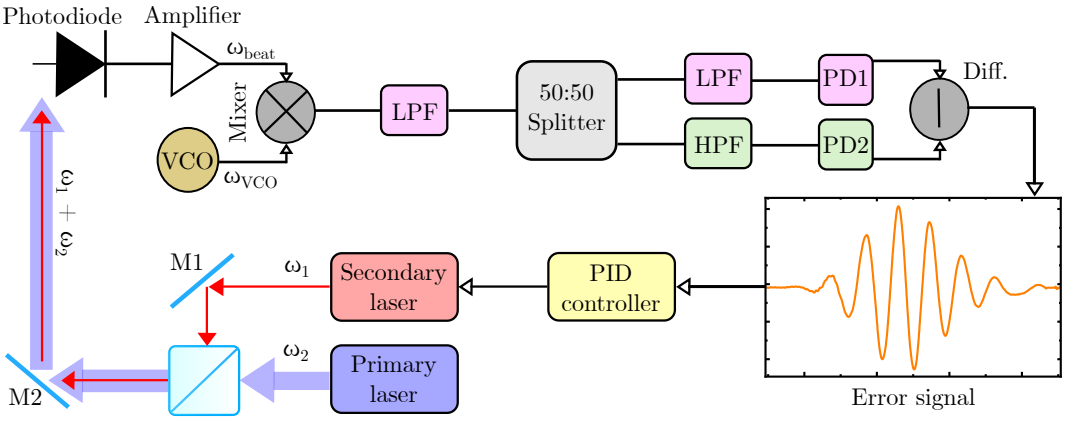

Figure 3.4: *A diagram illustrating the offset locking scheme used in our system.*

stead of just one. These are annotated in blue in Fig. 3.2. Thus, by employing this technique in a configuration similar to that shown in Fig. 3.3 and scanning over Doppler-broadened transitions, we can reveal the hyperfine structure peaks, which enables laser stabilisation for our experiments (see Fig. 3.2).

In the third case, the two beams are resonant with various velocity classes due to Doppler shifts, resulting in the light from the original beam being lost in each path.

3.2.1.2 Offset Lock

Laser frequency offset locking is used in our setup to adjust the detuning for the cooling laser relative to a reference frequency. In this approach (see Fig. 3.4), the frequency of a secondary laser (the cooler laser, in our case) is stabilised and detuned relative to the frequency of a primary laser (the reference laser); which has been locked using Doppler-free saturation absorption spectroscopy. This form of locking enables the frequency difference between the primary and secondary lasers to be adjusted according to the voltage applied to a voltage-controlled oscillator (VCO) [144, 145].

To understand the principle of the offset locking technique, consider the angular frequencies of the two well-aligned and overlapped lasers on the photodiode as ω_1 and ω_2, with a beat frequency of $\omega_{beat} = |\omega_2 - \omega_1|$. The resulting

signal of this superposition is given by:

$$\cos\omega_1 t + \cos\omega_2 t = 2\cos\left(\frac{\omega_1+\omega_2}{2}t\right)\cos\left(\frac{\omega_1-\omega_2}{2}t\right). \tag{3.1}$$

That is, the superposition of two electric fields with frequencies ω_1 and ω_2 can also be thought of as an electric field oscillating with frequency $(\frac{\omega_1+\omega_2}{2})$, modulated by a frequency of $(\frac{\omega_1-\omega_2}{2})$. The sum-frequency is up to hundreds of terahertz, which is far beyond the bandwidth of the photodiode, which is only few gigahertz. Therefore, this frequency range should be filtered out and averaged, such that the beat frequency $\omega_{beat} = |\omega_2 - \omega_1|$ can be measured. After that, a radio-frequency interferometer is used to generate an error signal of the resulting beat signal. The beat signal is mixed with the VCO sine wave signal of frequency ω_{VCO}, according to the trigonometric identity:

$$\cos\theta\cos\phi = \frac{\cos(\theta-\phi)+\cos(\theta+\phi)}{2}. \tag{3.2}$$

After the mixing, the resulting signal of the photodiode and the VCO signals is $\omega_{beat} + \omega_{VCO}$, superimposed with $\Delta\omega = \omega_{beat} - \omega_{VCO}$. A low pass filter (LPF) then is used to remove unwanted components from the $\Delta\omega$ signal. Following that, the signal is split in half (50:50 splitter) and passed through filters (LPF and HPF), which are chosen such that their fall-off patterns overlap. The difference between the two signals is then measured on two power detectors, and the resulting error 'difference' signal is generated. Once the error signal is fed into a PID loop, it is used to lock the laser by adjusting the tuning voltage of the VCO, which results in a change in $\Delta\omega$ and, consequently, in ω_2 and ω_{beat}.

The offset lock technique is used in our system to stabilise the cooling laser generated from a Toptica TA laser relative to the reference laser sourced from a DFB laser. The reference 'primary' laser is locked at ^{85}Rb D_2 line $F_g = 3 \rightarrow F_e = 3 \times 4$ via saturated absorption spectroscopy, while the cooling

laser is detuned by ∼15 MHz below the cycling 'cooling' transition $F_g = 3 \rightarrow F_e = 4$. For reasons of compactness, this scheme in our setup is built on an Arduino-based printed circuit board (PCB), which allows for a direct locking of the cooler laser relative to the reference laser (see Appendix C).

3.2.1.3 Two-laser spectroscopy

The technique of two-laser spectroscopy was exploited our system to enhance the conventional locking via saturated absorption spectroscopy. In order to construct a compact spectroscopy device (Fig. 3.6), light of two different frequencies was guided through the same vapour cell simultaneously (see Fig. 3.5). It was observed that the spectral peaks became sharper and gained in amplitude, while when only one laser passed through the cell, the amplitudes decreased. The application of two frequencies led to optical pumping effects, which created additional peaks in the spectroscopic signal.

This observation prompted us to investigate the potential benefits of dual-laser spectroscopy for laser frequency stabilisation, which are discussed in this section. Therefore, besides the saturated absorption spectroscopy technique, dual-laser spectroscopy has been used in our system for its advantages. The technique not only allows for a reduction in the system's size and area by reducing the number of optics used, but also enhances the performance of the laser stabilisation. A theoretical rate model is derived in [131] (see Chapter 7), which demonstrates that when two laser beams overlap in a vapour cell, this results in an enhancement of the spectral absorption signals of the two beams and extra lock points appear in the spectroscopic signals as well, both of which cannot be achieved by using a single laser spectroscopy alone.

The fundamental principle of this technique is based on the optical pumping effect, which is also what necessitates the use of a repumper laser in magneto-optical traps. Optical pumping causes the atoms to populate atomic transitions which are inaccessible by the frequency of the laser beam used for spectroscopy. In a single laser spectroscopy scheme, optical pumping causes

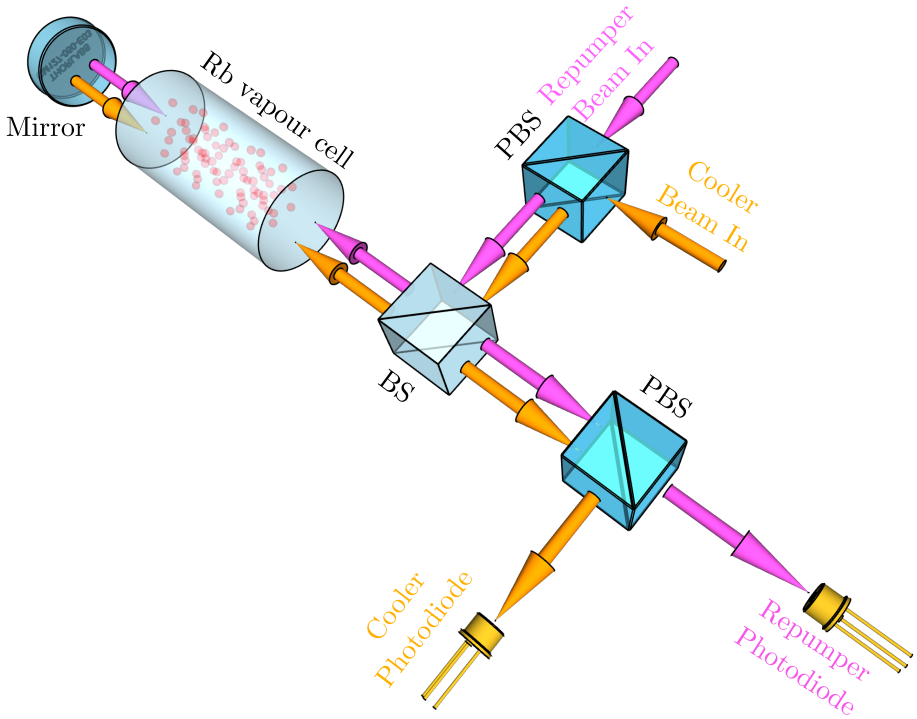

Figure 3.5: *Two-laser spectroscopy experimental setup. Two laser beams of two frequencies share the same optical path across a common vapour cell. The reflected components of the two beams are detected seperately on two photodiodes, resulting in enhanced spectroscpic features displayed in orange in Fig. 3.7.*

the spectroscopic signal to be attenuated [138, 146], whereas in a dual-laser spectroscopy system, the absorption of the lasers is augmented by one another and the spectroscopic signals appear sharper. The presence of the new lock points is attributed to the fact that the two lasers interact with atoms of different groups of velocities, resulting in multiple crossovers and peaks in the spectroscopic signals.

An excited state in a multi-level atom may decay into ground states. The ratio of excited state coupling strengths (Clebsch-Gordan coefficients) to dipole-allowed ground states determines the probability of decay into a specific level. For an ^{85}Rb atom in the $F_e = 3$ state, the atom can decay with nearly equal probability into either $F_g = 2$ or $F_g = 3$ states. If the incident beam is tuned to the transition $F_g = 3 \rightarrow F_e = 3$, any atom decaying into the $F_g = 2$ is transparent 'dark' to the laser and has been optically pumped.

Dual spectroscopy arrangement is incorporated into the 3D-printed CSPD mount (see Fig. 3.6 and Fig. C.2 in Appendix C). Figure 3.5 depicts a close

view of the experimental setup, highlighting the paths of the two beams. Both beams are in orthogonal linear polarisation, combined in a polarising beam splitter (PBS), and travel back and forth through a vapour cell, where they are eventually split by another PBS to be detected separately using two photodiodes, as shown in the diagram. The beams are operating in the repumping and cooling transitions of the ^{85}Rb D_2 line: $F_g = 2 \rightarrow F_e = 3$ and $F_g = 3 \rightarrow F_e = 4$.

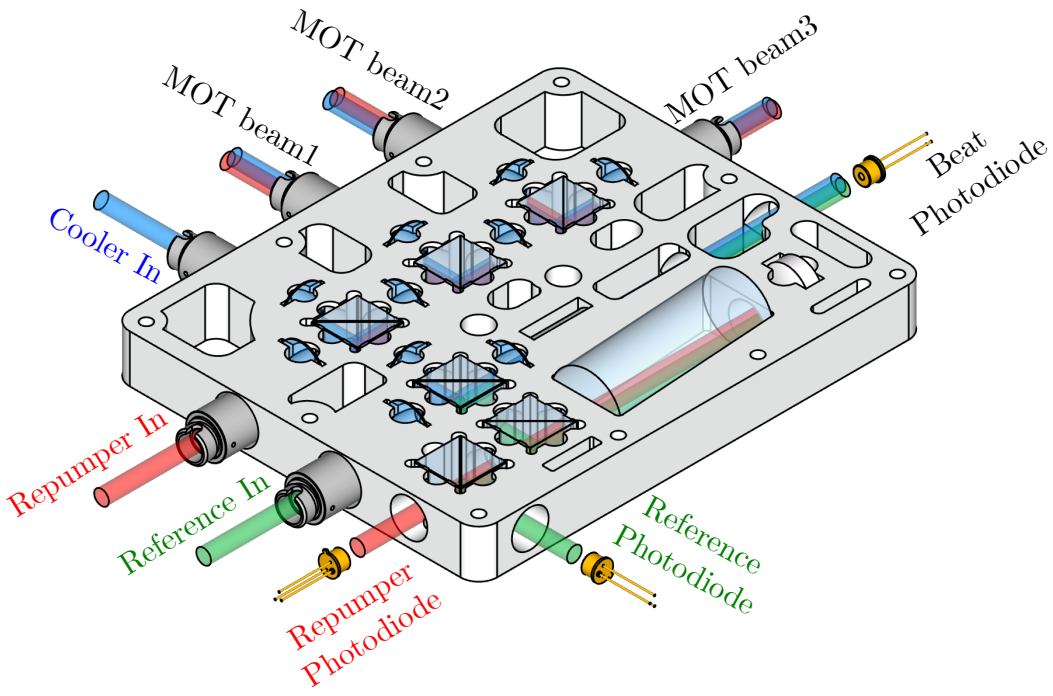

Figure 3.6: *3D rendering of the compact spectroscopy and power distribution framework (CSPD) used in the experiment. The system has a footprint of 128 mm× 103mm×12 mm.*

The output signals from each of the photodiodes displayed in Fig. 3.5 are plotted in Fig. 3.8 as a function of the cooler and repumper frequencies. The diagonal features were achieved by scanning both frequencies concurrently over the desired atomic frequency range. In order to do this, the controlling current fed to each DFB laser used in the experiment was ramped up linearly by adding static offsets using signal generators. The dark regions illustrated in Fig. 3.8 represent regions of high absorption strength. The frequency range was chosen relative to the cooling transition $F_g = 3 \rightarrow F_e = 4$. The diameters of both beams were 1.2 mm and the output powers were 0.36 mW and 0.25 mW for

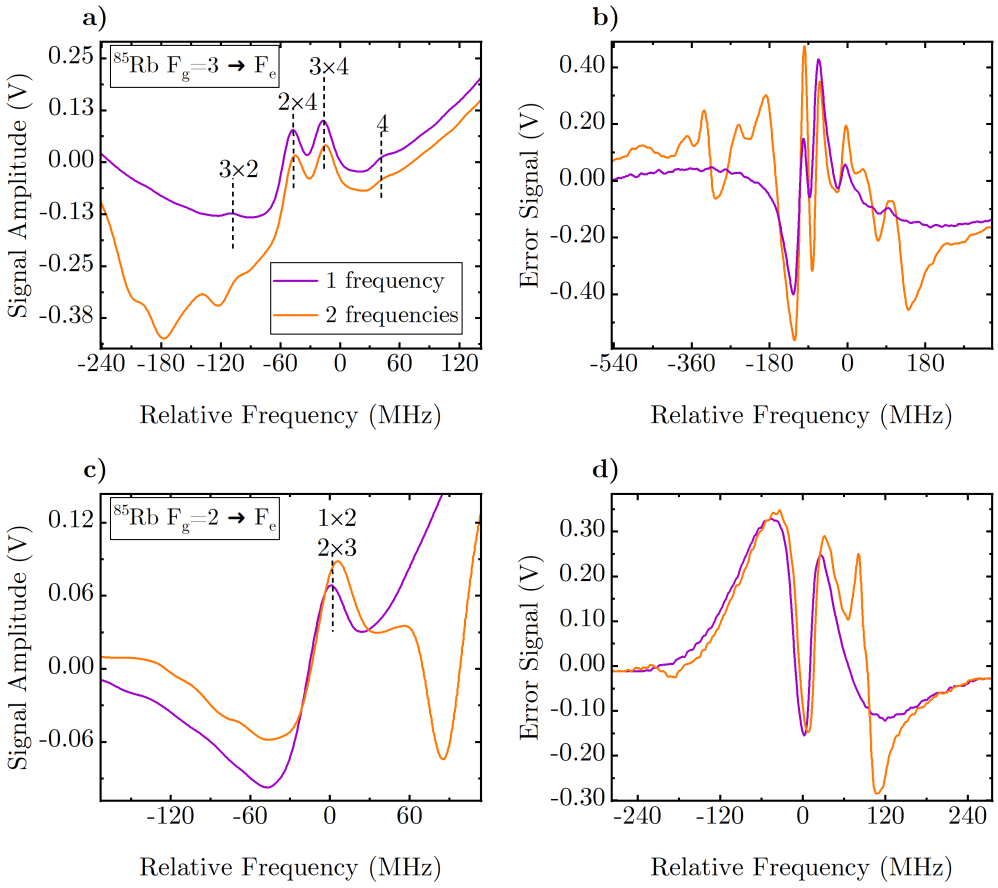

Figure 3.7: *(a, c): Standard Doppler-free saturated absorption spectroscopy signals from the cooler and repumper photodiodes (see Fig. 3.5) and the corresponding error signals of the same transitions (b,d) in the presence of one laser (purple lines) or two lasers (orange lines). The standard Doppler-free saturated absorption spectroscopy signals (purple lines) is shown for reference. As shown in the orange traces, the presence of a laser results in the appearance of a number of new spectroscopic features 'crossovers' in the feature of the other laser.*

cooler and repumper beams, respectively.

Figure 3.7 (a) and (c) represents vertical slices of Fig. 3.8(a) and (b), while Fig. 3.8 depicts equivalent slices of saturated absorption spectroscopic signals taken within the limits of far-detuned cooler and repumper lasers. According to the results in figures 3.7 and 3.8, the presence of extra cooler/repumper frequency light enhances the absorption signal of the repumper/cooler light by the atoms. An increased absorption signal provides a better feedback signal for laser frequency stabilisation, as shown in orange traces in Fig. 3.7(b) and (d). A diagonal grid pattern of sharp response features is developed across more than 400 MHz, which is far wider than the range produced by standard,

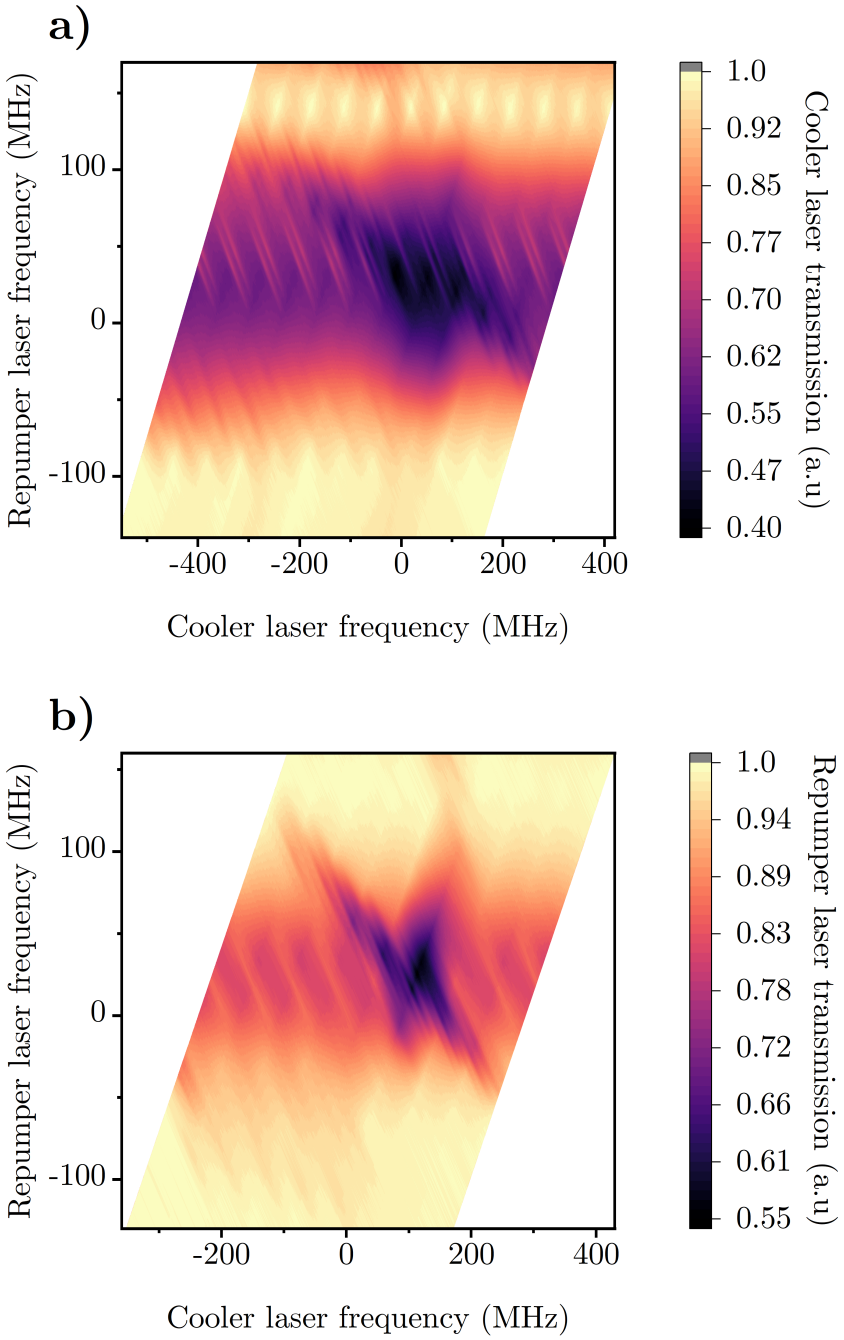

Figure 3.8: *Contour plots of spectroscopic signals from the cooler laser photodiode (a) and repumper laser photodiode (b) as a function of the frequencies of both lasers. The dark areas represent regions of high absorption strength resulting from dual-laser spectroscopy.*

single-beam Doppler-free resonance patterns which are 184 MHz for the cooler and 92 MHz for the repumper. Dual-frequency spectroscopy was applied in Chapter 5 [80] and analysed in detail in Chapter 7 [131].

3.3 MOT characterisation

In the 3D-printed setup discussed in Ref. [80], 2×10^8 ^{85}Rb atoms were trapped. Measurements of the physical properties of the trapped atoms, including the atom number N and the trap lifetime τ, were carried out in order to study the MOT behaviour [65]. The characterisation of a MOT can be accomplished using several methods. One of these methods relies on fluorescence imaging, which involves measuring the number of fluorescent photons emitted by the atoms when exposed to a near-resonant beam. This can be done by taking a MOT loading curve measurement, in which a trapping magnetic field is present and atoms are allowed to accumulate in the trap over time while the time-dependent fluorescence signal is measured. This also involves using the initial signal obtained when no atoms are trapped as a reference for background correction, and then measuring the signal from atomic fluorescence. This simple method allows for the MOT lifetime and other parameters such as the background pressure to be determined.

To make a magneto-optical trap using the setup displayed in Fig. 3.1, three pairs of orthogonal counter-propagating laser beams and a specific magnetic field are required. Each MOT beam has a total optical power of 20 mW, of which 15 mW is a cooling beam and 5 mW is a repumping beam. The beams are telescopically expanded to 15 mm in diameter using a pair of lenses with focal lengths of $f = 20$ mm and $f = 15$ mm assembled inside outcouplers. The counter-propagating configuration is created by mirrors installed in the viewports on the opposite sides of the MOT beams' propagation directions. The total distance travelled back and forth by each beam is ∼100 mm for the horizontal beam and 150 mm for the two vertical beams (see Fig 3.16).

The non-uniform magnetic field for the MOT is generated by a ferro-

magnetic array of N42 strength neodymium magnets contained in two AM polymer rings. This array produces the same field distribution as conventional anti-Helmholtz MOT coils (see Appendix B). Each of these rings contains 29 magnets, each of which measures 6 mm in diameter and 3 mm in depth. Without the need for any electrical current, a magnetic field gradient of $\sim$15 G cm^{-1} is generated near the centre of the trapping area. For comparison and testing purposes, conventional magnetic field coils were made to fit the size of the UHV chamber (see the Appendix B), but they were not used in the experiment and were replaced by the permanent magnets rings.

The experiment begins with operating the rubidium dispenser current at a starting value of $\sim$2.15 A. The laser frequencies are locked at the ^{85}Rb D_2 line repumping and cooling transitions (shown in Fig. 3.2) using the compact Arduino-based controlling electronics presented in Appendix C. The cooler laser is offset-locked relative to the reference laser, with a detuning of $\sim$15 MHz below $F_g = 3 \rightarrow F_e = 4$ transition. Because the magnetic field is generated by permanent magnets, it is always present in the confinement area and thus does not need to be turned on and off. Once the frequencies of the lasers are fixed, the MOT is created and the required measurements can be directly performed. At first, the dependence of the MOT loading curve on the rubidium dispenser current was recorded. During the measurement, the dispenser current is gradually increased, with an interval of 30-40 minutes between every two values to allow for the equilibrium state to be reached before taking the loading curve for the next set value.

The MOT was formed with beams of total intensity of $\sim I$=20 mW, starting with minimum current value at $\sim$2.15 A and up to 2.75 A. The fluorescence light was collected using a $f = 25$ mm plano-convex lens to focus light onto the detector area of a Thorlabs DET100A/M silicon detector-based photodiode positioned outside the top viewport of the vacuum chamber, with a solid angle of $\Omega = 0.04$ sr. The MOTs loadings are recorded as exponential curves over time, as shown in Fig. 3.9.

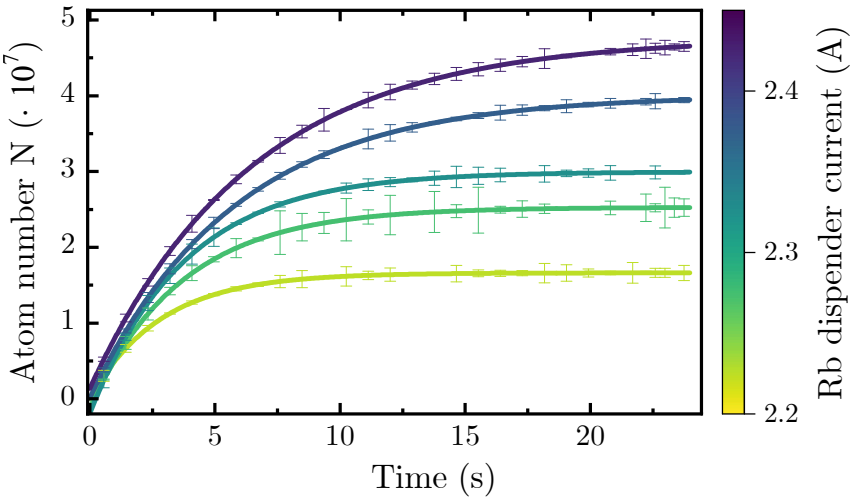

Figure 3.9: *Example of experimental MOT loading curves taken at different values of Rb dispenser current. Error bars are derived from the exponential fit of each loading curve and the statistical standard deviation.*

The number of atoms within the MOT can be determined by the voltage returned by the photodiode in response to an incident power generated by N atoms. This yields:

$$N = \frac{4\pi\lambda M V_{\mathrm{PD}}}{hc\Omega\gamma_{\mathrm{sc}}S}, \tag{3.3}$$

where N is the number of atoms, λ is the wavelength of the emitted photons and M is the magnification factor of the lens used to capture the MOT fluorescence. The term V_{PD} is the photodiode's acquired voltage signal, γ_{sc} is the photon scattering rate of ^{85}Rb atoms (see Eq. 2.11), and S is the photodiode's sensitivity to 780 nm light. It is important to correct the signal by subtracting the background fluorescence of the intersected beams from the MOT signal to ensure a precise estimation of the atom number. The atom number N for each loading curve is then plotted with a software and fitted to Eq. 2.27.

The loss rate Γ can be then evaluated as the inverse of the trap lifetime τ [67, 73], which can be extracted as a free fitting parameter along with the loading time R from the loading curves. Figure 3.10 shows a single loading curve measured by the photodiode; it has an equilibrium atom number of $N_{eq} = (2.3 \pm 0.5) \times 10^7$, a loading rate of $R = (1.1 \pm 0.5) \times 10^7$ atoms/seconds, and a trap lifetime of $\tau = (12 \pm 2)$ s, taken at a dispenser current of 2.40 A. Figure 3.11 displays the atom number as a function of the MOT lifetime for a

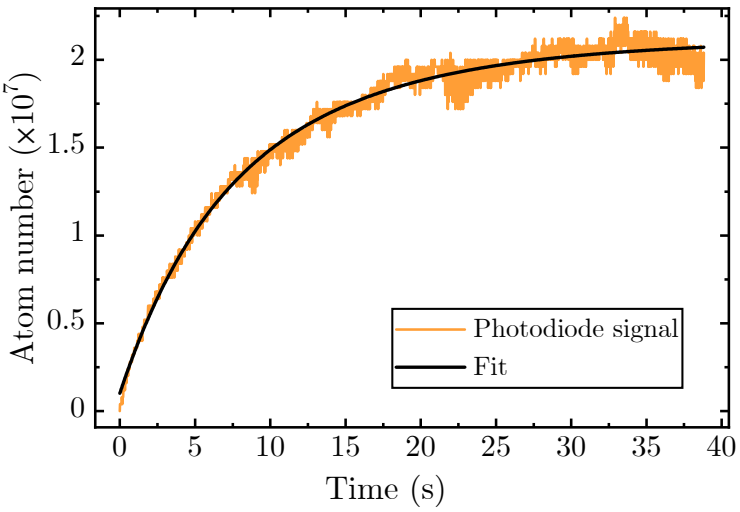

Figure 3.10: *Typical magneto-optical trap measured loading curve for determining the atom number N and MOT loading rate and lifetime. The orange trace represents the raw voltage signal, which has been background corrected by subtracting the initial value at $t = 0\,s$ and scaled to N using a constant scaling factor. The black line represents the exponential fit to the data, from which the steady state N was reached $N_{eq} = (2.3 \pm 0.5) \times 10^7$ and a trap lifetime $\tau = (12 \pm 2)\,s$ was calculated.*

set of MOT loading curves at various Rb dispenser current values. The same series of loading curves are plotted in terms of atom number as a function of the Rb dispenser current values in Fig. 3.12. Please note that the terms Γ and γ are slightly different; Γ is defined in Eq. 2.28, but they are assumed equal in our measurements, as the term $\beta\bar{n}$ is neglected. Also, the time for which a MOT has been loaded thus far, t, should not be confused with the characteristic timescale of exponential loading, τ, which is defined here as the trap lifetime.

3.3.1 MOT characterisation via absorption imaging

Absorption imaging is a common technique used in cold atom experiments from which information about the MOT, such as atom number, size, density, and temperature, can be identified from the spatial density distribution of the atomic cloud. The atomic cloud can be detected by using a CCD camera to capture the shadow cast by the atom sample illuminated by near-resonance and collimated light. Although this method was not used in the majority of the MOT measurements described in this thesis, an absorption imaging system

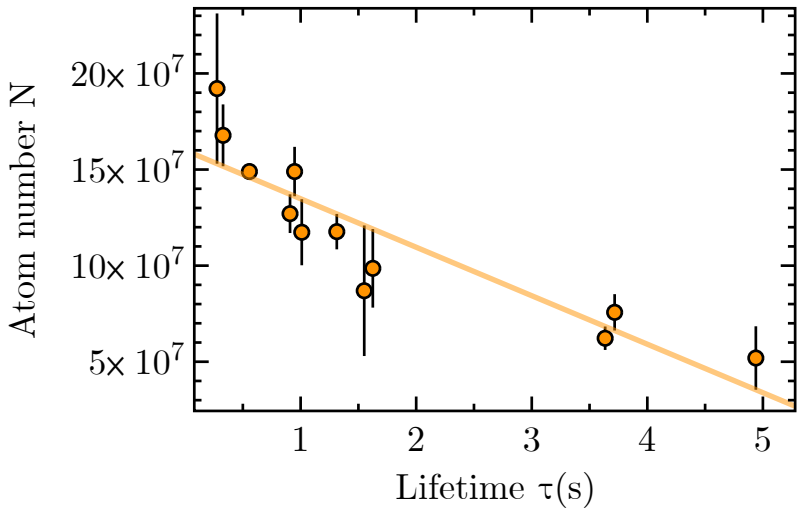

Figure 3.11: *Steady state atom number N as a function of trap lifetime τ at various Rb dispenser current values. Error bars are derived from the fit and the statistical standard deviation.*

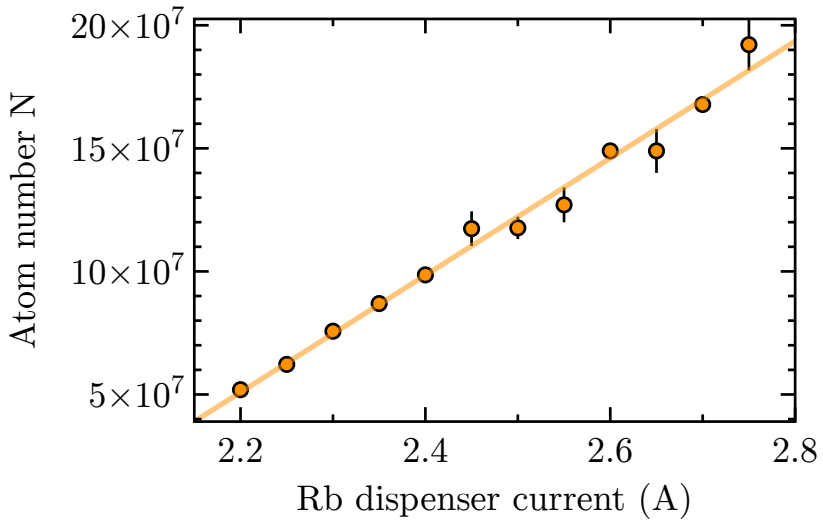

Figure 3.12: *Steady state atom number N as a function of Rb dispenser current. Error bars are derived from the fit and the statistical standard deviation.*

was built in the setup in order to take advantage of it for future experiments and measurements.

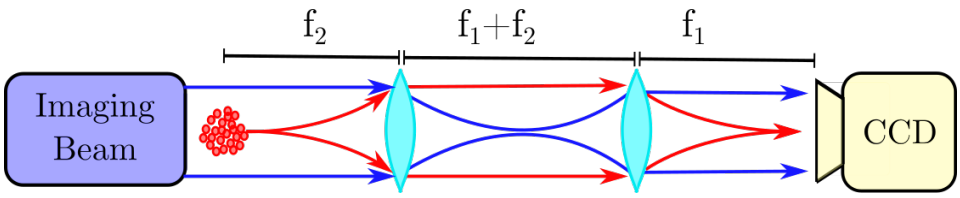

Figure 3.13: *Geometrical arrangement of the imaging system. The telescope lenses used are $f_1 = 100\,mm$ and $f_2 = 50\,mm$ with magnification factor of $M = 2$.*

This method involves directing a beam of light at an atomic cloud and counting the amount of light absorbed and scattered. The higher the atomic density, the greater the absorption, allowing for mapping the density into a light intensity pattern, which is then measured by a CCD camera. During absorption imaging, three images are taken: one with atoms, one with light after the atoms have dissipated, and one with no light and no atoms. The atom number N and the atoms' density distribution $n(x, y)$ can be estimated for an atomic cloud by measuring the attenuation of a resonant probe 'imaging' beam, according to the equation:

$$n(x.y) = -\frac{1}{\sigma_0} \ln\left(\frac{I_{out}}{I_0}\right) = \frac{OD_{x,y}}{\sigma_0}, \tag{3.4}$$

where σ_0 represents the resonant atomic absorption cross section, I_0 represents the incident beam intensity, I_{out} represents the transmitted beam intensity, and OD represents the optical depth. The atom number can be expressed in terms of the density n as:

$$N = \int n(x, y) dx dy. \tag{3.5}$$

For the light source, a beam from the reference DFB laser is split and used as an imaging beam. The imaging beam has a total power of 10 mW and was attenuated using ND filters to have lower intensity than the atoms' saturation intensity of below 2.50399(73) $\mathrm{mW/cm^2}$ [134]. It is then magnified after passing through a telescope of two lenses of focal lengths $f_1 = 100\,\mathrm{mm}$ and $f_2 = 50\,\mathrm{mm}$,

as shown in Fig. 3.13 to have finally a spot size of $d = 20\,\text{mm}$ and a total intensity of $\sim 0.5\,\text{mW/cm}^2$. To test the imaging system, a MOT was formed

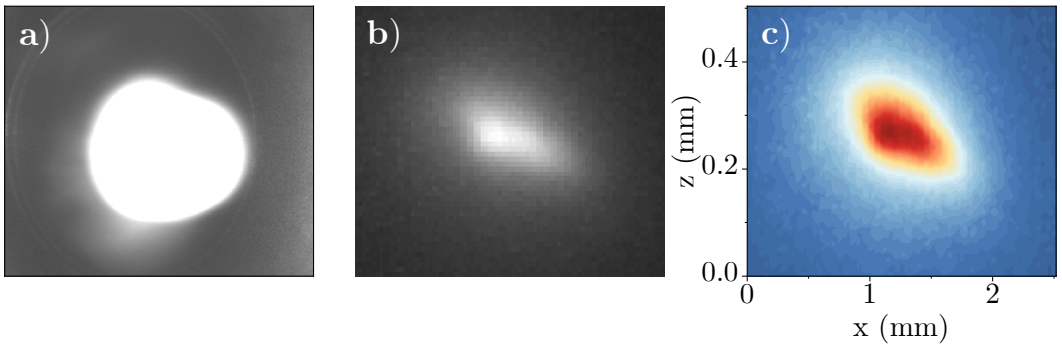

Figure 3.14: *2D false-colour fluorescence image taken by a CCD camera of a MOT of $N = 4.13 \times 10^7$ atoms calculated using the loading curve method (a). The atom number also can be found via absorption imaging, as shown in (b) and (c), where (b) is the shadow of a MOT of $N = 2.73 \times 10^6$ and (c) is the processed image of the same MOT.*

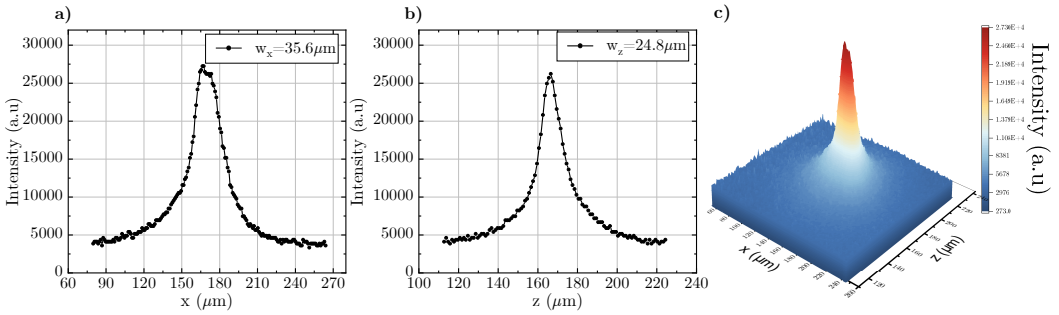

Figure 3.15: *Results from a MOT profile measurement performed using a CCD (Guppy Pro 125-B). (a) and (b) show data points from horizontal and vertical cuts through the centre of a MOT cloud and fit to Gaussian profiles for waist measurements, and (c) displays a 3D profile of the same cloud.*

first. The imaging laser frequency was then tuned by manually scanning the laser controlling current around the atomic transition of $F_g = 3 \rightarrow F_e = 4$ (the cooling transition), while multiple images were taken and saved in the software program to be analysed. Figure 3.14 (b and c) shows an example of an imaged and analysed atomic cloud.

The peak density of the MOT, n, can be directly estimated by measuring the radius of the cloud image on the CCD camera. An example of the density measurement of the same cloud in Fig. 3.14 (c and b) is shown in Fig. 3.15. Given that the cloud consists of $N = 2.73 \times 10^6$ atoms, and using the rela-

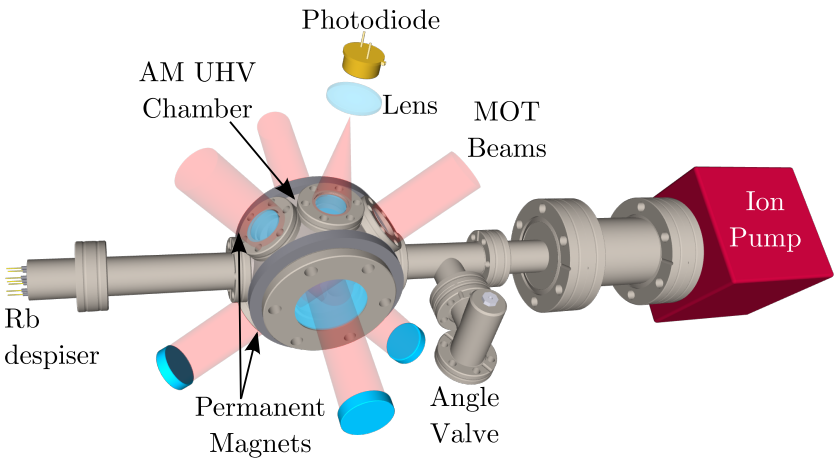

Figure 3.16: *The UHV assembly in the experimental setup. The photodiode is installed on the top window to capture the MOT light.*

tion $n = \frac{N}{(2\pi)^{3/2}\sigma_x\sigma z}$ explained in [147], the cloud is estimated to have a peak density of $n = 5.51 \times 10^8 \text{atoms/cm}^3$. This method was not used in further MOT characterisations and measurements for reasons of time constraints and a lack of additional equipment to control the frequency of the imaging laser independently from the reference laser.

3.4 Background pressure measurements

As briefly discussed in Sec. 1.2.2, the investigation of the vacuum background pressure via measuring the MOT loading has recently attracted some interest in the field of portable cold atom-based applications, where miniaturising UHV components is critical. The approach was utilised in our system to estimate the background vacuum pressure for the same purpose. There are several methods for applying this approach to cold atom experiments, all of which begin with the collection of multiple MOT loading curves at incremental or decremental pressure values.

3.4.1 Background pressure estimation using calculated loss coefficient $\frac{\gamma}{P_i}$:

One method for estimating background pressure is based on the knowledge of specific coefficients about the trapped atoms and the background species,

particularly the loss rate coefficient γ, the collisional cross section σ_i, and the van der Waals coefficients C_i. These parameters have already been derived and calculated in the literature for collisions between alkali atoms and most possible background species [67, 148].

Dispenser current (A)	Loss rate $\gamma\,(\mathrm{s}^{-1})$	P_{Rb-H_2} $(\times 10^{-10}\,\mathrm{mbar})$
2.15	0.06($\pm$0.01)	9.18($\pm$2.1)
2.18	0.07($\pm$0.001)	10.8($\pm$0.001)
2.20	0.10($\pm$0.02)	15.4($\pm$0.2)
2.25	0.09($\pm$0.03)	13.9($\pm$0.6)
2.30	0.12($\pm$0.04)	18.5($\pm$0.6)
2.35	0.24($\pm$0.04)	36.9($\pm$0.7)

Table 3.1: *Loss rate coefficients and background pressure values for a series of MOT loading curves taken at a range of dispenser current values, calculated using the conversion factor $\gamma/P = 4.9 \times 10^7$ $Torr^1\,s^1$ for collisions between Rb and H_2 atoms.*

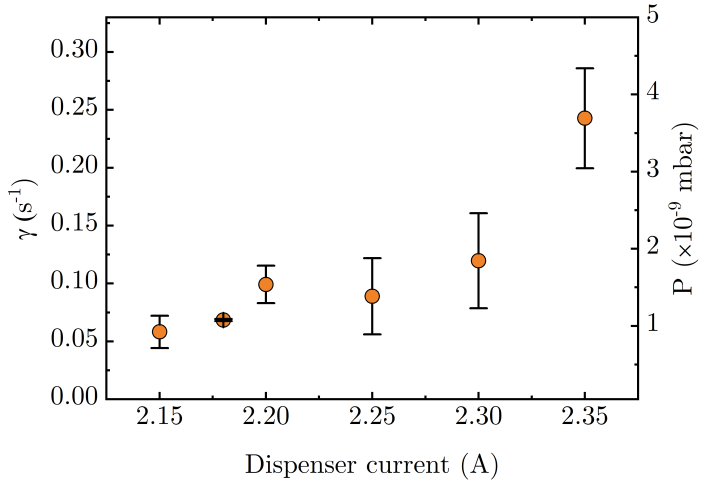

Figure 3.17: *Loss rate coefficients γ extracted from fitting loading curves to the MOT rate equation and corresponding background pressure values calculated using the conversion factor γ_i/P for collisions between Rb and H_2 atoms. The error bars are derived from the exponential fits and the standard deviation from three repetitions for each dispenser current value.*

The loss coefficient of collisions between background species and cold atoms γ can be given in terms of the species density n_i and the speed of the gas v_i as:

$$\gamma = \sum_i n_i \langle \sigma_i v_i \rangle, \tag{3.6}$$

where the term $\sigma_i v_i$ is averaged over a Maxwell-Boltzman distribution at a

temperature T, and the summation i is over all background species. The collisional loss cross section σ_i is given by:

$$\sigma_i = \int_{\theta > \theta_{sc}} \frac{d\sigma}{d\Omega} d\Omega, \tag{3.7}$$

where θ_{sc} is the minimum scattering angle required for a cold trapped atom to gain enough energy to break out of the trap, and $\frac{d\sigma}{d\Omega}$ is the differential scattering cross section. The classical small-angle approximation can be used to estimate the cross-section for a typical MOT of trap depth D of 1 K, and assuming that the background atoms are moving at room temperature ~ 300 K [67, 69, 148]. Thus $d\sigma/d\Omega$ can be given for a van der Waals potential by:

$$\frac{d\sigma}{d\Omega} = \frac{1}{6}\left(\frac{15\pi}{8}\frac{C_i}{m_i v_i^2}\right)^{1/3} \theta^{-7/3}, \tag{3.8}$$

where m_i is the mass of the background species, and the minimum angle of trapped atoms of mass m_0 is defined as:

$$\theta_{sc} = \frac{\sqrt{2 m_0 D}}{m_i v_i}. \tag{3.9}$$

Substituting Eq. 3.8 into Eq. 3.7 yields the collisional cross section σ_i:

$$\sigma_i = \left(\frac{15\pi^4}{16}\right)^{1/3} \left(\frac{m_i C_i^2}{m_0 E_i D}\right)^{1/6}, \tag{3.10}$$

where E_i is the incident energy and it is given by the relation $E_i = m_i v_i^2/2$.

And from the ideal gas law, the gas density n_i can be written as:

$$n_i = \frac{P_i}{k_B T}. \tag{3.11}$$

The loss rate constant in Eq. 3.6 can then be defined in terms of equations

3.10 and 3.11 as:

$$\gamma_i \approx 6.8 \frac{P_i}{(k_B T)^{2/3}} \left(\frac{C_i}{m_i}\right)^{1/3} (D m_0)^{-1/6}. \tag{3.12}$$

In the measurement group reported in Table. 3.1 and plotted in Fig. 3.17, a series of loading curves was taken at various dispenser currents and $\gamma = 0.06(\pm 0.01) s^{-1}$ was obtained for minimum applied dispenser current value. This value can be used to estimate the background pressure along with the conversion factor γ_i / P derived from Eq. 3.12. Under the assumption that it is more likely to have gaseous hydrogen residues in the background [148], pressure in a range between 9.2×10^{-10} and 3.7×10^{-9} mbar was estimated for this data set. These values are higher than the corresponding reading from the ion gauge of $< 10^{-10}$ mbar. Since the pressure gauges do not measure the pressure in the MOT position [149], this difference can be attributed to the vacuum conductance. In addition, the trap lifetime τ varies significantly with MOT parameters such as dispenser current, detuning, laser intensity, and alignment, influencing the background pressure values obtained.

3.4.2 Background pressure estimation from N vs. τ plot:

Another option to evaluate the background UHV pressure is through an N vs. τ plot, as shown in Fig. 3.11, which was obtained by taking MOT loading curves. Similar to the MOT characterisation method, this approach, introduced in Ref. [73], begins by taking MOT loading curves at various Rb dispenser current values (see Fig. 3.9) and fitting the curves to the MOT rate equation to extract and separate the parameters contributing to the atomic loss and the base pressure. Assuming that our MOT is large enough to be in constant density limit, we use the two-body loss coefficient already calculated in Ref. [67] for similar MOTs. Recalling the solution of the MOT dynamics rate equation

Species	Ref. [67] P_{Rb-i} ($\times 10^{-9}$ mbar)	Ref. [73] P_{Rb-i} ($\times 10^{-9}$ mbar)
H_2	0.918 ($\pm$0.27)	1.00 ($\pm$0.24)
He	2.00 ($\pm$1.05)	2.00 ($\pm$1.00)
N_2	2.00 ($\pm$1.05)	2.00 ($\pm$1.00)

Table 3.2: *Estimated non-rubidium pressure values in the MOT trapping region using approaches introduced in the indicated literature, with the assumption that the background gases are mostly the species specified in the first 'left' column.*

given in Eq. 2.27, which can be written as:

$$N(t) = N_{eq}(1 - e^{-t/\tau}), \tag{3.13}$$

where N_{eq} is the atom number at equilibrium given by:

$$N_{eq} = \alpha P_{Rb} \tau, \tag{3.14}$$

with the trap lifetime τ which can be defined as [73]:

$$\tau = \frac{1}{(\beta P_{Rb} + \gamma)}. \tag{3.15}$$

By combining Eq. 3.14 and Eq. 3.15, an expression for N_{eq} is obtained excluding P_{Rb} and directly relating the loss parameters α , β, and γ as:

$$N_{eq} = \frac{\alpha}{\beta}(1 - \gamma\tau). \tag{3.16}$$

By fitting the data points of Fig. 3.11 to Eq. 3.16, parameters α, γ, and τ can be extracted and the MOT characterised. The inverse of γ provides information on the upper limit of the trapping lifetime in the system, and α/β represents the largest MOT that can be obtained in the system.

In a set of measurements for dispenser current range between 2.15 to 2.75 A, $\alpha/\beta = 3.02(\pm 0.1) \times 10^6$, $\tau = 14.2(\pm 0.2)$ s, and $\gamma = 0.07(\pm 0.001)\,\mathrm{s}^{-1}$ were acquired. Since γ is directly proportional to the non-rubidium pressure in the system, and on the assumption that the background collisions are dominated by hydrogen atoms, the conversion factor in Ref. [67] for Rb atom

collisions with background species can be used to estimate the base pressure, (see Table. 3.2). The non-rubidium pressure values obtained with this method are also higher than the pressure gauge readings, which indicated values below 10^{-10} mbar during the whole course of the experiment.

The inconsistencies between the pressure gauge readings and the reported pressure values obtained using the loading curves methods viewed in Sec. 3.4.1 and this section emphasise the importance of further investigation into this subject. This variation in results does not necessarily arise from a defect in our UHV system or the pressure gauge. It is expected because the pressure readings vary depending on the measurement location, namely the MOT and the pressure gauge. In addition, this discrepancy could be partially attributed to our numerical and theoretical analysis routine followed for linking the background pressure to the collisions dynamics of the species in the UHV regime. These are what were thought to have contributed to increasing the calculation errors and, hence, the variant results. Therefore, it is necessary to conduct this experiment under carefully adjusted and controlled conditions in order to achieve consistent results and reduce associated errors.

Chapter 4

Additively manufactured ultra-high vacuum chamber for portable quantum technologies

Published in Additive Manufacturing

DOI: 10.1016/j.addma.2021.101898

Additive Manufacturing 40 (2021) 101898

Contents lists available at ScienceDirect

Additive Manufacturing

journal homepage: www.elsevier.com/locate/addma

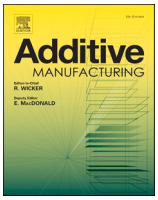

Research Paper

Additively manufactured ultra-high vacuum chamber for portable quantum technologies

N. Cooper [a,*], L.A. Coles [b,*], S. Everton [b], I. Maskery [d], R.P. Campion [a], S. Madkhaly [a], C. Morley [a], J. O'Shea [a], W. Evans [c], R. Saint [c], P. Krüger [c], F. Oručević [c], C. Tuck [b,d], R.D. Wildman [b,d], T. M. Fromhold [a], L. Hackermüller [a]

[a] School of Physics and Astronomy, University of Nottingham, NG7 2RD, UK
[b] Added Scientific Ltd., Isaac Newton Centre, Nottingham Science Park NG7 2RH, UK
[c] Department of Physics and Astronomy, University of Sussex, Brighton BN1 9QH, UK
[d] Centre for Additive Manufacturing, Faculty of Engineering, University of Nottingham, NG7 2RD, UK

ARTICLE INFO

Keywords:
Ultra-high vacuum
Quantum sensors
AlSi10Mg

ABSTRACT

Additive manufacturing is having a dramatic impact on research and industry across multiple sectors, but the production of additively manufactured systems for ultra-high vacuum applications has so far proved elusive and widely been considered impossible. We demonstrate the first additively manufactured vacuum chamber operating at a pressure below 10^{-10} mbar, measured via an ion pump current reading, and show that the corresponding upper limit on the total gas output of the additively manufactured material is 3.6×10^{-13} mbar l/(s mm^2). The chamber is produced from AlSi10Mg by laser powder bed fusion. Detailed surface analysis reveals that an oxidised, Mg-rich surface layer forms on the additively manufactured material and plays a key role in enabling vacuum compatibility. Our results not only enable lightweight, compact versions of existing systems, but also facilitate rapid prototyping and unlock hitherto inaccessible options in experimental science by removing the constraints that traditional manufacturing considerations impose on component design. This is particularly relevant to the burgeoning field of portable quantum sensors — a point that we illustrate by using the chamber to create a magneto-optical trap for cold ^{85}Rb atoms — and will impact significantly on all application areas of high and ultra-high vacuum.

1. Introduction

We demonstrate that additive manufacturing (AM) is suitable for the production of ultra-high vacuum (UHV) equipment, thus opening up opportunities for rapid prototyping, weight reduction and enhanced functionality across the high and ultra-high vacuum sectors.

Applications of UHV systems are numerous, ranging from established technologies such as photosensors, cameras, cryostats, electron microscopes and x-ray photoelectron spectroscopy (XPS) analyzers to important emerging research areas such as portable quantum sensors based on cold atoms [1–4]. AM methods could accelerate both fundamental research and technological development across all of the above areas, by allowing substantial reductions in the size, weight and development lead time of the associated UHV apparatus. For example, the UHV chamber described here, which is fabricated via a laser powder bed fusion (LPBF) technique [5] from aluminium alloy AlSi10Mg, weighs just 245 g — 70% less than equivalent standard chambers. Such mass reduction is particularly critical for space-based applications of UHV, for example experimental tests of fundamental physics using space-borne quantum sensors [6–9].

However, despite recent advances in AM processing of metals [10,11], a complete UHV chamber is yet to be produced via AM. Identified challenges for vacuum compatibility are surfaces roughness, porosity and limited hardness. Rough surfaces are associated with increased outgassing rates, porosity [12,13] can create leaks or virtual leaks from trapped gas-pockets and limited hardness [10] reduces the effectiveness of traditional knife-edge seals at vacuum connections.

These characteristics of AM metals have led to legitimate doubts as to their suitability for the production of UHV components. The alloy AlSi10Mg offers a higher thermal conductivity than alternatives such as

* Corresponding authors.
E-mail addresses: nathan.cooper@nottingham.ac.uk (N. Cooper), laurence.coles@addedscientific.com (L.A. Coles).

https://doi.org/10.1016/j.addma.2021.101898

Available online 12 February 2021

titanium or stainless steel, which may help to improve uniformity and reduce build defects when printing. Here, we conduct a detailed analysis of the surface of AM AlSi10Mg, employing optical and electron microscopy, mass spectrometry and x-ray photoelectron spectroscopy. This not only reveals a material structure free from significant porosity or lateral cracking, but also that the surface chemistry associated with AM AlSi10Mg is critical to obtaining high vacuum performance — specifically that a heavily oxidized, Mg-rich layer on the surface of the AM material strongly suppresses the outgassing of magnesium from the material bulk. As a result, the chamber described herein readily sustains a pressure below 10^{-10} mbar.

This vacuum performance is more than sufficient to permit the capture of a cloud of cold ^{85}Rb atoms in a magneto-optical trap (MOT) [14], as shown in Fig. 1(b); MOTs are the starting point for nearly all cold-atom based experiments and devices. These include atomic clocks for precision timekeeping [15–17], high-precision gravimeters for applications in geology, navigation and civil engineering [18–20] and cold atom magnetometers [21,22] for navigation and medical imaging. This important and burgeoning field stands to benefit strongly from the application of AM methods to UHV equipment..

Although there are prior examples of AM materials being subject to a UHV environment [23,24], such as the conflat flange demonstrated in [24], and work towards vacuum-based applications of AM components has been conducted [25–28,29], a full vacuum chamber produced via AM methods has yet to reach the UHV regime. The chamber we demonstrate herein represents a significant increase in size and complexity over previous AM UHV components - an essential step towards the exploitation of the benefits of AM within the UHV sector. We also demonstrate the compatibility of our chamber with industry-standard components and sealing techniques, a detail that has been absent from most previous work.

2. Methods

2.1. Chamber design and manufacture

The AM UHV chamber was designed to meet the functional requirements of a magneto-optical trap (MOT) [30] — the first essential component of nearly all quantum technologies based on cold atoms. These requirements are: optical access for three orthogonal beam pairs, magnetic coils, a UHV environment and the ability to connect to standard components, such as vacuum pumps — see Fig. 2.

"Design for LPBF" methodology [5] was applied to reduce the overall weight without affecting mechanical stability. Light-weighting of the chamber core was achieved by refining the port geometry and minimizing the spacing between ports. A 2.5 mm thick internal skin was added between the ports to hold the UHV, as shown in Fig. 2(b). Effort was made to keep symmetry where possible in the chamber design, thus keeping the ports perpendicular to the optical paths under the external pressure loading. The resulting (negligible) deformation of the chamber under an external pressure load was analyzed via 'Finite Element Analysis' (FEA) based simulation using 'MSc Marc 2017.1.0′ — see Supplementary Material (Supplementary Fig. 2).

Within a predefined volume (Fig. 2(c)) a variable density triply periodic minimal surface lattice was integrated with the symmetric internal core design to add a layer of robustness and increase stiffness; this took the form of a matrix based gyroid surface [31,32], as shown in Fig. 2(d). The variable volume fraction (density) of the lattice permits reinforcement of areas that need more support, such as those adjacent to the ports. The final chamber design (Fig. 2(e)) consists of multiple conflat ports (2 × CF40 ports and 8 × CF16), making it compatible with standard UHV equipment, as shown in Fig. 4(a). Building on the design approach demonstrated here, it will be possible to produce complex, multi-functional, part-consolidated chamber designs that can only be realized by AM.

Of the metallic alloys available for AM processing, which also include titanium, stainless steel and silver, aluminium alloy AlSi10Mg was selected because of its high specific strength, low density and good thermal conductivity [33]; a higher thermal conductivity allows faster dissipation of the heat generated during the LPBF process, reducing the likelihood of build imperfections occurring due to build-up of temperature gradients and the resulting thermal stresses. LPBF fabrication was chosen over alternatives such as inkjet binder printing [34] to avoid the use of any non-UHV compatible materials in the fabrication process, thus removing the possibility that incomplete burnoff might lead to contamination of the vacuum system. Materials produced by LPBF have a characteristically ultra-fine grain structure with epitaxial grain growth aligned with the build direction [35]. Solution heat treatments can be applied to homogenize the microstructure or control the grain size. These methods are often utilised to increase the ductility of the alloy; subsequently an ageing heat treatment is applied to promote precipitate hardening and increase the material strength [36,37]. The resulting material performance after the selected heat treatment regime was verified for knife edge seal repeatability and thread torque requirements — see Appendix. The Vickers hardness was measured for a machined surface (as in Fig. 3(g)) as (105 ± 0.8) HV5.

Following design and material testing the chamber was printed using a Renishaw AM250 laser powder bed fusion machine, as described in detail below.

2.1.1. Material

The pre-alloyed, gas atomised AlSi10Mg powder from TLS Technik GmbH, contains Al 89.8 wt%, Si 9.7 wt% and Mg 0.3 wt% with powder particles in the range 10 μm to 100 μm, measured using a Malvern UK

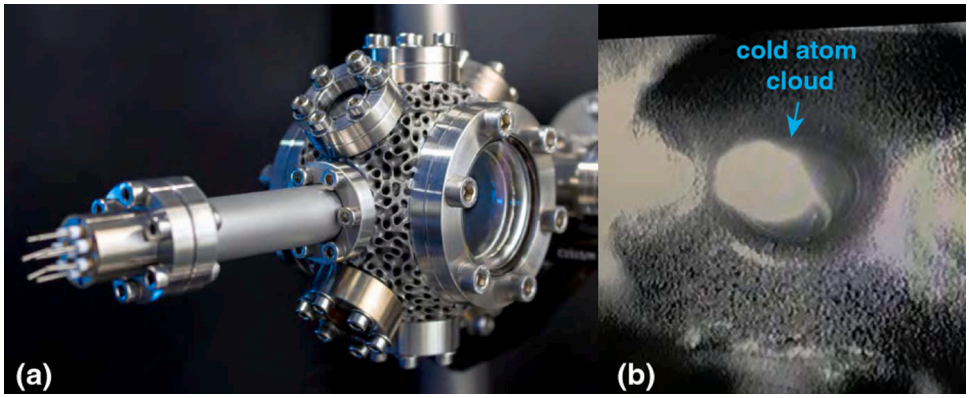

Fig. 1. An additively manufactured UHV chamber for quantum technologies (a) Photograph of the final, assembled AM-built UHV chamber with standard UHV components. For scale, the larger ports on the AM vacuum chamber are CF40 and the smaller CF16. (b) Fluorescence image of a cold cloud of ^{85}Rb atoms confined in a magneto-optical trap inside the chamber. The diameter of the atomic cloud is approximately 10 mm.

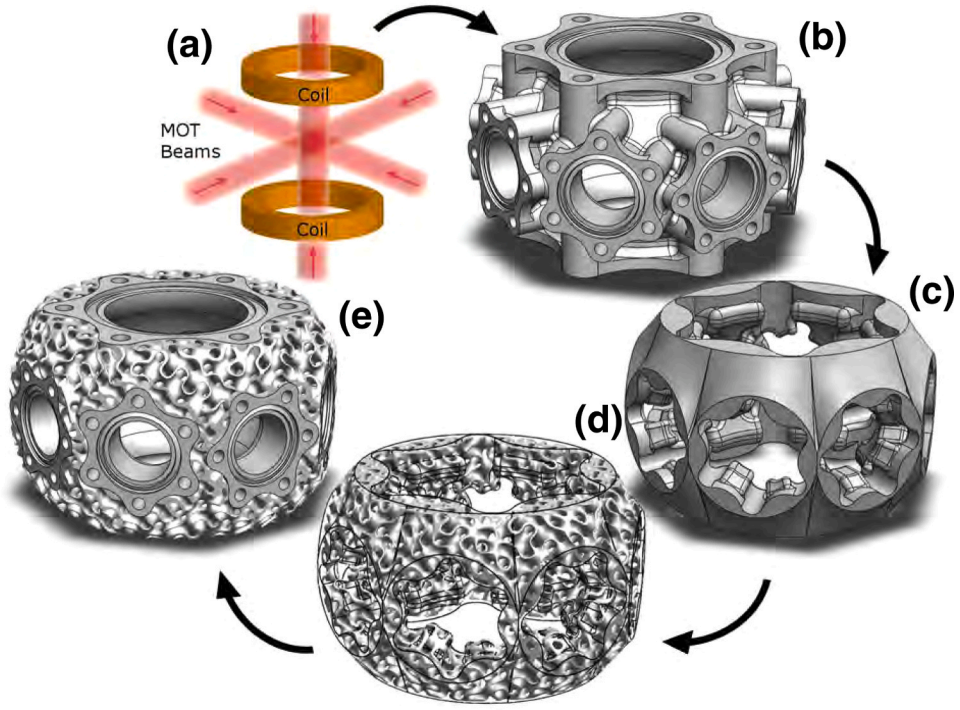

Fig. 2. Overview of the design process (a) Illustration of the functional requirements for cold atom cloud trapping. (b) Thin wall internal chamber design with conflat ports. (**c**) Volume identified for additional lattice support. (d) The variable density triply periodic minimal surface gyroid matrix lattice, which has been generated from the previous volume in (c) to add a layer of robustness and increase structural stiffness. (e) Final lightweight chamber design.

Mastersizer 3000.

2.1.2. Manufacture

A Renishaw AM250 laser powder bed fusion machine was used to manufacture all test pieces and the final vacuum chamber. The machine uses a Yb fiber laser at 1064 nm wavelength, with a laser power of 200 W, and heats the powder bed to 180 °C during build. The parts were built on an aluminium baseplate using a powder layer thickness of 25 μm. A hatch spacing of 80 μm, point distance of 70 μm and exposure time of 220 μs were selected, giving an effective scanning speed of 318 mm s^{-1}. A chequerboard pattern was used to minimise the accumulation of residual stresses and after each layer, the scan pattern was rotated by 67 degrees.

2.1.3. Post processing and mechanical machining

Once processed and removed from the build machine, the parts were stress-relieve heat treated on the build plate for 2 h at 300 °C and furnace cooled. The parts were removed from the build plate by wire electro-discharge machining and bead blasted to remove any loosely adhered powder particles. Finally, a T6-like series of heat treatments were applied to modify the microstructure of the material [36]. The components were subject to a solution heat treatment for 1 h at ~ 500 °C followed by a water quench and then aged for 6 h at ~ 150 °C. To ensure a good tolerance at the mating surfaces between the chamber interfaces and the standard off-the-shelf UHV parts, the interfaces were machined, and knife edges and threaded bolt holes added. The internal chamber surface was left in the as-built condition.

2.2. Outgassing behaviour and surface material analysis

LPBF components and materials tend to have rough surfaces [10] and have therefore been thought unsuitable for UHV applications. Fig. 3 (a) shows a focus variation microscopy (FVM) image of a 1.5 mm by 1.5 mm area on the upper surface of an unmachined test sample, built and post-processed identically to the UHV chamber. The image was obtained using an Alicona G5 Infinite Focus microscope. The surface roughness *Sq*, the root mean square height over the area sampled, was measured as $Sq = 5.3 \pm 0.1$ μm. Scanning Electron Microscopy (SEM) of the same surface reveals a rich surface structure with lateral features as small as 1–10 μm (Fig. 3(b, c)), but no evidence of cracks, tears or deep pores. The dense, high-quality structure of the material is also seen in SEM images of machined surfaces. Fig 3(d) shows an image of the machined knife-edge, with some machining marks but no material defects visible at this zoom level. An image taken at higher magnification (Fig. 3(e)) shows small, micrometer-sized defects aligned with the direction of the machining tool, but none orthogonal to it. This anisotropy suggests that the defects stem from the machining rather than the AM build process. Importantly, the defects seen on the machined surface are isolated and discontinuous, and no evidence of lateral cracking is observed.

To characterize the outgassing behaviour and gain information about the surface composition, we conducted a mass spectrometric study on the LPBF alloy used to build the vacuum chamber, while varying the temperature from 20 to 500°C. In addition, x-ray photo-electron spectroscopy (XPS) of a machined and unmachined surface was performed at room temperature.

The results of both measurements suggest the formation of an Mg-enriched, oxidised layer on the surface of the material, which is likely to play a role in suppressing outgassing.

Ten test samples of the LPBF material (10 × 10 × 4 mm cuboids) were fabricated using the same build parameters and feedstock as the chamber. The samples were placed in a temperature-controlled Knudsen Cell connected to a line-of-sight mass spectrometer. The molecular/atomic beam from the source can be interrupted by a rotating chopper, which allows the line of sight beam to be distinguished from background signals [38]. Scans were run across the mass range of 1–200 amu, while the material was heated up as far as 500 °C with a heating rate of 10 °C/min as shown in Fig. 4(f). The experiment was then repeated in a quasi-stable situation, holding the sample for 48 h each at temperatures of 250 °C, 350 °C, 400 °C and 450°C in turn. In both cases similar

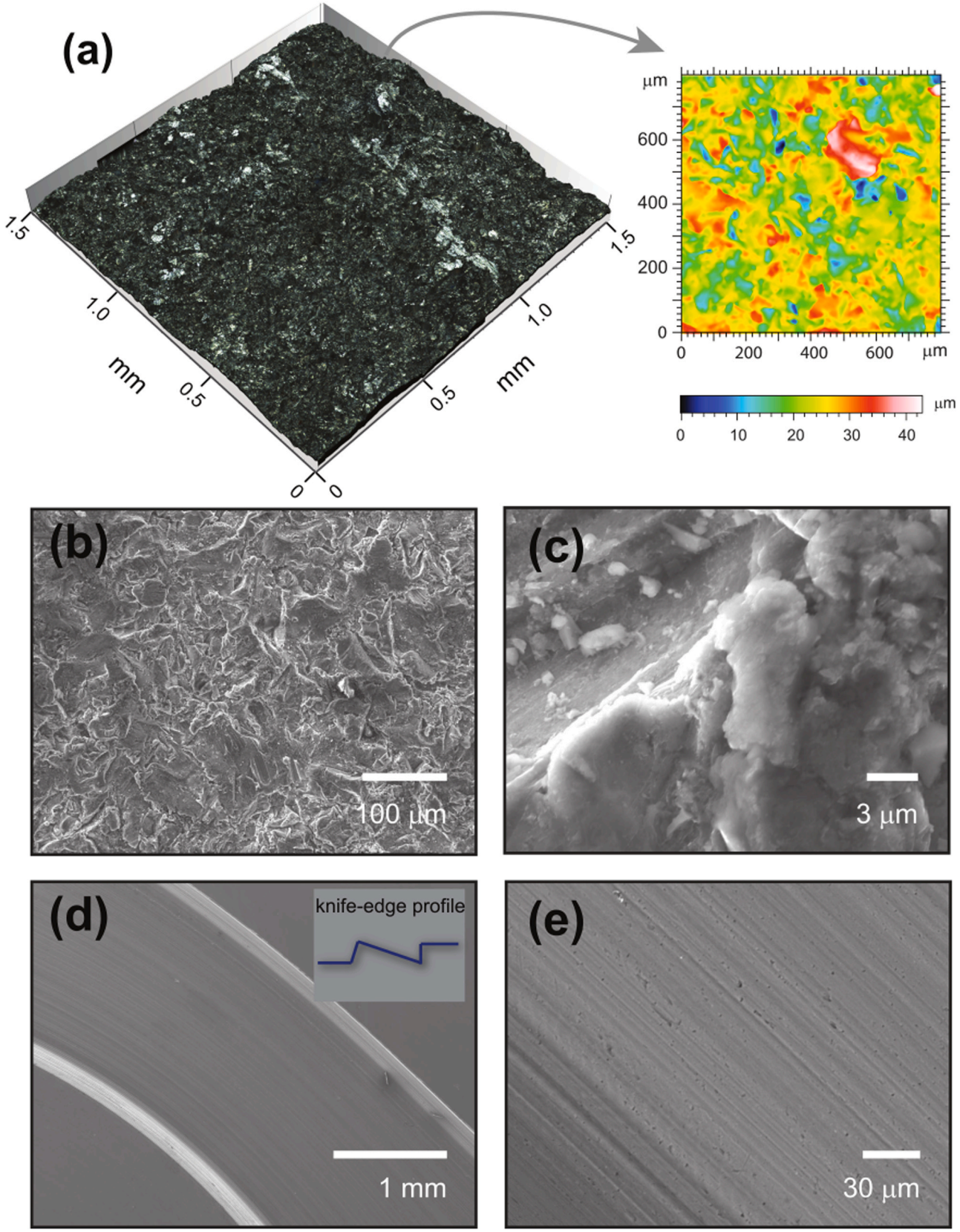

Fig. 3. Surface and material characterization (a) Focus Variation Microscopy image of the untreated surface of an additively manufactured sample of AlSi10Mg (left) and color map showing the corresponding surface profile (right). (b,c) SEM images of the untreated surface vs. (d,e) SEM images of the machined surface and knife-edge (For interpretation of the references to colour in this figure legend, the reader is referred to the web version of this article.).

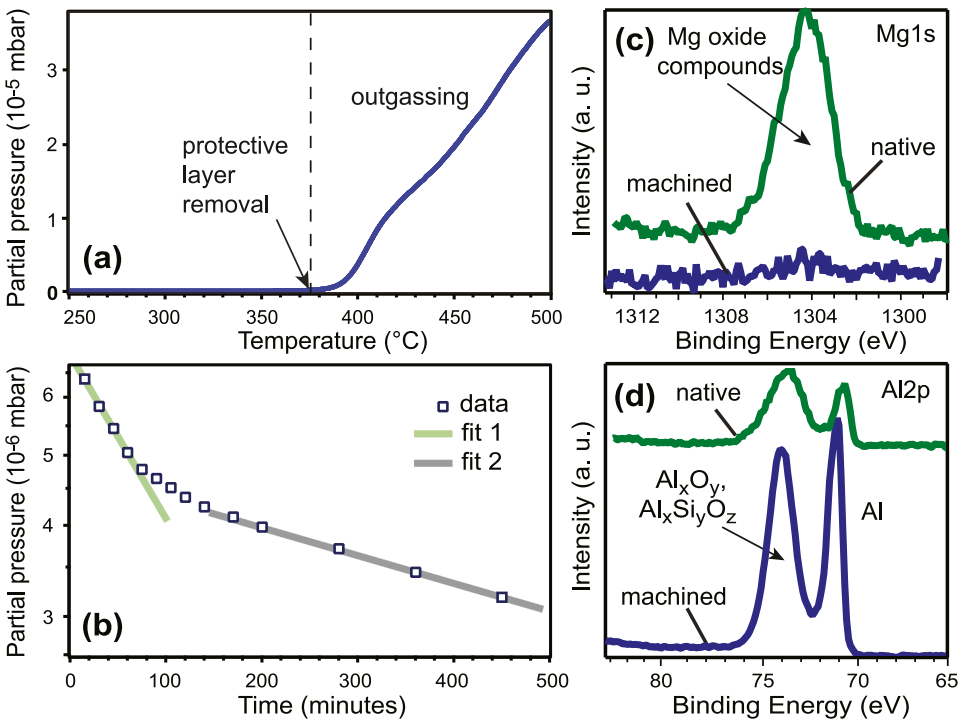

Fig. 4. Mass spectrometry results and XPS material characterisation. (a) Material characterization with mass spectrometry - partial pressure of ^{24}Mg in the Knudsen Cell as a sample of AM AlSi10Mg is heated to 500 °C at 10 °C per minute. (b) Partial pressure of ^{24}Mg in the Knudsen Cell as a function of time after a sample of AM AlSi10Mg has been heated rapidly to 420 °C and held at this temperature. Lines are linear fits at short and long timescales. (c,d) XPS spectra showing a high content of Mg oxides in the untreated surface vs. a low abundance of Mg oxides in the machined surface (c) and a similar but smaller discrepancy for Al (d). A vertical offset has been applied to improve visibility (For interpretation of the references to colour in this figure legend, the reader is referred to the web version of this article.).

behaviour was observed. Other than (expected and unavoidable) atmospheric species, the only peaks detected were for magnesium (primarily ^{24}Mg), which became evident above 400°C°C. Below 375 °C, no ^{24}Mg signal is measurable, as determined by the noise level, while above that temperature a sharp rise in the magnesium signal is visible.

If the temperature is raised above 400 °C and then subsequently decreased, the ^{24}Mg signal does not return to its original value, but remains at a considerably higher level (factor 10^3 at 350 °C). The signal then persists at temperatures far below 350°C. We interpret these results as the removal of a protective layer. The presence of this layer reduces the rate of Mg emission from the sample, and may have a similar effect on outgassing of other particle species.

This interpretation is supported by a second experiment, where samples were held at 420 °C for 150 min and the time variation of the emission was measured (see Fig. 4(g)). All samples show a rapid initial reduction in Mg emission (fit 1 in Fig. 4(g) with a gradient of $g_1 = -5.1(4)\exp(-3)$ ln(mbar)/min) followed by a much slower subsequent tail-off (fit 2 with a gradient of $g_2 = -9.1(2)\exp(-4)$ ln(mbar)/min).

For Fig. 4(f, g) the system was calibrated with a pure magnesium sample of the same dimensions as the LPBF material and the observed count rate for the LPBF samples normalised to the magnesium counts and expressed as a partial pressure.

Temperature dependent emission data taken immediately after the removal of the oxide layer can be plotted as an Arrhenius plot, resulting in a gradient proportional to the activation energy that corresponds within 1% to that of a pure magnesium sample (see Supplementary Fig. 4). Therefore the behaviour seen in Fig. 4(f) is consistent with a relatively fast removal of a protective top-surface layer leading to the exposure of a thin, unoxidised, Mg-enriched layer at the sample surface. This layer is then rapidly depleted (regime of fit 1) and Mg emission eventually becomes limited by the rate of diffusion of Mg from the bulk to the surface (regime of fit 2). A formation process for magnesium oxides at high temperatures during the LPBF build process for AlSi10Mg has been suggested in [39,40].

The measured outgassing properties of the test samples represent an average over their exposed surfaces, for which the relative representation of the different surface orientations relative to the build direction is comparable to that of the chamber's interior; due to the complexity of the chamber's form exact correspondence was not practical. Use of the same build parameters and feedstock should ensure similar surface characteristics (e.g. grain size, surface roughness etc.) for the test samples and chamber.

XPS measurements were performed on an untreated surface of the AM material and on a machined surface of the same sample (Fig. 4(h)). The XPS data confirm the hypothesis of a surface layer with a larger content of magnesium oxides. Fig 4(h) (left) shows a peak at 1304.2 eV corresponding to magnesium oxide compounds such as MgO or Mg $(OH)_2$, illustrating the difference in abundance of Mg in the untreated surface (green line) and the machined surface (blue line). Fig 4(h) (right) features two peaks for both surfaces. The low binding energy peak around 71 eV is attributed to metallic aluminium, while the second peak with a binding energy around 74 eV is indicative of aluminium oxide or aluminosilicate [41]. The relative abundance of Si is similar on both surfaces (see Supplementary Fig. 5). From the XPS spectra the composition of the unmachined surface was determined to be 22% Mg, 69% Al and 9% Si, while the machined surface was 1% Mg, 90% Al and 9% Si, consistent with the composition of the powder within the measurement uncertainties. The high concentration of Mg on the untreated surface is remarkable, given that Mg only accounts for 0.3% of the powder composition, but consistent with the hypothesis developed above. Note that XPS only characterises the surface up to a depth of 10 nm. On both surfaces the Mg component was detected exclusively within a range of binding energies consistent with its oxidised forms, e.g. MgO and Mg $(OH)_2$, rather than pure metal [42]. By contrast, the Si and Al components were detected as pure and oxidised forms.

Both approaches confirm the existence of a layer with a high abundance of oxidised Mg at the native surface. The mass spectrometry results also demonstrate that this layer can withstand temperatures up to 350 °C and reduces the outgassing of volatile species. For high temperature applications of AM parts (e.g. for use in scanning tunneling microscopes), the development of methods to enhance the stability of this protective layer is a promising line of investigation.

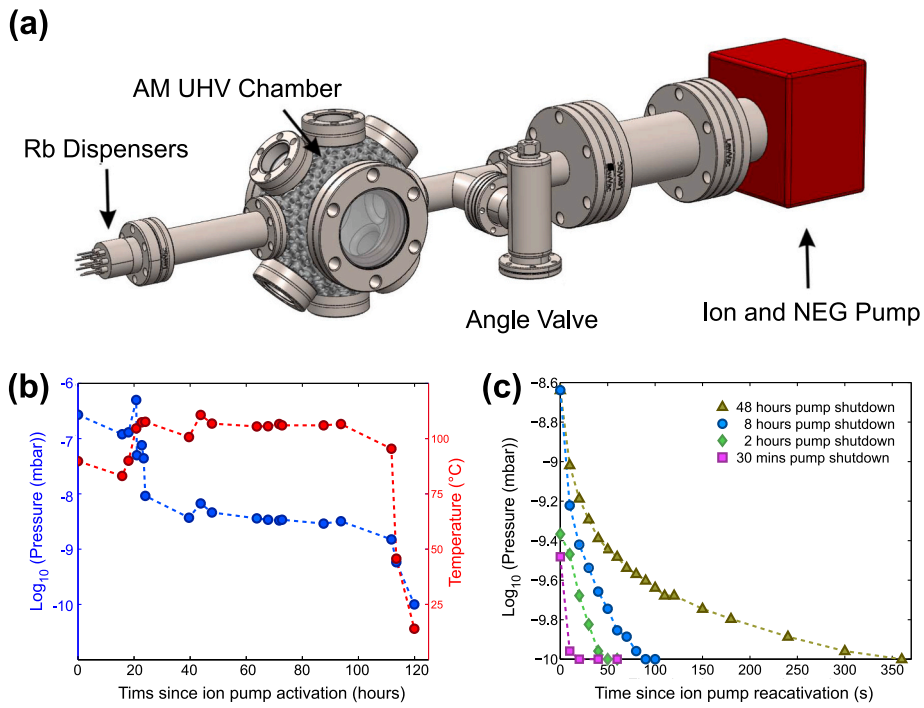

Fig. 5. UHV test setup and results (a) Schematic diagram illustrating the test setup of the vacuum system. For scale, the larger ports on the AM vacuum chamber are CF40 and the smaller CF16. (b) Pressure evolution (blue points) during bakeout (temperature represented by red points). (c) Recovery of vacuum after periods without active pumping. The pump contains a passive element (non-evaporable getters) and an active ion pump. The data shown are the pressures recorded following reactivation of the ion pump after a long period of only passive pumping. Note that the lower limit on the pressure that can be read is 10^{-10} mbar, and under-range readings are displayed as 10^{-10} mbar in both (b) and (c). Errors are $\pm$ 1. 5 °C in temperature and $\pm$ 10% in pressure, the size of the markers exceeds the size of the error bars.

3. Results

A total of four chambers were produced via the methods described above, with visual inspection suggesting a similar build quality across all four. To test the performance resulting from the design and the surface characteristics, one finished chamber was assembled into a vacuum system using off-the-shelf stainless-steel viewports and tubes, mounted using standard CF flanges, as shown schematically in Fig. 5(a). Bake-out of the system was carried out for a period of 120 h, during which the temperature did not exceed 120°C. Once baked, the assembly was pumped using a combined ion / non-evaporable getter (NEG) pump (NEXTorr D100 − 5, SAES Getters) and was found to achieve a pressure in the UHV range. The ion pump current reading indicates a pressure $< 1 \times 10^{-10}$ mbar, the lower limit of what can be read using our device and close to the generally accepted reliability limit of ion-pump current measurements [43].

To place an upper limit on the total outgassing rate of the AM material we compare the achieved pressure to the pumping rate of the system. The pumping speed of the NEXTorr D100 − 5 is dependent upon the exact particle species being pumped; we consider the 40 l/s pumping speed applicable to nitrogen, as this is not only a common and plausible background gas constituent but also provides a mid-range pumping speed estimate likely to be broadly representative of the average properties of a multi-component residual gas. Based on this, and on the 11283 mm^2 nominal internal surface area of the AM vacuum chamber, we can place an upper limit on the outgassing rate of the AM vacuum chamber's internal surface of 3.6×10^{-13} mbar l/(s mm^2). While slightly above values typically measured for baked stainless steel, which are on the order of 5×10^{-14} mbar l/(s mm^2) [44], it is important to stress that this is only an upper limit on the material's outgassing rate. We have assumed that all of the gas pumped from the system originates from the AM material; this not only means that we determine the total gas load produced by the material, including micro-leaks and virtual leaks resulting from material porosity, but also that we underestimate the vacuum performance of the material by attributing to it all of the gas entering the system, when in fact contributions from the standard vacuum components connected to the AM chamber are likely to be substantial.

For a portable system, particularly relevant to quantum sensing applications, operation without external power supplies is highly desirable – therefore, the effect of turning off the ion pump for up to 48 h was tested. During this time span the chamber was pumped only via the passive NEG elements of the NEXTorr D100 − 5. When the ion pump was reactivated, the initial pressure was measured and its decay back to the under-range reading following ion pump activation was recorded.

The results of these tests are shown in Fig. 5(c). These tests demonstrate that the chamber can maintain pressures in the 10^{-10} mbar range for over two hours without active pumping and that even after 48 h, the pressure remains in the 10^{-9} mbar range. After the switch-on of the pump the chamber returns to below 10^{-10} mbar in less than 6 min. The background pressure achieved was more than sufficient to permit the capture of a cloud of cold Rb atoms in a magneto-optical trap. Fig. 1(b) shows a fluorescence image of the trapped atomic cloud, which contains up to 2×10^8 rubidium atoms. Loading times vary between < 1 s and ~ 10 s, depending on the amount of Rb vapour dispensed into the chamber; this provides independent confirmation that the pressure is no higher than $\sim 5 \times 10^{-9}$ mbar [45]. These values are typical of the performance of MOTs in conventional vacuum chambers and suggest the suitability of AM UHV equipment for use in portable quantum technologies.

Since the acquisition of these initial results a second of the four chambers has been assembled into a vacuum system and also achieves pressures in the UHV regime with comparable pumping speeds.

3.1. Technical details of assembly and bake-out

The chamber was cleaned before assembly — first with water and detergent, then with acetone and finally with isopropanol. Following this the chamber was attached to standard conflat vacuum components using standard silver-plated copper gaskets. The bolts used to close the joins and compress the gaskets secure directly into the machined bolt holes in the chamber itself. M6 bolts, tightened with a torque of 16 Nm, were used for the CF40 fittings and M4 bolts, tightened with a torque of 9 Nm, for the CF16. The assembled system was baked for 120 h at a maximum temperature of 120°C. During bake-out, a 300 l/s turbomolecular pump (Pfeiffer HiPace 300) was fitted via the angle valve shown

in Fig. 4(a).

4. Conclusions

In summary, we have demonstrated an additively manufactured vacuum chamber operating in the pressure range below 10^{-10} mbar and used it to trap a cold cloud of ^{85}Rb atoms. No degradation of the chamber's performance has been observed over several months of operation, and standard pumping methods appear able to sustain the stated pressure indefinitely. We described the design steps that lead to a significant reduction in weight while retaining stability and analyzed the surface structure and outgassing behaviour of the AM material. Introducing AM methods to UHV apparatus has enormous potential for reducing the size, weight and material consumption of existing systems and enabling new portable systems with increased functionality.

Promising areas for future investigation include the use of advanced lattice structures to increase passive cooling rates or enable external cooling, reduce eddy current generation in response to changes in magnetic field and damp or isolate mechanical vibrations. Another line of investigation is the use of AM to produce high surface area elements to enhance the efficiency of passive pumping devices such as Ti sublimation pumps. It may also be of interest to study the mechanism by which Mg enrichment of the surface layer occurs. If this is related to melt-pool dynamics [46] then the process will likely be common to many AM alloys, and could have broader implications for refinement of LPBF methodology. Finally, research into achieving comparable vacuum compatibility via alternative AM methodologies besides LPBF [34] may help to further broaden the options available for AM of UHV systems.

Declaration of Competing Interest

The authors have complied with Elsevier's ethical requirements. The presented work has not been published previously and is not under consideration for publication elsewhere. Also, its publication is approved by all authors and if accepted, it will not be published elsewhere in the same form, in any language, without the written consent of the Publisher. The authors do not have any conflicts of interest to declare.

Data Availability

All data necessary to support the conclusions are given in the article. All data collected as part of the research can be obtained from the authors upon reasonable request.

Acknowledgements

We are thankful to Dominic Sims[1] and the University of Nottingham Manufacturing Metrology Team for helpful discussions. **Funding:** This work was supported by Innovate UK [project No. 133086]; the UK Engineering and Physical Sciences Research Council [grant numbers EP/R024111/1, EP/M013294/1]; and by the European Union's Horizon 2020 programme [grant number 800942, "ErBeStA"].

Appendix: mechanical testing

The durability of the knife-edges machined in the AlSi10Mg LPBF material was tested for repeated opening-closure cycles of a test flange. The performance of the seal was assessed using a leak detector (Pfeiffer Vacuum ASM 340). During all performed tests (up to 10 cycles) no measurable degradation of the seal was detected and the suitability of the selected post-processing heat treatment was thus confirmed. The performance of the threads machined into the blind holes was tested against the recommended bolt torque (9.5 Nm for M4, 16.3 Nm for M6 from Kurt J. Lesker) using standard stainless steel bolts within a similarly threaded test piece with M4 and M6 threaded holes. A torque wrench was used to apply the recommended bolt torque. No failure or noticeable degradation of the threads was observed.

Appendix A. Supporting information

Supplementary data associated with this article can be found in the online version at doi:10.1016/j.addma.2021.101898.

References

[1] P. Knight, et al., The Quantum Age: Technological Opportunities. Blackett Review, Government of Science, UK, 2016.
[2] K. Bongs, et al., The UK National Quantum Technologies Hub in sensors and metrology (Keynote Paper), Proc. SPIE 9900 (2016).
[3] S. Battersby, Core concept: quantum sensors probe uncharted territories, from earth's crust to the human brain, PNAS 116 (2019) 16663–16665.
[4] J. Kitching, S. Knappe, E. Donley, Atomic sensors - a review, IEEE Sens. J. 11 (2011) 1749–1758.
[5] I. Gibson, D. Rosen, B. Stucker, Additive Manufacturing for Technologies, Springer-Verlag, New York, 2015.
[6] D. Becker, et al., Space-borne Bose-Einstein condensation for precision interferometry, Nature 562 (2018) 391–395.
[7] S. Dimopoulos, et al., Gravitational wave detection with atom interferometry, Phys. Lett. B 678 (2009) 37–40.
[8] O. Carraz, et al., A spaceborne gravity gradiometer concept based on cold atom interferometers for measuring earthas gravity field, Microgravity Sci. Technol. 26 (2014) 139–145.
[9] L. Liu, et al., In-orbit operation of an atomic clock based on laser-cooled 87Rb atoms, Nat. Comm. 9 (2018), 2760.
[10] J.H. Martin, et al., 3D printing of high-strength aluminium alloys, Nature 549 (2018) 365–369.
[11] P. Barriobero-Vila, et al., Peritectic titanium alloys for 3D printing, Nat. Comm. 9 (2018), 3426.
[12] A.A. Martin, et al., Dynamics of pore formation during laser powder bed fusion additive manufacturing, Nat. Comm. 10 (2019), 1987.
[13] S.K. Everton, et al., Review of in-situ process monitoring and in-situ metrology for metal additive manufacturing, Mater. Des. 95 (2016) 431–445.
[14] E. Raab, et al., Trapping of neutral sodium atoms with radiation pressure, Phys. Rev. Lett. 59 (1987), 2631.
[15] S. Falke, et al., A strontium lattice clock with 3×10^{-17} inaccuracy and its frequency, N. J. Phys. 16 (2014), 073023.
[16] A.D. Ludlow, et al., Optical atomic clocks, Rev. Mod. Phys. 87 (2015) 637–701.
[17] F. Riehle, Optical clock networks, Nat. Photon. 11 (2017) 25–31.
[18] Y. Bidel, et al., Absolute marine gravimetry with matter-wave interferometry, Nat. Comm. 9 (2018), 627.
[19] W. Bin, et al., The investigation of a microgal-level cold atom gravimeter for field applications, Metrologia 51 (2014), 452.
[20] V. Menoret, et al., Gravity measurements below 10–9 g with a transportable absolute quantum gravimeter, Sci. Rep. 8 (2018), 12300.
[21] J.M. McGuirk, et al., Sensitive absolute-gravity gradiometry using atom interferometry, Phys. Rev. A 65 (2002), 033608.
[22] N. Behbood, et al., Real-time vector field tracking with a cold-atom magnetometer, Appl. Phys. Lett. 102 (2013), 173504.
[23] R. Saint, et al., 3D-printed components for quantum devices, Sci. Rep. 8 (2018), 8368.
[24] J. Vovrosh, et al., Additive manufacturing of magnetic shielding and ultra-high vacuum flange for cold atom sensors, Sci. Rep. 8 (2018), 2023.
[25] S. Jenzer, et al., Study of the suitability of 3D printing for ultra-high vacuum applications, Phys. Conf. Ser. 874 (2017), 012097.
[26] Z. Sun, G. Vladimirov, E. Nikolaev, L. Velasquez-Garcia, Exploration of metal 3-D printing technologies for the microfabrication of freeform, finely featured, mesoscaled structures, J. Micro Syst. 27 (2018) 1171–1185.
[27] C. Yang, L. Velasquez-Garcia, Low-cost, additively manufactured electron impact gas ionizer with carbon nanotube field emission cathode for compact mass spectrometry, J. Phys. D Appl. Phys. 52 (2018) 7.
[28] F. Motschmann, R. Gerard, F. Gilles, Purification of selective laser melting additive manufactured niobium for superconducting rf-applications transactions on applied superconductivity, IEEE Trans. Appl. Supercond. 29 (2019), 3500805.
[29] S. Jenzer, N. Delerue, Prospects of Additive Manufacturing for Accelerators.10th Int. Particle Accelerator Conf., 2019 10.18429/JACoW-IPAC2019-THPTS008.
[30] H.J. Metcalf, P. Van der Straten, Laser Cooling and Trapping, Springer-Verlag,, New York, 1999.
[31] I. Maskery, et al., Effective design and simulation of surface-based lattice structures featuring volume fraction and cell type grading, Mater. Des. 155 (2018) 220–232.
[32] D. Li, W. Liao, N. Dai, Y.M. Xie, Comparison of Mechanical Properties and Energy Absorption of Sheet-Based and Strut-Based Gyroid Cellular Structures with Graded Densities, Materials 12 (2019) 2183.
[33] B. Chen, et al., Strength and strain hardening of a selective laser melted AlSi10Mg alloy, Scr. Mater. 141 (2017) 45–49.
[34] S. Mirzababaei, S. Pasebani, A review on binder jet additive manufacturing of 316L stainless steel, J. Manuf. Mater. Process. 3 (2019) 82.

[35] L. Thijs, et al., Fine-structured aluminium products with controllable texture by selective laser melting of pre-alloyed AlSi10Mg powder, Acta Mater. 61 (2013) 1809–1819.
[36] N.T. Aboulkhair, et al., On the precipitation hardening of selective laser melted AlSi10Mg, Met. Mater. Trans. A 46 (2015) 3337–3341.
[37] N.T. Aboulkhair, et al., The microstructure and mechanical properties of selectively laser melted AlSi10Mg: the effect of a conventional T6-like heat treatment, Mat. Sci. Eng. A 667 (2016) 139–146.
[38] R.P. Campion, C.T. Foxon, R.C. Bresnahan, Modulated beam mass spectrometer studies of a Mark V Veeco cracker, J. Vac. Sci. Technol. B 28 (3) (2010).
[39] M. Tang, P.C. Pistorious, Oxides, porosity and fatigue performance of AlSi10Mg parts produced by selective laser melting, Int. J. Fatigue 94 (2017) 192–201.
[40] M. Simonelli, et al., A study on the laser spatter and the oxidation reactions during selective laser melting of 316L stainless steel, Al-Si10-Mg, and Ti-6Al-4V, Metall. Mater. Trans. A 46 (2015) 3842–3851.
[41] P. Sherwood, Introduction to studies of aluminium and its compounds by XPS, Surf. Sci. Spectra 5 (1) (1998).
[42] N. Haider, J. Alonso, W. Swartz, Valence and core electron spectra of Mg in MgO in evaporated thin films, Z. Naturforsch. A 30 (1975) 1485–1490.
[43] K. Welch, Capture pumping technology, Pergamon Press, 1991.
[44] C. Park, S. Kim, S. Ki, T. Ha, B. Cho, Measurement of outgassing rates of steels, J. Vis. Exp. 118 (2016), 55017.
[45] T. Arpornthip, C. Sackett, K. Hughes, Vacuum pressure measurements using a magneto-optical trap, Phys. Rev. A 85 (2012), 033420.
[46] S. Khairallah, A. Anderson, A. Rubenchik, W. King, Laser powder-bed fusion additive manufacturing: physics of complex melt flow and formation mechanisms of pores, spatter, and denudation zones, Acta Mater. 108 (2016) 36–45.

Chapter 5

Performance-optimized components for quantum technologies via additive manufacturing

Published in PRX Quantum

DOI: 10.1103/PRXQuantum.2.030326

Featured in Physics

Performance-Optimized Components for Quantum Technologies via Additive Manufacturing

S.H. Madkhaly,[1,2,*] L.A. Coles,[3] C. Morley,[1] C.D. Colquhoun,[1] T.M. Fromhold,[1] N. Cooper,[1,†] and L. Hackermüller[1,‡]

[1] *School of Physics and Astronomy, University of Nottingham, University Park, Nottingham NG7 2RD, United Kingdom*

[2] *Department of Physics, Jazan University, Jazan 45142, Kingdom of Saudi Arabia*

[3] *Added Scientific Ltd., Unit 4, Isaac Newton Centre, Nottingham NG7 2RH, United Kingdom*

(Received 2 March 2021; accepted 28 June 2021; published 12 August 2021)

Novel quantum technologies and devices place unprecedented demands on the performance of experimental components, while their widespread deployment beyond the laboratory necessitates increased robustness and fast affordable production. We show how the use of additive manufacturing, together with mathematical optimization techniques and innovative designs, allows the production of compact lightweight components with greatly enhanced performance. We use such components to produce a magneto-optical trap that captures approximately 2×10^8 rubidium atoms, employing for this purpose a compact and highly stable device for spectroscopy and optical power distribution, optimized neodymium magnet arrays for magnetic field generation, and a lightweight additively manufactured ultrahigh-vacuum chamber. We show how the use of additive manufacturing enables substantial weight reduction and stability enhancement, while also illustrating the transferability of our approach to experiments and devices across the quantum technology sector and beyond.

DOI: 10.1103/PRXQuantum.2.030326

I. INTRODUCTION

While the growing range of quantum technologies offers great promise for both fundamental research [1–3] and practical applications [4–10], their realization places ever greater demands on component performance. In particular, the production of portable quantum sensors [11–17] will require compact lightweight components capable of operating in a range of harsh environmental conditions; compactness, stability, and robustness will be critical for such components and conventional laboratory-based systems are not appropriate [18,19].

The rapid transition of quantum technologies from research experiments to commercial devices also opens up space for innovation and the use of unconventional implementations of known techniques. We show how additive manufacturing (AM), also known as three-dimensional (3D) printing, can be used to create performance-optimized components, unimpeded by the constraints of conventional manufacturing methods, while at the same time allowing quick and easy production of customized components and thus greatly accelerating the prototyping and testing of novel component designs. The approach is generalizable to a wide range of experimental components and will transform applications as diverse as miniaturized optical devices, vacuum systems, and magnetic field generation. Our work complements previous studies of integrated laser sources [20–22] and miniaturized vacuum chambers [23] and expands preliminary studies of the utility of additive manufacturing in the setting of quantum technologies [24,25]. Specifically, we demonstrate a new approach to experimental design in free-space optics, where the overwhelming majority of the adjustable components are eliminated and most of the optical elements are mounted in a monolithic additively manufactured mount within prealigned push-fit slots. This new approach offers improvements in stability as well as significant reductions in cost and in size, weight, and power (SWAP) consumption. We apply this technique to create a stable mount for an optically isolated laser source and a compact and highly stable apparatus for optical power distribution and laser frequency stabilization.

*somaya1407@gmail.com
†nathan.cooper@nottingham.ac.uk
‡lucia.hackermuller@nottingham.ac.uk

The described components are combined with an AM ultrahigh-vacuum chamber [26] to form a magneto-optical trap (MOT), which captures 2×10^8 cold ^{85}Rb atoms. The MOT is the starting point for nearly all cold-atom-based experiments and quantum technologies [27]. The magnetic fields required for our MOT are produced using an array of neodymium magnets in a custom-built AM mount, offering significant SWAP reductions over conventional MOT coils. An optimization algorithm is developed to determine the placement of the permanent magnets in order to accurately replicate the conventional anti-Helmholtz field used in a MOT; the algorithm is transferable to the recreation of other field structures. Our results demonstrate the power of AM to directly implement the outcome of an optimization process, without reference to traditional manufacturing constraints. Measurements of the atomic lifetime within the MOT are used to place an upper limit on the background pressure in the AM vacuum chamber of approximately 3×10^{-9} mbar. An overview of the MOT system is given in Fig. 1.

The remainder of this paper is organized as follows. The overall setup is explained in Sec. II, including a description of the laser sources used (Sec. II A), followed by a discussion of the compact AM spectroscopy and power-distribution system (Sec. II B). The placement of the ferromagnets used for MOT field generation and the corresponding optimization algorithm are described (Sec. II C) and a brief overview of the AM vacuum chamber is given (Sec. II D). The performance of the MOT is characterized in Sec. III.

II. SYSTEM ARCHITECTURE AND COMPONENTS

A. Laser sources

With the atomic structure of alkali metal atoms in mind—in particular, ^{85}Rb [see Figs. 5(a)–5(c)]—the typical roles of lasers employed for magneto-optical trapping are used here [27]: "reference" and "repumper" lasers, each frequency stabilized directly to an atomic transition via saturated absorption spectroscopy [28,29] and a "cooler" laser that is stabilized at a fixed frequency offset from the reference laser via an optical beat signal [30].

Figure 1, box A shows the distributed feedback lasers (DFBs) used as our reference and repumper lasers; DFBs are chosen for their stability, large mode-hop free tuning range, and compact size. Specifically, an Eagleyard laser diode is used with an output power of 80 mW at 780 nm. Although this is sufficient to produce a MOT, a tapered amplifier (Toptica TA-100, cooler laser), which provides up to 1 W of output power, is also used to facilitate further experiments and provides the "cooler" light for our MOT. The DFB packages are encased in an AM mount with an optical isolator (Isowave I-780-LM), as seen in Fig. 2. The optical isolator has an external diameter of 4 mm and a depth of approximately 2.9 mm. It is mounted inside an AM ring with a small grip to facilitate adjusting the isolation angle manually. The total weight of the laser ensemble is only 51 g. After optimizing the isolation efficiency, the isolator mount is secured in the DFB housing using epoxy adhesive.

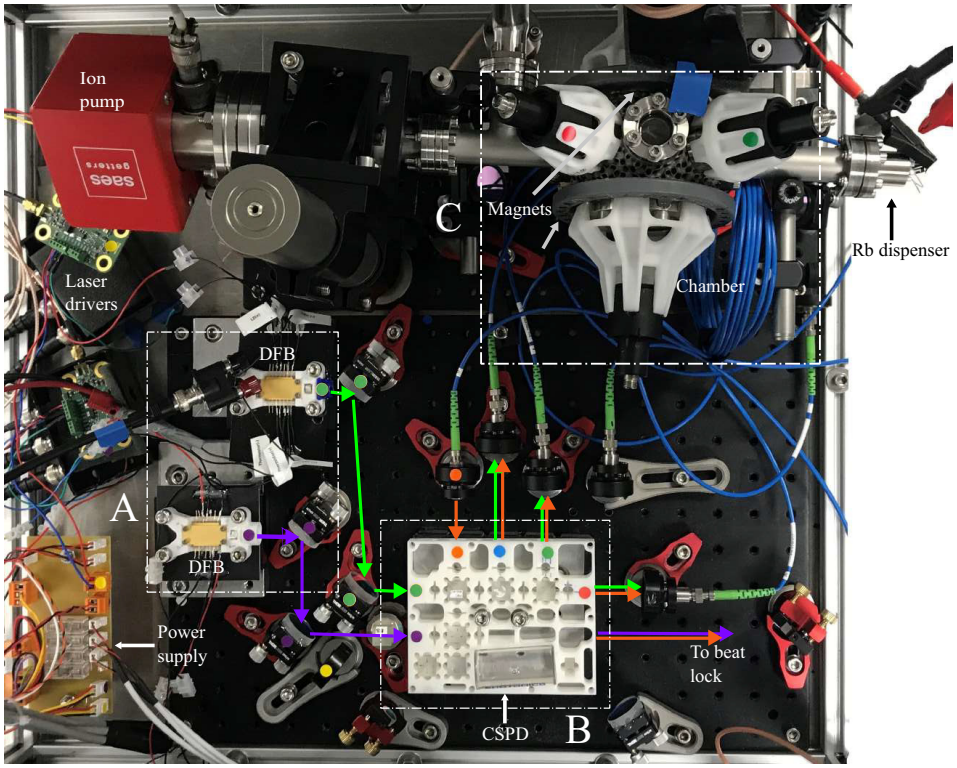

FIG. 1. An overview of the complete setup, showing 3D-printed and optimized components in the areas marked with dashed boxes A, B, and C. A indicates the distributed feedback lasers (DFBs) used as master light sources, B indicates the compact spectroscopy and power-distribution (CSPD) apparatus, and C indicates the trapping apparatus including the AM UHV chamber, the optimized permanent-magnet arrays, and a set of self-aligning AM fiber outcoupler mounts. The setup takes up a volume of 0.15 m^3 and the custom parts indicated have a cumulative mass of 3.2 kg.

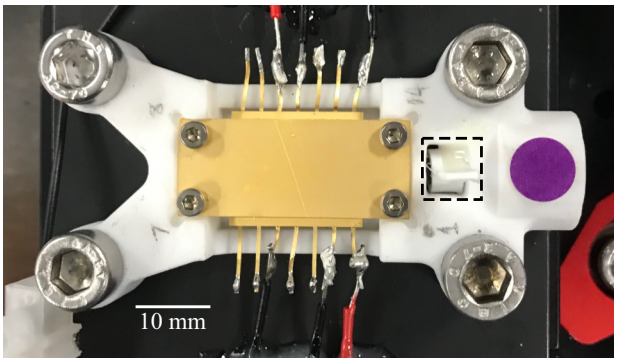

FIG. 2. A photograph of a butterfly-packaged DFB laser and optical isolator (indicated with the dashed rectangle) in an AM mount. Note how the DFB laser module is mounted such that the original base plate remains exposed to the air, to facilitate passive cooling.

Figure 2 shows the physical implementation of the corresponding systems. The AM mount leaves the back plane of the laser package exposed to the air in order to facilitate passive heat sinking. This is sufficient to regulate the temperature of the laser module during normal operation.

The polymer casing surrounding these systems and holding the various components in place is produced from photopolymer resin (Formlabs "Rigid Resin") via stereolithographic additive manufacturing (SLA) [31]. SLA allows a customized mount to be produced to meet the component and alignment requirements of the user. Once the casing is printed, the components simply slot into position, reducing the need for user alignment. The photopolymer resin offers a good balance between weight and thermal and/or mechanical stability (for more details, see Appendix A). The completed reference and repumper source assemblies both provide output powers of 42 mW, consistent with 80 mW output power from the DFBs and 2.8 dB losses in the isolators when used optimally. The 40 mW of optical power dissipated in the isolators is much less than the ($>$ 700 mW) electrical power dissipated in the diode module and does not necessitate additional heat-sinking measures. The DFB lasers are powered using the Koheron DRV200-A-200 compact driver board, which provides diode currents of up to 200 mA and allows current modulation at up to 6 MHz.

B. Laser spectroscopy and optical power distribution

To enhance laser stability, all of the optics required for laser stabilization via vapor-cell spectroscopy [28] and optical beat locking [30,32], as well as those needed to distribute the optical power of the cooler and repumper lasers appropriately between the MOT beams, are secured in a custom-designed optics mount with few adjustable elements. This mount, designated the "compact spectroscopy and power-distribution" (CSPD) apparatus, uses fixed beam paths and prealigned components (via push fitting into specially designed slots in the AM mount) to eliminate the need for adjustment screws or tunable mirror-mounts. The result is a robust and stable setup [see Fig. 1, box B]. Like the laser mounts, the CSPD is manufactured from Formlabs "Rigid Resin" via an SLA process. The CSPD is shown in Fig. 3 and has dimensions of 128 $\times$ 103 $\times$ 12 mm, and a mass of 84 g. "Rigid Resin" is selected as its build material based on a thorough assessment of the physical properties of the available build materials (for more details, see Appendix A). The CSPD design uses the fewest optical elements possible, in order to enhance stability and reduce cost and SWAP.

To improve stability, the optical beam paths in the CSPD are kept as short as possible and the number of reflections

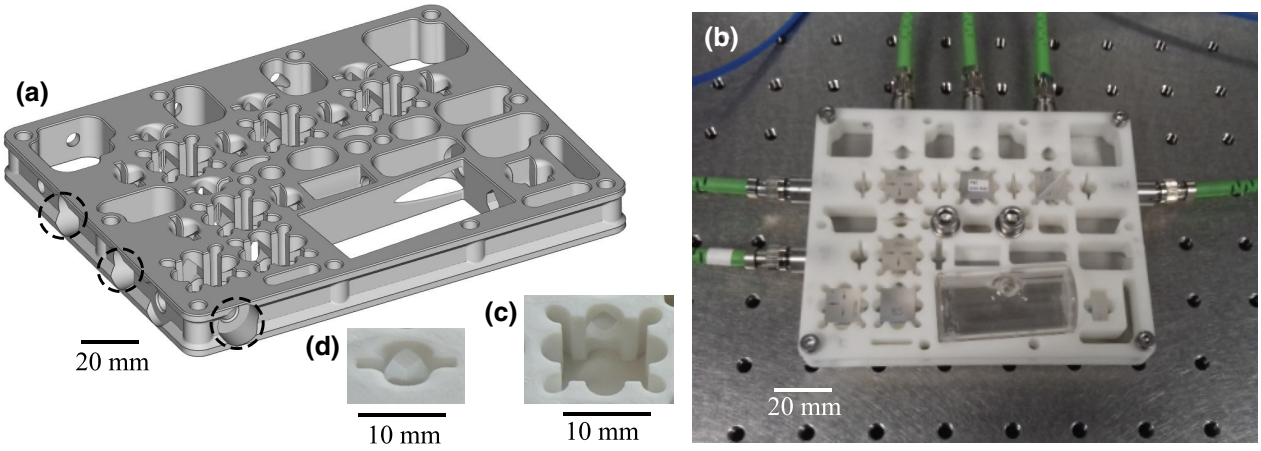

FIG. 3. The CSPD apparatus. (a) A 3D render of the mount. The holes that can be used as fiber inputs or outputs are indicated. (b) A photograph of the CSPD with optics, a reference cell, and fibers adhered to the appropriate positions. (c),(d) Close-ups of the wave-plate and beam-splitter slots. The rounded recesses on the edges and corners prevent scuffing of the optically active surfaces and improve push fit alignment accuracy, respectively.

undergone by each beam is also minimized. Each beam that is fiber coupled for transmission to the MOT undergoes a maximum of two reflections in this arrangement, as does each of the two beams combined to produce the optical beat signal. The maximum path length for any of these beams is 120 mm. The (less alignment-sensitive) saturated absorption spectroscopy beams each undergo four reflections, with a maximum optical path length of 290 mm.

To illustrate the importance of this, consider the following simple model of a beam path subject to experimental imperfections. The expected positional deviation of a beam from its target at the end of an optical beam path is given by

$$\Delta r = \left[\sum_{\mathrm{i}} (2\Delta\phi L_{\mathrm{i}})^2\right]^{1/2}, \qquad (1)$$

where the sum is taken over all reflective components in the beam path, which are all assumed to have independent alignment inaccuracies of magnitude $\Delta\phi$. The values of L_{i} are the remaining path lengths between each component and the end of the optical beam path and we apply the small-angle approximation $\tan\theta \approx \theta$. We can now compare the CSPD with a more conventional setup. In the CSPD, prior to fiber coupling, the cooler beam undergoes two reflections with $L_1 = 30$ mm and $L_2 = 90$ mm, yielding $\Delta r = 190\Delta\phi$ mm. By contrast, a more conventional system might involve, say, ten reflective components, roughly equally spaced along a 1-m path length. In this case, we find that $\Delta r = 3920\Delta\phi$ mm, more than 20 times the equivalent value for the CSPD.

Each of the optics slots within the CSPD is designed to leave clearance in the center of the optical component; this prevents direct contact between the mount and the central part of the optical element on which the beam impinges, thus ensuring that device performance is not degraded by scuffing of the optical surfaces when components are inserted. Slots for cube beam splitters have rounded recesses in each corner (similar to an undercut) [see Fig. 3(c)]. This improves the accuracy of the push-fit alignment by ensuring that cube position and/or orientation is controlled via extended contact with defined flat surfaces that can be built accurately using the SLA process. This is important because AM methods are not well suited to producing sharp internal features, such as the corners of the beam-splitter slots. The wave-plate slots are designed to facilitate smooth rotation of the wave plates via a friction contact with the exposed upper rim of the plate. For stable long-term operation, the wave plates can be secured at a fixed angle using epoxy adhesive.

No special equipment or methodology is required for component installation: the optics are simply manually pushed into the designated slots and then secured with adhesive if required. Additional voids (that do not hold optics) are also built into the design of the CSPD, as seen in Fig. 3. These reduce the weight of the CSPD and decrease the amount of heat buildup within the structure during the additive manufacturing process, thus preventing warping of the frame.

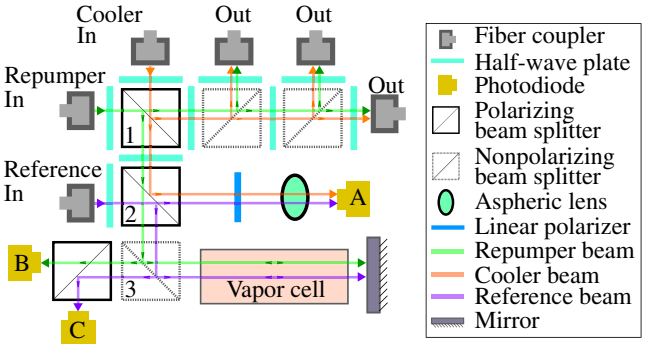

FIG. 4. A schematic of the optics layout in the CSPD and how each input laser beam is directed through it. The purple beams represent reference light, the orange beams cooler light, and the green beams repumper light.

The layout of the optics and optical paths within the CSPD are designed to minimize the number of optical components required. A schematic of the beam paths used in the CSPD is shown in Fig. 4. The cooler beam first passes through a half-wave plate that controls the distribution of the power between the MOT beams and the spectroscopy setup, which happens at the polarizing beam splitter marked "1." The reflected component is divided among the three output fiber couplers that provide the MOT beams. This happens at the two nonpolarizing beam splitters immediately to the right of polarizing beam splitter "1." The first of these has a transmission-to-reflection ratio of 67:33, while the second splits the power 50:50. The repumper beam also reaches polarizing beam splitter "1" via a wave plate to control power distribution. In this case, the transmitted polarization component is distributed among the MOT beams.

The reflected component of the repumper beam and the transmitted component of the cooler beam then pass through a half-wave plate with its fast axis fixed at 45° relative to the polarizing beam splitters. Thus, when they are combined with the reference beam at polarizing beam splitter "2," the cooler light is reflected and the repumper light transmitted. The component of the reference light transmitted at beam splitter "2" is mixed with the cooler light on the same pathway by the polarizing filter, fixed with its transmitted polarization axis at 45° relative to the polarizing beam splitters, such that an optical beat signal can be produced on photodiode "A." This is used to stabilize the frequency difference between the cooler and reference lasers via feedback to the diode current of the cooler laser.

This leaves the repumper light transmitted at beam splitter "2" and the component of the reference light reflected at beam splitter "2." These enter what is a conventional saturated-absorption-spectroscopy setup for one laser—the difference here is that two beams overlap on the same spatial path in orthogonal polarizations. After re-emerging from the spectroscopy setup, they are ultimately separated onto their respective photodiodes by the polarizing beam splitter "3." To generate an error signal suitable for feedback stabilization of the laser frequencies, the laser currents are sinusoidally modulated and the modulation signals are combined with the photodiode outputs using analog multipliers—a standard practice in laser stabilization [33].

By sharing the same spatial path in the vapor cell, the reference and repumper beams influence each other's spectroscopy signals via optical pumping effects [34]. Provided that both lasers are to be stabilized simultaneously, this does not prove detrimental to the operation of the device but, rather, increases the strength of the locking signals (for more details, see Appendix C). The design of the CSPD allows fixed-focus fiber collimators to be inserted directly into the fiber access ports (see Fig. 3) and fixed in place using epoxy once aligned. However, the stability of standard fiber-optic connectors is found to be insufficient to allow long-term operation without adjustable components. This could be fixed by a custom fiber mount. In principle, this device can be extended to unite the laser source housing with the power-distribution and spectroscopy optics, thus eliminating the need for any external optics (or an associated baseplate/breadboard) and providing all of the light-generation requirements for a MOT in a single stand-alone fiber-coupled device.

1. Thermal stability and resistance tests

Temperature fluctuations are a major source of drifts in optical alignment, even in a temperature-stabilized laboratory environment; outside the laboratory, these problems become much more significant. To test the thermal stability of the CSPD, the environmental temperature is adjusted between 288 and 298 K, while monitoring key parameters of the system.

Figure 5(d) shows the error signal generated for feedback stabilization of the reference laser frequency at a range of environmental temperatures within this window. Note that the results for different temperatures are intentionally offset relative to one another to improve visibility. It can be seen from the figure that the overall form of the signal is unaffected by beam misalignment due to temperature variations; it remains appropriate for laser stabilization over the entire temperature window. The change in signal amplitude occurs due to an increased vapor pressure in the reference cell at higher temperatures.

One experimental parameter that is extremely sensitive to beam misalignment is the coupling efficiency of light into optical fibers. The optical power coupled into the fibers at the outputs of the CSPD is monitored and only 10% power variation is observed over the entire 10 K temperature window, with a maximum relative power variation coefficient of 0.02 K^{-1}. This result represents a significant advance over standard laboratory optics and optomechanics, where typically a change of approximately 1 K can lead to a complete coupling loss, and is comparable to results obtained with much heavier and more costly systems built out of materials specifically selected for thermal stability, such as Invar and Zerodur [35].

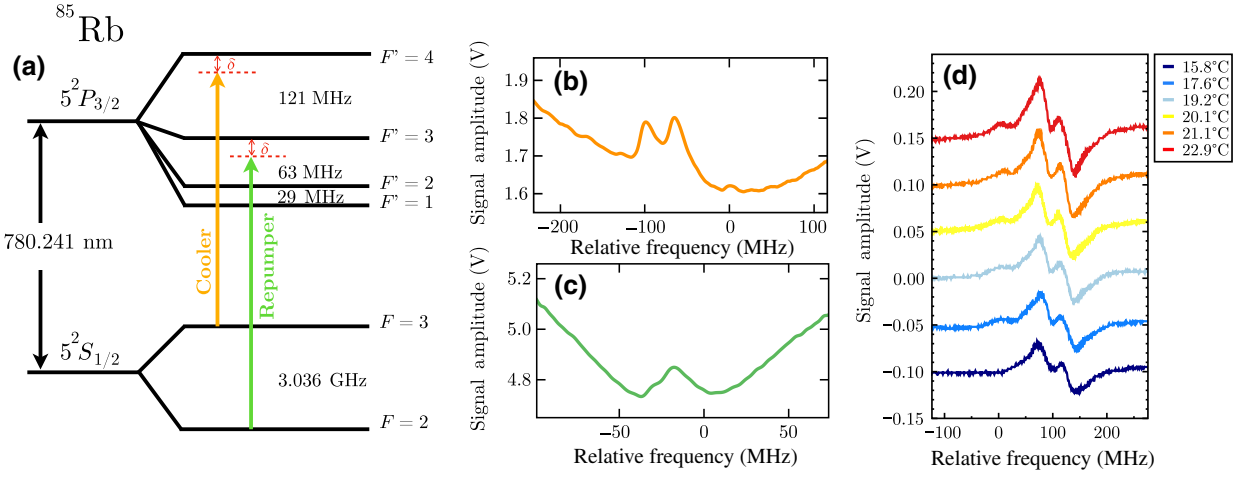

FIG. 5. (a) The laser locking frequencies relative to ^{85}Rb D_2 transitions and the corresponding saturated absorption spectroscopy features of the (b) cooler and (c) repumper beams. (d) The spectroscopic error signal for the cooler laser (see text for details). The form of the signal can be seen to remain consistent and appropriate for feedback stabilization of the laser frequency despite substantial variations in environmental temperature. Note that vertical offsets of −0.1, −0.05, 0, 0.05, 0.1, and 0.15 V are added to the displayed signals (in order of increasing temperature, respectively), to improve visibility.

The design concept behind the CSPD, i.e., the use of a monolithic additively manufactured optics mount as a replacement for conventional optomechanics, is generalizable to almost any desired arrangement of free-space optics. Our results show that this approach offers major advantages in terms of compactness, stability, cost, and assembly time. Further work in this area may lead to the establishment of a new paradigm for experimental design with free-space optics.

C. Magnetic field generation

The efficient creation of a linear MOT field, prioritizing both field fidelity and power consumption, is an important consideration for a portable apparatus. In conventional systems, the required fields are generated by coils drawing many watts of power. The apparatus developed here instead utilizes an array of ferromagnets to generate MOT-suitable magnetic fields, thus eliminating the power consumption of the coils entirely. This technique has not traditionally been employed for SWAP reduction because many experiments require the magnetic fields to be briefly extinguished following the collection of an atomic cloud. However, we show that even in such cases, it is still possible to augment MOT coils with permanent-magnet arrays and that doing so reduces time-averaged power consumption by a factor of $1/(1-T_M)$, where T_M is the fraction of the experimental cycle time for which the magnetic field should be present (for full details, see Appendix D).

In order to open up these experimental possibilities, it is necessary to design a ferromagnetic array that produces the same field distribution as conventional MOT coils. This can be done via well-established numerical optimization methods [36] and computer-science algorithms [37] allowing the optimal placement of ferromagnets to be determined *a priori* for any given apparatus, thereby greatly reducing testing and manufacturing times. Neodymium magnets are manufactured in a variety of standardized shapes and strengths. This makes them an ideal choice for an optimization algorithm designed to determine the optimal placement of a set of magnetized defined volume elements (voxels) on a predetermined initial grid to create a required field profile, allowing multiple magnet configurations to be designed and tested to establish their suitability before manufacture. Such algorithms are frequently used in the context of magnetic resonance imaging (MRI) [38] in the process of shimming, which employs optimization algorithms to inform the placement of permanent magnets or current carrying wires to remove unwanted spherical-harmonic contributions in a given region. These techniques for passive shimming [39] are exploited in the design of the ferromagnet array. A voxel of volume dV, magnetized entirely along the z axis with strength M_z, at a position $\underline{Q} = (\rho, \alpha, \psi)$, produces a scalar potential at a position $\underline{P} = (r, \theta, \phi)$ given by

$$\Psi = -\frac{dVM_z}{4\pi\rho^2}\sum_{n=0}^{\infty}\sum_{m=0}^{n}\epsilon_m\frac{(n-m+1)!}{(n+m)!}P_{n+1}^m \times (\cos\alpha)\left(\frac{r}{\rho}\right)^n P_n^m(\cos\theta)\cos[m(\phi-\psi)], \quad (2)$$

where P_n^m are the associated Legendre polynomials and ϵ_m is the Neumann factor, defined as $\epsilon_{m=0}=1$ and $\epsilon_{m>0}=2$. This can be related to the magnetic fields by $B=-\nabla\Psi$. From this, a matrix equation can be formed relating the spherical-harmonic contributions from each voxel (out of a total of N voxels) and its magnetization to the required overall spherical harmonics:

$$\begin{pmatrix} A_{(z,1)}(1,0) & \cdots & A_{(z,N)}(1,0) \\ \vdots & \ddots & \vdots \\ A_{(z,1)}(n_{\max},m_{\max}) & \cdots & A_{(z,N)}(n_{\max},m_{\max}) \end{pmatrix} \times \begin{pmatrix} m_1 \\ \vdots \\ m_N \end{pmatrix} = \begin{pmatrix} b_z(1,0) \\ \vdots \\ b_z(n_{\max},m_{\max}) \end{pmatrix}. \quad (3)$$

Here, the matrix contains $A_{(z,i)}(n,m)$, the contribution from the ith voxel to the n,m spherical-harmonic mode to the magnetic field in the z direction. This is then multiplied by the vector containing the magnetization of each voxel, m_i, to be optimized. The elements of this vector can take values of either $m_i=1$, for the magnetization directed entirely along positive z, $m_i=-1$, for the magnetization directed entirely along negative z, or $m_i=0$ for no magnetic material required. The result of the matrix expression in Eq. (3) is the vector of total contributions from each (n,m) spherical-harmonic mode, $b_z(n,m)$, which are set by the user to constrain the optimization. All that remains, therefore, is to define the b elements. The magnetic field for a MOT is well described by first-order spherical harmonics; therefore, these can be targeted to produce the required linear fields. In theory, this technique could be expanded to any required field, provided that it can be decomposed into spherical-harmonic components. This is then similar to the standard form of a linear optimization problem [37], as utilized previously in Ref. [40]. Thus, the method employs the spherical-harmonic decomposition from the process of shimming to produce a linear optimization problem to constrain the field to the desired form. This is then combined with an optimization function that seeks to maximize the contribution of the magnet strength to the field, resulting in a final placement of magnets, which produces the desired field while acting to reduce the required M_z.

The voxels are then defined as an assortment of readily available premanufactured neodymium magnets. The chosen magnets can form initial placement grids tailored

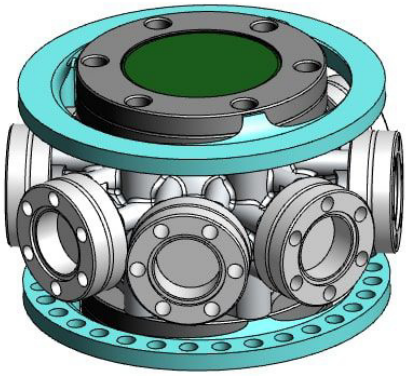

FIG. 6. A 3D model of the vacuum chamber seen in Fig. 1, without the lattice structure. The blue rings attached to the top and bottom of the chamber represent the permanent-magnet arrays.

to the experimental apparatus, based on their individual sizes and the required spacing between voxels (see Fig. 7). Application of the optimization method then determines the required magnetization, m_i, of each voxel and therefore the required positions and orientations of the magnets. For this specific setup, the initial grids are designed to allow optical access, though in theory any distribution of voxels could be defined. Examples of initial and optimized grids are shown in Fig. 7. Figure 7(a) shows the initial grid for cylindrical voxels of radius 6 mm and depth 3 mm, while Fig. 7(b) illustrates the initial grid for cylindrical voxels of radius 6 mm and depth 6 mm. The optimized structures for each case are then shown in Figs. 7(c) and 7(d), respectively.

The design shown in Fig. 7(d) is chosen for the magnetic-field-generating structure, utilizing N42-strength-grade neodymium magnets, and AM polymer mounts to position the magnets. The choice of final design is based on both the fidelity of the resulting field structure and the practical consideration that this design allows the magnet rings to be centered to the CF40 view ports on the vacuum system via a simple push-fit mechanism, thus reducing the likelihood of any misalignment. The rapid prototyping provided by AM methods allows swift manufacture and application to the experiment.

The resulting fields, calculated using the derivatives of Eq. (2) for the optimized magnet arrangement, are compared to the target field and experimentally measured fields in Fig. 8. Figure 8(a) illustrates good agreement between the target field and the numerically calculated field produced by the optimized structure of Fig. 7(d), for the B_x and B_z components along the x and z axes, respectively. Figure 8(b) then illustrates the agreement between the field formed by one ring (measured experimentally using a Hall-probe system) and the fields produced by the same ring calculated numerically. Figure 8(b) shows good agreement between the numerically calculated and experimentally obtained fields; the error bars represent a combination of the uncertainties in sensor calibration and alignment. Thus, the algorithm provides a powerful method of determining a magnetic structure tailored to a given apparatus, which is capable of producing a wide variety of fields accurately.

D. Vacuum system

The central component of the vacuum system is an additively manufactured octagonal chamber carrying eight CF16 ports and two CF40 ports, as shown in Fig. 6. This chamber and its production are fully described in

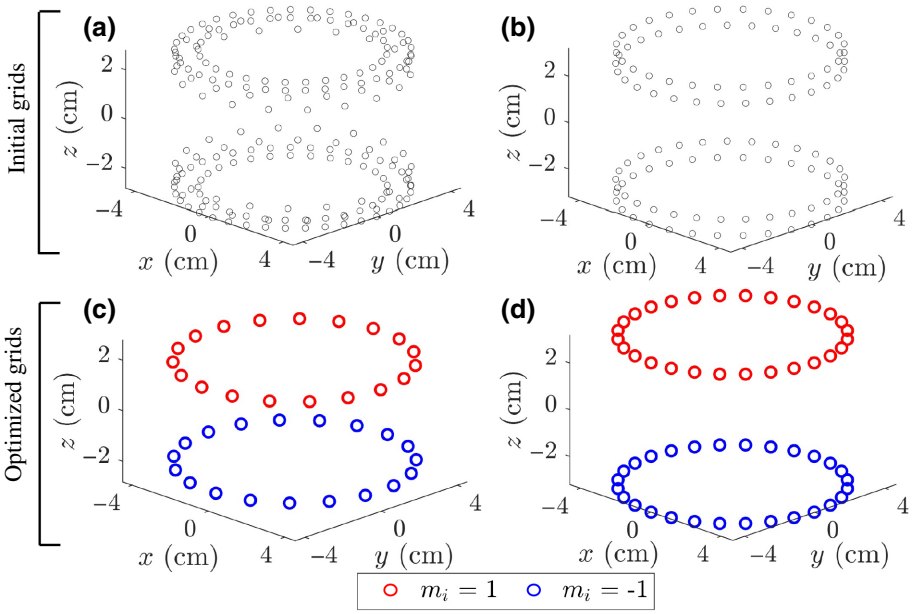

FIG. 7. Grids of the possible positions for two different types of magnetized voxels: (a) diameter of 6 mm and depth of 3 mm; (b) diameter of 6 mm and depth of 6 mm. The optimized arrangements to produce a MOT field are shown in (c) and (d) for the initial grids of (a) and (b), respectively. The geometry in (d) is used as a basis for the magnet rings shown in Fig. 6, as the increased distance between the rings and the trapping region is necessary to accommodate the vacuum chamber.

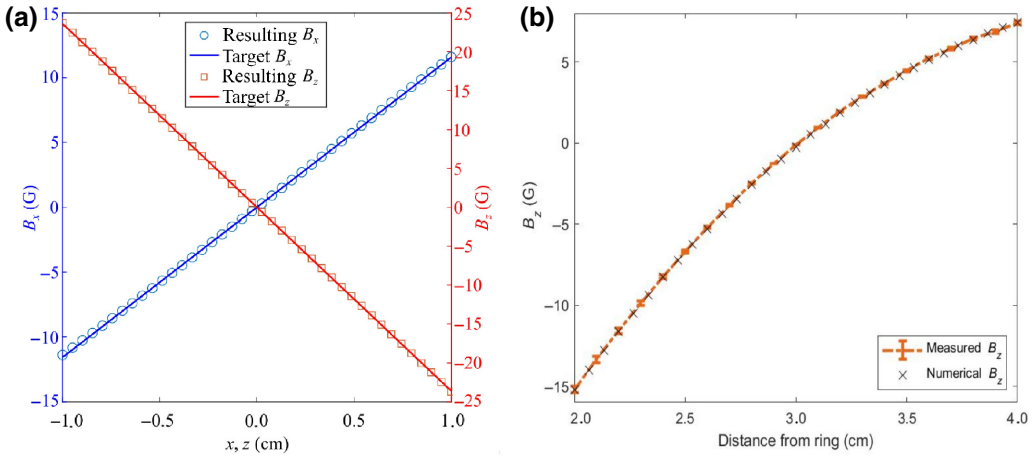

FIG. 8. (a) A graph showing the similarities between the numerically calculated fields produced by the optimized magnet structure (circles and squares) of Fig. 7(d) and target magnetic fields (lines) for B_x along the x direction (blue) and B_z along the z direction (red). (b) A comparison between the numerically calculated and the experimentally measured axial magnetic field components produced by a single ring of magnetic voxels, along the axis of the ring, versus the distance from the ring (see text for details).

Ref. [26]; here, we give a brief summary. The mass of the chamber (excluding externally attached components) is 245 g, considerably less than that of equivalent commercial chambers, which typically weigh approximately 1 kg. The chamber is additively manufactured from the aluminum alloy AlSi10Mg by a selective laser-melting process [41–43]. The choice of build material, and latticing of large regions of the structure to decrease the volume of solid material while preserving mechanical strength, are jointly responsible for the greatly reduced chamber mass.

Attached to this central chamber for demonstration purposes are standard vacuum components, including a hybrid ion-nonevaporable getter pump (NEXTorr D100-5), a valve for roughing and turbopumping of the chamber, and Rb dispensers (SAES Getters). An important long-term vision is the gradual elimination of the standard vacuum components and reaching a full additive manufacture of the entire system as a single optimized lightweight component. The consolidation of multiple modular components into one customized vacuum vessel will eliminate most of the vacuum joints present in a conventional system, improving stability while further reducing the cost and the SWAP parameters.

The system is baked at 393 K for 5 days, following which a pressure of $<10^{-10}$ mbar is achieved, as measured via the ion pump current.

III. MAGNETO-OPTICAL TRAPPING

The components described above are used to produce a magneto-optical trap (MOT), capturing up to 2.5×10^8 ^{85}Rb atoms.

The light used to form the MOT consists of three retroreflected laser beams produced by the DFB laser systems and tapered amplifier. The cooler and the repumper beams are equally distributed via the CSPD into three optical fibers that deliver the light to the chamber. Each MOT beam contains 15 mW of cooler light and 4.5 mW of repumper light, with a beam diameter of 1.2 cm. The maximum total intensity of the six beams is approximately 40 mW/cm^2. The MOT is generated in a magnetic field gradient of 12 G/cm provided by the ferromagnet array.

A. Atom-number measurement and pressure limit determination

For an estimate of the atom number, fluorescence light from the trapped atoms is collected onto a photodiode using a planoconvex lens (for details, see Appendix E).

Figure 10 shows MOT loading curves obtained for various values of the Rb dispenser current from 2.20 to 2.75 A. The loading curves enable a direct measurement of the pressure in the trapping region under certain conditions [44,45]. For each loading curve, the atom number with

FIG. 9. The fluorescence image of the cloud of cold ^{85}Rb atoms captured by our MOT, which is produced using the optimized components described herein.

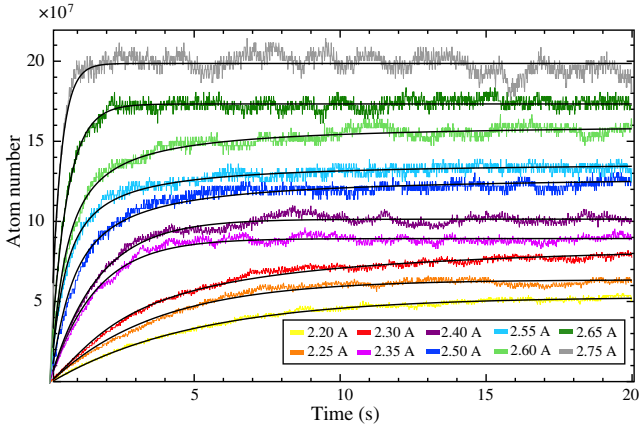

FIG. 10. MOT loading curves based on fluorescence data for various values of the Rb dispenser current. The colored lines show raw data and the black lines are fits to the data based on Eq. (4).

respect to time, N, is fitted to the form

$$N(t) = \frac{R}{L}(1 - e^{-Lt}), \tag{4}$$

where the loading rate R and the single-body loss rate L are used as free parameters.

This description neglects two-body and higher-order loss processes and is therefore only valid in the limit of low density of trapped atoms. In order to remain in this limit, the loading profile taken with the lowest dispenser current (2.2 A) is used to determine an upper limit on our background pressure.

A fit to this loading profile, according to Eq. (4), is shown in Fig. 10. The extracted single-body loss rate is $L = (0.0834 \pm 0.0003\ \mathrm{s}^{-1})$. This single-body loss rate is the total loss rate resulting from collisions with all thermal background-gas species present, including thermal Rb atoms. A pressure estimate based on this figure therefore represents the overall pressure in the trapping region, including the contribution from the intentionally introduced Rb atoms. Since our measurements cannot distinguish the different partial pressures of individual background species, our result represents an upper limit on the pressure of unwanted gas species, rather than a direct measurement of it. The resulting pressure estimate depends on the assumed composition of the residual background gas. The loss coefficients per unit pressure for various common background gases have been measured in Ref. [44]. We use these coefficients to estimate the upper bound on the pressure in the trapping region under the assumption of various different dominant background-gas species. The results are displayed in Table I. The background gas is most likely a mixture of the species listed, placing the resulting pressure limit somewhere within the range of values presented. These results represent an upper limit on the pressure of non-Rb species in the chamber and are therefore consistent with the results of the ion-pump-current readings. While the pressure limit imposed by this measurement is much less stringent than that obtained via the ion-pump-current reading, it nevertheless represents an independent confirmation that the pressure is far into the high-vacuum regime. The result is particularly relevant for the future use of printed vessels in quantum technologies, opening the door for future highly complex and compact printed chambers with designs not realizable by conventional methods.

TABLE I. Estimated pressures in the MOT trapping region under the assumption that the background gas consists primarily of the species indicated, corresponding to an upper limit on the non-Rb pressure.

Species	Pressure ($\times 10^{-9}$ mbar)
H_2	2.27 ($\pm$0.01)
He	4.45 ($\pm$0.02)
N_2	4.27 ($\pm$0.02)

IV. CONCLUSION

We demonstrate a fundamentally new approach to experimental component design that exploits the potential of AM techniques to offer greatly improved performance. AM allows direct implementation of simulation results and optimization processes. Our results illustrate the remarkable potential of AM to facilitate experimental research in all areas currently relying on free-space optics, tailored magnetic fields, or high vacuum apparatus. The demonstrated techniques enable rapid prototyping alongside improvements in stability and substantial reductions in cost and SWAP parameters—many component weights are reduced by 70%–90% compared to standard equivalents. One important area of application is the field of cold-atom experiments and portable quantum technologies based on magneto-optical trapping. AM components will allow widespread use of these technologies, including in field applications and space-borne experiments.

The use of AM to produce these components opens many future avenues of research. Optimum thermomechanical performance can be achieved via the freedom AM offers when considering material distribution; for example, enabling the use of variable-density latticing [46,47]—optical frameworks such as the CSPD could be designed so that thermal expansion has a minimal effect on the key alignment variables of the components. Lattice structures can also, in principle, be designed to isolate or damp specific frequencies of mechanical vibration [48]; this will be a useful feature in many experiments, as there are generally specific narrow frequency ranges within which an experiment or device is most sensitive to environmental noise.

For AM vacuum apparatus, one promising avenue is part consolidation, in which a substantial part of a custom vacuum system could be printed as a single piece. This eliminates the overwhelming majority of the vacuum joints, further reducing the SWAP parameters, increasing the mechanical stability, and reducing the susceptibility of the system to leaks. Another option is to exploit AM to produce high-surface area elements such as small-scale lattices or fractal surfaces. These could be coated in reactive materials to produce enhanced getter pumps for passive pumping in portable devices.

Our demonstrated design of customized ferromagnetic arrays paves the way for progress beyond the standard magnetic field distribution used for magneto-optical trapping; systematically tailored magnetic field shapes can be produced in order to optimize selected experimental parameters, such as the total atom number or loading rate.

While AM techniques have only just started to be used in the context of quantum technologies, they hold the promise of providing a clear pathway for miniaturization and expanded functionality.

ACKNOWLEDGMENTS

This work was supported by Innovate UK Project No. 133086 and the Engineering and Physical Sciences Research Council (EPSRC) Grants No. EP/R024111/1 and No. EP/M013294/1 and by the European Commission Error-Proof Optical Bell-State Analyzer (ErBeStA) project (Grant No. 800942).

APPENDIX A: MATERIAL SELECTION

Different 3D printing materials are tested to ensure their relevance and compatibility with the optical systems. Formlabs "Rigid Resin" is chosen as the build material for the DFB housing, lens tubes mounts, and CSPD on the basis of its low coefficient of thermal expansion and high elastic modulus, which offer improved alignment stability when compared to alternative build materials. Table II details physical and thermal properties of the selection of build materials considered. The material from which our system parts are 3D printed, "Rigid Resin," is shaded in gray [49].

APPENDIX B: SYSTEM COMPONENTS AND COSTINGS

Table III gives a list of the parts used in the construction of the key experimental components described in the main text and their costs from commercial suppliers. It should be noted that although we give specific manufacturers and part numbers for many components, equivalent products are available from a range of suppliers with comparable cost and performance. Many components, such as the beam-splitter cubes and wave plates, come in standard sizes, thus enabling components from multiple manufacturers to be used within the same AM frame.

APPENDIX C: OPTICAL PUMPING EFFECTS

As described in Sec. II B of the main text, the use of overlapping repumper and reference beams in the spectroscopy cell of the CSPD results in a modification of the spectroscopy signals. This means that accurate frequency stabilization for either laser requires both lasers to be frequency stabilized. However, it also enhances the amplitude of the spectroscopic and stabilization signals generated by the CSPD, improving the signal-to-noise ratio and consequently enabling more stable locking—particularly for the repumper laser. Figure 11 shows the "error signals" used for feedback stabilization of the laser frequencies, generated by modulating the laser current and then combining the spectroscopic and current modulation signals via an analog multiplier. The amplitude enhancement resulting from the presence of the second laser on the same spatial path can clearly be seen in each case and results in more pronounced locking signals and steeper lock points.

TABLE II. The physical and thermal properties of commonly used materials, as well as candidate AM build materials for the CSPD [50–52], spaced by a thick line.

Material	Supplier	Elastic modulus (GPa)	Glass transition temperature (°C)	Thermal expansion coefficient, α [(μm/m)/°C]	Reference(s)
Austenitic stainless steel		215.3		14.1	[53]
Aluminum		70.3		23.1	[53]
Borosilicate crown glass (BK7)		71.3	570 [54]	7–8	[53]
Polycarbonate (PC)	Ultimaker	2.13	147	69	[55–58]
Polylactic acid (PLA)	Ultimaker	2.35	60	68	[55,56]
Acrylonitrile butadiene styrene (ABS)	Ultimaker	1.62	105	90	[55–58]
Copolyester (CPE)	Ultimaker	1.54	82	70	[55,56]
Photopolymer (rigid) resin (white)	Formlabs	4.1	88 (heat deflection)	53	[59]
Photopolymer (tough) resin (green)	Formlabs	2.7	45 (heat deflection)	119.4	[60]

TABLE III. The component parts required for construction of the key experimental systems and approximate costs. Some components are optional or variable depending on the performance required by the user; these are indicated in the table. Material costs for the AM frames are omitted as these are negligible compared to the cost of the optics used to populate them.

Part	Subpart	Supplier and part number	Cost (GBP)
Auxiliary CSPD components	Mirrors & mounts	Thorlabs	420
	Fibres & outcouplers	Thorlabs	1700
Core CSPD components	Polarizing beam-splitter cube (×3)	Thorlabs PBS122	465
	Nonpolarizing beam-splitter cube (×2)	Thorlabs BS005	290
	Nonpolarizing beam-splitter cube 70:30	Thorlabs BS053	145
	Half-wave plate (one essential, up to nine can be used)	Lens Optics (custom order)	∼ 150 (each)
	Linear polarizer	Thorlabs LPNIRE050-B	70
	Mirror	Thorlabs BB05-E03	40
	Aspheric lens	Thorlabs C220TMD-B	60
	Rb vapor-cell	Photonics technologies	∼ 400
	Photodiodes	Thorlabs FD11A, FDS100 and/or FDS015	60 (total)
DFB source module (each)	DFB butterfly package	Eagleyard EYP-DFB-0780-00080-1500-BFW01-0002	2300
	Optical isolator	Isowave I-780-LM	220
Magnet ring assembly	Neodymium magnets	Bunting E-magnets	∼ 20

APPENDIX D: HYBRID MAGNETIC FIELD GENERATION—DETAILED DERIVATION

In Sec. II C of the main text, we claim that augmentation of coils with permanent magnets can reduce the time-averaged power requirements for magnetic field generation by a factor equal to $1/(1 - T_M)$ compared to using coils alone, where T_M is the fraction of the experimental cycle time for which the magnetic field must be active. Here, we provide a full derivation of this result. The strength of the magnetic field generated by a coil is proportional to the current through it, I, while the power dissipated in that coil is equal to I^2R, where R is the resistance of the coil. We neglect inductive effects because in practice experimental cycle times are usually sufficiently long to make them negligible as a source of power consumption, while from a purely theoretical perspective they do not necessarily have to result in a net energy loss from an appropriately designed system. It follows that the power dissipation in a set of coils is equal to $R\overline{I^2}$ and hence also to $C\overline{B^2}$, where B is a scalar proportional to the magnetic

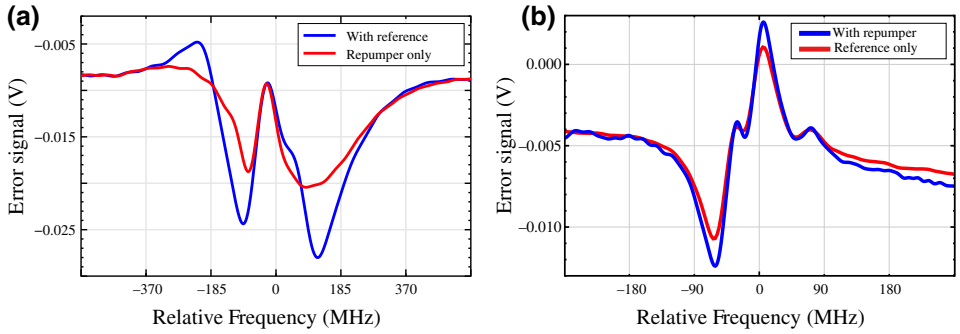

FIG. 11. The error signals resulting from saturated absorption spectroscopy (with laser current modulation and phase-sensitive detection) of (a) the ^{85}Rb D_2 line $|F = 2\rangle \rightarrow |F = 1, 2, 3\rangle$ "repumper" transition and (b) the ^{85}Rb $|F = 3\rangle \rightarrow |F = 2, 3, 4\rangle$ "reference" transition. The red curves represent the signals generated when only the laser performing the spectroscopy is present in the vapor cell, while the blue lines represent the signals obtained when a beam resonant with the other transition spatially overlapped with this beam in the same vapor cell. As can be seen from the figures, optical pumping effects result in an enhancement of the error signal amplitude—particularly for the laser addressing the repumper transition.

field strength produced by the coils and C is a constant coefficient dependent on the exact system parameters.

Let us now define a fraction, F, of the required magnetic field that is to be produced by a ferromagnetic array, with the remaining fraction, $1-F$, being produced by coils. We assume that the fields are of the same form and consider only their relative magnitudes. The power consumption while the field is to be on is now equal to $C(1-F)^2B^2$. However, while the field is required to be off, the coils must be used to cancel the field component of the permanent magnets by running current in the opposite direction. The power consumption for this process is clearly now equal to CF^2B^2.

We now define the fraction of the experimental cycle for which the MOT fields are to be active as T_M. From this, we see that the time-averaged power consumption $\overline{P}$ is given by

$$\overline{P} = T_M C(1-F)^2B^2 + C(1-T_M)F^2B^2. \tag{D1}$$

In order to find the value of F that minimizes the time-averaged power consumption, we set the first derivative of $\overline{P}$ with respect to F equal to zero. This gives

$$CB^2[-2T_M(1-F) + 2F(1-T_M)] = 0, \tag{D2}$$

the solution to which is $F = T_M$.

Using a standard approach where the entire required field is generated by the coils, the time-averaged power consumption would simply be equal to $T_M CB^2$. Setting $F = T_M$ in Eq. (D1) and dividing through by this value, we find that the use of permanent magnets to create part of the MOT field reduces the time-averaged power consumption by a factor of $1/(1-T_M)$.

APPENDIX E: ATOM-NUMBER ESTIMATION

The MOT atom number N is calculated from the photodiode voltage V_{PD} using

$$N = \frac{4\pi\lambda\alpha V_{\mathrm{PD}}}{hc\Omega\gamma_{\mathrm{sc}}s}, \tag{E1}$$

where N is the number of atoms, λ represents the wavelength of the emitted photons, α is the magnification factor of the lenses used to capture the MOT fluorescence, and Ω is the solid angle subtended by the photodetector, such that the effective solid angle from which light is collected is equal to Ω/α, The term V_{PD} denotes the amplitude of the voltage signal of the photodiode as measured on the oscilloscope, γ_{sc} denotes the photon scattering rate of the MOT atoms (which can be approximated as saturated by the illumination of the MOT beams, and is therefore equal to half of the spontaneous decay rate of the excited state), and s is the sensitivity of the photodiode to 780-nm light (in volts per watt, including the postamplification circuit). The loading curves (see Fig. 10 in the main paper) are obtained for various values of the Rb dispenser current ranging from 2.20 A (the minimum current value at which an atomic cloud can be formed) to 2.75 A.

[1] F. Sorrentino, K. Bongs, P. Bouyer, L. Cacciapuoti, M. De Angelis, H. Dittus, W. Ertmer, A. Giorgini, J. Hartwig, M. Hauth, *et al.*, A compact atom interferometer for future space missions, Microgravity Sci. Technol. **22**, 551 (2010).

[2] S. Herrmann, H. Dittus, and C. Laemmerzahl, Testing the equivalence principle with atomic interferometry, Class. Quantum Gravity **29**, 184003 (2012).

[3] G. Rosi, G. D'Amico, L. Cacciapuoti, F. Sorrentino, M. Prevedelli, M. Zych, C. Brukner, and G. Tino, Quantum test of the equivalence principle for atoms in coherent superposition of internal energy states, Nat. Commun. **8**, 15529 (2017).

[4] S. Falke, N. Lemke, C. Grebing, B. Lipphardt, S. Weyers, V. Gerginov, N. Huntemann, C. Hagemann, A. Al-Masoudi, S. Häfner, *et al.*, A strontium lattice clock with 3×10^{-17} inaccuracy and its frequency, New J. Phys. **16**, 073023 (2014).

[5] A. D. Ludlow, M. M. Boyd, J. Ye, E. Peik, and P. O. Schmidt, Optical atomic clocks, Rev. Mod. Phys. **87**, 637 (2015).

[6] F. Riehle, Optical clock networks, Nat. Photonics **11**, 25 (2017).

[7] M. Kasevich and S. Chu, Atomic Interferometry Using Stimulated Raman Transitions, Phys. Rev. Lett. **67**, 181 (1991).

[8] F. Riehle, Th. A. Witte, J. Helmcke, and C. J. Bordé, Optical Ramsey Spectroscopy in a Rotating Frame: Sagnac Effect in a Matter-Wave Interferometer, Phys. Rev. Lett. **67**, 177 (1991).

[9] P. Knight and I. Walmsley, UK national quantum technology programme, Quantum Sci. Technol. **4**, 040502 (2019).

[10] K. Bongs, V. Boyer, M. Cruise, A. Freise, M. Holynski, J. Hughes, A. Kaushik, Y.-H. Lien, A. Niggebaum, M. Perea-Ortiz, *et al.*, in *Quantum Optics* (International Society for Optics and Photonics, 2016), Vol. 9900, p. 990009.

[11] S. Knappe, P. Schwindt, V. Gerginov, V. Shah, L. Liew, J. Moreland, H. Robinson, L. Hollberg, and J. Kitching, Microfabricated atomic clocks and magnetometers, J. Opt. A: Pure Appl. Opt. **8**, S318 (2006).

[12] E. A. Salim, J. DeNatale, D. M. Farkas, K. M. Hudek, S. E. McBride, J. Michalchuk, R. Mihailovich, and D. Z. Anderson, Compact, microchip-based systems for practical applications of ultracold atoms, Quantum Inf. Process. **10**, 975 (2011).

[13] B. Barrett, P.-A. Gominet, E. Cantin, L. Antoni-Micollier, A. Bertoldi, B. Battelier, P. Bouyer, J. Lautier, and A. Landragin, in *International School of Physics "Enrico Fermi" on Atom Interferometry* (2013).

[14] M. Schmidt, A. Senger, M. Hauth, C. Freier, V. Schkolnik, and A. Peters, A mobile high-precision absolute gravimeter based on atom interferometry, Gyroscopy Navig. **2**, 170 (2011).

[15] K. Bongs, J. Malcolm, C. Ramelloo, L. Zhu, V. Boyer, T. Valenzuela, J. Maclean, A. Piccardo-Selg, C. Mellor, T. Fernholz, *et al.*, in *Quantum Information and Measurement* (Optical Society of America, 2014), pp. QTu3B–1.

[16] B. Battelier, B. Barrett, L. Fouché, L. Chichet, L. Antoni-Micollier, H. Porte, F. Napolitano, J. Lautier, A. Landragin, and P. Bouyer, in *Quantum Optics* (International Society for Optics and Photonics, 2016), Vol. 9900, p. 990004.

[17] D. R. Scherer, R. Lutwak, M. Mescher, R. Stoner, B. Timmons, F. Rogomentich, G. Tepolt, S. Mahnkopf, J. Noble, S. Chang, and D. Taylor, in *Proceedings of the 46th Annual Precise Time and Time Interval Systems and Applications Meeting, Boston, Massachusetts* (2014), p. 154, arXiv:1411.5006.

[18] J. Rushton, M. Aldous, and M. Himsworth, Contributed review: The feasibility of a fully miniaturized magneto-optical trap for portable ultracold quantum technology, Rev. Sci. Instrum. **85**, 121501 (2014).

[19] S. Eckel, D. S. Barker, J. A. Fedchak, N. N. Klimov, E. Norrgard, J. Scherschligt, C. Makrides, and E. Tiesinga, Challenges to miniaturizing cold atom technology for deployable vacuum metrology, Metrologia **55**, S182 (2018).

[20] V. Schkolnik, K. Döringshoff, F. B. Gutsch, M. Oswald, T. Schuldt, C. Braxmaier, M. Lezius, R. Holzwarth, C. Kürbis, A. Bawamia, *et al.*, Jokarus—design of a compact optical iodine frequency reference for a sounding rocket mission, EPJ Quantum Technol. **4**, 1 (2017).

[21] A. N. Dinkelaker, M. Schiemangk, V. Schkolnik, A. Kenyon, K. Lampmann, A. Wenzlawski, P. Windpassinger, O. Hellmig, T. Wendrich, E. M. Rasel, *et al.*, Autonomous frequency stabilization of two extended-cavity diode lasers at the potassium wavelength on a sounding rocket, Appl. Opt. **56**, 1388 (2017).

[22] X. Zhang, J. Zhong, B. Tang, X. Chen, L. Zhu, P. Huang, J. Wang, and M. Zhan, Compact portable laser system for mobile cold atom gravimeters, Appl. Opt. **57**, 6545 (2018).

[23] J. P. McGilligan, K. Moore, A. Dellis, G. Martinez, E. de Clercq, P. Griffin, A. Arnold, E. Riis, R. Boudot, and J. Kitching, Laser cooling in a chip-scale platform, Appl. Phys. Lett. **117**, 054001 (2020).

[24] J. Vovrosh, G. Voulazeris, P. G. Petrov, J. Zou, Y. Gaber, L. Benn, D. Woolger, M. M. Attallah, V. Boyer, K. Bongs, *et al.*, Additive manufacturing of magnetic shielding and ultra-high vacuum flange for cold atom sensors, Sci. Rep. **8**, 1 (2018).

[25] R. Saint, W. Evans, Y. Zhou, T. Barrett, T. Fromhold, E. Saleh, I. Maskery, C. Tuck, R. Wildman, F. Oručević, *et al.*, 3D-printed components for quantum devices, Sci. Rep. **8**, 1 (2018).

[26] N. Cooper, L. Coles, S. Everton, I. Maskery, R. Campion, S. Madkhaly, C. Morley, J. O'Shea, W. Evans, R. Saint, P. Krüger, F. Oručević, C. Tuck, R. Wildman, T. Fromhold, and L. Hackermüller, Additively manufactured ultra-high vacuum chamber for portable quantum technologies, Addit. Manuf. **40**, 101898 (2021).

[27] E. L. Raab, M. Prentiss, A. Cable, S. Chu, and D. E. Pritchard, Trapping of Neutral Sodium Atoms with Radiation Pressure, Phys. Rev. Lett. **59**, 2631 (1987).

[28] D. W. Preston, Doppler-free saturated absorption: Laser spectroscopy, Am. J. Phys. **64**, 1432 (1996).

[29] K. MacAdam, A. Steinbach, and C. Wieman, A narrow-band tunable diode laser system with grating feedback, and a saturated absorption spectrometer for Cs and Rb, Am. J. Phys. **60**, 1098 (1992).

[30] G. Puentes, Laser frequency offset locking scheme for high-field imaging of cold atoms, Appl. Phys. B **107**, 11 (2012).

[31] A. Bagheri and J. Jin, Photopolymerization in 3D printing, ACS Appl. Polym. Mater. **1**, 593 (2019).

[32] U. Schünemann, H. Engler, R. Grimm, M. Weidemüller, and M. Zielonkowski, Simple scheme for tunable frequency offset locking of two lasers, Rev. Sci. Instrum. **70**, 242 (1999).

[33] R. W. Fox, C. W. Oates, and L. W. Hollberg, in *Experimental Methods in the Physical Sciences* (Elsevier, 2003), Vol. 40, pp. 1–46.

[34] D. A. Smith and I. G. Hughes, The role of hyperfine pumping in multilevel systems exhibiting saturated absorption, Am. J. Phys. **72**, 631 (2004).

[35] H. Duncker, O. Hellmig, A. Wenzlawski, A. Grote, A. J. Rafipoor, M. Rafipoor, K. Sengstock, and P. Windpassinger, Ultrastable, Zerodur-based optical benches for quantum gas experiments, Appl. Opt. **53**, 4468 (2014).

[36] P. Adby, *Introduction to Optimization Methods* (Springer Science & Business Media, Dordrecht, 2013).

[37] J. Matousek and B. Gärtner, *Understanding and Using Linear Programming* (Springer Science & Business Media, Berlin, 2007).

[38] P. T. While, L. K. Forbes, and S. Crozier, 3D gradient coil design for open MRI systems, J. Magn. Reson. **207**, 124 (2010).

[39] F. X. Li, J. P. Voccio, M. C. Ahn, S. Hahn, J. Bascuñán, and Y. Iwasa, An analytical approach towards passive ferromagnetic shimming design for a high-resolution NMR magnet, Supercond. Sci. Technol. **28**, 075006 (2015).

[40] R. Schmied, J. H. Wesenberg, and D. Leibfried, Optimal Surface-Electrode Trap Lattices for Quantum Simulation with Trapped Ions, Phys. Rev. Lett. **102**, 233002 (2009).

[41] L. Thijs, K. Kempen, J.-P. Kruth, and J. Van Humbeeck, Fine-structured aluminium products with controllable texture by selective laser melting of pre-alloyed AlSi10Mg powder, Acta Mater. **61**, 1809 (2013).

[42] N. T. Aboulkhair, C. Tuck, I. Ashcroft, I. Maskery, and N. M. Everitt, On the precipitation hardening of selective laser melted AlSi10Mg, Metall. Mater. Trans. A **46**, 3337 (2015).

[43] N. T. Aboulkhair, I. Maskery, C. Tuck, I. Ashcroft, and N. M. Everitt, The microstructure and mechanical properties of selectively laser melted AlSi10Mg: The effect of a conventional T6-like heat treatment, Mater. Sci. Eng.: A **667**, 139 (2016).

[44] T. Arpornthip, C. Sackett, and K. Hughes, Vacuum-pressure measurement using a magneto-optical trap, Phys. Rev. A **85**, 033420 (2012).

[45] R. W. Moore, L. A. Lee, E. A. Findlay, L. Torralbo-Campo, G. D. Bruce, and D. Cassettari, Measurement of vacuum pressure with a magneto-optical trap: A pressure-rise method, Rev. Sci. Instrum. **86**, 093108 (2015).

[46] D. Becker, M. D. Lachmann, S. T. Seidel, H. Ahlers, A. N. Dinkelaker, J. Grosse, O. Hellmig, H. Müntinga, V. Schkolnik, T. Wendrich, *et al.*, Space-borne Bose-Einstein

condensation for precision interferometry, Nature **562**, 391 (2018).
[47] S. Dimopoulos, P. W. Graham, J. M. Hogan, M. A. Kasevich, and S. Rajendran, Gravitational wave detection with atom interferometry, Phys. Lett. B **678**, 37 (2009).
[48] S. A. Khairallah, A. T. Anderson, A. Rubenchik, and W. E. King, Laser powder-bed fusion additive manufacturing: Physics of complex melt flow and formation mechanisms of pores, spatter, and denudation zones, Acta Mater. **108**, 36 (2016).
[49] For enquiries related to the design or manufacture of the AM components, please contact either Laurence Coles (laurence.coles@addedscientific.com) or Nathan Cooper (nathan.cooper@nottingham.ac.uk).
[50] S. K. Gaggar, in *Instrumented Impact Testing of Plastics and Composite Materials* (ASTM International, 1986).
[51] D. J. Brunelle and W. E. Smith, Polycarbonate transesterification process, U.S. Patent No. 4,217,438.
[52] F. T. Tan, D. G. Cooper, M. Marić, and J. A. Nicell, Biodegradation of a synthetic co-polyester by aerobic mesophilic microorganisms, Polym. Degrad. Stab. **93**, 1479 (2008).
[53] G. W. C. Kaye, T. H. Laby, and J. G. Noyes, *Tables of Physical and Chemical Constants* (Harlow, Longman, 1995), 16th ed.
[54] P. Mosaddegh, S. Akbarzadeh, M. Zareei, and H. Reiszadeh, Tribological behavior of BK7 optical glass at elevated temperatures, Proc. Inst. Mech. Eng. J: J. Eng. Tribol. **233**, 580 (2019).
[55] Ultimaker, The widest material choice on the market, https://ultimaker.com/materials (2011–2020).
[56] Simplify3D, Filament properties table, https://www.simplify3d.com/support/materials-guide/properties-table/ (2021).
[57] J. T. Cantrell, S. Rohde, D. Damiani, R. Gurnani, L. DiSandro, J. Anton, A. Young, A. Jerez, D. Steinbach, C. Kroese, and P. G. Ifju, Experimental characterization of the mechanical properties of 3D-printed ABS and polycarbonate parts, Rapid. Prototyp. J. **23**, 811 (2017).
[58] H. Kim, E. Park, S. Kim, B. Park, N. Kim, and S. Lee, Experimental study on mechanical properties of single-and dual-material 3D printed products, Procedia Manuf. **10**, 887 (2017).
[59] Rigid photopolymer resin for form 2, material data sheet, https://formlabs-media.formlabs.com/datasheets/Rigid_Technical.pdf (2018).
[60] Photopolymer resin for form 1+ and form 2, https://archivemedia.formlabs.com/upload/XL-DataSheet.pdf (2019).

Chapter 6

High-performance, additively-manufactured atomic spectroscopy apparatus for portable quantum technologies

Published in Optics Express

DOI: 10.1364/OE.455678

Research Article | Vol. 30, No. 14 / 4 Jul 2022 / Optics Express 25753
Optics EXPRESS

High-performance, additively-manufactured atomic spectroscopy apparatus for portable quantum technologies

S. H. MADKHALY,[1,2] N. COOPER,[1,4] L. COLES,[3] AND L. HACKERMÜLLER[1,5]

[1]School of Physics and Astronomy, University of Nottingham, University Park, Nottingham NG7 2RD, UK
[2]Department of Physics, Jazan University, Jazan, Saudi Arabia
[3]Added Scientific Ltd, Unit 4, Isaac Newton Centre, Nottingham NG7 2RH, UK
[4]nathan.cooper@nottingham.ac.uk
[5]lucia.hackermuller@nottingham.ac.uk

Abstract: We demonstrate a miniaturised and highly robust system for performing Doppler-free spectroscopy on thermal atomic vapour for three frequencies as required for cold atom-based quantum technologies. The application of additive manufacturing techniques, together with efficient use of optical components, produce a compact, stable optical system, with a volume of 0.089 L and a weight of 120 g. The device occupies less than a tenth of the volume of, and is considerably lower cost than, conventional spectroscopic systems, but also offers excellent stability against environmental disturbances. We characterise the response of the system to changes in environmental temperature between 7 and 35 °C and exposure to vibrations between 0 - 2000 Hz, finding that the system can reliably perform spectroscopic measurements despite substantial vibrational noise and temperature changes. Our results show that 3D-printed optical systems are an excellent solution for portable quantum technologies.

1. Introduction

Experiments involving cold atoms allow high-precision tests of fundamental physics [1–6], simulation of condensed matter systems [7–9] and the study of new states of matter [10–13]. They also offer one of the most promising routes towards quantum information processing [14–16] and quantum communication [17–20]. Furthermore, the techniques used in these experiments underpin an important emerging field of technological development, in the form of atomic quantum sensors and cold atom clocks [21–24].

These experiments require one or more lasers to be frequency-stabilised via feedback based on thermal vapour spectroscopy, and most require the production of a magneto-optical trap (MOT) [25]. The frequency stability of these lasers is key to the performance of the experiment, yet the optical systems used for vapour spectroscopy are often not well-optimised, bulky and occupy a large fraction of an optical table. Recently, the use of additive manufacturing (AM, also known as 3D printing) methods, together with novel approaches to experimental design, has been demonstrated to enable a compact magneto-optical trap system that captures $> 2 \times 10^8$ atoms [26,27]. AM techniques allow devices to be fully optimised for their intended function, without reference to traditional design constraints [28].

Herein, we apply these broader principles to the construction of a separate, specialised device for laser frequency stabilisation and characterise its performance under environmental stress such as temperature changes and vibrations. While the specific prototype device we demonstrate as an example is aimed at applications within atomic physics, the techniques and design principles

#455678 https://doi.org/10.1364/OE.455678
Journal © 2022 Received 8 Feb 2022; revised 31 Mar 2022; accepted 8 Apr 2022; published 1 Jul 2022

Optics EXPRESS

employed are transferable and may be of use in any field relying on hitherto complex free-space optics.

Our methods have been deliberately chosen so as to facilitate replication and augmentation of this approach: we focus on low-cost, widely-available hardware components and open source software, while keeping the complexity of the techniques and devices employed to a minimum. Our AM-based approach enables remarkable stability and robustness against environmental changes and makes devices constructed along these lines a cost-effective option for deployment in quantum technologies. For portable quantum technologies [29–31] and fundamental experiments in space [32–35], stability with respect to temperature changes and vibrations is of key importance. The device demonstrated here also employs an unconventional spectroscopy scheme, in which light resonant with two different atomic transitions is spatially-overlapped in the atomic vapour, that has been found to offer some advantages in terms of signal strength and sensitivity [36]. The different features and components of the device are discussed in more detail below.

2. Monolithic optomechanical framework

Our prototype device consists of a monolithic, AM framework that is populated with off-the-shelf optical components, as seen in Fig. 1.

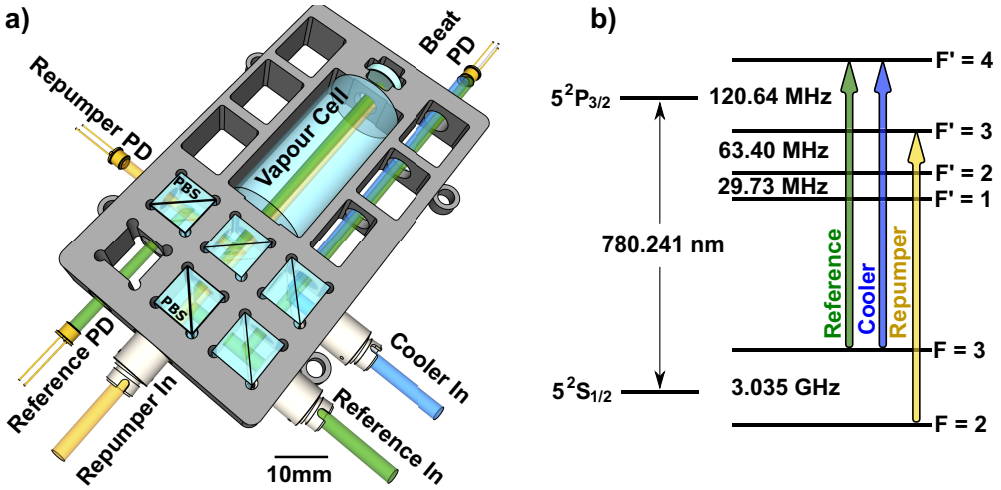

Fig. 1. a) Compact system for performing spectroscopic measurements on three lasers simultaneously, exploiting a monolithic, additively manufactured frame. b) Transition structure of the ^{85}Rb D2 line, indicating the names traditionally given to lasers used for magneto-optical trapping and cold atom experiments, as well as the transitions they address.

This framework was additively manufactured from polylactic acid via Fused Deposition Modelling (FDM) printing [37–39] and designed to house a minimal optical setup for simultaneous frequency stabilisation of three lasers via saturated absorption spectroscopy [40]. The total print time was about 3 hours with no post processing required. A model of the framework, with optical components implanted, is shown in Fig. 1, and the relevant beam pathways are shown schematically in Fig. 2.

The device has outer dimensions of 110×65×12.5 mm and a total weight of 120 g (including optics). The design of the framework keeps optical path lengths as short as possible to improve stability. The maximum optical path length for any of the beams in the device is 230 mm, while a typical path length in a standard experimental apparatus would be on the order of 1-2 m. Stability is also achieved by omitting adjustable elements.

Optics EXPRESS

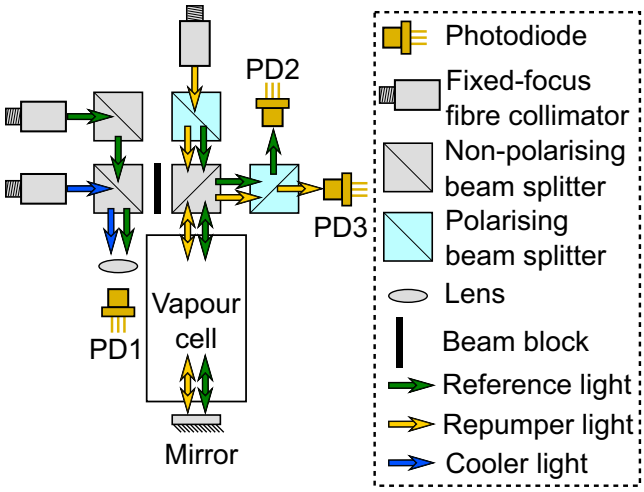

Fig. 2. Schematic diagram showing the optical pathways within the compact spectroscopy device.

The optical components push-fit directly into the polymer framework, exploiting AM design features described in more detail in [27]; holes in the framework allow the passage of the laser beams where required and recesses over the central regions of the optics allow them to be slotted into the framework without risk of scuffing the optically-active surfaces. Small holes in the corners of the component slots improve push-fit alignment by favouring an extended contact region rather than a point contact, and also avoid the build defects that can otherwise result from filament dragging [41]. A grid-like structure adds stability, reduces material and supports a homogeneous printing process. The layout of the beam paths is shown in Fig. 2.

3. Optical components and pathways, control electronics

The layout of the spectroscopy apparatus is shown in Fig. 1 (a). All components are of industry standard sizes and the device can be reproduced with components from a range of manufacturers. Fig. 2 shows the schematic outline of the optical pathways within the device, indicating how light from each of the three input connectors is employed to generate the required spectroscopic signals and optical beat note. The photodiodes are operated using homebuilt transimpedance amplifiers with buffered outputs. The LM324N quadruple operational amplifier chip is employed for the spectroscopic photodiodes and the (higher bandwidth) AD8001A operational amplifier is used for the optical beat note (note that some data was collected using commercial photodiode-amplifier packages, prior to the construction of the homebuilt models — see e.g. Fig. 6).

All beams are brought into the optical framework via fixed-focus fibre collimators and then distributed and routed via beam splitters. Fig. 2 shows a diagram of the beam paths. The reference beam is immediately split into two pathways: one for vapour spectroscopy and one to produce an optical beat note. The component used for the optical beat note is combined with the cooler light, at a non-polarising beam splitter, following which the two beams are overlapped on the photodiode 'PD1.' The component to be used for spectroscopy is combined at a polarising beam splitter with the repumper light. The two beams then propagate through the vapour cell and back, with a portion of the return light picked-off using a non-polarising beam splitter; the reference and repumper frequency components of the return light are then separated via a polarising beam splitter and directed onto photodiodes 'PD2' and 'PD3' respectively. The double-pass beam configuration within the vapour cell [36] allows for Doppler-free spectroscopy to be performed,

Optics EXPRESS

resulting in the saturated absorption signal of D2 line of ^{85}Rb and ^{87}Rb shown in Fig. 3 (a). The device also produces an optical beat note (Fig. 3 (b)), on photodiode PD1, which allows the cooler laser to be stabilised with a controllable frequency separation from the reference laser.

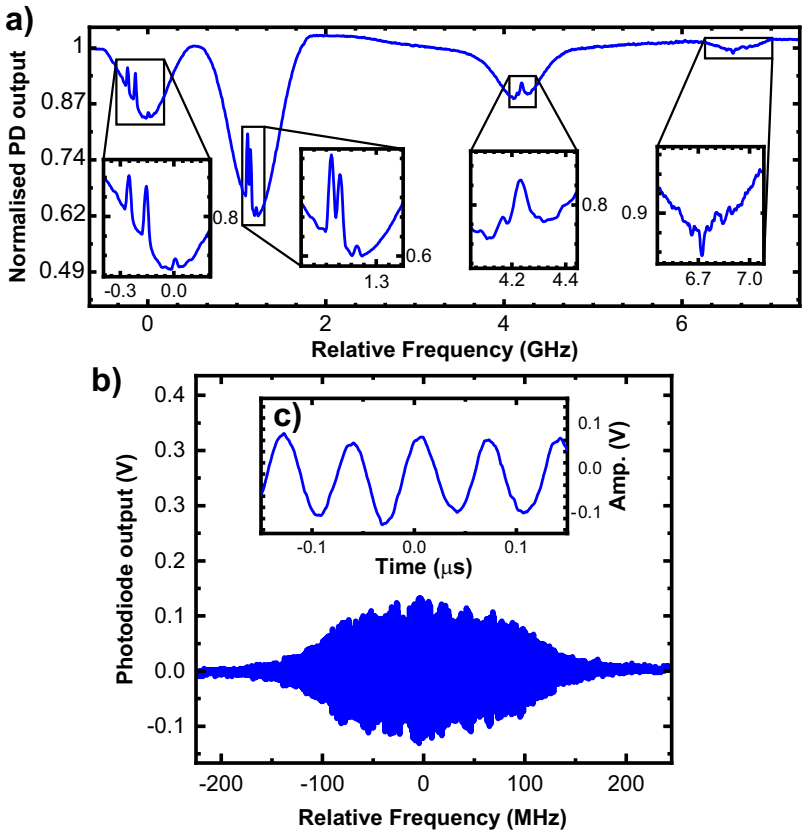

Fig. 3. Saturated absorption spectra of ^{85}Rb and ^{87}Rb isotopes (a), and beat signal between a laser tuned to the ^{85}Rb cooler transition and the reference laser (b), both obtained using the optical system illustrated in Fig. 1. The inset (c) displays a single-frequency beat note at (13.4±0.1) MHz.

Fig. 3 (b) shows the beat note created between the reference laser and the cooler laser, obtained from the reference laser being stabilised to the ^{85}Rb $F = 3 \rightarrow F' = 4$ transition and the cooler laser being scanned over the full range. The main panel shows the beat signal envelope as the cooler laser is scanned; this gives an indication of the frequency range and signal to noise ratio of the beat signal, but necessarily undersamples the individual beat frequencies present at any given point within the scan; the inset therefore displays an example of a single-frequency beat note at (13.4±0.1) MHz.

To improve the laser frequency stability while reducing size, weight and cost, control electronics based on digital microcontrollers were utilised. Specifically, the Arduino Uno development board was used, in combination with its associated open-source software, as the central component of our control and feedback electronics.

The system has been tested using both external cavity diode lasers (e.g. for the data in Fig. 7) and distributed feedback lasers (e.g. as used for Figs. 3(a) and 4). A $1/e^2$ beam diameter of 2.1 mm was used and spectroscopy signals were obtained with beam powers ranging from 0.5 to 5 mW. By dividing the r.m.s. voltage noise on the gradient of the spectroscopic signal (which is

Optics EXPRESS

typically used as a feedback signal for laser frequency stabilisation) by its sensitivity to frequency variations about the laser lock point, we estimate the spectroscopic limit on laser linewidth using our current system, with a feedback bandwidth of 10 kHz, to be (1.28±0.02) MHz. This would be more than sufficient for most applications, such as the creation of a magneto-optical trap (shown in [27]), though certain specialist applications may require narrower linewidths. These could be obtained at relatively modest cost through the use of superior photodiode amplifiers; alternatively, if the majority of the contributions to the free-running laser's frequency variations come from the low-frequency end of the spectrum, as is usually the case, then the spectroscopic output can be time-averaged or put through a low-pass filter to improve signal-to-noise by sacrificing bandwidth.

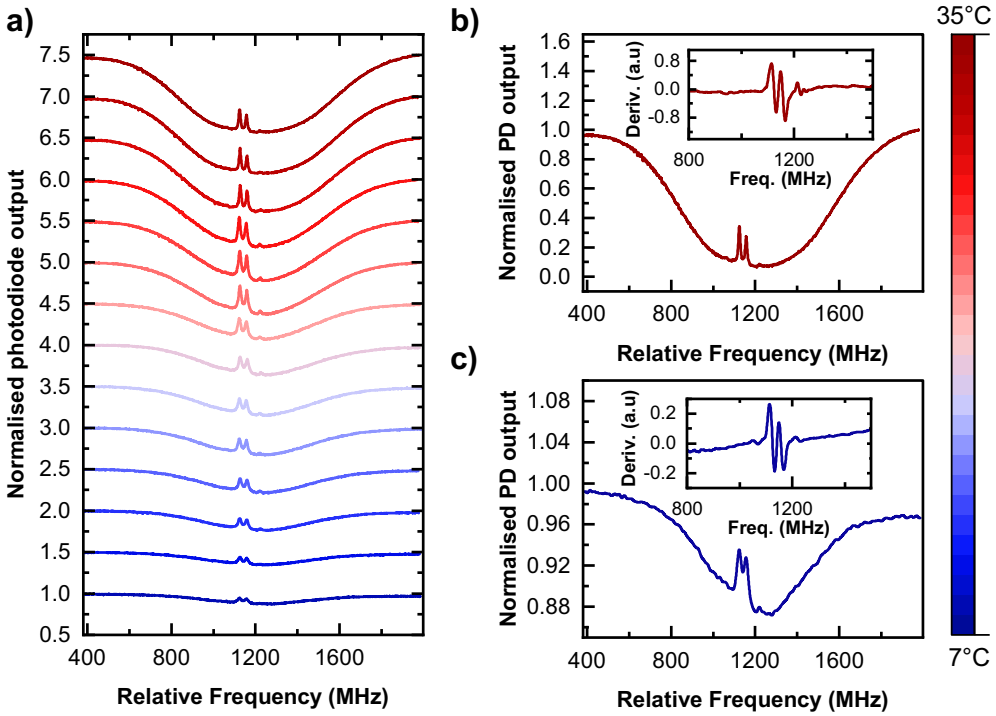

Fig. 4. (a) Spectroscopic signal line shape of ^{85}Rb $F = 3 \rightarrow F' = 2, 3, 4$ transition corresponding to temperature changes from 7° C to 35° C. For visibility, an offset of 0.5 is applied between successive traces. As the temperature rises from 7° C (panel (c)) to 35° C (panel (b)), the spectroscopic signal amplitude increases while its form remains unchanged. The insets in (b) and (c) represent the derivative signals of the corresponding traces.

4. Stability measurements

To ensure that our system is suitable for use outside the laboratory, a series of stability tests under harsh environmental conditions was performed.

4.1. Thermal stability test

In order to test the optical system's thermal stability, it was subjected to changes in the environmental temperature while monitoring the resulting spectroscopic signals. The optical framework was placed inside an aluminium box to create a uniform thermal distribution around the system, and the temperature was gradually raised using a heating tape. This process was

Optics EXPRESS

performed sufficiently slowly to ensure that the system reached thermal equilibrium prior to data collection. The change in temperature was monitored using three temperature and humidity sensors placed at different points inside and outside the metal box. The laser frequency was continuously scanned across the $F = 3 \rightarrow F' = 2, 3, 4$ transitions of the ^{85}Rb D2 line, in order to measure the system's response to the temperature changes. The spectroscopic signal was captured at a range of temperatures and is plotted in Fig. 4.

As seen in the figure, the device performs its intended function over the full temperature range, from 7° C to 35° C. The form of the spectroscopic response is largely unchanged, while its amplitude increases at higher temperatures due to the increased vapour pressure of the alkali metal within the vapour cell. The spectroscopy traces for the highest (35° C) and lowest temperatures (7° C) are shown separately in Fig. 4 (b), (c). The derivatives for these traces are given in the insets and depict an error signal with good signal-to-noise. The observed performance is at least comparable to that reported for considerably more expensive systems, made out of materials specifically selected for thermal stability, such as Invar and Zerodur [42].

The derivatives according to frequency have been calculated for all traces shown in Fig. 4 (a), together with additional data of the same nature that was omitted from Fig. 4 (a) to avoid overcrowding, and were used to obtain a quantitative, temperature dependent comparison of the relative capture range and the relative stabilisation signal gradient. Figure 5 shows the variation of the sensitivity of a laser stabilisation feedback signal (corresponding to the gradient of the spectroscopic signal) to laser frequency (blue data points), normalized to the result at lab temperature (20° C). In order to obtain these results, the first and second derivatives of the spectroscopic signals were obtained via a 3-point central difference method. Since the dominant source of error in the plotted data comes from high-frequency electrical noise in the photodiode amplifier circuit, such that the noise contributions even to adjacent sample points show very little correlation, multiple gradient estimates with different sample widths can be used to obtain an average value and associated statistical error estimate, which is plotted in the figure.

The dash-dotted green line indicates the expected variation due to vapor pressure changes; we obtain this result by assuming that all points in the observed signal individually obey the Beer-Lambert law, and that the absorption coefficient for each laser frequency scales in proportion to the vapor pressure in the cell. This model is sufficient to yield most of the variation observed over the relevant parameter range. It can be seen that our experimental data shows a slightly stronger temperature response, particularly in the higher temperature range. This can be attributed to the fact that our model neglects saturation effects; at high vapor pressure, the increased attenuation of the light reduces the saturation level, and consequent power broadening, that occurs at positions further along the optical path. This reduction in power broadening sharpens the sub-Doppler features slightly and hence can be expected to lead to a small increase in the gradient of the stabilisation signal, as observed. Importantly, our results do not indicate any degradation of the performance of the spectroscopic system over the full temperature window.

Also plotted is the relative capture range of the stabilisation signal (orange data points); this is given by the frequency range about the desired stabilisation frequency within which the gradient of the feedback signal does not change sign, normalised to the result at lab temperature (20° C). This parameter is a measure of the robustness of a laser stabilisation technique. Derivative and error determination relies on a 3-point central difference approach, together with standard error propagation to convert uncertainty in the values of the second derivative of the spectroscopic signal to uncertainty in the laser frequency at which it changes sign. The results show that the performance of the spectroscopic system is not degraded as the temperature moves away from the standard operating temperature of 20° C. The slight downward trend in capture range as temperature is increased can be attributed to the same mechanism of reduced power-broadening as described above.

Optics EXPRESS

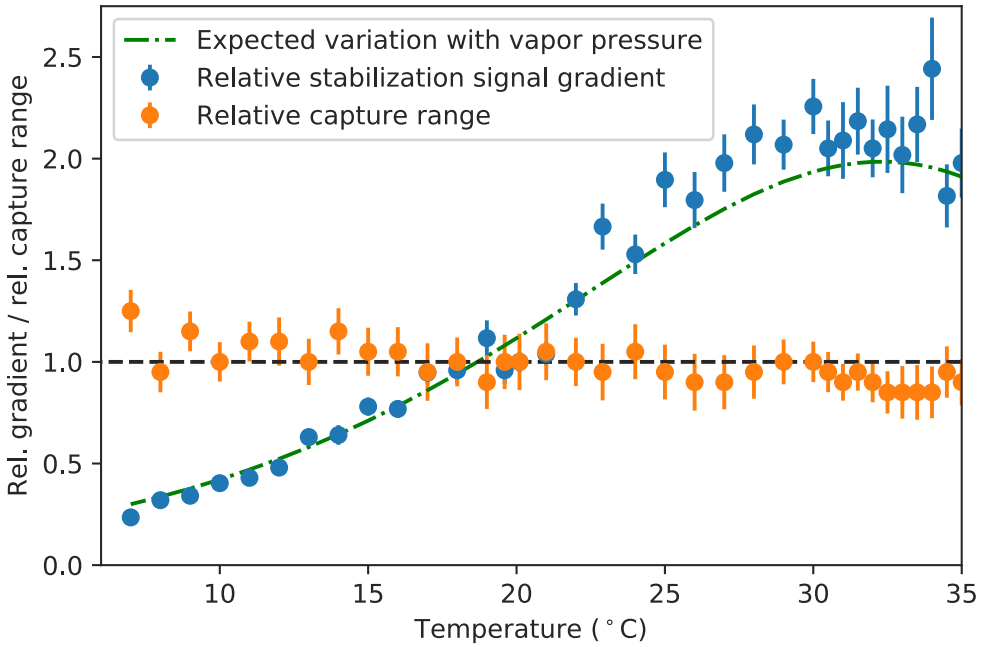

Fig. 5. Relative sensitivity of laser stabilisation feedback signal (given by the maximum second derivative of the spectroscopic signal with respect to laser frequency) as a function of device temperature (blue data). The green line indicates the expected variation due to the change in Rb vapor pressure. The orange data shows the capture range. In both cases, normalization is relative to the values measured at 20 °C.

4.2. Response to vibrations

Mechanical instability is a major challenge that needs to be overcome when designing portable systems for space applications and work outside laboratory walls [43]. For this purpose, we simulated a vibrating environment by placing the device onto an aluminium plate, as shown in Fig. 6.

An analog monitoring accelerometer (Te-connectivity 820M1), placed as shown in the figure, was used to measure and record the vibrations to which the device was exposed. Sinusoidal vibrations were introduced at several frequencies, between 0 Hz and 2 kHz, generated by a frequency generator and a loudspeaker. Additionally, manual shaking of the plate was used to simulate a noisy environment.

Figure 7 displays the power spectral density of the control voltage used to drive the loudspeaker (black, lowest panel), the measured acceleration of the vibrating plate (orange), and the resulting photodiode output voltages from the reference photodiode, PD2, with the laser's frequency stabilisation active (green) and inactive (blue). For reference, the DC voltage level of the photodiode output voltages was ~ 50 mV. This is shown for driving frequencies of 100 Hz, 500 Hz, 1 kHz and 2 kHz (panels a) to d) respectively) as well as for manual shaking (panel e)). For sinusoidal, single-frequency vibrations, an amplitude of $\pm 0.2\,\mathrm{ms}^{-2}$ was applied, corresponding to the maximum output of the speaker. For the random shaking test (panel e)), vibrations were applied both manually and through the loudspeaker, with amplitudes going far beyond what was possible with the speaker alone; corresponding data was collected at frequencies up to 15 kHz. Despite clear contributions to the measured acceleration spectrum, very little contribution is made to the power spectrum of the optical signal by the presence of vibrations.

Optics EXPRESS

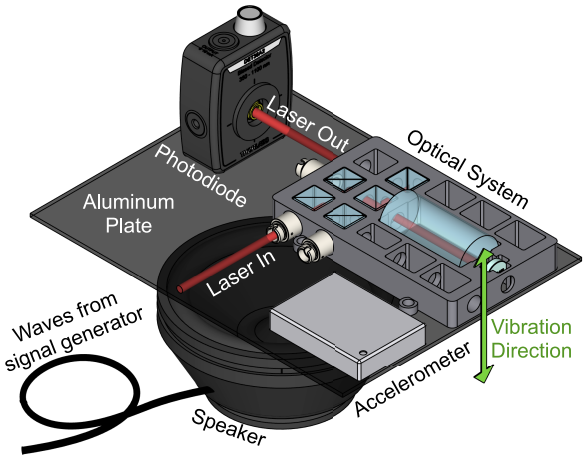

Fig. 6. Mechanical stability test setup. A loudspeaker was used to generate a vibrating environment with varying frequencies to evaluate the optical framework's stability —see text for details.

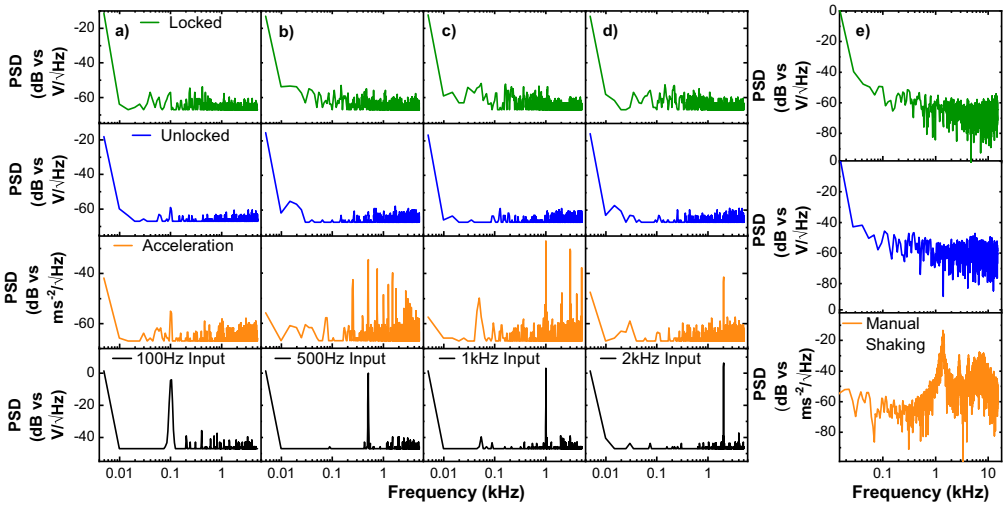

Fig. 7. Measurements of the optical system's response to single-frequency vibrations (100Hz, 500Hz, 1kHz, 2kHz) generated from a loudspeaker (a,b, c, and d) and to manual shaking (e). The power spectral density (PSD) of the output signal from the reference photodiode (PD2) is shown as a function of frequency, both when the laser is stabilised on resonance with the ^{85}Rb $F = 3 \rightarrow F' = 4$ transition (green), and when the laser is free-running about the same frequency (blue). The PSD of the vibrations measured by 820M1-TE accelerometer (see Fig. 6) is also shown (orange), along with the PSD of the driving voltage applied to the loudspeaker (black).

Optics EXPRESS

A requirement for a device to be suitable for portable quantum technologies is that it can withstand the acceleration and vibrations caused by transportation, e.g. those experienced in a moving vehicle [44] or during a space launch [45], then operate in a stationary but un-isolated environment. Our data shows that the device described herein can operate well not only after, but also during, manual shaking, which produced acceleration amplitudes comparable to those experienced during high-speed transportation [44,45]. Perturbation in an uncontrolled but stable environment outside the lab (e.g. standing on the ground or on a platform) are likely to be of similar amplitudes to what we have tested in Fig. 7.

The advantages of the 3D printed setup can be qualitatively illustrated by comparison to a conventional system. For these measurements, the aluminium plate shown in Fig. 6 was cantilevered from the side of a standard optical bench. Data was simultaneously collected from both the compact spectroscopy apparatus on the vibrating plate and from a conventional spectroscopy apparatus located approximately two meters away on the optical bench. This apparatus employed a 130 cm optical beam pathway from an external cavity diode laser (inside a Toptica TA pro box), through a total of six mirrors on standard kinematic mounts, terminating on a Thorlabs PD10A amplified photodiode. Note that the light was sourced from the same laser for both measurements, so disturbance of the laser cannot explain the observed differences. Fig. 8 shows a comparison of the performance of the two systems. Fig. 8(a) shows that the form of the Doppler-free spectroscopy signal obtained from our compact spectroscopy device, mounted directly onto the vibrating plate, was barely affected by the presence of the vibrations. The same vibrations can be seen to have a substantial and deleterious effect on the spectroscopic signal produced by the conventional apparatus, despite its lesser degree of proximity to the source of

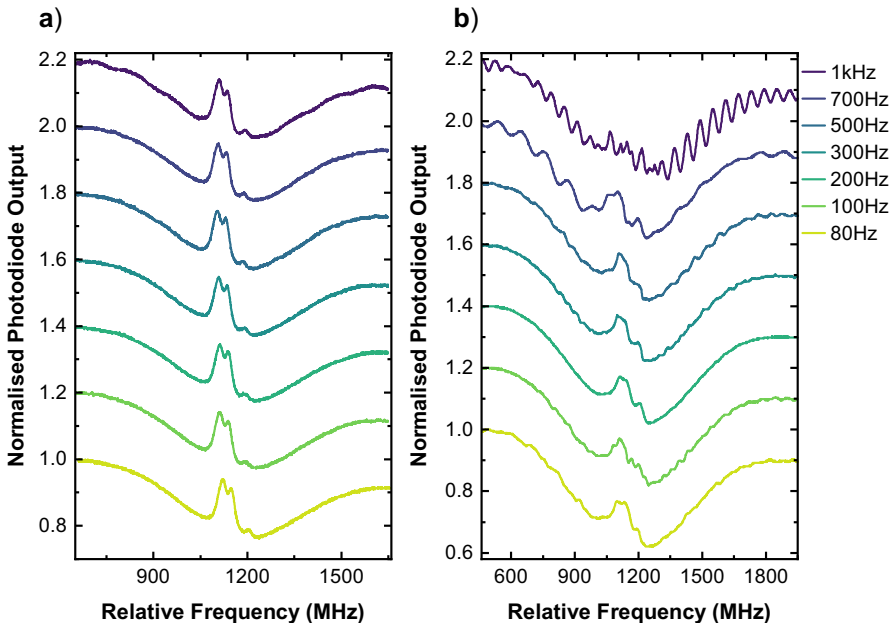

Fig. 8. The effect of different ranges of single-frequency vibrations on the saturated absorption spectroscopy signal of (a) the AM optical framework directly exposed to the vibrations, and (b) a conventional setup constructed on the other side of the same optical bench. For reference, the ^{85}Rb F=3 → F'=2,3, and 4 transition is shown. As can be seen, the compact optical system exhibits a high level of resistance to vibrational disturbance, whereas the conventional setup is extremely susceptible to the same range of oscillations. For visibility, an offset of 0.2 is applied between successive traces.

Optics EXPRESS

the vibrations — see Fig. 8(b). The range of frequencies applied were between 80Hz and 1kHz with an amplitude of $\pm 0.2\,\mathrm{ms}^{-2}$. Note that this measurement demonstrates that the compact system can be operated while the vibrations are applied without major disturbance. This clearly shows the advantages of compact AM-design, and additively manufactured frame, minimisation of the use of adjustable components and fully-surrounding support structures for the mechanical stabilisation of optical systems.

5. Conclusions and outlook

We have demonstrated a compact, inexpensive experimental system, based on 3D-printing methods, for performing Doppler-free spectroscopy on two lasers simultaneously, as well as generating an optical beat note with a third laser. Its response to vibrations and temperature changes has been analysed. We have thus demonstrated that the use of 3D-printing methods can lead to robust systems which can be tailored in performance to a required task. The demonstrated device shows comparable robustness against temperature changes and vibrations to specialised, integrated systems, but at a much lower cost. It is able to operate consistently over a 28 degree temperature range and in the presence of such vibrations as might be found in an un-isolated environment, demonstrating its suitability for use in portable quantum technologies. These methods are transferable and through the application of similar techniques to other complex optical systems are likely to transform current experimental hardware.

The system as shown is suitable for laser stabilisation for magneto-optical trapping, as needed for cold-atom-based quantum technologies. The use of the AM mount in this context allows an advanced design, tailored to the task, and can deliver high stability and reduced size and weight - and is thus relevant for the development of portable quantum technologies or the use of quantum technologies in space. In the future, the capacities of 3D printing can be exploited further by tailoring stiffness and thermo-mechanical response following optimisation in a computer simulation model e.g. via latticing, structural reinforcement or material combinations. We believe that our approach of using AM materials is critical for quantum technologies and applicable to all applications requiring fixed optical configurations.

Funding. School of Physics and Astronomy, University of Nottingham; European Commission (grant ErBeStA 800942); Engineering and Physical Sciences Research Council (EP/M013294/1, EP/R024111/1, EP/T001046/1).

Acknowledgment. We would like to thank Sarah Everton and Dominic Sims for useful comments, and Lisa Knbelreiter for assistance with data collection.

Disclosures. The authors declare the following competing interests: N.C., L.C. and L.H. are inventors on a UK pending patent application GB 1916446.6 (applicant: University of Nottingham, inventors: Nathan Cooper, Lucia Hackermüller, Laurence Coles) for the device described in the article.

Data Availability. All data necessary to support the conclusions of the article are presented in the article. Any additional data related to this paper may be obtained from the authors upon reasonable request.

References

1. F. Yver, A. Landragin, N. Dimarcq, A. Clairon, D. Holleville, P. Cheinet, P. Bouyer, C. Salomon, and C. Borde, "A cold atom interferometer for high precision measurements," in *2003 European Quantum Electronics Conference. EQEC 2003 (IEEE Cat No. 03TH8665)*, (IEEE, 2003), p. 309.
2. R. Geiger, A. Landragin, S. Merlet, and F. Pereira Dos Santos, "High-accuracy inertial measurements with cold-atom sensors," AVS Quantum Sci. **2**(2), 024702 (2020).
3. G. M. Tino, "Testing gravity with cold atom interferometry: Results and prospects," Quantum Sci. Technol. **6**(2), 024014 (2021).
4. L. Cacciapuoti, M. Armano, R. Much, O. Sy, A. Helm, M. P. Hess, J. Kehrer, S. Koller, T. Niedermaier, F. X. Esnault, D. Massonnet, D. Goujon, J. Pittet, P. Rochat, S. Liu, W. Schaefer, T. Schwall, I. Prochazka, A. Schlicht, U. Schreiber, P. Delva, C. Guerlin, P. Laurent, C. L. Poncin-Lafitte, M. Lilley, E. Savalle, P. Wolf, F. Meynadier, and C. Salomon, "Testing gravity with cold-atom clocks in space," Eur. Phys. J. D **74**(8), 164 (2020).
5. M. Takamoto, I. Ushijima, N. Ohmae, T. Yahagi, K. Kokado, H. Shinkai, and H. Katori, "Test of general relativity by a pair of transportable optical lattice clocks," Nat. Photonics **14**(7), 411–415 (2020).

Optics EXPRESS

6. F. Kaiser, P. Vergyris, A. Martin, D. Aktas, M. P. D. Micheli, O. Alibart, and S. Tanzilli, "Quantum optical frequency up-conversion for polarisation entangled qubits: towards interconnected quantum information devices," Opt. Express **27**(18), 25603–25610 (2019).
7. J. P. Hague, S. Downes, C. MacCormick, and P. E. Kornilovitch, "Cold rydberg atoms for quantum simulation of exotic condensed matter interactions," J. Supercond. Nov. Magn. **27**(4), 937–940 (2014).
8. M. Lewenstein, A. Sanpera, V. Ahufinger, B. Damski, A. Sen, and U. Sen, "Ultracold atomic gases in optical lattices: mimicking condensed matter physics and beyond," Adv. Phys. **56**(2), 243–379 (2007).
9. E. Demler and T. Kitagawa, "Strongly correlated systems in atomic and condensed matter physics," Lect. Notes Phys. 284, 28 (2014).
10. F. Dalfovo, S. Giorgini, L. P. Pitaevskii, and S. Stringari, "Theory of bose-einstein condensation in trapped gases," Rev. Mod. Phys. **71**(3), 463–512 (1999).
11. A. J. Leggett, "Bose-einstein condensation in the alkali gases: Some fundamental concepts," Rev. Mod. Phys. **73**(2), 307–356 (2001).
12. I. Bloch, J. Dalibard, and W. Zwerger, "Many-body physics with ultracold gases," Rev. Mod. Phys. **80**(3), 885–964 (2008).
13. S. Giorgini, L. P. Pitaevskii, and S. Stringari, "Theory of ultracold atomic fermi gases," Rev. Mod. Phys. **80**(4), 1215–1274 (2008).
14. P. Farrera, G. Heinze, B. Albrecht, M. Ho, M. Chávez, C. Teo, N. Sangouard, and H. De Riedmatten, "Generation of single photons with highly tunable wave shape from a cold atomic ensemble," Nat. Commun. **7**(1), 13556 (2016).
15. J. J. Garcia-Ripoll, P. Zoller, and J. I. Cirac, "Quantum information processing with cold atoms and trapped ions," J. Phys. B At. Mol. Opt. Phys. **38**(9), S567–S578 (2005).
16. I. I. Ryabtsev, I. I. Beterov, D. B. Tretyakov, V. M. Entin, and E. A. Yakshina, "Spectroscopy of cold rubidium rydberg atoms for applications in quantum information," Phys.-Uspekhi **59**(2), 196–208 (2016).
17. P. Roztocki, M. Kues, C. Reimer, B. Wetzel, S. Sciara, Y. Zhang, A. Cino, B. E. Little, S. T. Chu, D. J. Moss, and R. Morandotti, "Practical system for the generation of pulsed quantum frequency combs," Opt. Express **25**(16), 18940–18949 (2017).
18. P. Schneeweiss, A. Dareau, and C. Sayrin, "Cold-atom-based implementation of the quantum rabi model," Phys. Rev. A **98**(2), 021801 (2018).
19. A. Kuzmich, W. Bowen, A. Boozer, A. Boca, C. Chou, L.-M. Duan, and H. Kimble, "Generation of nonclassical photon pairs for scalable quantum communication with atomic ensembles," Nature **423**(6941), 731–734 (2003).
20. X.-H. Bao, A. Reingruber, P. Dietrich, J. Rui, A. Dück, T. Strassel, L. Li, N.-L. Liu, B. Zhao, and J.-W. Pan, "Efficient and long-lived quantum memory with cold atoms inside a ring cavity," Nat. Phys. **8**(7), 517–521 (2012).
21. K. Bongs, J. Malcolm, C. Ramelloo, L. Zhu, V. Boyer, T. Valenzuela, J. Maclean, A. Piccardo-Selg, C. Mellor, T. Fernholz, M. Fromhold, P. Krüger, O. Hellmig, A. Grote, S. Dörscher, H. Duncker, P. Windpassinger, K. Sengstock, C. Becker, B. Pelle, A. Hilico, M. Zhou, M.-C. Angonin, P. Wolf, F. P. Dos Santos, F. Bertoldi, P. Bouyer, T. Mazzoni, N. Poli, F. Sorrentino, M. Tarallo, G. Tino, S. Stellmer, F. Schreck, M. Popp, W. Herr, T. Wendrich, W. Ertmer, E. Rasel, and A. Kürbis, "A. Wicht, "iSense: A technology platform for cold atom based quantum technologies," in *Quantum Information and Measurement*, (Optical Society of America, 2014), pp. QTu3B–1.
22. S. Falke, N. Lemke, C. Grebing, B. Lipphardt, S. Weyers, V. Gerginov, N. Huntemann, C. Hagemann, A. Al-Masoudi, S. Häfner, S. Vogt, U. Sterr, and C. Lisdat, "A strontium lattice clock with 3×10^{-17} inaccuracy and its frequency," New J. Phys. **16**(7), 073023 (2014).
23. A. D. Ludlow, M. M. Boyd, J. Ye, E. Peik, and P. O. Schmidt, "Optical atomic clocks," Rev. Mod. Phys. **87**(2), 637–701 (2015).
24. F. Riehle, "Optical clock networks," Nat. Photonics **11**(1), 25–31 (2017).
25. S. L. Kemp, K. L. Butler, R. Freytag, S. A. Hopkins, E. A. Hinds, M. R. Tarbutt, and S. L. Cornish, "Production and characterization of a dual species magneto-optical trap of cesium and ytterbium," Rev. Sci. Instrum. **87**(2), 023105 (2016).
26. N. Cooper, L. Coles, S. Everton, I. Maskery, R. Campion, S. Madkhaly, C. Morley, J. O'Shea, W. Evans, R. Saint, P. Krüger, F. Orucevic, C. Tuck, R. Wildman, T. Fromhold, and L. Hackermüller, "Additively manufactured ultra-high vacuum chamber for portable quantum technologies," Addit. Manuf. **40**, 101898 (2021).
27. S. Madkhaly, L. Coles, C. Morley, C. Colquhoun, T. Fromhold, N. Cooper, and L. Hackermüller, "Performance-optimized components for quantum technologies via additive manufacturing," PRX Quantum **2**(3), 030326 (2021).
28. B. H. Jared, M. A. Aguilo, L. L. Beghini, B. L. Boyce, B. W. Clark, A. Cook, B. J. Kaehr, and J. Robbins, "Additive manufacturing: Toward holistic design," Scr. Mater **135**, 141–147 (2017).
29. J. P. McGilligan, P. F. Griffin, R. Elvin, S. J. Ingleby, E. Riis, and A. S. Arnold, "Grating chips for quantum technologies," Sci. Rep. **7**(1), 384 (2017).
30. V. Schkolnik, K. Döringshoff, F. B. Gutsch, M. Oswald, T. Schuldt, C. Braxmaier, M. Lezius, R. Holzwarth, C. Kürbis, A. Bawamia, M. Krutzik, and A. Peters, "Jokarus-design of a compact optical iodine frequency reference for a sounding rocket mission," EPJ Quantum Technol. **4**(1), 9–10 (2017).
31. A. Strangfeld, S. Kanthak, M. Schiemangk, B. Wiegand, A. Wicht, A. Ling, and M. Krutzik, "Prototype of a compact rubidium-based optical frequency reference for operation on nanosatellites," J. Opt. Soc. Am. B **38**(6), 1885–1891 (2021).

Optics EXPRESS

32. A. Belenchia, M. Carlesso, Ö. Bayraktar, D. Dequal, I. Derkach, G. Gasbarri, W. Herr, Y. L. Li, M. Rademacher, J. Sidhu, D. K. Oi, S. T. Seidel, R. Kaltenbaek, C. Marquardt, H. Ulbricht, V. C. Usenko, L. Wörner, A. Xuereb, M. Paternostro, and A. Bassi, "Quantum physics in space," Phys. Rep. **951**, 1–70 (2022).
33. K. Frye, S. Abend, W. Bartosch, A. Bawamia, D. Becker, H. Blume, C. Braxmaier, S.-W. Chiow, M. A. Efremov, W. Ertmer, P. Fierlinger, T. Franz, N. Gaaloul, J. Grosse, C. Grzeschik, O. Hellmig, V. A. Henderson, W. Herr, U. Israelsson, J. Kohel, M. Krutzik, C. Kürbis, C. Lämmerzahl, M. List, D. Lüdtke, N. Lundblad, J. P. Marburger, M. Meister, M. Mihm, H. Müller, H. Müntinga, A. M. Nepal, T. Oberschulte, A. Papakonstantinou, J. Perovsek, A. Peters Achim, Prat E. M. Rasel, A. Roura, M. Sbroscia, W. P. Schleich, C. Schubert, S. T. Seidel, J. Sommer, C. Spindeldreier, D. Stamper-Kurn, B. K. Stuhl, M. Warner, T. Wendrich, A. Wenzlawski, A. Wicht, P. Windpassinger, N. Yu, and L. Wörner, "The bose-einstein condensate and cold atom laboratory," EPJ Quantum Technol. **8**(1), 1 (2021).
34. A. Bertoldi, K. Bongs, P. Bouyer, O. Buchmueller, B. Canuel, L.-I. Caramete, M. L. Chiofalo, J. Coleman, A. De Roeck, J. Ellis, P. W. Graham, M. G. Haehnelt, A. Hees, J. Hogan, W. von Klitzing, M. Krutzik, M. Lewicki, C. McCabe, A. Peters, E. Rasel, A. Roura, D. Sabulsky, S. Schiller, C. Schubert, C. Signorini, F. Sorrentino, Y. Singh, G. M. Tino, V. Vaskonen, and M.-S. Zhan, "Aedge: Atomic experiment for dark matter and gravity exploration in space," Exp. Astron. **51**(3), 1417–1426 (2021).
35. E. R. Elliott, M. C. Krutzik, J. R. Williams, R. J. Thompson, and D. C. Aveline, "Nasa's cold atom lab (cal): system development and ground test status," NPJ Microgravity **4**(1), 16 (2018).
36. N. Cooper, S. Madkhaly, D. Johnson, D. Baldolini, and L. Hackermüller, "Dual-frequency spectroscopy for compact systems and enhanced laser stabilisation," arXiv preprint arXiv:2106.11014 (2021).
37. Ultimaker, "The widest material choice on the market (2011-2020)," https://ultimaker.com/materials.
38. Simplify3D, "Filament properties table," https://www.simplify3d.com/support/materials-guide/properties-table/ (2021).
39. K. Friedrich and R. Walter, *Structure and Properties of Additive Manufactured Polymer Components* (Woodhead Publishing, 2020).
40. D. W. Preston, "Doppler-free saturated absorption: Laser spectroscopy," Am. J. Phys. **64**(11), 1432–1436 (1996).
41. G. D. Goh, Y. L. Yap, H. Tan, S. L. Sing, G. L. Goh, and W. Y. Yeong, "Process–structure–properties in polymer additive manufacturing via material extrusion: A review," Crit. Rev. Solid State Mater. Sci. **45**(2), 113–133 (2020).
42. H. Duncker, O. Hellmig, A. Wenzlawski, A. Grote, A. J. Rafipoor, M. Rafipoor, K. Sengstock, and P. Windpassinger, "Ultrastable, zerodur-based optical benches for quantum gas experiments," Appl. Opt. **53**(20), 4468–4474 (2014).
43. S. Ressel, M. Gohlke, D. Rauen, T. Schuldt, W. Kronast, U. Mescheder, U. Johann, D. Weise, and C. Braxmaier, "Ultrastable assembly and integration technology for ground-and space-based optical systems," Appl. Opt. **49**(22), 4296–4303 (2010).
44. V. Chonhenchob, S. P. Singh, J. J. Singh, J. Stallings, and G. Grewal, "Measurement and analysis of vehicle vibration for delivering packages in small-sized and medium-sized trucks and automobiles," Packaging Technol. Sci. **25**(1), 31–38 (2012).
45. V. Schkolnik, O. Hellmig, A. Wenzlawski, J. Grosse, A. Kohfeldt, K. Döringshoff, A. Wicht, P. Windpassinger, K. Sengstock, C. Braxmaier, M. Krutzik, and A. Peters, "A compact and robust diode laser system for atom interferometry on a sounding rocket," Appl. Phys. B **122**(8), 217 (2016).

Chapter 7

Dual-frequency Doppler-free spectroscopy for simultaneous laser stabilisation in compact atomic physics experiments

In arXiv

arXiv: 2106.11014v1

Dual-frequency Doppler-free spectroscopy for simultaneous laser stabilisation in compact atomic physics experiments

Nathan Cooper[1], Somya Madkhaly[1], David Johnson[1], Daniele Baldolini[1] and Lucia Hackermüller[1]

[1]School of Physics and Astronomy, University of Nottingham, University Park, Nottingham, NG7 2RD, UK

E-mail: nathan.cooper@nottingham.ac.uk

August 2021

Abstract. Vapour cell spectroscopy is an essential technique in many fields; in particular, nearly all atom and ion trapping experiments rely on simultaneous spectroscopy of two atomic transitions, traditionally employing separate apparatus for each transition. Here, we demonstrate simultaneous spectroscopy on two atomic transitions using spatially-overlapped beams from two independent lasers, within a single spectroscopic apparatus. We show that, in addition to aiding compactness, this approach offers superior performance, leading to sharper spectroscopy peaks and stronger absorption signals. Doppler-free locking features become visible over a frequency range several hundred MHz wider than for standard saturated absorption spectroscopy. By exploring the full, 2D parameter space associated with dual-frequency spectroscopy, we reveal a lattice-like structure of sharp resonance features in 2D frequency space, which enhances experimental versatility by allowing laser frequency stabilisation anywhere within a wide manifold of locations in 2D frequency space. The process of simultaneous frequency stabilisation of two lasers is analysed in detail, revealing that it can be expected to produce significant improvements in laser stability when compared to conventional, single-frequency spectroscopy.

1. Introduction

Experiments employing cold, trapped atoms or ions underpin a wide range of fundamental research [1, 2, 3] and technological applications [4, 5, 6, 7, 8]. Such experiments require lasers that are accurately frequency-stabilised relative to specific atomic transitions, a function typically performed via feedback based on spectroscopy of a thermal atomic vapour. In addition, many important direct applications rely on atomic vapour spectroscopy — for example the use of thermal atomic magnetometers in medical imaging [9, 10], or of atomic spectroscopy to search for dark matter [11]. Improving the signal strength and the frequency sensitivity of atomic vapour spectroscopy is therefore beneficial across a wide range of applications and research areas.

Frequency-stabilisation of lasers for atom cooling and trapping experiments is achieved via a feedback servo that controls the laser diode current and/or other feedback parameters. Typically at least two independent lasers are required, as light resonant with two different atomic transitions — typically referred to as the "cooler" and "repumper" transitions — is essential [12]. The signal used for this feedback is generated from spectroscopic measurements on an atomic vapour cell. A common technique for this is based on saturated absorption spectroscopy [13, 14], combined with modulation of the laser current and phase-sensitive detection of the spectroscopic signal [15].

Dual-frequency Doppler-free spectroscopy, in which two optical frequencies are overlapped on a single spatial path within an atomic vapour, can increase the strength and sharpness of Doppler-free resonance features [16, 17, 18, 19] and enhance frequency stabilisation of a single, modulated laser. We demonstrate that dual-frequency spectroscopy with two independent laser sources enables precise, simultaneous spectroscopy on the two transition manifolds relevant to atomic cooling and trapping experiments. The variation of both lasers' frequencies opens up a two-dimensional parameter space where optical pumping effects create a lattice of Doppler-free resonance features, offering an expanded set of potential "locking points" for laser frequency stabilisation. We explain how two lasers can be stabilised simultaneously based on the resulting spectroscopic signals, finding that the method enables both miniaturisation of the experimental apparatus and increased laser frequency stability. In [20], the technique is employed to stabilise two lasers simultaneously for the creation of a magneto-optical trap; here we provide a detailed analysis of the technique and its potential benefits for laser frequency stability.

These results are of particular relevance to the burgeoning field of portable quantum technologies [21, 22]. Here, the achievable reductions in size, weight and complexity offered by allowing multiple beams to share one spatial pathway are important [20]. Furthermore, the drive for miniaturisation will increase the desirability of using small vapour cells with correspondingly reduced optical depths [23, 24], thus making enhancement of the strength and sensitivity of the locking signal yet more important. The ambition to operate these systems outside the laboratory, with potential exposure to increased environmental noise, also adds to the desirability of increasing signal strength.

The paper is structured as follows: we give a brief overview of the experimental arrangement employed in this technique and present a rate-equation model that explains many of the observed key features of the approach. We then present experimental results spanning the full 2D frequency space associated with dual-frequency spectroscopy, before analysing the relative merits of this technique for laser stabilisation when compared to the status quo.

2. Setup and layout

We consider two orthogonally polarised laser beams from independent lasers, which are combined at a polarising beamsplitter. The two beams co-propagate through a Doppler-

free spectroscopy setup [14], sharing the same optical components, as illustrated in figure 1(a). This configuration is chosen as required for most atomic physics experiments, which rely on two frequencies ('cooler' and 'repumper') for atom cooling, as shown for the example of ^{133}Cs in Fig. 1(b).

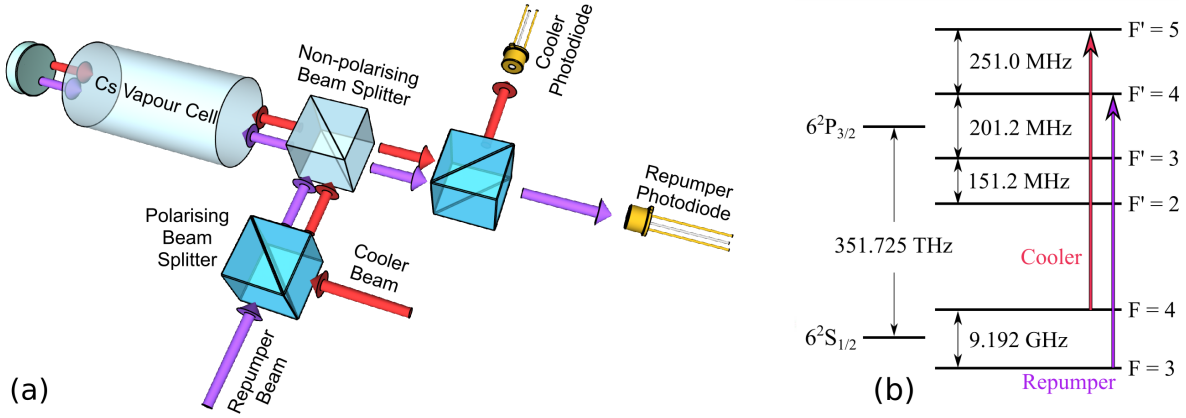

Figure 1. (a): Experimental setup used for dual-beam spectroscopy. For clarity, the spatially-overlapped laser beams are illustrated as side-by-side in the figure. (b): Level structure for ^{133}Cs, indicating the role of the 'cooler' and 'repumper' lasers.

The use of only a single optical frequency for spectroscopy on the D lines of alkali metal atoms results in pumping of the atomic population into a state not addressed by the pumping light, just as observed in magneto-optical trapping experiments [12], leading to a substantial attenuation of the atomic response and a weaker spectroscopic signal. When light from two lasers is overlapped on the same spatial pathway in an atomic vapour, the absorption of each laser beam is affected by the presence of the other, leading e.g. to coherent effects such as electromagnetically-induced transparency [25] as well as bringing back parts of the atomic population into the cycling transition through 'repumping'. Simultaneous use of light resonant with transitions from both hyperfine states of the lower manifold (see figure 1(b)) can therefore be expected to improve spectroscopic signal strength.

Both beams have frequencies tuned close to resonance with the caesium D2 line: the 'repumper' laser is resonant with transitions from the $F = 3$ hyperfine state of the lower manifold to the upper manifold, and the 'cooler' laser with transitions from the $F = 4$ state of the lower manifold, matching the standard naming convention in the field — see figure 1(b). After interacting with the cell the laser beams are separated at a polarising beamsplitter and their intensity is individually recorded on separate photodiodes shown in figure 1(a).

As an example, figure 2 shows the results of a 1D experiment in which 0.37 mW of cooler light, at a fixed frequency of -365 MHz (relative to the F=4→F′=5 transition), was directed into the apparatus alongside 0.25 mW of repumper light, while the frequency of the repumper laser was scanned. The resulting absorption of the repumper light was determined by recording the output of the repumper photodiode from figure 1(a)

and is shown in figure 2(a). For comparison, the figure also shows the result when the light from the cooler laser was blocked, which then corresponds to a standard saturated absorption spectroscopy signal. Fig. 2(a) clearly shows that the use of dual-frequency spectroscopy (blue line) substantially increases both the overall absorption of the light by the atomic vapour and the size and spread of Doppler-free resonance features in comparison to standard Doppler-free spectroscopy with only a single laser beam (grey line). Figure 2(b) shows the corresponding "normalised error signal," which is defined as the fractional change in light transmission per unit frequency, given by $T^{-1}\,(dT/dF_r)$, where T is the fraction of the repumper light that is transmitted through the atomic vapour and F_r is the frequency of the repumper laser. This derivative represents the 'ideal' form of the error signal typically employed for spectroscopic feedback stabilisation of a laser's frequency. The comparison in Figure 2(b) displays a steeper gradient around the locking points when two frequencies are present as well as an increased number of potential locking points; and related to that a wider frequency space over which lock points are available. The "normalised error signal" demonstrates the relevance of this method with respect to laser frequency stabilisation. The increase in the maximum gradient of the error signal will improve frequency stability when applied for feedback stabilisation of a laser, and the increase in the amplitude of the features will improve the robustness of laser stabilisation in noisy environments by offering an increased "capture range" about the desired stabilisation frequency.

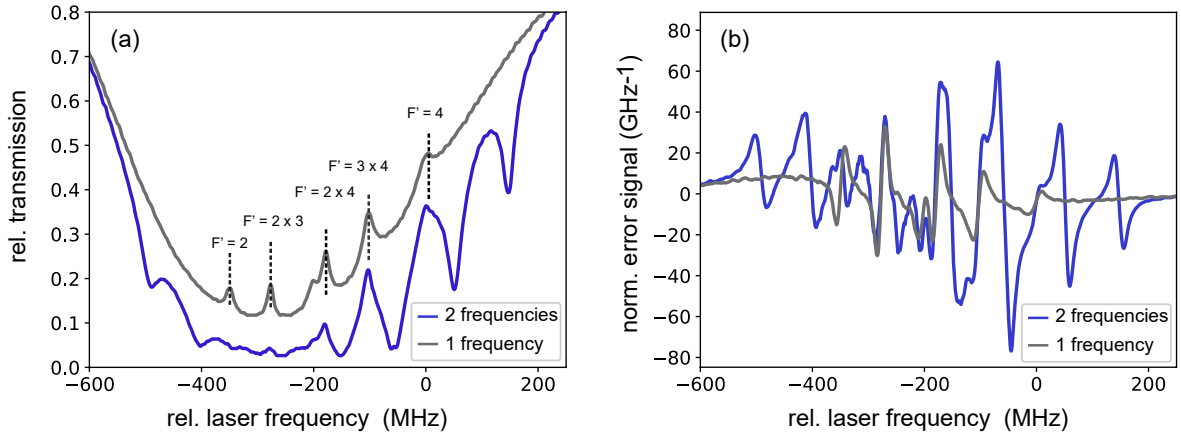

Figure 2. (a): Spectroscopy signal from the repumper photodiode (see figure 1(a)) while light from the cooler laser, tuned 365 MHz below the $F = 4 \rightarrow F' = 5$ transition, is also present in the cell (purple line). A standard Doppler-free saturated absorption spectroscopy signal (grey line) is shown for reference. The addition of light tuned to the cooler transition substantially increases the size and spread of the Doppler-free features. (b): Normalised error signal (see text) resulting from the spectroscopic signals in (a). In both panels, the laser frequency axis is that of the repumper laser relative to the F=3→F′=4 transition.

3. Model and Theory

An intuitive analysis of this system can explain the enhanced absorption and the increased number of absorption peaks. We will also see, in panel (a) of figures 3 and 4, that a lattice-like structure is observed in 2D frequency space; the same intuitive analysis of optical pumping effects within a thermal velocity distribution can explain this phenomenon. Consider, for example, the absorption of the cooler light. When the repumper light is on resonance with transitions in the same atoms, within the thermal atomic velocity distribution, as the light from the cooler beam, it enhances the absorption of the cooler light. For co-propagating beams the simultaneous resonance condition requires that the two laser frequencies are separated by a fixed amount, thus creating a set of sharp features, similar to those seen in saturated absorption spectroscopy, that map out diagonal lines of positive slope in 2D frequency space. For counter-propagating beams, the same effect is present but the sign of the slope is reversed. Since both co-propagating and counter-propagating beams are present in the vapour cell, the dual-frequency optical pumping effects can be expected to produce diagonal line features with both positive and negative slope.

To go beyond this intuitive description, we develop a simple theoretical model that correctly predicts the key features of our results and elucidates the underlying physical mechanisms.

We approximate the transient behaviour of atoms as they traverse the beam in the following way: we assume that some fraction of the atoms, F_N, have recently entered the laser beam and remain in an equal mixture of the two hyperfine states of the $6S_{1/2}$ level. The remaining atomic population is assumed to be in a state of dynamic equilibrium. This is likely to be a reasonable approximation, as very few cycles of optical pumping are required to redistribute the atomic population.

In order to determine the influence of these 'equilibrium state' atoms on the spectroscopic signals, we adopt a similar approach to that presented in previous work on atom trapping using optical pumping effects [26], developing a rate-equation based model in which we consider the six-level system shown in figure 1(b). For convenience, we label the atomic states A-F, as shown in the figure. For now we consider only a single atom with fixed laser detunings — the thermal distribution of atomic velocities and corresponding Doppler shifts will be factored in later. We define a set of rate coefficients, τ_{ij} and Γ_{ij}, such that the stimulated and spontaneous transition rates between, for example, states E and B are given by $\tau_{EB}I_{EB}$ and Γ_{EB} respectively, where I_{EB} is the intensity of the laser light tuned to the relevant set of transitions (i.e. cooler or repumper). The spontaneous decay rates for the relevant transitions are already known accurately — see for example [27]. To determine the rate coefficients for stimulated transitions, we equate the steady-state results for the upper state population produced by our rate equation model to those produced by solving the full optical Bloch equations for a two level system. For a transition with spontaneous decay rate Γ, illumination of

detuning δ and intensity I, with Rabi frequency Ω, we obtain

$$\frac{\Omega^2/4}{\delta^2 + \Omega^2/2 + \Gamma^2/4} = \frac{\tau I}{2\tau I + \Gamma}. \tag{1}$$

Therefore, labeling the dipole matrix element $\langle \mathrm{E}|x|\mathrm{B}\rangle$ between two levels as X_{EB}, we find that

$$\tau_{\mathrm{EB}} = \frac{\Omega_{\mathrm{EB}}^2 \Gamma_{\mathrm{EB}}}{4 I_{\mathrm{EB}} (\delta_{\mathrm{EB}}^2 + \Gamma_{\mathrm{EB}}^2/2)} = \frac{e^2 \left|X_{\mathrm{EB}}\right|^2 \Gamma_{\mathrm{EB}}}{2\hbar^2 c \epsilon_0 (\delta_{\mathrm{EB}}^2 + \Gamma_{\mathrm{EB}}^2/2)} \tag{2}$$

and similar results for the other transitions. Hence, using each state's label to denote the population fraction in that state, the rate equations governing the system are given by:

$$\frac{\mathrm{dF}}{\mathrm{dt}} = (\mathrm{B} - \mathrm{F}) \tau_{\mathrm{FB}} I_{\mathrm{FB}} - \mathrm{F} \Gamma_{\mathrm{FB}}, \tag{3}$$

and corresponding expressions for the time derivatives of the populations of the remaining states (see Supplementary Materials). Setting all time derivatives to zero and the total fractional population across all states equal to 1, we solve the equations to find the fractional steady-state populations in each state. The full derivation is given in the supplementary material. Here we simply quote the result, first defining the following notation:

$$\gamma_{\mathrm{ij}} = \tau_{\mathrm{ij}} I_{\mathrm{ij}} + \Gamma_{\mathrm{ij}}, \tag{4}$$

$$k_{\mathrm{ij}} = \frac{\tau_{\mathrm{ij}} I_{\mathrm{ij}}}{\sum_{\mathrm{k}} \gamma_{\mathrm{ik}}}, \tag{5}$$

$$\zeta_{\mathrm{i}} = \frac{1}{\sum_{\mathrm{j}} \tau_{\mathrm{ji}} I_{\mathrm{ji}}}, \tag{6}$$

and the composite coefficient

$$C_1 = \frac{\left(k_{\mathrm{EA}} \gamma_{\mathrm{EB}} + k_{\mathrm{DA}} \gamma_{\mathrm{DB}}\right) \zeta_{\mathrm{B}}}{1 - \left(k_{\mathrm{FB}} \gamma_{\mathrm{FB}} + k_{\mathrm{EB}} \gamma_{\mathrm{EB}} + k_{\mathrm{DB}} \gamma_{\mathrm{DB}}\right) \zeta_{\mathrm{B}}}, \tag{7}$$

where the summations are carried out over all dipole-allowed transitions. Note that repeated indices do not imply summation here — summations are used only where explicitly stated. We now find that in the steady state

$$A = \left[1 + \sum_{\mathrm{i}} k_{\mathrm{iA}} + C_1 \left(1 + \sum_{\mathrm{j}} k_{\mathrm{jB}}\right)\right]^{-1}, \tag{8}$$

with the remaining fractional populations given by

$$B = C_1 A, \tag{9}$$

and for the upper manifold

$$i = k_{\mathrm{iA}} A + k_{\mathrm{iB}} B. \tag{10}$$

Having obtained the steady state populations we can now determine the rate of photon loss per equilibrium-state atom, L_{eq}, from a given beam as

$$L_{eq} = \sum (j - i)\tau_{\mathrm{ij}} I_{\mathrm{ij}}, \tag{11}$$

where the sum is taken over all combinations of upper manifold states i and lower manifold states j between which dipole-allowed transitions can be stimulated by the chosen beam (ignoring the negligible stimulation of cooler/repumper transitions by repumper/cooler lasers respectively). The un-pumped atoms can be taken into consideration at this stage as well, yielding

$$L = (1 - F_N) \sum (j - i)\tau_{\mathrm{ij}} I_{\mathrm{ij}} + F_N \sum \frac{1}{2} \tau_{\mathrm{ij}} I_{\mathrm{ij}}. \tag{12}$$

Equation (12) can be used to determine the rate of attenuation of a laser beam by stationary atoms subject to known illumination conditions. In order to accurately model a thermal atomic vapour, the velocity distribution of the atoms and corresponding Doppler shift in each beam's effective detuning must be taken into account. This can be done by integrating equation (12) over the atomic velocity distribution, where the dependence of L on atomic velocity comes in via the dependence of the values of δ_{ij} in equation (2) on atomic velocity (due to the Doppler shift) and the corresponding variation in the values of τ_{ij}. We define a new variable, L_{thermal}, as the average loss rate of photons from the beam per atom, given the atoms' thermal velocity distribution. In the case of a thermal atomic vapour at temperature T, considering only the first-order Doppler shift, this is given by

$$L_{\mathrm{thermal}} = \frac{1}{N} \int_{-\infty}^{\infty} L(v) \exp\left(-mv^2/2k_{\mathrm{B}}T\right) dv, \tag{13}$$

where m is the mass of the atoms, k_{B} is the Boltzmann constant and the integration variable v corresponds to the atomic velocity component along the axis of the laser beams. N is the normalisation constant for the 1D Boltzmann distribution. Furthermore, we must consider that there are counter-propagating beams within the vapour cell. These can be taken into account simply by summing the contributions of the different beams to the stimulated transition rates, such that in the equations above $\tau_{\mathrm{ij}} I_{\mathrm{ij}}$ becomes $\tau_{\mathrm{ij}} I_{\mathrm{ij}}(\mathrm{beam1}) + \tau_{\mathrm{ij}} I_{\mathrm{ij}}(\mathrm{beam2})$. Note that for counter-propagating beams the sign of the Doppler shift on the value of δ_{ij} in equation (2) will be opposite for the two beams. With this substitution made equation (13) can then be applied individually to each laser beam present.

Equation (13) can now be used to deduce the mean optical absorption cross-section per atom as a function of both laser frequencies. The results of this are shown alongside our experimental data in figures 3 and 4. The expected key features can clearly be seen: the presence of each beam increases the strength of the absorption of the other beam and creates sharp locking features, similar to those seen in saturated absorption spectroscopy, in a diagonal 'criss-cross' pattern across the whole Doppler valley. While the output of the model does not exactly match the experimental data, this is expected

given the assumptions made in the model — a much more complex model would be necessary to show quantitative agreement with experimental results, but ours provides a useful guide to the overall trends in the system and the nature of the observed features.

4. Experimental results

Figures 3 and 4 show the output signals from each of the photodiodes shown in figure 1(a), as a function of the frequencies of both the cooler and repumper lasers. These were obtained by synchronously scanning both laser frequencies across the relevant frequency range. This was done by adding a linear ramp to the current supplied to each laser diode, and by simultaneously ramping the voltage supplied to piezoelectric transducers that control the alignment of diffraction gratings used for external cavity feedback. The result is laser frequencies described by the equations

$$F_1 = A + Bt \qquad \text{and} \qquad F_2 = C + Dt, \tag{14}$$

where t is the time since the start of the ramp, F_1 and F_2 are the frequencies of the cooler and repumper lasers, respectively, and A-D are constant coefficients. The resulting equation expressing F_2 as a function of F_1 is

$$F_2 = \frac{D}{B}F_1 + \left(C - \frac{DA}{B}\right). \tag{15}$$

This equation clearly describes a diagonal line in the parameter-plane displayed in figure 3, with gradient D/B and offset C-(DA/B). By adjusting either of the static frequency offsets, A and C, it is then possible to collect data along multiple such lines and build up a full, 2D dataset as displayed. Note that the boundaries of the region within which data was collected consequently form diagonal lines in 2D frequency space — hence the greyed-out triangles in the corners of figures 3 and 4. An absolute frequency reference was provided by simultaneously directing light from each of the lasers to a standard saturated absorption spectroscopy apparatus; this enables independent confirmation of each laser's frequency via a well established technique. The diameter of each beam was 1.25 mm and the powers used were 0.14 mW for the cooler laser and 0.23 mW for the repumper laser.

The results in figures 2, 3 and 4 clearly show that the presence of the additional cooler/repumper frequency light enhances the absorption signal of the repumper/cooler light by the atomic vapour; figure 2 represents a vertical slice through figure 3(a), while conventional spectroscopy corresponds to an equivalent slice in the limit of a far-detuned cooler laser, which is approached at the boundaries of the cooler-frequency axis in figure 3(a). An enhancement of the absorption signal translates to more accurate laser frequency stabilisation by providing a feedback signal with improved signal to noise ratio. In addition, figures 3 and 4 also demonstrate that sharp response features are created in a diagonal grid pattern over a frequency range of about 700 MHz — considerably broader than the 450 MHz (for the cooler laser) or 350 MHz (for the repumper laser) over which conventional saturated absorption spectroscopy produces

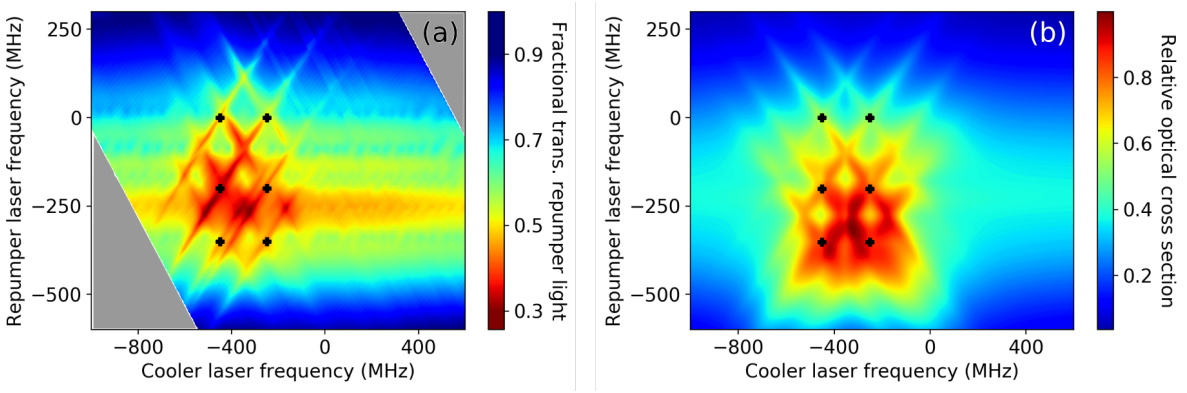

Figure 3. Spectroscopic signal from the repumper laser photodiode (a) as a function of the frequencies of both lasers. See text for details. Frequencies for the cooler and repumper lasers are given relative to the F=4→F′=5 and F=3→F′=4 transitions respectively. Panel (b), shows the prediction of our rate-equation model for the relative optical absorption cross-section per atom from the repumper beam. To guide the eye, black '+' symbols indicate the points where the two lasers are simultaneously resonant with relevant transitions in stationary atoms, such that optical pumping effects lead to diagonal line features. The the rate equation model describes the observed key features very well. The simulation assumes that the intensity of the return beam is always half of that of the in going beam.

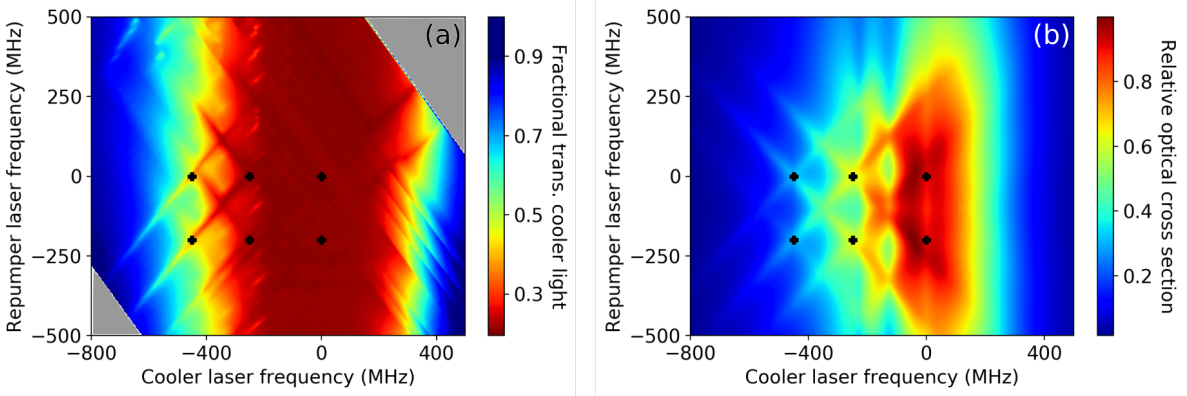

Figure 4. Spectroscopic signal from the cooler laser photodiode (a) as a function of the frequencies of both lasers. See figure 1 and main text for details. Shown alongside, in panel (b), is the prediction of our rate-equation model (see above) for the relative optical absorption cross-section per atom from the cooler beam.

Doppler-free resonance features. This enables the technique to be used for frequency stabilisation at a much wider range of frequency offsets than is usually possible.

5. Application to laser frequency stabilisation

We focus on simultaneous frequency stabilisation of two lasers using the same apparatus. The technique could also be of use for enhanced frequency stabilisation of a single laser via the injection of light from an independently stabilised laser — this possibility is

considered in detail in the Supplementary Material.

An appropriate figure of merit is the factor by which the frequency deviations of a laser stabilised via dual-frequency spectroscopy could be reduced, compared to those of a laser stabilised using conventional techniques, under the assumption that the feedback hardware works perfectly and stability is limited entirely by the quality of the spectroscopic signal. We shall refer to this as the "signal-limited stability factor" (SLSF). This is an appropriate figure of merit for characterisation of the spectroscopic technique being used; other measures, such as a direct measurement of a stabilised laser's frequency stability, can conflate the efficacy of the spectroscopic technique with other issues, such as the finite bandwidth of feedback hardware or electronic noise in the feedback circuitry.

To determine numerical values for the SLSF, we must consider a specific laser stabilisation scheme. We examine the case of saturated absorption spectroscopy, combined with laser current modulation and phase-sensitive detection of the corresponding spectroscopic signal [15]. Note that dual-frequency spectroscopy is not limited to use with this method and similar results are expected for alternative schemes, such as dichroic atomic vapour laser locking [28, 29] or polarisation spectroscopy [30, 31].

Locking based on saturated absorption spectroscopy and current modulation generates a response signal, S, approximately proportional to the rate of change of the saturated absorption signal voltage with laser frequency:

$$S \approx C\frac{dV}{dF}, \tag{16}$$

where C is a system-specific constant, F is the laser frequency and V is the normalised output voltage of the photodiode. The parameter of interest — the sensitivity of the response signal to changes in laser frequency — is therefore given by

$$\frac{dS}{dF} \approx C\frac{d^2V}{dF^2}. \tag{17}$$

For simultaneous stabilisation of two lasers, composite feedback signals must be generated that depend (at least to first order about the desired 'lock point' - the position in 2D frequency space where it is intended to stabilise both lasers) only on the frequency of one laser. We consider two lasers with frequencies F_1 and F_2 generating corresponding photodiode outputs V_1 and V_2. We assume that the currents of the two lasers are modulated at different frequencies to avoid direct cross-talk.

Assuming that all derivatives are evaluated at the chosen locking point, the gradient of the spectroscopic signal after demodulation, S_1, is given by

$$\frac{dS_1}{dF_1} = C_1\frac{d^2V_1}{dF_1^2} \tag{18}$$

and

$$\frac{dS_1}{dF_2} = C_1\frac{d^2V_1}{dF_1\ dF_2}, \tag{19}$$

with corresponding expressions for the gradient of S_2. We can therefore define a composite parameter χ_1 with no first-order dependence on F_2:

$$\chi_1 = S_1 - \upsilon_1 S_2, \tag{20}$$

where

$$\upsilon_1 = \frac{C_1}{C_2}\frac{d^2V_1}{dF_1\ dF_2}\left(\frac{d^2V_2}{dF_2^2}\right)^{-1}. \tag{21}$$

Corresponding expressions obviously exist for χ_2, following the same derivation. Thus it is possible to generate a feedback signal for each laser that is independent of the frequency of the other laser. This makes it possible to stabilise both lasers simultaneously based on the generated feedback signals.

We now determine the expected laser frequency stability and compare it to that achieved with conventional saturated absorption spectroscopy. The SLSF is equal to the ratio of the sensitivity of the spectroscopic signal (to changes in laser frequency, about the desired lock point) in dual-frequency spectroscopy to the same parameter in a conventional spectroscopic setup; in this case the SLSF for laser 1 ('E_1') is therefore given by

$$E_1 = \frac{d\chi_1}{dF_1}\Bigg/\left(\frac{dS_{\mathrm{con}}}{dF_{\mathrm{con}}}\sqrt{1+\nu_1^2}\right), \tag{22}$$

where $dS_{\mathrm{con}}/dF_{\mathrm{con}}$ is the gradient of the feedback signal about the lock point in an equivalent conventional saturated absorption spectroscopy apparatus. The factor of $\sqrt{1+\nu_1^2}$ normalises against the amplification of the feedback signal that has been performed via post-processing, and consequently therefore amplifies the experimental noise as well as the desired signal and cannot produce an improvement in frequency stability. We thus find that

$$E_1 = \left(\frac{dS_1}{dF_1} - \upsilon_1\frac{dS_2}{dF_1}\right)\Bigg/\left(\frac{dS_{\mathrm{con}}}{dF_{\mathrm{con}}}\sqrt{1+\nu_1^2}\right), \tag{23}$$

and the equivalent expression for E_2. As an example, the SLSF was calculated for a 1D subset of the experimental data shown in figures 3 and 4, for both cooler and repumper lasers. This is displayed in figure 5; for illustrative purposes, the SLSF of conventional spectroscopy (which is by definition equal to 1 at the optimum locking point for single-frequency spectroscopy) is also plotted. Here, the repumper laser frequency is set 370 MHz below the F=3 to F′=4 transition and the cooler laser frequency is varied. It can be seen that there are multiple locations in frequency space where the SLSF exceeds 1 for both lasers simultaneously. This shows that, even when stabilising two lasers using the same apparatus, and when considering only the laser for which the result is least favourable, dual-frequency spectroscopy still offers better performance than conventional Doppler-free spectroscopy.

It is worth noting that, by selecting an appropriate lock point in 2D frequency space, the technique allows one to prioritise the frequency stability of one laser, further enhancing performance for one laser at the expense of worse performance for the

other. This may be useful in situations where specific experimental applications have asymmetric frequency tolerances for the two lasers — consider, for example, the very different tolerances of a MOT to frequency deviations of the cooler and repumper lasers [12].

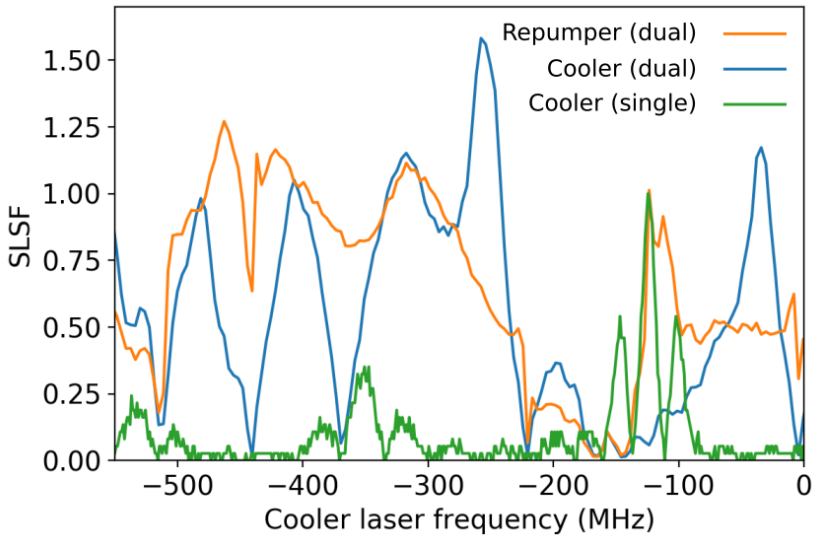

Figure 5. Signal-limited stability factor (SLSF — see text for full definition) resulting from laser stabilisation based on dual-frequency spectroscopy, compared to the maximum achievable using conventional saturated absorption spectroscopy with only a single frequency component. The repumper laser frequency is set to -370 MHz and the SLSF is determined by applying equation (23) to our data. It can be seen that dual-frequency spectroscopy offers generally improved stability, over a wider range of frequencies, than conventional spectroscopy. In addition, multiple locations exist at which the stability of *both* lasers is simultaneously greater than the maximum achievable with single-frequency spectroscopy. Note that this figure displays only a 1D slice through 2D frequency space; the broader manifold of locations that can be accessed by tuning both laser frequencies offers high stability at an even greater range of lock points. Frequencies for the cooler and repumper lasers are given relative to the F=4 to F′=5 and F=3 to F′=4 transitions respectively.

6. Conclusions

Our results show that the use of spatially overlapping beams tuned to different atomic transitions can allow optical pumping effects to be exploited to enhance signal strength in atomic vapour spectroscopy. The technique also allows the two beams to share the same optical path, thus reducing total system size and component usage, as well as allowing laser stabilisation at a greater range of frequencies than is possible via conventional spectroscopic techniques. In our experimental arrangement, which generates a feedback signal for laser stabilisation to the D2 line of Caesium via laser current modulation and demodulation of the corresponding spectroscopic signal at the same frequency, we found that a single apparatus could perform spectroscopy on two lasers simultaneously,

while also producing a feedback signal that was more sensitive to frequency deviations of either laser than that generated using only one laser.

The technique is likely to be of use wherever space, weight and optical components are at a premium as well as in situations where signal strength and frequency sensitivity are important. This will range from portable devices where reductions in size and weight are important, through to precision lab-based experiments where the accuracy of laser frequency stabilisation is paramount.

Future extensions of this technique could include demodulation of the signal from one photodiode at two different frequencies — corresponding to the two laser current modulation frequencies. This would allow measurement of, for example, dV_1/dF_1 and dV_1/dF_2 from a single photodiode; in the situation considered above dV_1/dF_1 is obtained by demodulation of the signal from one photodiode and dV_2/dF_2 from the other. In principle this could allow for both lasers to be stabilised using only one photodiode, or alternatively the extra information obtained by using two photodiodes, each demodulated at two different frequencies and thus generating four distinct feedback signals, could allow for yet more accurate stabilisation of both lasers. Two-laser forms of modulation transfer spectroscopy [32] should also be possible, allowing this important technique to be exploited through current modulation of either one of the two lasers, avoiding the need for costly electro-optic modulation equipment.

References

[1] Georgescu I 2020 *Nature Reviews Phys.* **2** 396
[2] Sorrentino F *et al.* 2010 *Microgravity science and technology* **22** 551
[3] Herrmann S, Dittus H and Lammerzahl C 2012 *Class. Quantum Grav.* **29** 184003
[4] Bize S, Laurent P, Abgrall M, Marion H, Maksimovic I, Cacciapuoti L, Grünert J, Vian C, Dos Santos F P, Rosenbusch P *et al.* 2005 *J. Phys. B* **38** S449
[5] Bidel Y, Carraz O, Charriere R, Cadoret M, Zahzam N and Bresson A 2013 *Appl. Phys. Lett.* **102** 144107
[6] Menoret V, Vermeulen P, Le Moigne N, Bonvalot S, Bouyer P, Landragin A and Desruelle B 2018 *Scientific Reports* **8** 12300
[7] Fregosi A, Gabbanini C, Gozzini S, Lenci L, Marinelli C and Fioretti A 2020 *Appl. Phys. Lett.* **117** 144102
[8] Kitching J, Knappe S and Donley E 2011 *IEEE sensors journal* **11** 9
[9] Boto E, Holmes N, Legget J, Roberts G, Shah V, Meyer S, Munoz L, Mullinger K, Tierney T, Bestmann S, Barnes G, Bowtell R and Brookes M 2018 *Nature* **555** 657–661
[10] Deans C, Marmugi L and Renzoni F 2020 *Appl. Phys. Lett.* **116** 133501
[11] Tilburg K, Leefer N, Bougas L and Budker D 2015 *Phys. Rev. Lett.* **115** 011802
[12] Raab E, Prentiss M, Cable A, Chu S and Pritchard D E 1987 *Physical Review Letters* **59** 2631
[13] Preston D W 1996 *American Journal of Physics* **64** 1432–1436
[14] Demtröder W 2008 *Laser spectroscopy* (Springer)
[15] Riehle F 2006 *Frequency standards: basics and applications* (John Wiley & Sons)
[16] Hafiz M, Coget G, Clercq E and Boudot R 2016 *Optics Letters* **41** 13
[17] Hafiz M, Brazhnikov D, Coget G, Taichenachev A, Yudin V, Clercq E and Boudot R 2017 *N. J. Phys.* **19** 073028
[18] Brazhnikov D, Ignatovic S, Mesenzova I, Mikhailov A, Boudot R and Skortsov M 2020 *Quantum Electron.* **50** 1015

[19] Zhao M, Jiang X, Fang R, Qiu Y, Ma Z, Han C, Lu B and Lee C 2021 *Applied Optics* **60** 5203
[20] Madkhaly S, Coles L, Morley C, Colquhoun C, Fromhold M, Cooper N and Hackermüller L 2021 *PRX Quantum* **2** 030326
[21] Knight P and Walmsley I 2019 *Quantum Science and Technology* **4** 040502
[22] Bongs K, Boyer V, Cruise M, Freise A, Holynski M, Hughes J, Kaushik A, Lien Y H, Niggebaum A, Perea-Ortiz M *et al.* 2016 The UK national quantum technologies hub in sensors and metrology (keynote paper) *Quantum Optics* vol 9900 (International Society for Optics and Photonics) p 990009
[23] Losev S, Sevostianov D, Vassiliev V and Velishansky V 2015 *Physics Procedia* **71** 242–246
[24] Ji Y, Shang J, Li G, Zhang J and Zhang J 2020 *IEEE Sensors Lett.* **4** 2
[25] Fleischhaur M, Imamoglu A and Marangos J 2005 *Rev. Mod. Phys.* **77**
[26] Cooper N and Freegarde T 2013 *J. Phys. B* **46** 215003
[27] Steck D Alkali D line data *https://steck.us/alkalidata/* (updated 2019, accessed 26/03/2021 14:31) URL `https://steck.us/alkalidata/`
[28] Corwin K, Lu Z, Hand C, Epstein R and Wieman C 1998 *Applied Optics* **37** 3295
[29] Millett-Sikking A, Hughes I G, Tierney P and Cornish S L 2006 *J. Phys. B* **40** 187
[30] Pahwa K, Mudarikwa L and Goldwin J 2012 *Optics Express* **20** 17456
[31] Harris M, Adams C, Cornish S, McLeod I, Tarleton E and Hughes I 2006 *Physical Review A* **73** 062509
[32] McCarron D, King S and Cornish S 2008 *Meas. Sci. Technol.* **19** 10

Acknowledgements

This work was supported by IUK project No.133086 and the EPSRC grants EP/R024111/1 and EP/M013294/1 and by the European Comission grant ErBeStA (no. 800942). The authors thank Bethany Foxon and Igor Lesanovsky for useful discussions.

Additional information

The authors declare the following competing interests: N.C. and L.H. are inventors on UK pending patent application GB 1916446.6 (applicant: University of Nottingham, inventors: Nathan Cooper, Lucia Hackermüller, Laurence Coles) for a miniaturised spectroscopy device in which dual-frequency beam overlap is exploited as an aid to compactness. All data necessary to support the conclusions of this article are given in the article. All further data related to this work are available from the authors upon request.

Supplementary material for: Dual-frequency Doppler-free spectroscopy for simultaneous laser stabilisation in compact atomic physics experiments

Nathan Cooper[1], Somya Madkhaly[1], David Johnson[1], Daniele Baldolini[1] and Lucia Hackermüller[1]

[1]School of Physics and Astronomy, University of Nottingham, University Park, Nottingham, NG7 2RD, UK

E-mail: nathan.cooper@nottingham.ac.uk

August 2021

Abstract. Herein we give the full derivation of the solutions of our rate-equation model of the pumped atomic vapour system. We also provide full details of our method of numerical estimation of second derivatives — the method is not novel or of inherent interest, but the exact details of the estimation method used can affect the final results displayed in figure 4 of the main article, and we therefore provide them for completeness. We briefly review some of the complications that would be involved in constructing a full theoretical model of the system, capable of accurately reproducing experimental results. Though such a model would be complex and unlikely to reveal new fundamental physics, it does have significant practical applications and is intended to be the subject of future research. We present the data from figure 3(a) of the main article on a logarithmic scale, which illustrates how the technique is likely to be even more effective in miniaturised devices that contain only small vapour cells, with a correspondingly lower optical depth. We discuss the likely efficacy of the technique for enhanced frequency-stabilisation of a single laser via the injection of light from an independently stabilised source. Finally, we consider how the technique is likely to be of particular use in experiments involving atomic Lithium.

1. Solution to rate equations

First, we give the expressions for the time derivatives of the remaining atomic state populations:

$$\frac{\mathrm{dE}}{\mathrm{dt}} = (\mathrm{A}-\mathrm{E})\tau_{\mathrm{EA}} I_{\mathrm{EA}} + (\mathrm{B}-\mathrm{E})\tau_{\mathrm{EB}} I_{\mathrm{EB}} - \mathrm{E}\Gamma_{\mathrm{EB}} - \mathrm{E}\Gamma_{\mathrm{EA}}, \tag{1}$$

$$\frac{\mathrm{dD}}{\mathrm{dt}} = (\mathrm{B}-\mathrm{D})\tau_{\mathrm{DB}} I_{\mathrm{DB}} + (\mathrm{A}-\mathrm{D})\tau_{\mathrm{DA}} I_{\mathrm{DA}} - \mathrm{D}\Gamma_{\mathrm{DB}} - \mathrm{D}\Gamma_{\mathrm{DA}}, \tag{2}$$

$$\frac{\mathrm{dC}}{\mathrm{dt}} = (\mathrm{A}-\mathrm{C})\tau_{\mathrm{CA}} I_{\mathrm{CA}} - \mathrm{C}\Gamma_{\mathrm{CA}}, \tag{3}$$

$$\frac{\mathrm{dB}}{\mathrm{dt}} = (\mathrm{F}-\mathrm{B})\tau_{\mathrm{FB}} I_{\mathrm{FB}} + (\mathrm{E}-\mathrm{B})\tau_{\mathrm{EB}} I_{\mathrm{EB}} + (\mathrm{D}-\mathrm{B})\tau_{\mathrm{DB}} I_{\mathrm{DB}} + \mathrm{F}\Gamma_{\mathrm{FB}} + \mathrm{E}\Gamma_{\mathrm{EB}} + \mathrm{D}\Gamma_{\mathrm{DB}}, \tag{4}$$

and

$$\frac{\mathrm{dA}}{\mathrm{dt}} = (\mathrm{E}-\mathrm{A})\tau_{\mathrm{EA}} I_{\mathrm{EA}} + (\mathrm{D}-\mathrm{A})\tau_{\mathrm{DA}} I_{\mathrm{DA}} + (\mathrm{C}-\mathrm{A})\tau_{\mathrm{CA}} I_{\mathrm{CA}} + \mathrm{E}\Gamma_{\mathrm{EA}} + \mathrm{D}\Gamma_{\mathrm{DA}} + \mathrm{C}\Gamma_{\mathrm{CA}}. \tag{5}$$

Then, employing the terms defined in equations (1)-(2) and (4)-(7) of the main article, and setting all time derivatives to zero, as is the case in the steady state, equation (3) of the main text, together with its counterparts above, can then be re-arranged to give

$$F = \frac{B\tau_{FB} I_{FB}}{\gamma_{FB}} = Bk_{FB}, \tag{6}$$

$$E = \frac{A\tau_{EA} I_{EA} + B\tau_{EB} I_{EB}}{\gamma_{EA} + \gamma_{EB}} = Ak_{EA} + Bk_{EB}, \tag{7}$$

$$D = \frac{A\tau_{DA} I_{DA} + B\tau_{DB} I_{DB}}{\gamma_{DA} + \gamma_{DB}} = Ak_{DA} + Bk_{DB}, \tag{8}$$

$$C = \frac{A\tau_{CA} I_{CA}}{\gamma_{CA}} = Bk_{CA}, \tag{9}$$

$$B = \frac{D\gamma_{DB} + E\gamma_{EB} + F\gamma_{FB}}{\tau_{DB} I_{DB} + \tau_{EB} I_{EB} + \tau_{FB} I_{FB}} = \frac{D\gamma_{DB} + E\gamma_{EB} + F\gamma_{FB}}{\zeta_B}, \tag{10}$$

and

$$A = \frac{C\gamma_{CA} + D\gamma_{DA} + E\gamma_{EA}}{\tau_{CA} I_{CA} + \tau_{DA} I_{DA} + \tau_{EA} I_{EA}} = \frac{C\gamma_{CA} + D\gamma_{DA} + E\gamma_{EA}}{\zeta_A}. \tag{11}$$

Substitution of eqns (6) to (8) into (10) then yields

$$B = \frac{\gamma_{DB}(Ak_{DA} + Bk_{DB}) + \gamma_{EB}(Ak_{EA} + Bk_{EB}) + \gamma_{FB} Bk_{FB}}{\zeta_B}. \tag{12}$$

Collecting terms in A and B and dividing through by the coefficient of B, one finds that

$$B = C_1 A. \tag{13}$$

We can now express all other state populations in terms of A. As a final constraint, we impose the condition that the sum over all state population fractions must be equal to 1. Expressing all state populations in terms of A and setting their sum equal to 1 yields equation (8) of the main article. Combining this with equations (6) to (9) and (13) above directly gives all of the steady state population fractions.

2. Numerical estimation of second derivatives

Before gradient estimation is performed, linear interpolation is used to obtain, from our irregularly-spaced raw data points, data corresponding to the fractional absorption of each laser beam at each point on a regular, 2500 × 2500 point grid, running between the minimum and maximum frequencies of each laser. Once this regularised data is obtained, each first derivative is estimated using a symmetric, linear estimation based on the values at grid points ten spaces in either direction of the point in question, such that, for example

$$\left.\frac{dS_1}{dx}\right|_{x,y} \approx \frac{S_1(x+10,y) - S_1(x-10,y)}{20}, \tag{14}$$

where x and y correspond to the indices of the grid points, such that dS_1/dF_{cooler} etc. are ultimately found by multiplying the corresponding dS_1/dx values by the frequency spacing between points on the corresponding axis. Equivalent expressions clearly exist for the three remaining first derivatives.

The calculated first derivatives are saved as arrays. This enables the corresponding second derivatives to be calculated, from the first derivative estimates, using exactly the method shown above.

This is a simplistic and un-optimised method of numerical derivative estimation, and more advanced techniques are certainly available. However, it was intentionally chosen in order to more accurately simulate the kind of low-complexity calculation that is likely to be performed in real time by experimental hardware, and to therefore better reflect a realistic implementation of our technique in an actual technological application. The use of more advanced gradient estimation techniques, potentially with a lower susceptibility to experimental noise, would likely improve upon the results given here but might overestimate the performance of the technique in realistic experimental implementations.

3. Complications of a full, theoretical model

In addition to requiring a quantum master-equation approach to achieve high accuracy under all conditions [1], such a model would have to include a full analysis of transient, non-equilibrium effects in atoms that traverse the (spatially non-uniform) laser beam, integrated over all possible traversal speeds and trajectories in the thermal atomic vapour. It would also need to allow for the fact that the approximations typically made when analysing saturated absorption spectroscopy — that the 'probe' beam is weak and the 'pump' beam is strong [1, 2, 3] — are not valid in this system. It would have to correctly handle the attenuation of the laser light as it passes through the atomic vapour, including the fact that the returning beam's intensity will depend on the attenuation of the outward beam, which in turn depends on the return beam's properties. The lifetime of the hyperfine states of the $6S_{1/2}$ manifold against collisional redistribution can not be neglected, even for atoms that leave the beam and might return to it later, necessitating

an in-depth analysis of both interatomic collisions and collisions with the walls of the cell. All of the above effects can have non-negligible consequences for our results, and the authors do not believe the omission of any to be a good approximation in realistic systems of this kind. In short, the complexity of a model capable of providing accurate quantitative agreement with our results is very high, and since such a model is not necessary to support our conclusions or elucidate the underlying principles we leave it for future work.

4. Application within small vapour cells in miniaturised devices

Figure 3(a) of the main article was taken using a 75 mm long vapour cell. This size of cell is typical of existing, lab-based experiments but is not plausible in the next generation of miniaturised technologies for use outside the lab, or for spectroscopic devices that require a high spatial resolution. A smaller cell necessarily leads, for a given vapour pressure, to a lower 2D (projected) atom density and thus to a lower optical depth for laser beams passing through the cell. In addition, the experiment for which we give results was performed with Cs atoms, which have the highest vapour pressure of any commonly-used alkali metal species at 298 K.

As a result of the high total optical absorption in our experiment, our results — in particular figure 2(a) — do not make the degree of enhancement of the optical absorption via the use of dual-frequency spectroscopy immediately obvious. In order to see how large an enhancement of the spectroscopic signal is likely to be possible when using a lower total optical depth, it is necessary to view the results in logarithmic space, thus illustrating the strength of the response per unit of atomic density. Supplementary figure 1 (below) shows the same results as given in figure 2(a) of the main article, but plotted on a logarithmic scale. Here, the degree of benefit offered by this technique in portable devices with small vapour cells, or in any other situation with reduced total optical depth, is clearly evident.

5. Spectroscopy with injected light from an independently stabilised laser

In the main article, we focussed on the more common experimental scenario of wanting to frequency-stabilise two lasers simultaneously. However, here we consider the possibility — which may be of use in certain applications — of using injected light from an independently stabilised laser to enhance the spectroscopic stabilisation signal for a second laser.

In this case the SLSF is determined by two factors: the sensitivity of the spectroscopic feedback signal to changes in the frequency of the target laser about its 'lock point' (the frequency at which it is stabilised), and the scale of unwanted shifts in the lock point of the target laser that will result from changes in the frequency of the injected light. Since there is no reason for these two sources of instability to be correlated they can be added in quadrature when determining the likely magnitude of

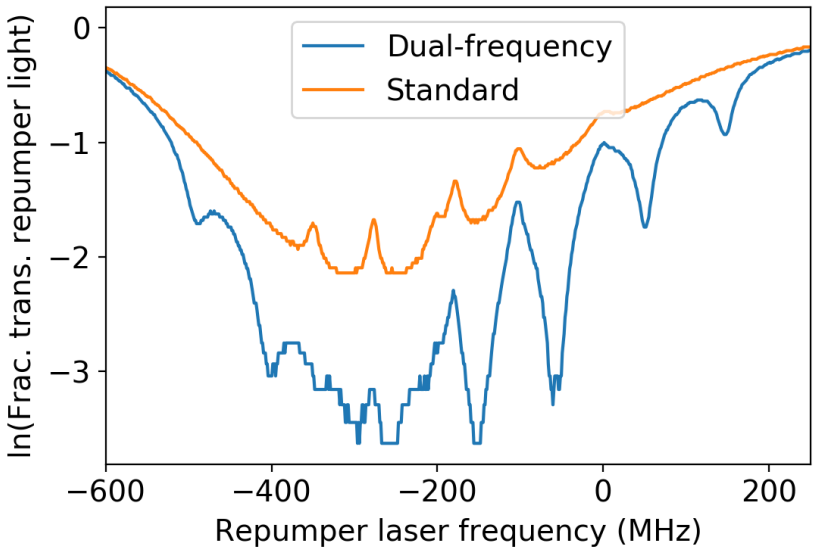

Figure 1. Natural logarithm of the spectroscopy signal from "Photodiode Repumper" (see figure 2(a) of main article) while light from the cooler laser, tuned 365 MHz below the $F = 4 \rightarrow F' = 5$ transition, is also present in the cell (blue line). For reference, a standard saturated absorption spectroscopy signal from the same apparatus (taken by blocking the light from the cooler laser) is also shown (orange line). Repumper laser frequency is given relative to the F=3→F′=4 transition.

the laser's frequency deviations from its desired value.

If we assume that the injected laser is stabilised using standard saturated absorption spectroscopy we can label the likely scale of its frequency deviations from its setpoint as δF_0. Locking based on saturated absorption spectroscopy and current modulation generates a response signal S approximately proportional to the rate of change of the saturated absorption signal voltage with laser frequency:

$$S \approx C\frac{dV}{dF}, \tag{15}$$

where C is a system-specific proportionality constant, F is the laser frequency and V is the output voltage of the photodiode following the spectroscopy apparatus, normalised against its maximum value when the laser light is far off resonance and there is negligible absorption in the atomic vapour. The parameter of interest — the sensitivity of the response signal to changes in laser frequency — is therefore given by

$$\frac{dS}{dF} \approx C\frac{d^2V}{dF^2}. \tag{16}$$

To compare the efficacy of dual-laser spectroscopy to standard saturated absorption spectroscopy, we therefore compare the maximum values of d^2V/dF^2 measured with and without the second beam present in the vapour cell, defining the ratio between them as R. This ratio reaches values >3 for our experimental data. However, we must also take into account the effects of deviations in the injected light's frequency, giving

$$\delta F \approx \sqrt{(\delta F_0 R)^2 + (\delta F_0 Q)^2}, \tag{17}$$

where Q is defined by

$$Q = \frac{d^2V}{dF\ dF_{\text{injected}}} \Big/ \frac{d^2V}{dF^2}\ , \tag{18}$$

and we have assumed that the two different contributions to laser frequency variation — deviation from the lock point and lock-point mobility arising from variations of the injected laser frequency — are independent and can be added in quadrature. The derivatives of photodiode voltage with respect to F in (18) are assumed to be evaluated at the chosen lock point and in the presence of the injected beam. We denote our figure of merit, the SLSF, by $E = \delta F_0/\delta F$. Figure 2 shows a colour plot of the experimentally derived values of the SLSF for the repumper laser with cooler light injection, as a function of both laser frequencies. Note that the experimentally derived SLSF value requires numerical estimation of local gradient functions, and that the exact method by which these are calculated can have some influence on the result — see §2 above for more details. It can be seen that there are numerous regions in the plane where $E > 1$, with the maximum value of E equal to 2.26. This demonstrates the clear advantages of the technique in terms of laser stability.

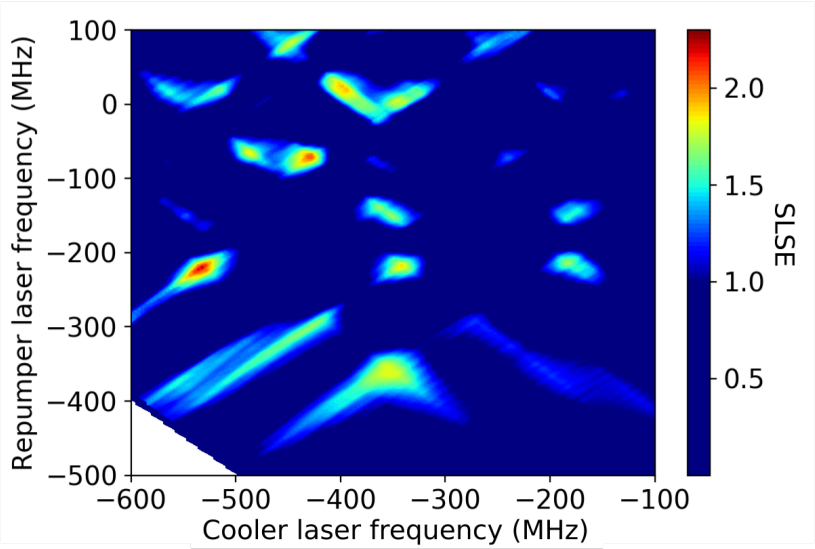

Figure 2. Signal-limited stability enhancement (SLSF — see main text for full definition) resulting from laser frequency stabilisation based on dual-frequency spectroscopy of the repumper laser, with injected light independently stabilised close to resonance with the cooler transition, compared to the maximum achievable using conventional saturated absorption spectroscopy. The SLSF is plotted as a function of both laser frequencies. Frequencies for the cooler and repumper lasers are given relative to the F=4 to F′=5 and F=3 to F′=4 transitions respectively. The results clearly show the potential advantages of this form of spectroscopy.

6. Trapping and cooling Lithium atoms: an important application area

The technique may prove particularly useful for spectroscopy of atomic Lithium. Lithium reacts chemically with most standard glasses, meaning that vapour cells for Lithium are typically much larger and more costly than those for other alkali metals; the benefit of using only one vapour cell to stabilise two lasers is correspondingly enhanced. Furthermore, the absence of a 'cycling transition' in atomic Lithium, brought about by the small energy separation of the hyperfine states of the upper manifold of the D2 line, suggests that the benefits of avoiding optical pumping to dark states may be further enhanced for Lithium spectroscopy.

References

[1] Haroche S and Hartmann F 1972 *Phys. Rev. A* **6**
[2] Preston D W 1996 *American Journal of Physics* **64** 1432–1436
[3] Lindvall T and Tittonen I 2007 *J. Mod. Optics* **54** 2779

Chapter 8

Summary, conclusion and outlook

This thesis has reported the design, construction and characterisation of an AM experimental apparatus capable of producing MOT that captures approximately 2×10^8 of ^{85}Rb atoms. Additive manufacturing has several advantages over traditional machining, and this technique was exploited in our setup to realise the first cold atom system built of 3D-printed components. The AM device was developed in the pursuit of cold atom-based sensors with the SWAP characteristics required for deployment and operation outside the walls of laboratories. With a footprint of $550\,\text{mm}\times600\,\text{mm}\times450\,\text{mm}$, a volume of $0.15\,\text{m}^3$, and a weight of $3.2\,\text{kg}$, excluding the commercial components, the setup was shown to have comparable quality of performance to conventional setups. Our method of utilising the approach of AM in cold atom sensors is believed to be of great interest to a broad range of researchers in the atomic, molecular, and optical physics research community.

Further experiments and techniques used in the AM system, which were not addressed in the chapters based on published works, are covered in Chapter 3. A closer overview of the setup was given in this chapter, together with a brief discussion about the techniques and methods used to operate the device and conduct the MOT experiments, such as laser frequency stabilisation, cre-

ating MOTs, characterising the atomic clouds, and the methods of estimating the UHV background pressure in terms of parameters of atomic collisions.

The successful, first-of-its-kind UHV chamber manufactured purely via AM was presented in Chapter 4. The chamber, which is one-third the weight of industrial equivalents, is believed to have a potential great impact on the fields of cold atoms, UHV, and AM manufacturing. The pressure measured in the chamber reaches below 10^{-10} mbar, which is far below the lowest pressure that any AM UHV chamber has previously attained. It was analytically shown that the surface oxides generated from the AM process, in fact, enhanced the vacuum quality.

Chapter 5 presented the compact, lightweight and optimised cold atom apparatus and discussed the rest of the 3D-printed components, such as the CSPD optical framework, laser mounts, and lens tubes holders, in detail. It was demonstrated that the approach of additive manufacturing along with optimisation algorithms significantly enables both substantial weight reduction and stability enhancement, as well as customisability and rapid prototyping. It was also shown in the chapter that the AM experimental components are robust and capable of creating dense magneto-optical traps of rubidium atoms. The methods and considerations discussed in this chapter are transferable and applicable to a wide range of other areas of experimental research, most notably cold atoms, quantum optics, UHV environments, and the generation of tailored magnetic fields.

A triple frequency spectroscopy apparatus based on AM was introduced in Chapter 6. The apparatus is economical, occupies almost only hand-size, and can lock three laser frequencies at once. By subjecting the device to a varying thermal environment and severe mechanical vibrations of frequencies up to tens of kilohertz, it was proven that the apparatus has unprecedented durability and stability by remaining capable of locking the laser frequency over the course of the tests. The techniques used in this apparatus are also transferable to different setups and configurations inside and outside the lab

environment. More stability results of the 3D-printed optical components are presented in Appendix D.

Chapter 7 discussed dual-frequency Doppler-free spectroscopy of two counter-propagating laser beams passing through the same atomic vapour cell. The advantages of this dual spectroscopy technique over standard spectroscopy in terms of enhancing laser frequency stabilisation have been demonstrated theoretically and experimentally. The chapter also shows how this approach can be used in compact systems to further reduce system's SWAP.

8.1 Outlook

This is the first cold atom device of its kind that has been developed. To the best of our knowledge, there is yet no integrated cold atom device based mostly on 3D-printed elements in the literature. The experiments and results introduced in this thesis (and the resulting papers) are therefore the only proof that verifies the efficiency of the device so far. Accordingly, it will be desirable to do more experiments with it in order to increase the reliability and credibility of the design.

For our system to be upgraded to a portable sensor, however, additional functions and performance improvements must be implemented while meeting the requirements for the operation of atomic systems in changing and harsh environments. To further optimise the system's SWAP, the device footprint can be reduced by eliminating the heavy metallic and commercial mounts used in the current layout, in order to achieve a weight comparable to the compact systems highlighted in references [14, 33, 34, 39], for example.

The fibre coupling was one of the difficulties encountered when installing the setup's sub-parts, as the initial plan was to glue the fibres outcouplers into the CSPD framework. The MOT beams were walked from the CSPD outputs into the fibres using commercial mounts to temporarily attach the outcouplers into the framework. Once sufficient coupling efficiencies were attained, the outcouplers were glued into the CSPD body. However, the drying process of

the adhesive and the removal of the mounts both caused mechanical shifts in the outcouplers, resulting in a significant reduction in the coupling efficiencies. This issue was persistent regardless of how cautiously the process was conducted, and thus Thorlabs kinematic mounts were introduced as a temporary solution. It is, however, crucial to find a way to eliminate these relatively bulky mounts in order to achieve greater compactness of the setup.

There are a number of experiments and side projects that were scheduled to be carried out using the apparatus, but the circumstances of the time constraints and the COVID-19 pandemic prevented them. Among these is the further development of the compact system to include compact electronics for efficient laser frequency stabilisation, which is why the development of the Arduino-based cards should be a priority. The laser locking PCBs (see figures C.3 and C.4 in Appendix C) have shown adequate performance by functioning according to the working principle according to which they were made, but some problems have arisen that compromise the quality of the lock. One example of the problems involved is the existence of a digitisation 'quantisation' noise in the feedback error signal used to modulate the laser frequency. This noise was found to be caused by the Arduino UNO being very slow compared to analog and fast components, such as the laser's frequency. Therefore, to improve the setup, these PCBs must be upgraded with faster microcontrollers in the near future, and the locking performance under unstable conditions must be quantified.

By capturing MOT loading curves on a photodiode, the MOT properties in the experiments of this thesis were determined. However, when information about the cloud density and temperature is required, this method is inadequate; and thus other methods, such as absorption imaging, are desirable. In Sec. 3.3.1, absorption imaging installed within the AM system was briefly described, and cloud absorption images taken to test the performance of the imaging setup were presented. As was also mentioned, the imaging setup was never used to characterise the MOTs again afterward. If it is intended to take

measurements of the atomic cloud and gather further information that cannot be obtained using the loading curves technique, it would be desirable to have an absorption imaging device permanently installed within the setup.

Certain cold and ultracold atom experiments require modulation of the magnetic field, which is not possible with the permanent magnets currently used in the setup. A pair of MOT anti-Helmholtz coils for the AM UHV chamber was constructed, and the resulting axial magnetic gradient was measured; see Appendix B for more details. These coils were less suitable for the purpose of creating a low SWAP system and thus were not installed in the main setup, as they are heavy and drain an excessive amount of power. Nevertheless, conventional coils would be preferable if the setup is to be used for other experiments that require manipulating the magnetic field.

Cold atom experiments are extremely complex and necessitate a high level of precision and care. Currently, all parts of the system are manually controlled, with the exception of the Arduino-based laser frequency lock cards that allow for the programmatic control of certain parameters. Thus, a robust analog-to-digital software control system that drives, monitors, and synchronises the experiment's components and variables with microsecond precision is desirable for future experiments for obtaining the best results. And perhaps the COVID-19 pandemic, which paralysed daily life and forced laboratories to close for several months, taught us that system automation is critical.

More background pressure measurements will be of interest given that the material of our UHV chamber is unprecedented, and also to make the device more compact. The measurements reported in Sec. 3.4 of background pressure indicate that the heavy pressure gauge can be replaced by using the cold atomic cloud itself as a pressure gauge. However, there was a discrepancy between the pressure gauge readings and the pressure values reported using the loading curves method; therefore, additional research on this subject is needed. This variation is not attributed to a flaw in our system, as such inconsistency has been reported in the literature that has used this approach. Additionally, the

pressure results obtained using this method are highly dependent on the MOT parameters such as cloud density, light intensity and alignment, laser detuning, loading time, and so on. Therefore, taking the pressure measurements with fixed and controlled experimental parameters will reduce the discrepancy and enable more consistent results to be obtained.

In conclusion, the device consists of several AM components, including the vacuum chamber, optical system, and mechanical mounts. Since these parts are transferable, they can be used separately or together in various systems. As a result, and based on the results presented in this thesis, it can be confirmed that these parts are robust and function in lab environments as effectively as traditional alternatives. Nevertheless, the system as a whole and integrated structure in its current form shown in Fig. 3.1 and explained in Chapter 5 cannot be deemed ready for use in portable quantum devices until a number of obstacles to its operation in external environments are resolved. These issues are, fortunately, identified and addressed in the previous paragraphs. The most important of these are the improvement of the system's SWAP to a form comparable to the many successful existing mobile quantum devices explored in Chapter 1, as well as other challenges related to the automation and control system. All in all, by determining the future goal for which the device is to be used and employed, for instance, the work on these issues can be prioritised and planned.

Appendix A

Sub-Doppler cooling of ^{6}Li

This appendix shows the work that was performed for the lithium BEC experiment.

The name Doppler cooling refers to the Doppler effect, which sets a limit on the lowest temperature achievable by two-level atoms in optical molasses. When atoms undergo counter-propagating laser beams with frequencies different than the atomic resonance frequency, their velocities, and hence, their momenta, randomly change. The variance in atomic velocities results in an increase in the temperature of the atomic sample, preventing it from reaching temperatures below the Doppler temperature limit. Thus, sup-Doppler cooling techniques such as Sisyphus cooling, or Gray molasses cooling are required to further cool the atoms.

As explained in Sec. 2.2, the MOT temperature is limited by the Doppler limit, which is generally difficult to reach for lithium atoms. Due to the extremely narrow excited state structure of the $P_{3/2}$ level of ^{6}Li (in comparison to the linewidth Γ), efficient Doppler cooling is not possible. The minimum temperature of a ^{6}Li MOT achieved in the lab was $\sim$300μK and the numerical Doppler temperature of ^{6}Li is 141μK. Thus, it is needed to implement

an additional sub-Doppler cooling setup in order to allow for reaching lower temperatures after the MOT and molasses stage. Implementing this setup was my task during the first year of my PhD.

Sisyphus cooling

When two linearly polarised beams with polarisation axes perpendicular to each other are used in laser cooling, Sisyphus cooling occurs. In this case, the polarisation of the resulting light field varies in space over half a wavelength, as illustrated with red arrows in Fig. A.1. The polarisation of the light oscillates between π to σ^+ and π to σ^- over every $\lambda/2$. These steep polarisation changes cause the m_J states of the fine-structure levels in alkali atoms to shift up and down, depending on the polarisation state.

To explain this cooling mechanism, consider a two-level atom radiated by two counter-propagating laser beams with orthogonal linear polarisations travelling in one dimension. Consider the atom with a transition from $J = 1/2$ to $J = 3/2$, as shown in Fig. A.2. The ground state population is pumped to the $m_g = +1/2$ sub-level in regions that are purely σ^+, and similarly, the ground state population is pumped to the $m_g = -1/2$ sub-level in purely σ^- regions. Also at regions of linearly polarised light Lin, the states are equally shifted. The atoms in this arrangement of polarisation shift their ground state populations from $m_g = -1/2$ to $m_g = +1/2$ recurringly over a period of $\frac{\lambda}{2}$ of the driving field. That is, the most strongly light-shifted states are reached by the atoms, i.e. the atoms are pumped to states of the highest energy levels.

Now, an atom travelling at the right velocity v will experience a friction effect because it takes a finite amount of time τ for transitions between the ground states. This occurs when an atom moves along z-direction from the σ^- region at the potential valley with a velocity where the $z = \frac{\lambda}{8}$ (see Fig. A.2)-(b) with velocity $v = (\lambda/4)/\tau$ towards σ^+ region at $\lambda/4$. We notice then that the

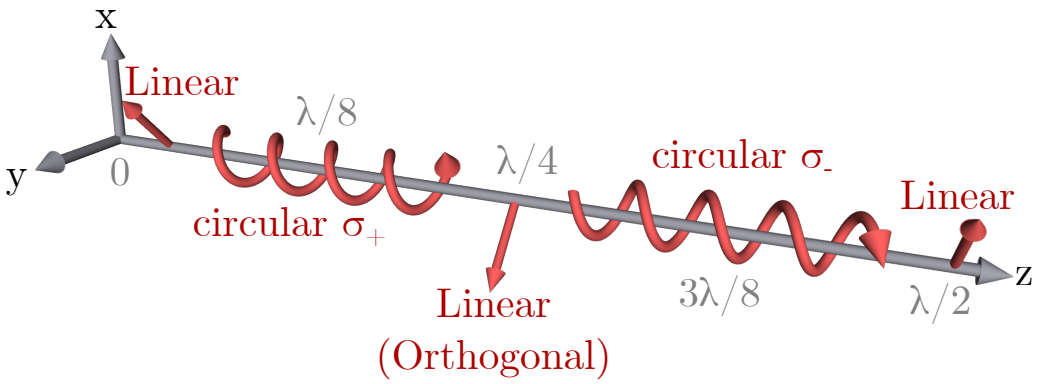

Figure A.1: *Starting at 0 position, the polarisation gradient seen by the atom in a 1D optical molasses with linear orthogonally polarised beams.*

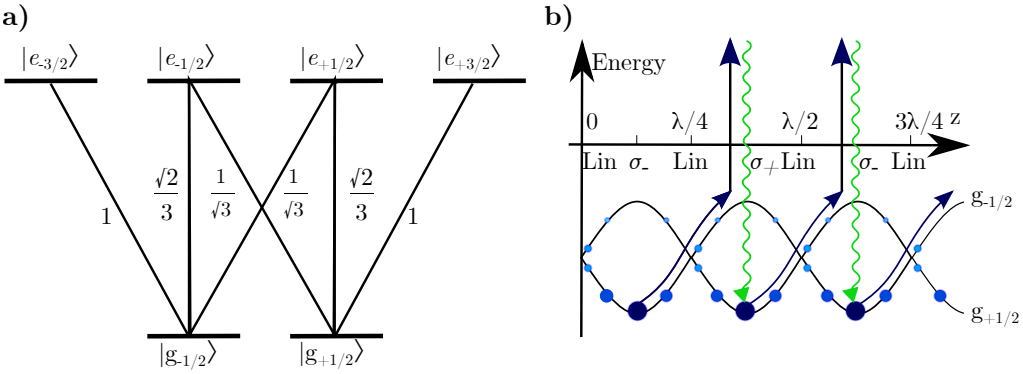

Figure A.2: *The Sisyphus effect in the Lin⊥Lin polarisation gradient configuration adapted from Ref. [132]. (a) The atomic level scheme and Clebsh-Gordan coefficients for a $J_g = 1/2 \rightarrow J_e = 3/2$ transition. (b) The potential shift of the ground state of an atom propagating in two orthogonally polarised beams configuration and steady state populations. The lowest energy state is always the more populated one.*

atom will reach the top hill of the ground state potential and pump to the next excited sublevels and comes back again, and optically pumps again to the next ground sublevel $\frac{3\lambda}{8}$.

Because the ascension takes a length of time τ, the atom is pushed into the other ground state as soon as it reaches the zenith. The other ground state, $\lambda/4$, is at the bottom of a new potential well, which the atom climbs out of before being pumped back to the original state, where the process repeats. The atom converts some of its kinetic energy into potential energy while ascending the potential hills; this energy is then radiated away as the atom decays spontaneously. Because the released photons have a greater frequency than the absorbed photons, the energy is dissipated.

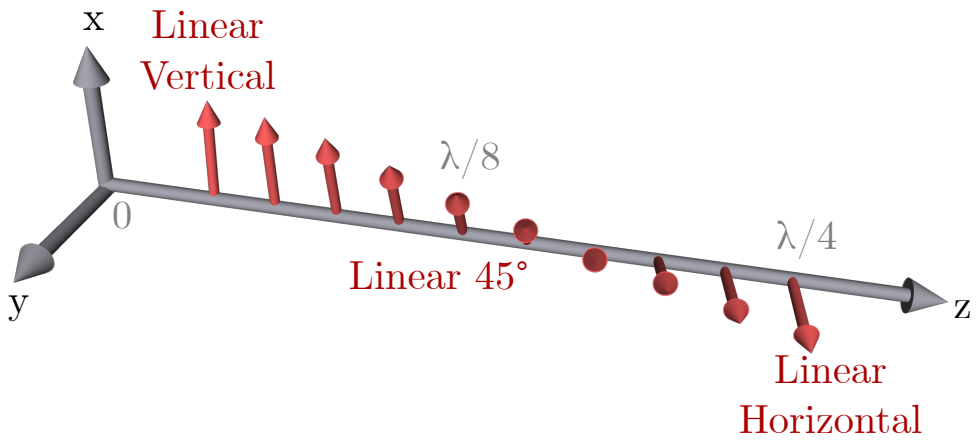

Figure A.3: *Starting at 0 position, the polarisation gradient seen by the atom in a 1D optical molasses with oppositely circular polarised beams.*

The polarisation gradient

There is no chance of a Sisyphus effect in $\sigma^+ - \sigma^-$ configuration since the ground state sublevels are not spatially modulated like they are in Lin⊥Lin configuration. Rather than that, in $\sigma^+ - \sigma^-$, the atomic motion in the light field perturbs the distribution of ground state sublevel populations, resulting in an imbalance in the radiation pressures exerted by the two counter-propagating laser beams. This cooling force was first described by Dalibard and Cohen-

Tannoudji in their key paper [150]. The two lasers in this configuration have opposite circular polarisations; however, the laser polarisation remains linear and rotates around $\hat{e}$ along the z-direction in a helix form with pitch λ (see Fig. A.3).

^{6}Li D_1 grey molasses

Using so-called D_1 grey molasses cooling, lithium atoms can be cooled to significantly lower temperatures. Figure A.4 shows the hyperfine structure energy levels of ^{6}Li D_1 line. The molasses scheme includes cooling on the ^{6}Li D_1 transition $2^2S_{1/2}, F_g = 3/2 \rightarrow 2^2P_{1/2}, F_e = 3/2$ and repumping on the $2^2S_{1/2}, F_g = 1/2 \rightarrow 2^2P_{1/2}, F_e = 1/2$ transition.

There were some attempts by former lab members [151, 152] to implement a ^{6}Li D_1-line setup, but the project was stalled for some reasons. Some issues delayed achieving the goal, like limited laser power, the high cost of advanced light sources and optical elements, and the restricted area for constructing a D_1-line beam path on the same optical bench where the Li oven is located.

The first step to do was to test Thorlabs laser diode (HL6545MG) which emits light of 660 nm and output power of ∼60 mW at room temperature, and up to 690.992 nm and ∼100 mW at ∼75°C temperature. The struggle with this laser diode was to find a stable and inexpensive temperature controller that can heat up the laser diode without showing any fluctuations, which unfortunately could not be achieved with the available parts in the lab.

The light source used was a homebuilt external cavity diode laser 'ECDL', constructed using an (eagleyard, AD-0618) laser diode. The laser emits a beam at wavelength of 690.992 nm and has a total output power of ∼45 mW after the optical isolator. The optical setup was built (see Fig. A.5) on the main optics table of ^{6}Li to let the D_1 and D_2 beams travel along the same path to

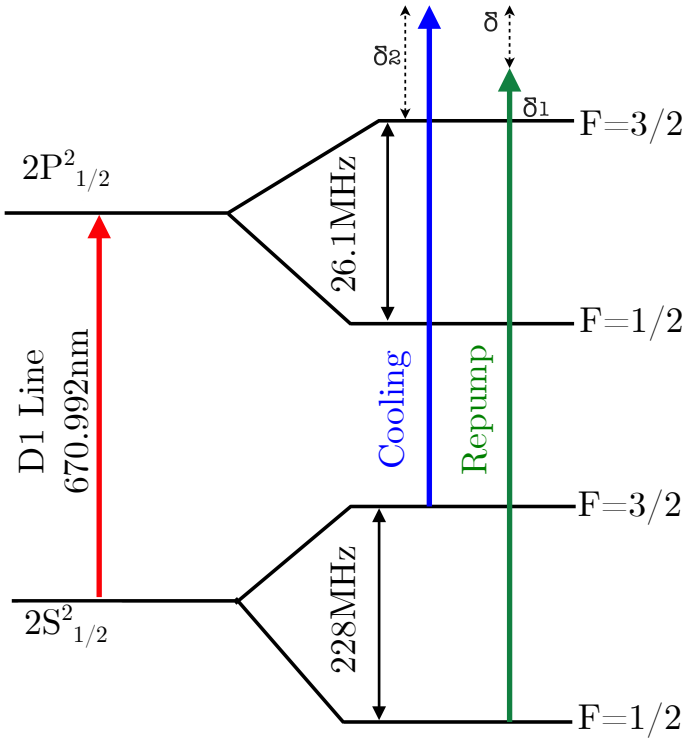

Figure A.4: *Atomic energy levels of* ^{6}*Li D1 line transition. The corresponding spectroscopic Doppler-free saturated absorption spectroscopy of this transition is shown in Fig. A.6.*

the MOT experiment. The saturated absorption spectroscopy signal of ^{6}Li D_1 line was successfully obtained, as shown in Fig. A.6, and the laser was locked using a PID card.

Because of other simpler methods to increase the atom number in the lithium system, this setup change was not implemented.

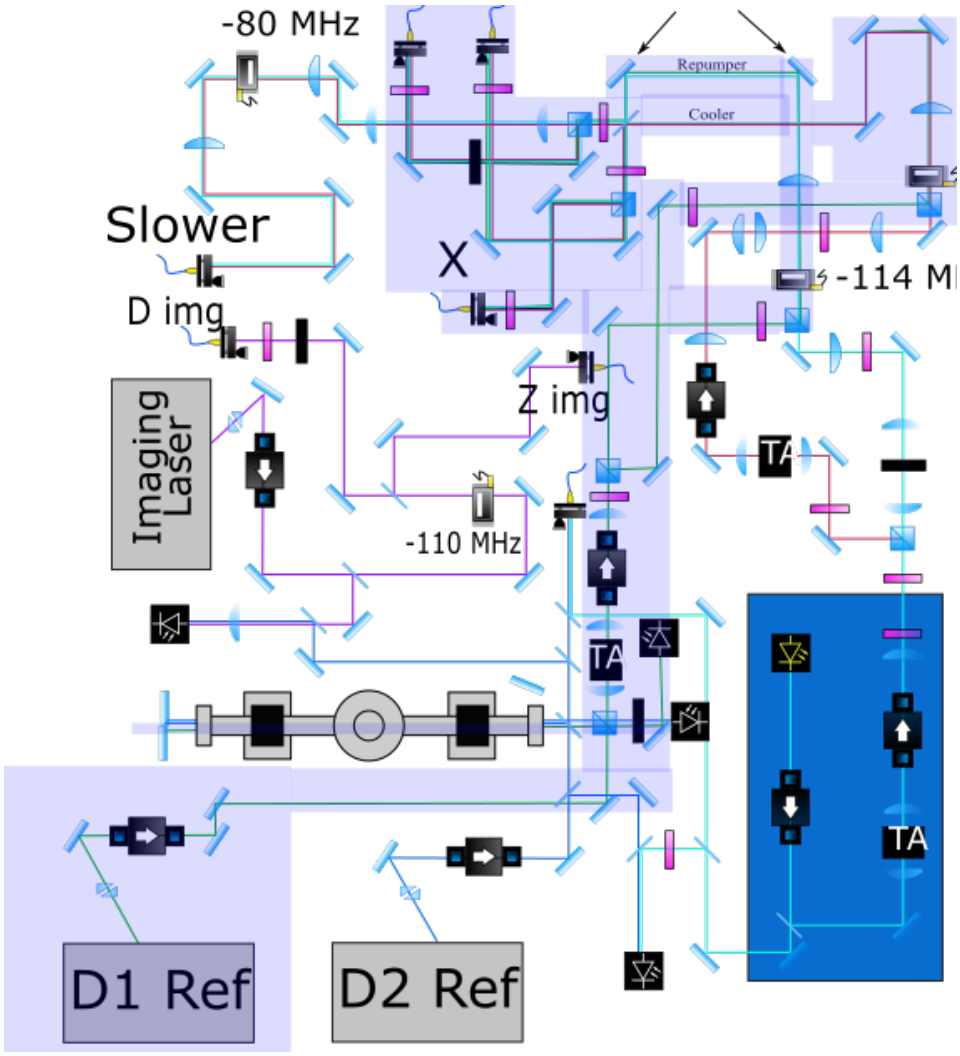

Figure A.5: *Schematic of the optical table of ^6Li. The D_1 line setup including optical components and the beam path are illustrated in the shaded area.*

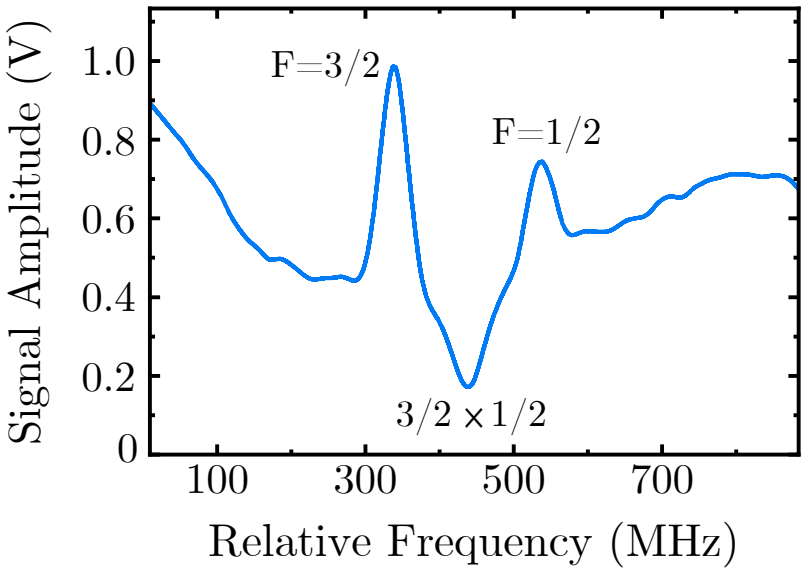

Figure A.6: *Doppler-free saturated absorption spectroscopy feature of D_1 line of ^6Li.*

Appendix B

Coils of UHV chamber

The magnetic field in our device is generated by two rings made up of arrays of permanent magnets that create a constant magnetic field in an anti-Helmholtz configuration. These rings were discussed previously in chapter 5. However, some cold atom experiments necessitate switching the magnetic field on and off, and thus a pair of standard MOT coils were made in order to enable using the AM apparatus in future experiments. Although the coils have not yet been installed in the outer flanges of the chamber or utilised in any experiments, they have been tested for compatibility with our system.

Prior to winding the coils, the magnetic field required for the MOT was numerically calculated to match the chamber's geometric dimensions and specifications. The coils have 50 mm inner diameter and they are separated by a 50 mm distance. Figure B.1 shows the simulated magnetic fields for a range of current values. After that, the coils were manually wound with 30 windings per coil, using a copper tape with a height of 20 mm and a thickness of 1 mm. The magnetic field probe was then mounted on a translation stage to measure the axial magnetic field by moving it steadily towards the centre of the coils, as shown in Fig. B.2. The resulting magnetic field of the experiment and the corresponding simulated curve are shown in Fig. B.3.

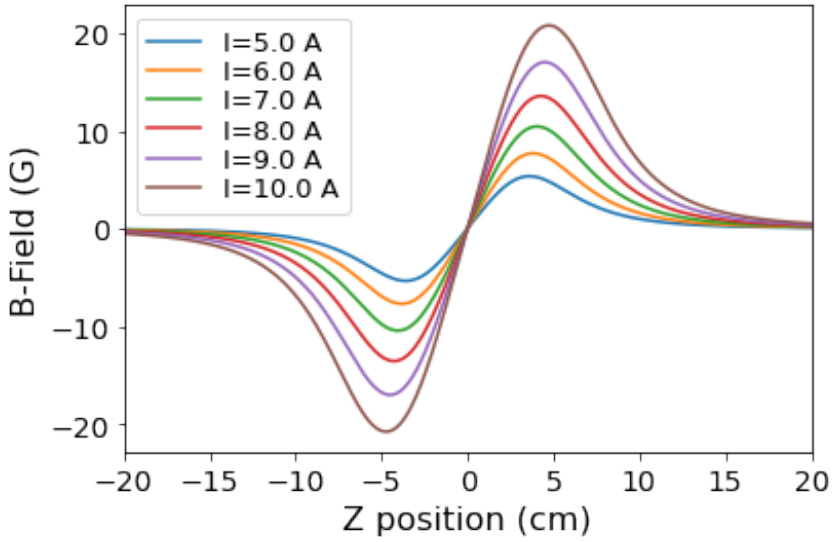

Figure B.1: *Axial magnetic fields simulated for the AM chamber's MOT coils over a range of currents.*

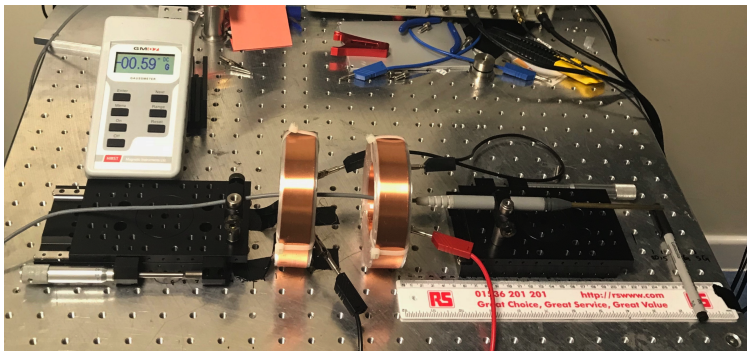

Figure B.2: *Experimental setup of the axial magnetic field measurements of the MOT anti-Helmholtz coils.*

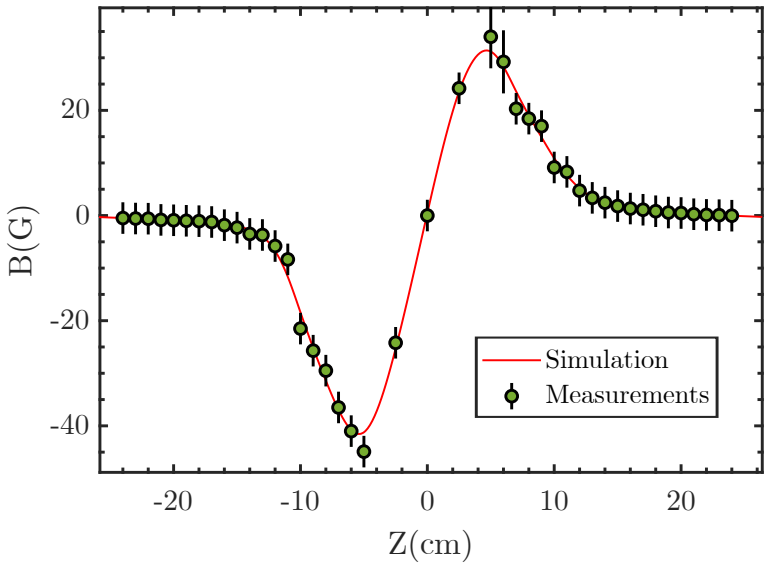

Figure B.3: *Experimental data points of measured axial magnetic field obtained via applying a current of ∼10 A to anti-Helmholtz coils using the setup shown in Fig. B.2. The errors associated with the data points arise from the uncertainty in the perfect alignment of the gaussmeter used in the measurements.*

Appendix C

Mechanical and electronic parts and drawings

This appendix contains all the drawings I made of different parts of the AM-based device. Please note that all components are designed by members of Additive Scientific Ltd., but I helped draw them for the purpose of publications and displaying.

AM parts

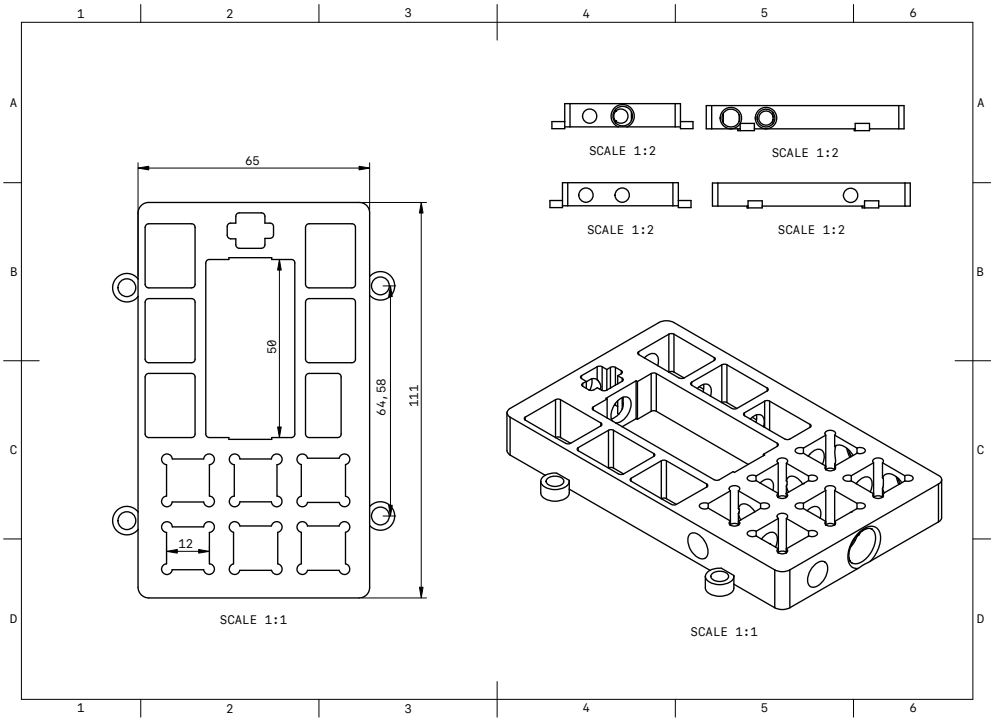

Figure C.1: *Triple frequency AM-based optical framework.*

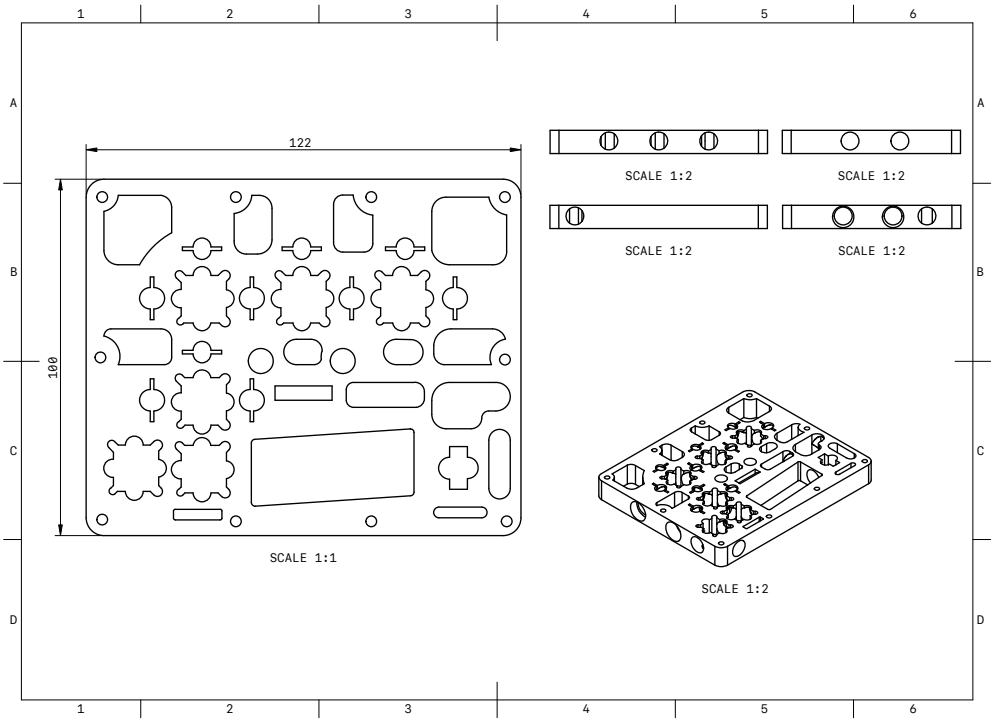

Figure C.2: *Compact spectroscopy and power distribution AM framework.*

Laser Frequency Stabilising PCBs

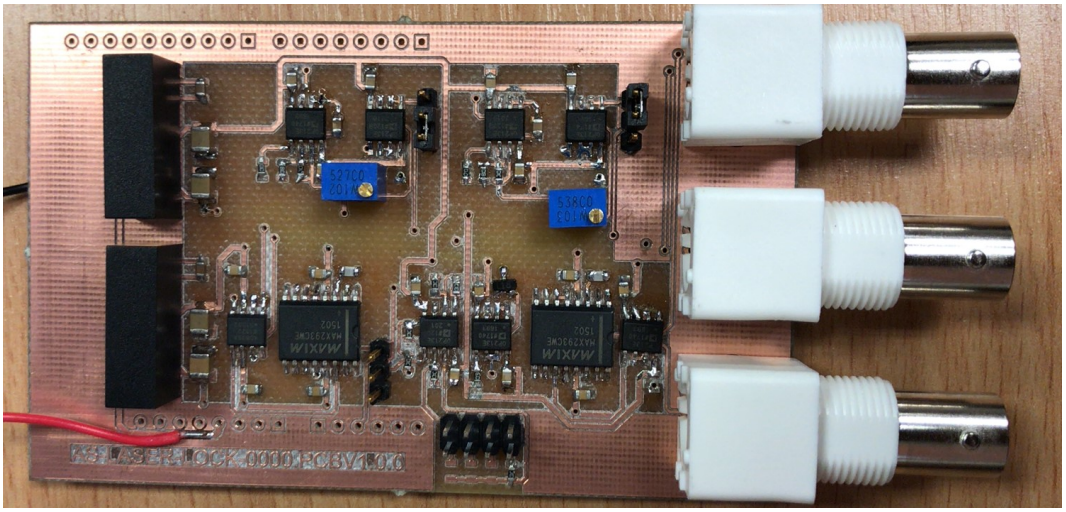

Figure C.3: *Real image of the Arduino-based printed circuit board for stabilising one laser frequency.*

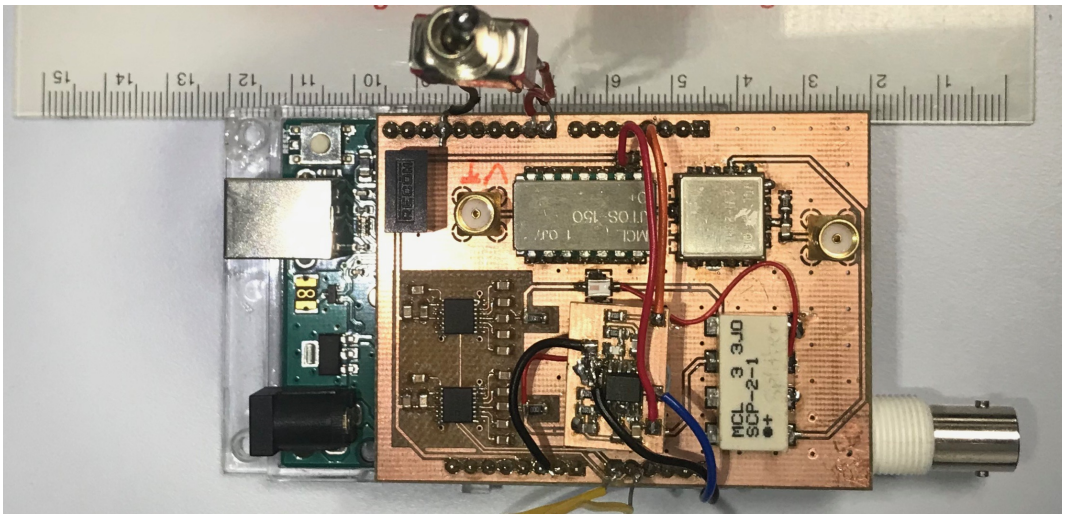

Figure C.4: *Real image of the offset lock printed circuit board for stabilising one laser relative to another frequency.*

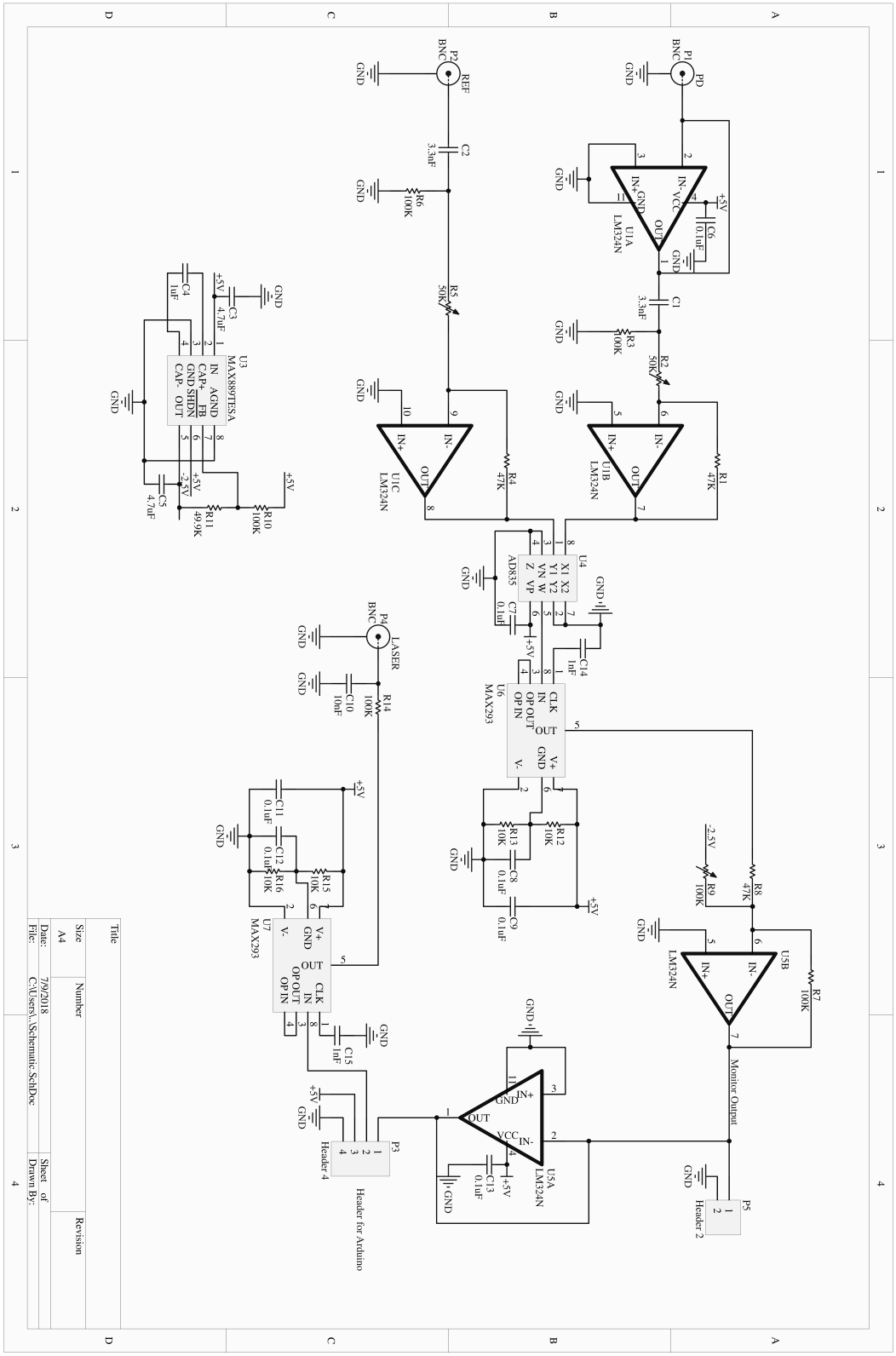

Figure C.5: *Circuit diagram of the Arduino-based laser locking card, made via Altium Designer software.*

Appendix D

Additional information on system's stability

Further results to show the superior stability of the AM system are provided in this appendix.

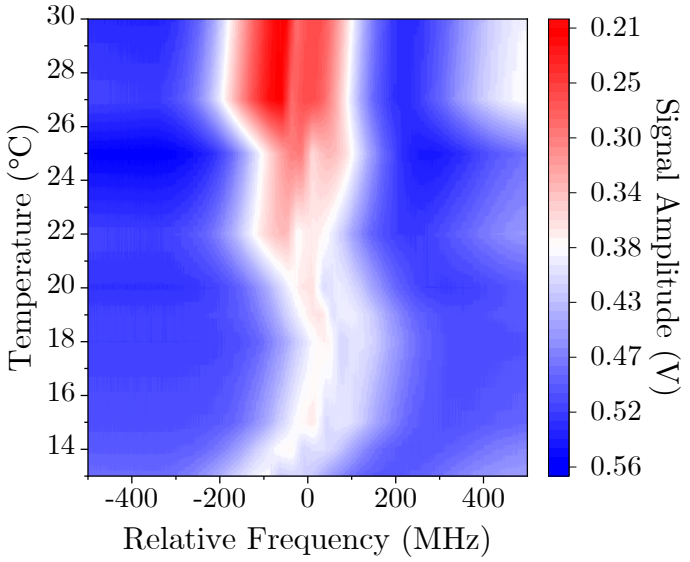

Figure D.1: *A contour plot of the AM compact spectroscopy apparatus response to temperature changes presented in chapter 5 as a function of the signal amplitude on the photodiode. The redder areas represent the increase in amplitudes as the temperatures increase. The x-axis represents the frequency of the atomic transition relative to* ^{85}*Rb F=3→F=4 transition. It is clear from the small deviation in the relative frequencies that the temperature fluctuations barely affect the quality of the laser locking, as the laser remains in the required frequency range throughout the experiment.*

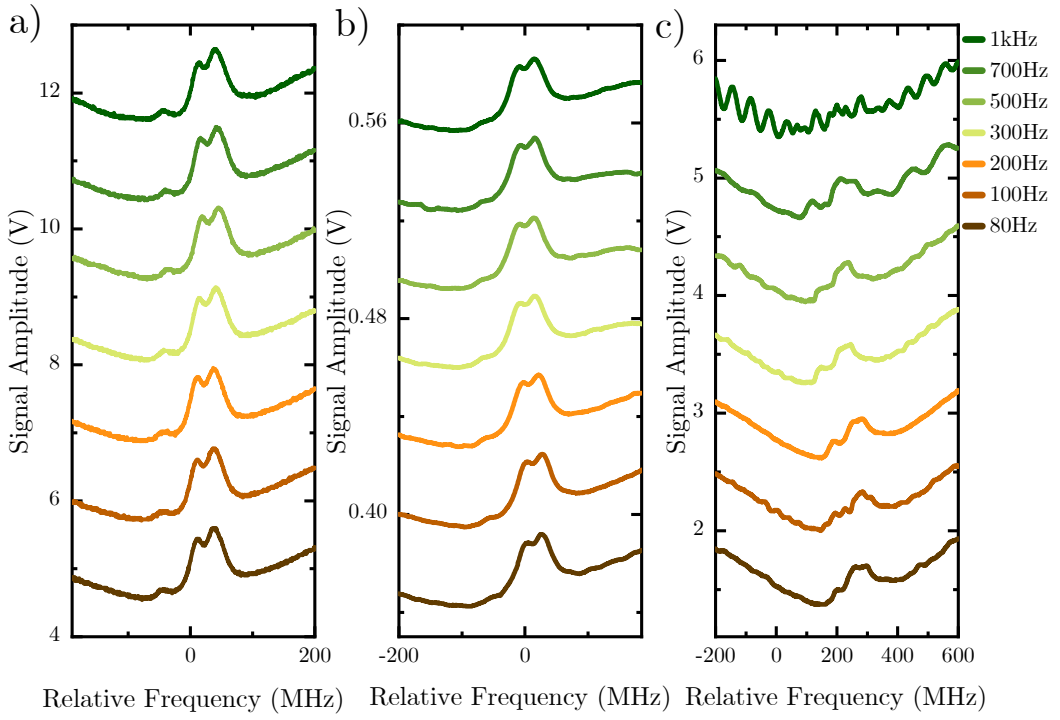

Figure D.2: *The effect of single-frequency vibrations on the saturated absorption spectroscopy of the* ^{85}*Rb F=3 → F'= 2, 3, and 4 transition signal of (a) the AM optical framework directly exposed to the vibrations, (b) the AM CSPD device introduced in Chapter 4, and (c) a conventional setup constructed on the other side of the same optical bench. As can be seen, the compact AM systems exhibit a high level of resistance to vibrational disturbance, unlike the conventional setup.*

Bibliography

[1] T. W. Hänsch and A. L. Schawlow, "Cooling of gases by laser radiation," *Opt. Commun.*, vol. 13, no. 1, pp. 68–69, (1975).

[2] D. J. Wineland, R. E. Drullinger, and F. L. Walls, "Radiation-pressure cooling of bound resonant absorbers," *Phys. Rev. Lett.*, vol. 40, no. 25, p. 1639, (1978).

[3] W. D. Phillips and H. Metcalf, "Laser deceleration of an atomic beam," *Phys. Rev. Lett.*, vol. 48, no. 9, p. 596, (1982).

[4] P. D. Lett, R. N. Watts, C. I. Westbrook, W. D. Phillips, P. L. Gould, and H. J. Metcalf, "Observation of atoms laser cooled below the doppler limit," *Phys. Rev. Lett.*, vol. 61, no. 2, p. 169, (1988).

[5] E. L. Raab, M. Prentiss, A. Cable, S. Chu, and D. E. Pritchard, "Trapping of neutral sodium atoms with radiation pressure," *Phys. Rev. Lett.*, vol. 59, no. 23, p. 2631, (1987).

[6] M. H. Anderson, J. R. Ensher, M. R. Matthews, C. E. Wieman, and E. A. Cornell, "Observation of bose-einstein condensation in a dilute atomic vapor," *Science*, vol. 269, no. 5221, pp. 198–201, 1995.

[7] L. V. Hau, S. E. Harris, Z. Dutton, and C. H. Behroozi, "Light speed reduction to 17 metres per second in an ultracold atomic gas," *Nature*, vol. 397, no. 6720, pp. 594–598, (1999).

[8] M. Kasevich and S. Chu, "Atomic interferometry using stimulated raman transitions," *Phys. Rev. Lett.*, vol. 67, no. 2, p. 181, (1991).

[9] T. Schuldt, C. Schubert, M. Krutzik, L. G. Bote, N. Gaaloul, J. Hartwig, H. Ahlers, W. Herr, K. Posso-Trujillo, J. Rudolph, S. Seidel, T. Wendrich, W. Ertmer, S. Herrmann, A. Kubelka-Lange, A. Milke, B. Rievers, E. Rocco, A. Hinton, K. Bongs, M. Oswald, M. Franz, M. Hauth, A. Peters, and E. Rasel, "Design of a dual species atom interferometer for space," *Exp. Astron.*, vol. 39, no. 2, pp. 167–206, (2015).

[10] B. Stray, A. Lamb, A. Kaushik, J. Vovrosh, A. Rodgers, J. Winch, F. Hayati, D. Boddice, A. Stabrawa, A. Niggebaum, M. Langlois, Y.-H. Lien, S. Lellouch, S. Roshanmanesh, K. Ridley, G. de Villiers, G. Brown, T. Cross, G. Tuckwell, A. Faramarzi, N. Metje, K. Bongs, and M. Holynski, "Quantum sensing for gravity cartography," *Nature*, vol. 602, no. 7898, pp. 590–594, (2022).

[11] I. Buluta, S. Ashhab, and F. Nori, "Natural and artificial atoms for quantum computation," *Rep. Prog. Phys.*, vol. 74, no. 10, p. 104401, (2011).

[12] H. Levine, A. Keesling, G. Semeghini, A. Omran, T. T. Wang, S. Ebadi, H. Bernien, M. Greiner, V. Vuletić, H. Pichler, and M. D. Lukin, "Parallel implementation of high-fidelity multiqubit gates with neutral atoms," *Phys. Rev. Lett.*, vol. 123, no. 17, p. 170503, (2019).

[13] L. Henriet, L. Beguin, A. Signoles, T. Lahaye, A. Browaeys, G.-O. Reymond, and C. Jurczak, "Quantum computing with neutral atoms," *Quantum*, vol. 4, p. 327, (2020).

[14] E. R. Elliott, M. C. Krutzik, J. R. Williams, R. J. Thompson, and D. C. Aveline, "Nasa's cold atom lab (cal): system development and ground test status," *NPJ Microgravity*, vol. 4, no. 1, pp. 1–7, (2018).

[15] S. Dörscher, A. Thobe, B. Hundt, A. Kochanke, R. Le Targat, P. Windpassinger, C. Becker, and K. Sengstock, "Creation of quantum-degenerate gases of ytterbium in a compact 2D-/3D-magneto-optical trap setup," *Rev. Sci. Instrum.*, vol. 84, no. 4, p. 043109, (2013).

[16] D. R. Scherer, R. Lutwak, M. Mescher, R. Stoner, B. Timmons, F. Rogomentich, G. Tepolt, S. Mahnkopf, J. Noble, S. Chang, and D. Taylor, "Progress on a miniature cold-atom frequency standard," in *Proceedings of the 46th Annual Precise Time and Time Interval Systems and Applications Meeting*, pp. 154–163, (2014).

[17] R. Folman, P. Treutlein, and J. Schmiedmayer, "Atom chip fabrication," *Atom Chips*, pp. 61–117, (2011).

[18] C. S. Nichols, L. M. Nofs, M. A. Viray, L. Ma, E. Paradis, and G. Raithel, "Magneto-optical trap with millimeter ball lenses," *Phys. Rev. Appl.*, vol. 14, no. 4, p. 044013, (2020).

[19] C. Nshii, M. Vangeleyn, J. P. Cotter, P. F. Griffin, E. Hinds, C. N. Ironside, P. See, A. Sinclair, E. Riis, and A. S. Arnold, "A surface-patterned chip as a strong source of ultracold atoms for quantum technologies," *Nat. Nanotechnol.*, vol. 8, no. 5, pp. 321–324, (2013).

[20] K. Lee, J. Kim, H. Noh, and W. Jhe, "Single-beam atom trap in a pyramidal and conical hollow mirror," *Opt. Lett.*, vol. 21, no. 15, pp. 1177–1179, (1996).

[21] B. Xu, X. Chen, J. Wang, and M. Zhan, "Realization of a single-beam mini magneto-optical trap: A candidate for compact cpt cold atom-clocks," *Opt. Commun.*, vol. 281, no. 23, pp. 5819–5823, (2008).

[22] J. Rushton, M. Aldous, and M. Himsworth, "Contributed review: the feasibility of a fully miniaturized magneto-optical trap for portable ultracold quantum technology," *Rev. Sci. Instrum.*, vol. 85, no. 12, p. 121501, (2014).

[23] J. Kitching, "Chip-scale atomic devices," *Appl. Phys. Rev.*, vol. 5, no. 3, p. 031302, (2018).

[24] K. Bongs, M. Holynski, J. Vovrosh, P. Bouyer, G. Condon, E. Rasel, C. Schubert, W. P. Schleich, and A. Roura, "Taking atom interferometric quantum sensors from the laboratory to real-world applications," *Nat. Rev. Phys.*, vol. 1, no. 12, pp. 731–739, (2019).

[25] G. Rosi, F. Sorrentino, L. Cacciapuoti, M. Prevedelli, and G. Tino, "Precision measurement of the newtonian gravitational constant using cold atoms," *Nature*, vol. 510, no. 7506, pp. 518–521, (2014).

[26] P. Gillot, B. Cheng, A. Imanaliev, S. Merlet, and F. P. Dos Santos, "The LNE-SYRTE cold atom gravimeter," in *2016 European Frequency and Time Forum (EFTF)*, pp. 1–3, IEEE, (2016).

[27] R. H. Parker, C. Yu, W. Zhong, B. Estey, and H. Müller, "Measurement of the fine-structure constant as a test of the standard model," *Science*, vol. 360, no. 6385, pp. 191–195, (2018).

[28] V. Ménoret, P. Vermeulen, N. Le Moigne, S. Bonvalot, P. Bouyer, A. Landragin, and B. Desruelle, "Gravity measurements below 10- 9 g with a transportable absolute quantum gravimeter," *Sci. Rep.*, vol. 8, no. 1, pp. 1–11, (2018).

[29] R. Kaltenbaek, A. Acin, L. Bacsardi, P. Bianco, P. Bouyer, E. Diamanti, C. Marquardt, Y. Omar, V. Pruneri, E. Rasel, B. Sang, S. Seidel, H. Ulbricht, R. Ursin, P. Villoresi, M. van den Bossche, W. von Klitzing, H. Zbinden, M. Paternostro, and A. Bassi, "Quantum technologies in space," *Exp. Astron.*, vol. 51, no. 3, pp. 1677–1694, (2021).

[30] T. van Zoest, N. Gaaloul, Y. Singh, H. Ahlers, W. Herr, S. Seidel, W. Ertmer, E. Rasel, M. Eckart, E. Kajari, S. Arnold, G. Nandi, W. Schleich, R. Walser, A. Vogel, K. Sengstock, K. Bongs, W. Lewoczko-Adamczyk, M. Schiemangk, T. Schuldt, A. Peters, T. Könemann, H. Müntinga, C. Lämmerzahl, H. Dittus, T. Steinmetz, T. Hänsch, and J. Reichel, "Bose-Einstein condensation in microgravity," *Science*, vol. 328, no. 5985, pp. 1540–1543, (2010).

[31] S. Seidel, D. Becker, J. Grosse, M. Lachmann, M. Popp, T. Wendrich, E. Rasel, and Q. Collaboration, "Atom interferometry on sounding rockets," in *22nd ESA Symposium on European Rocket and Balloon Programmes and Related Research*, vol. 730, p. 309, (2015).

[32] D. Becker, M. D. Lachmann, S. T. Seidel, H. Ahlers, A. N. Dinkelaker, J. Grosse, O. Hellmig, H. Müntinga, V. Schkolnik, T. Wendrich, A. Wenzlawski, B. Weps, R. Corgier, T. Franz, N. Gaaloul, W. Herr, D. Lüdtke, M. Popp, S. Amri, H. Duncker, M. Erbe, A. Kohfeldt, A. Kubelka-Lange, C. Braxmaier, E. Charron, W. Ertmer, M. Krutzik, C. Lämmerzahl, A. Peters, W. P. Schleich, K. Sengstock, R. Walser, A. Wicht, P. Windpassinger, and E. M. Rasel, "Space-borne Bose–Einstein condensation for precision interferometry," *Nature*, vol. 562, no. 7727, pp. 391–395, (2018).

[33] B. Piest, W. Bartosch, J. Böhm, M. Lachmann, M. Misslisch, V. Vollenkemper, T. Wendrich, E. Rasel, and Q. Team, "Maius-b: Towards dual species matter wave interferometry in space," in *APS Division of Atomic, Molecular and Optical Physics Meeting Abstracts*, vol. 2020, pp. D07–006, (2020).

[34] D. Devani, S. Maddox, R. Renshaw, N. Cox, H. Sweeney, T. Cross, M. Holynski, R. Nolli, J. Winch, K. Bongs, K. Holland, D. Colebrook, N. Adams, K. Quillien, J. Buckle, A. Karde, M. Farries, T. Legg, R. Webb, C. Gawith, S. A. Berry, and L. Carpenter, "Gravity sensing: cold atom trap onboard a 6U cubesat," *CEAS Space J.*, vol. 12, no. 4, pp. 539–549, (2020).

[35] E. Gibney, "Universe's coolest lab set to open up quantum world," *Nature*, vol. 557, no. 7704, pp. 151–152, (2018).

[36] L. Liu, D.-S. Lü, W.-B. Chen, T. Li, Q.-Z. Qu, B. Wang, L. Li, W. Ren, Z.-R. Dong, J.-B. Zhao, W.-B. Xia, X. Zhao, J.-W. Ji, M.-F. Ye, Y.-G. Sun, Y.-Y. Yao, D. Song, Z.-G. Liang, S.-J. Hu, D.-H. Yu, X. Hou, W. Shi, H.-G. Zang, J.-F. Xiang, X.-K. Peng, and Y.-Z. Wang, "In-orbit operation of an atomic clock based on laser-cooled 87Rb atoms," *Nat. Commun.*, vol. 9, no. 1, pp. 1–8, (2018).

[37] W. Chaibi, R. Geiger, B. Canuel, A. Bertoldi, A. Landragin, and P. Bouyer, "Low frequency gravitational wave detection with ground-based atom interferometer arrays," *Phys. Rev. D*, vol. 93, no. 2, p. 021101, (2016).

[38] A. Hinton, M. Perea-Ortiz, J. Winch, J. Briggs, S. Freer, D. Moustoukas, S. Powell-Gill, C. Squire, A. Lamb, C. Rammeloo, B. Stray, G. Voulazeris, L. Zhu, A. Kaushik, Y.-H. Lien, A. Niggebaum, A. Rodgers, A. Stabrawa, D. Boddice, S. R. Plant, G. W. Tuckwell, K. Bongs, N. Metje, and M. Holynski, "A portable magneto-optical trap with prospects for atom interferometry in civil engineering," *Philosophical Transactions of the Royal Society A: Mathematical, Physical and Engineering Sciences*, vol. 375, no. 2099, p. 20160238, (2017).

[39] L. Earl, J. Vovrosh, M. Wright, D. Roberts, J. Winch, M. Perea-Ortiz, A. Lamb, F. Hayati, P. Griffin, N. Metje, K. Bongs, and M. Holynski, "Demonstration of a compact magneto-optical trap on an unstaffed aerial vehicle," *Atoms*, vol. 10, no. 1, p. 32, (2022).

[40] A. Bregazzi, S. Dyer, P. F. Griffin, D. P. Burt, A. S. Arnold, E. Riis, and J. P. McGilligan, "Enabling the mass production of a chip-scale laser cooling platform," vol. 11881, pp. 100–110, SPIE, (2021).

[41] S. Knappe, P. Schwindt, V. Shah, L. Hollberg, J. Kitching, L. Liew, and J. Moreland, "A chip-scale atomic clock based on 87Rb with improved frequency stability," *Opt. Express.*, vol. 13, no. 4, pp. 1249–1253, (2005).

[42] S. Knappe, V. Gerginov, P. Schwindt, V. Shah, H. Robinson, L. Hollberg, and J. Kitching, "Atomic vapor cells for chip-scale atomic clocks

with improved long-term frequency stability," *Opt. Lett.*, vol. 30, no. 18, pp. 2351–2353, (2005).

[43] M. F. Riedel, D. Binosi, R. Thew, and T. Calarco, "The european quantum technologies flagship programme," *Quantum Sci. Technol.*, vol. 2, no. 3, p. 030501, (2017).

[44] J. Denschlag, D. Cassettari, A. Chenet, S. Schneider, and J. Schmiedmayer, "A neutral atom and a wire: towards mesoscopic atom optics," *Appl. Phys. B*, vol. 69, no. 4, pp. 291–301, (1999).

[45] J. Fortagh, H. Ott, A. Grossmann, and C. Zimmermann, "Miniaturized magnetic guide for neutral atoms," *Appl. Phys. B*, vol. 70, no. 5, pp. 701–708, (2000).

[46] A. Haase, D. Cassettari, B. Hessmo, and J. Schmiedmayer, "Trapping neutral atoms with a wire," *Phys. Rev. A*, vol. 64, no. 4, p. 043405, (2001).

[47] J. Reichel, W. Hänsel, P. Hommelhoff, and T. Hänsch, "Applications of integrated magnetic microtraps," *Appl. Phys. B*, vol. 72, no. 1, pp. 81–89, (2001).

[48] J. Fortágh and C. Zimmermann, "Magnetic microtraps for ultracold atoms," *Rev. Mod. Phys.*, vol. 79, no. 1, p. 235, (2007).

[49] M. Keil, O. Amit, S. Zhou, D. Groswasser, Y. Japha, and R. Folman, "Fifteen years of cold matter on the atom chip: promise, realizations, and prospects," *J. Mod. Opt.*, vol. 63, no. 18, pp. 1840–1885, (2016).

[50] R. Saint, W. Evans, Y. Zhou, T. Barrett, T. Fromhold, E. Saleh, I. Maskery, C. Tuck, R. Wildman, F. Oručević, and P. Krüger, "3D-printed components for quantum devices," *Sci. Rep.*, vol. 8, no. 1, pp. 1–9, (2018).

[51] P. Hobson, J. Vovrosh, B. Stray, M. Packer, J. Winch, N. Holmes, F. Hayati, K. McGovern, R. Bowtell, M. Brookes, K. Bongs, T. M. Fromhold, and M. Holynski, "Bespoke magnetic field design for a magnetically shielded cold atom interferometer," *arXiv preprint arXiv:2110.04498*, (2021).

[52] M. Packer, P. Hobson, A. Davis, N. Holmes, J. Leggett, P. Glover, N. Hardwicke, M. Brookes, R. Bowtell, and T. Fromhold, "Magnetic field design in a cylindrical high-permeability shield: The combination of simple building blocks and a genetic algorithm," *J. Appl. Phys.*, vol. 131, no. 9, p. 093902, (2022).

[53] S. Kulas, C. Vogt, A. Resch, J. Hartwig, S. Ganske, J. Matthias, D. Schlippert, T. Wendrich, W. Ertmer, E. Maria Rasel, M. Damjanic, P. Weßels, A. Kohfeldt, E. Luvsandamdin, M. Schiemangk, C. Grzeschik, M. Krutzik, A. Wicht, A. Peters, S. Herrmann, and C. Lämmerzahl, "Miniaturized lab system for future cold atom experiments in microgravity," *Microgravity Sci. Technol.*, vol. 29, no. 1-2, pp. 37–48, (2017).

[54] Y.-C. Zhang, J.-Z. Wu, Y.-Q. Li, J. Ma, L.-R. Wang, Y.-T. Zhao, L.-T. Xiao, and S.-T. Jia, "Dependence of loading time on control parameters in a standard vapour—loaded magneto—optical trap," *Chin. Phys. B.*, vol. 20, p. 123701, 2011.

[55] J. Vovrosh, G. Voulazeris, P. G. Petrov, J. Zou, Y. Gaber, L. Benn, D. Woolger, M. M. Attallah, V. Boyer, K. Bongs, and M. Holynski, "Additive manufacturing of magnetic shielding and ultra-high vacuum flange for cold atom sensors," *Sci. Rep.*, vol. 8, no. 1, pp. 1–10, (2018).

[56] P. Manini, A. Conte, L. Viale, A. Bonucci, F. Siviero, and L. Caruso, "A novel approach in UHV pumping of accelerators: the nextorr® pump," *Proceedings of IPAC*, vol. 11, pp. 04–09, (2011).

[57] J. P. McGilligan, K. Moore, A. Dellis, G. Martinez, E. de Clercq, P. Griffin, A. Arnold, E. Riis, R. Boudot, and J. Kitching, "Laser cooling in a chip-scale platform," *App. Phys. Lett.*, vol. 117, no. 5, p. 054001, (2020).

[58] D. L. Butts, J. M. Kinast, B. P. Timmons, and R. E. Stoner, "Light pulse atom interferometry at short interrogation times," *JOSA B*, vol. 28, no. 3, pp. 416–421, (2011).

[59] P. A. Altin, M. T. Johnsson, V. Negnevitsky, G. R. Dennis, R. P. Anderson, J. E. Debs, S. S. Szigeti, K. S. Hardman, S. Bennetts, G. D. McDonald, L. D. Turner, J. D. Close, and N. P. Robins, "Precision atomic gravimeter based on bragg diffraction," *New J. Phys.*, vol. 15, no. 2, p. 023009, (2013).

[60] K. Weng, B. Wu, J. Lin, Y. Zhou, B. Cheng, and Q. Lin, "Compact magneto-optical trap with a quartz vacuum chamber for miniature gravimeters," *JOSA B*, vol. 37, no. 6, pp. 1637–1642, (2020).

[61] S. Kang, R. P. Mott, K. A. Gilmore, L. D. Sorenson, M. T. Rakher, E. A. Donley, J. Kitching, and C. S. Roper, "A low-power reversible alkali atom source," *App. Phys. Lett.*, vol. 110, no. 24, p. 244101, (2017).

[62] D. R. Scherer, D. B. Fenner, and J. M. Hensley, "Characterization of alkali metal dispensers and non-evaporable getter pumps in ultrahigh vacuum systems for cold atomic sensors," *J. Vac. Sci. Technol*, vol. 30, no. 6, p. 061602, (2012).

[63] L. Torralbo-Campo, G. D. Bruce, G. Smirne, and D. Cassettari, "Light-induced atomic desorption in a compact system for ultracold atoms," *Sci. Rep.*, vol. 5, no. 1, pp. 1–10, (2015).

[64] A. Basu and L. F. Velásquez-García, "An electrostatic ion pump with nanostructured si field emission electron source and ti particle collectors for supporting an ultra-high vacuum in miniaturized atom interferometry systems," *J. Micromech. Microeng.*, vol. 26, no. 12, p. 124003, (2016).

[65] C. Monroe, W. Swann, H. Robinson, and C. Wieman, "Very cold trapped atoms in a vapor cell," *Phys Rev Lett.*, vol. 65, pp. 1571–1574, 1990.

[66] J. Weiner, V. S. Bagnato, S. Zilio, and P. S. Julienne, "Experiments and theory in cold and ultracold collisions," *Rev. Mod. Phys.*, vol. 71, no. 1, p. 1, (1999).

[67] T. Arpornthip, C. Sackett, and K. Hughes, "Vacuum-pressure measurement using a magneto-optical trap," *Phys. Rev. A*, vol. 85, no. 3, p. 033420, (2012).

[68] S. Bartalini, I. Herrera, L. Consolino, L. Pappalardo, N. Marino, G. D'Arrigo, and F. Cataliotti, "Full characterization of the loading of a magneto–optical trap from an alkali metal dispenser," *Eur. phys. j., D, At. mol. opt.*, vol. 36, no. 1, pp. 101–104, (2005).

[69] J. Bjorkholm, "Collision-limited lifetimes of atom traps," *Phys. Rev. A*, vol. 38, no. 3, p. 1599, (1988).

[70] A. Cable, M. Prentiss, and N. Bigelow, "Observations of sodium atoms in a magnetic molasses trap loaded by a continuous uncooled source," *Opt. Lett.*, vol. 15, no. 9, pp. 507–509, (1990).

[71] D. E. Fagnan, J. Wang, C. Zhu, P. Djuricanin, B. G. Klappauf, J. L. Booth, and K. W. Madison, "Observation of quantum diffractive collisions using shallow atomic traps," *Phys. Rev. A*, vol. 80, 2009.

[72] J. Van Dongen, C. Zhu, D. Clement, G. Dufour, J. Booth, and K. Madison, "Trap-depth determination from residual gas collisions," *Phys. Rev. A*, vol. 84, no. 2, p. 022708, (2011).

[73] R. W. Moore, L. A. Lee, E. A. Findlay, L. Torralbo-Campo, G. D. Bruce, and D. Cassettari, "Measurement of vacuum pressure with a magneto-optical trap: A pressure-rise method," *Rev. Sci. Instrum.*, vol. 86, no. 9, p. 093108, (2015).

[74] O. S. Burrow, P. F. Osborn, E. Boughton, F. Mirando, D. P. Burt, P. F. Griffin, A. S. Arnold, and E. Riis, "Stand-alone vacuum cell for compact ultracold quantum technologies," *App. Phys. Lett.*, vol. 119, p. 124002, 2021.

[75] B. J. Little, G. W. Hoth, J. Christensen, C. Walker, D. J. De Smet, G. W. Biedermann, J. Lee, and P. D. Schwindt, "A passively pumped vacuum package sustaining cold atoms for more than 200 days," *AVS Quantum Science*, vol. 3, no. 3, p. 035001, (2021).

[76] W. Ren, J. Xiang, Y. Zhang, B. Wang, Q. Qu, J. Zhao, M. Ye, D. Lü, and L. Liu, "Development of an ultra-high vacuum system for space cold atom clock," *Vacuum*, vol. 116, pp. 54–59, (2015).

[77] D. Świerad, S. Häfner, S. Vogt, B. Venon, D. Holleville, S. Bize, A. Kulosa, S. Bode, Y. Singh, K. Bongs, E. M. Rasel, J. Lodewyck, R. Le Targat, C. Lisdat, and U. Sterr, "Ultra-stable clock laser system development towards space applications," *Sci Rep*, vol. 6, p. 33973, 2016.

[78] Q. Liu, Y. Xie, L. Li, J. Xiang, W. Wang, Q. Qu, S. Fang, B. Wang, D. Lü, and L. Liu, "Development of an ultra-high vacuum system for a cold atom physics rack in space," *Vacuum*, vol. 190, p. 110192, (2021).

[79] G. Zhang, J. Y. Haw, H. Cai, F. Xu, S. Assad, J. F. Fitzsimons, X. Zhou, Y. Zhang, S. Yu, J. Wu, W. Ser, L. Kwek, and A. Liu, "An integrated silicon photonic chip platform for continuous-variable quantum key distribution," *Nat. Photonics*, vol. 13, no. 12, pp. 839–842, (2019).

[80] S. Madkhaly, L. Coles, C. Morley, C. Colquhoun, T. Fromhold, N. Cooper, and L. Hackermüller, "Performance-optimized components for quantum technologies via additive manufacturing," *PRX Quantum*, vol. 2, no. 3, p. 030326, (2021).

[81] N. Cooper, L. Coles, S. Everton, I. Maskery, R. Campion, S. Madkhaly, C. Morley, J. O'Shea, W. Evans, R. Saint, P. Krüger, F. Oručević, C. Tuck, R. Wildman, T. Fromhold, and L. Hackermüller, "Additively manufactured ultra-high vacuum chamber for portable quantum technologies," *Addit. Manuf.*, vol. 40, p. 101898, 2021.

[82] R. Folman, P. Krüger, J. Schmiedmayer, J. Denschlag, and C. Henkel, "Microscopic atom optics: From wires to an atom chip," *Adv. At. Mol. Opt. Phys.*, vol. 48, pp. 263–356, (2002).

[83] S. Eriksson, M. Trupke, H. Powell, D. Sahagun, C. Sinclair, E. Curtis, B. Sauer, E. Hinds, Z. Moktadir, C. Gollasch, and M. Kraft, "Integrated optical components on atom chips," *Eur. Phys. J. D.*, vol. 35, no. 1, pp. 135–139, (2005).

[84] M. Trupke, E. A. Hinds, S. Eriksson, E. Curtis, Z. Moktadir, E. Kukharenka, and M. Kraft, "Microfabricated high-finesse optical cavity with open access and small volume," *Appl. Phys. Lett.*, vol. 87, no. 21, p. 211106, (2005).

[85] M. Trupke, F. Ramirez-Martinez, E. Curtis, J. Ashmore, S. Eriksson, E. A. Hinds, Z. Moktadir, C. Gollasch, M. Kraft, G. Vijaya Prakash, and J. J. Baumberg, "Pyramidal micromirrors for microsystems and atom chips," *Appl. Phys. Lett.*, vol. 88, no. 7, p. 071116, (2006).

[86] F. Shimizu, K. Shimizu, and H. Takuma, "Four-beam laser trap of neutral atoms," *Opt. Lett.*, vol. 16, no. 5, pp. 339–341, (1991).

[87] K. Dieckmann, R. Spreeuw, M. Weidemüller, and J. Walraven, "Two-dimensional magneto-optical trap as a source of slow atoms," *Phys. Rev. A*, vol. 58, no. 5, p. 3891, (1998).

[88] J. Reichel, W. Hänsel, and T. Hänsch, "Atomic micromanipulation with magnetic surface traps," *Phys. Rev. Lett.*, vol. 83, no. 17, p. 3398, (1999).

[89] R. Folman, P. Krüger, D. Cassettari, B. Hessmo, T. Maier, and J. Schmiedmayer, "Controlling cold atoms using nanofabricated surfaces: atom chips," *Phys. Rev. Lett.*, vol. 84, no. 20, p. 4749, (2000).

[90] S. Wildermuth, P. Krüger, C. Becker, M. Brajdic, S. Haupt, A. Kasper, R. Folman, and J. Schmiedmayer, "Optimized magneto-optical trap for experiments with ultracold atoms near surfaces," *Phys. Rev. A*, vol. 69, no. 3, p. 030901, (2004).

[91] R. Roy, J. Rushton, A. Dragomir, M. Aldous, and M. Himsworth, "A misaligned magneto-optical trap to enable miniaturized atom chip systems," *Sci. Rep.*, vol. 8, no. 1, pp. 1–7, (2018).

[92] R. Chutani, V. Maurice, N. Passilly, C. Gorecki, R. Boudot, M. Abdel Hafiz, P. Abbé, S. Galliou, J.-Y. Rauch, and E. De Clercq, "Laser light routing in an elongated micromachined vapor cell with diffraction gratings for atomic clock applications," *Sci. Rep.*, vol. 5, no. 1, pp. 1–12, (2015).

[93] L. Stern, D. G. Bopp, S. A. Schima, V. N. Maurice, and J. E. Kitching, "Chip-scale atomic diffractive optical elements," *Nat. Commun.*, vol. 10, no. 1, pp. 1–7, (2019).

[94] V. A. Henderson, M. Y. Johnson, Y. B. Kale, P. F. Griffin, E. Riis, and A. S. Arnold, "Optical characterisation of micro-fabricated fresnel zone plates for atomic waveguides," *Opt. Express.*, vol. 28, no. 7, pp. 9072–9081, (2020).

[95] L. Zhu, X. Liu, B. Sain, M. Wang, C. Schlickriede, Y. Tang, J. Deng, K. Li, J. Yang, M. Holynski, S. Zhang, T. Zentgraf, K. Bongs, Y.-H. Lien, and G. Li, "A dielectric metasurface optical chip for the generation of cold atoms," *Sci. Adv.*, vol. 6, no. 31, p. eabb6667, (2020).

[96] W. R. McGehee, W. Zhu, D. S. Barker, D. Westly, A. Yulaev, N. Klimov, A. Agrawal, S. Eckel, V. Aksyuk, and J. J. McClelland, "Magneto-optical trapping using planar optics," *New J. Phys.*, vol. 23, no. 1, p. 013021, (2021).

[97] J. Bliss, K. Libbrecht, J. Kohel, W. Klipstein, and L. Maleki, "Generation of a cold atom beam from a pyramidal magneto-optical trap," in *Technical Digest. Summaries of Papers Presented at the Quantum Electronics and Laser Science Conference*, p. 73, IEEE, (1992).

[98] M. Vangeleyn, P. F. Griffin, E. Riis, and A. S. Arnold, "Single-laser, one beam, tetrahedral magneto-optical trap," *Opt. Express.*, vol. 17, no. 16, pp. 13601–13608, (2009).

[99] J. Cotter, J. McGilligan, P. Griffin, I. Rabey, K. Docherty, E. Riis, A. Arnold, and E. Hinds, "Design and fabrication of diffractive atom chips for laser cooling and trapping," *Appl. Phys. B*, vol. 122, no. 6, pp. 1–6, (2016).

[100] M. Vangeleyn, P. F. Griffin, E. Riis, and A. S. Arnold, "Laser cooling with a single laser beam and a planar diffractor," *Opt. Lett.*, vol. 35, no. 20, pp. 3453–3455, (2010).

[101] X. Wu, F. Zi, J. Dudley, R. J. Bilotta, P. Canoza, and H. Müller, "Multiaxis atom interferometry with a single-diode laser and a pyramidal magneto-optical trap," *Optica*, vol. 4, no. 12, pp. 1545–1551, (2017).

[102] Q. Bodart, S. Merlet, N. Malossi, F. P. Dos Santos, P. Bouyer, and A. Landragin, "A cold atom pyramidal gravimeter with a single laser beam," *App. Phys. Lett.*, vol. 96, no. 13, p. 134101, (2010).

[103] R. Elvin, G. W. Hoth, M. Wright, B. Lewis, J. P. McGilligan, A. S. Arnold, P. F. Griffin, and E. Riis, "Cold-atom clock based on a diffractive optic," *Opt. Express.*, vol. 27, no. 26, pp. 38359–38366, (2019).

[104] J. Duan, X. Liu, N. Ru, C. Zou, and J. Qu, "Progress of compact CPT Rb atomic clock based on grating magneto-optical trap," in *2020 Conference on Precision Electromagnetic Measurements (CPEM)*, pp. 1–2, IEEE, (2020).

[105] J. McGilligan, K. Gallacher, P. Griffin, D. Paul, A. Arnold, and E. Riis, "Invited review: Micro-fabricated components for cold atom sensors," *Rev. Sci. Instrum.*, vol. 93, no. 9, p. 091101, (2022).

[106] K. J. Boller, A. van Rees, Y. Fan, J. Mak, R. E. Lammerink, C. A. Franken, P. J. van der Slot, D. A. Marpaung, C. Fallnich, J. P. Epping, R. M. Oldenbeuving, D. Geskus, R. Dekker, I. Visscher, R. Grootjans, C. G. Roeloffzen, M. Hoekman, E. J. Klein, A. Leinse, and R. G. Heideman, "Hybrid integrated semiconductor lasers with silicon nitride feedback circuits," in *Photonics*, vol. 7, p. 4, MDPI, (2019).

[107] C. Xiang, W. Jin, J. Guo, J. D. Peters, M. Kennedy, J. Selvidge, P. A. Morton, and J. E. Bowers, "Narrow-linewidth iii-v/si/si 3 n 4 laser using multilayer heterogeneous integration," *Optica*, vol. 7, no. 1, pp. 20–21, (2020).

[108] W. Jin, Q.-F. Yang, L. Chang, B. Shen, H. Wang, M. A. Leal, L. Wu, M. Gao, A. Feshali, M. Paniccia, K. J. Vahala, and J. E. Bowers, "Hertz-linewidth semiconductor lasers using cmos-ready ultra-high-q microresonators," *Nat. Photonics.*, vol. 15, no. 5, pp. 346–353, (2021).

[109] M. T. Hummon, S. Kang, D. G. Bopp, Q. Li, D. A. Westly, S. Kim, C. Fredrick, S. A. Diddams, K. Srinivasan, V. Aksyuk, and J. E. Kitching, "Photonic chip for laser stabilization to an atomic vapor with 10(-11) instability," *Optica*, vol. 5, no. 4, pp. 443–449, (2018).

[110] V. G. Lucivero, A. Zanoni, G. Corrielli, R. Osellame, and M. W. Mitchell, "Laser-written vapor cells for chip-scale atomic sensing and spectroscopy," *Opt. Express.*, vol. 30, no. 15, pp. 27149–27163, (2022).

[111] T. Schuldt, K. Döringshoff, A. Milke, J. Sanjuan, M. Gohlke, E. V. Kovalchuk, N. Gürlebeck, A. Peters, and C. Braxmaier, "High-performance optical frequency references for space," in *J. Phys. Conf. Ser.*, vol. 723, p. 012047, IOP Publishing, (2016).

[112] K. Döringshoff, F. B. Gutsch, V. Schkolnik, C. Kürbis, M. Oswald, B. Pröbster, E. V. Kovalchuk, A. Bawamia, R. Smol, T. Schuldt, M. Lezius, R. Holzwarth, A. Wicht, C. Braxmaier, M. Krutzik, and A. Peters, "Iodine frequency reference on a sounding rocket," *Phys. Rev. Appl.*, vol. 11, no. 5, p. 054068, (2019).

[113] A. Strangfeld, S. Kanthak, M. Schiemangk, B. Wiegand, A. Wicht, A. Ling, and M. Krutzik, "Prototype of a compact rubidium-based optical frequency reference for operation on nanosatellites," *JOSA B*, vol. 38, no. 6, pp. 1885–1891, (2021).

[114] A. Strangfeld, B. Wiegand, J. Kluge, M. Schoch, and M. Krutzik, "Compact plug and play optical frequency reference device based on Doppler-free spectroscopy of rubidium vapor," *Opt. Express.*, vol. 30, no. 7, pp. 12039–12047, (2022).

[115] B. Berman, "3D printing: The new industrial revolution," *Bus. Horiz.*, vol. 55, no. 2, pp. 155–162, (2012).

[116] R. Bogue, "3D printing: the dawn of a new era in manufacturing," *Assem. Autom.*, (2013).

[117] S. Ford and M. Despeisse, "Additive manufacturing and sustainability: an exploratory study of the advantages and challenges," *J. Clean. Prod.*, vol. 137, pp. 1573–1587, (2016).

[118] M. Attaran, "The rise of 3D printing: The advantages of additive manufacturing over traditional manufacturing," *Bus. Horiz*, vol. 60, no. 5, pp. 677–688, (2017).

[119] K. S. Prakash, T. Nancharaih, and V. S. Rao, "Additive manufacturing techniques in manufacturing-an overview," *Mater. Today: Proceedings*, vol. 5, no. 2, pp. 3873–3882, (2018).

[120] J. J. Lewandowski and M. Seifi, "Metal additive manufacturing: a review of mechanical properties," *Annu. Rev. Mater*, vol. 46, pp. 151–186, (2016).

[121] A. Bandyopadhyay, K. D. Traxel, M. Lang, M. Juhasz, N. Eliaz, and S. Bose, "Alloy design via additive manufacturing: Advantages, challenges, applications and perspectives," *Mater. Today*, (2022).

[122] N. T. Aboulkhair, C. Tuck, I. Ashcroft, I. Maskery, and N. M. Everitt, "On the precipitation hardening of selective laser melted alsi10mg," *Metall. Mater. Trans. A*, vol. 46, no. 8, pp. 3337–3341, (2015).

[123] A. P. Povilus, C. J. Wurden, Z. Vendeiro, M. Baquero-Ruiz, and J. Fajans, "Vacuum compatibility of 3D-printed materials," *JVST A: Vacuum, Surfaces, and Films*, vol. 32, no. 3, p. 033001, (2014).

[124] S. Jenzer, M. Alves, N. Delerue, A. Gonnin, D. Grasset, F. Letellier-Cohen, B. Mercier, E. Mistretta, C. Prevost, A. Vion, and J.-P. Wilmes,

"Study of the suitability of 3D printing for ultra-high vacuum applications," in *J. Phys. Conf. Ser.*, vol. 874, p. 012097, IOP Publishing, (2017).

[125] A. R. Gans, M. M. Jobbins, D. Y. Lee, and S. Alex Kandel, "Vacuum compatibility of silver and titanium parts made using three-dimensional printing," *J. Vac. Sci. Technol*, vol. 32, no. 2, p. 023201, (2014).

[126] Y. Zhou, N. Welch, R. Crawford, F. Oručević, F. Wang, P. Krüger, R. Wildman, C. Tuck, and T. M. Fromhold, "Design of magneto-optical traps for additive manufacture by 3D printing," *arXiv preprint arXiv:1704.00430*, (2017).

[127] A. A. Martin, M. Toth, and I. Aharonovich, "Subtractive 3D printing of optically active diamond structures," *Sci. Rep.*, vol. 4, no. 1, pp. 1–4, (2014).

[128] M. Sartison, K. Weber, S. Thiele, L. Bremer, S. Fischbach, T. Herzog, S. Kolatschek, M. Jetter, S. Reitzenstein, A. Herkommer, P. Michler, S. L. Portalupi, and H. Giessen, "3D printed micro-optics for quantum technology: Optimised coupling of single quantum dot emission into a single-mode fibre," *Light: Adv. Manuf.*, vol. 2, no. 2, p. 103, (2021).

[129] S. H. Park, R. Su, J. Jeong, S.-Z. Guo, K. Qiu, D. Joung, F. Meng, and M. C. McAlpine, "3D printed polymer photodetectors," *Adv. Mater.*, vol. 30, no. 40, p. 1803980, 2018.

[130] S. Madkhaly, N. Cooper, L. Coles, and L. Hackermüller, "High-performance, additively-manufactured atomic spectroscopy apparatus for portable quantum technologies," *Opt. Express.*, vol. 30, pp. 25753–25764, (2022).

[131] N. Cooper, S. Madkhaly, D. Johnson, D. Baldolini, and L. Hackermüller, "Dual-frequency Doppler-free spectroscopy for compact atomic physics experiments," *arXiv preprint arXiv:2106.11014*, (2021).

[132] H. J. Metcalf and P. van der Straten, *Laser Cooling and Trapping*. Springer-Verlag, (1999).

[133] D. A. Steck, *Quantum and atom optics*. (2007).

[134] D. A. Steck, "Alkali D line data," (1998).

[135] I. Georgescu, "Rubidium round-the-clock," *Nature chemistry*, vol. 7, no. 12, pp. 1034–1034, (2015).

[136] W. Ketterle, "Nobel lecture: When atoms behave as waves: Bose-Einstein condensation and the atom laser," *Rev. Mod. Phys.*, vol. 74, no. 4, p. 1131, (2002).

[137] A. L. Migdall, J. V. Prodan, W. D. Phillips, T. H. Bergeman, and H. J. Metcalf, "First observation of magnetically trapped neutral atoms," *Phys. Rev. lett.*, vol. 54, no. 24, p. 2596, (1985).

[138] C. Foot, *Atomic and molecular physics*. Oxford university press, (2005).

[139] E. Burt, R. Ghrist, C. Myatt, M. Holland, E. A. Cornell, and C. Wieman, "Coherence, correlations, and collisions: What one learns about Bose-Einstein condensates from their decay," *Phys. Rev. lett.*, vol. 79, no. 3, p. 337, (1997).

[140] T. Weber, J. Herbig, M. Mark, H.-C. Nägerl, and R. Grimm, "Three-body recombination at large scattering lengths in an ultracold atomic gas," *Phys. Rev. lett.*, vol. 91, no. 12, p. 123201, (2003).

[141] K. Overstreet, P. Zabawa, J. Tallant, A. Schwettmann, and J. Shaffer, "Multiple scattering and the density distribution of a cs mot," *Opt. Express.*, vol. 13, no. 24, pp. 9672–9682, (2005).

[142] C. Morley, *Optimisation and simulation of magneto-optical traps for quantum technologies*. PhD thesis, University of Nottingham, (2020).

[143] D. W. Preston, "Doppler-free saturated absorption: Laser spectroscopy," *Am. J. Phys.*, vol. 64, no. 11, pp. 1432–1436, (1996).

[144] U. Schünemann, H. Engler, R. Grimm, M. Weidemüller, and M. Zielonkowski, "Simple scheme for tunable frequency offset locking of two lasers," *Rev. Sci. Instrum.*, vol. 70, no. 1, pp. 242–243, (1999).

[145] G. Puentes, "Laser frequency offset locking scheme for high-field imaging of cold atoms," *Appl. Phys. B*, vol. 107, no. 1, pp. 11–16, (2012).

[146] C. Cohen-Tannoudji and A. Kastler, "I optical pumping," in *Progress in optics*, vol. 5, pp. 1–81, Elsevier, (1966).

[147] C. Townsend, N. Edwards, C. Cooper, K. Zetie, C. Foot, A. Steane, P. Szriftgiser, H. Perrin, and J. Dalibard, "Phase-space density in the magneto-optical trap," *Phys. Rev. A*, vol. 52, no. 2, p. 1423, (1995).

[148] S. Bali, K. O'Hara, M. Gehm, S. Granade, and J. Thomas, "Quantum-diffractive background gas collisions in atom-trap heating and loss," *Phys. Rev. A*, vol. 60, no. 1, p. R29, (1999).

[149] J. F. O'Hanlon, *A user's guide to vacuum technology*. John Wiley & Sons, (2005).

[150] J. Dalibard and C. Cohen-Tannoudji, "Laser cooling below the Doppler limit by polarization gradients: simple theoretical models," *JOSA B*, vol. 6, no. 11, pp. 2023–2045, (1989).

[151] J. Nute, *A quantum integrated light and matter interface*. PhD thesis, University of Nottingham, (2017).

[152] V. Naniyil, *Dynamics of non-equilibrium ^{6}Li Feshbach molecules via magnetic field ramp*. PhD thesis, University of Nottingham, (2021).